UCSF

UC San Francisco Electronic Theses and Dissertations

Title

Ultrathin Zwitterionic Polymer Coatings to Improve Hemocompatibility of Silicon-based Implantable Medical Devices

Permalink

https://escholarship.org/uc/item/75p5c6md

Author

Iqbal, Zohora

Publication Date

2019

Peer reviewed|Thesis/dissertation

Ultrathin Zwitterionic Polymer Coatings to Improve Hemocompatibility for
Silicon-based Implantable Medical Devices

by

Zohora Iqbal

DISSERTATION

Submitted in partial satisfaction of the requirements for the degree of

DOCTOR OF PHILOSOPHY

in

Bioengineering

in the

GRADUATE DIVISION

of the

UNIVERSITY OF CALIFORNIA, SAN FRANCISCO

AND

UNIVERSITY OF CALIFORNIA, BERKELEY

Approved:

....

Committee in Charge

To my Abba and Amma, Quazi Imaduddin and Sabina Iqbal

My sisters, Dola and Era, and my brother, Liton Bhai

My husband, Yeajur

and my daughter, Zoha

I am truly lucky to have all your love and support.

ACKNOWLEDGMENTS

First and foremost, I would like to thank my advisor and mentor, Dr. Shuvo Roy. He took a chance on me and allowed me to pursue a new project in his lab. Under his guidance, I grew as a scientist, learned to think of solutions outside the box, and learned to develop a project from scratch. Dr. Roy was always there to support me in my research, make sense of data that seemed meaningless, and go through countless drafts patiently for publications. His attention to detail and his tenacity is an inspiration for me. More than just in lab, Dr. Roy has been very understanding of my family life, and unbelievably supportive during my pregnancy and health issues. For that, I am very thankful.

I am particularly grateful to Drs. Tejal Desai, Alan Wu, Dorian Liepmann, Randall Lee, and Liang Ge for serving on my qualifying exam and thesis committees. Their time and feedback on the direction of the project over the years was invaluable for me.

I would also like to thank Drs. Rafael Davalos and Amy Herr. When I was a lost undergraduate student, they gave me the opportunity to explore what it is to conduct research. Their encouragement and mentorship allowed me to pursue graduate school and be where I am today.

As I have mentioned, research can be a very grueling, and at many times, disheartening. Roy Lab members are the kind of people who always come forward to help. They go above and beyond to help each other out. When you need to give practice presentation, they are there to be your audience; when you need feedback because an experiment isn't working, they will give you their time and help you think through things; when you need an extra pair of hands for running blood experiments, they are there with gloves on; when you need *blood*, even then they come to offer their veins. Beyond research, they are also there when you are afraid of the mouse running

ABSTRACT

Ultrathin Zwitterionic Polymer Coatings to Improve Hemocompatibility of Silicon-based Implantable Medical Devices

By Zohora Iqbal

Silicon-based bio-microelectromechanical systems (bioMEMS) have become increasingly attractive for medical implants due to their relative low cost and capacity for fabrication of intricate micro- and nanofeatures. However, when silicon surfaces encounter blood, device failure can occur as plasma proteins adhere to the surface and the coagulation cascade is activated leading to thrombosis. Modifying silicon surfaces with hemocompatible coatings may reduce protein adsorption and platelet activation, increasing the lifetime of the implant.

Using bioMEMS technology, our group has developed silicon nanopore membranes (SNMs) for application in bioartificial organs. Highly uniform pores of controllable size make SNMs attractive for immunoisolation and blood filtration. To improve hemocompatibility of SNMs, this dissertation investigates sub-5 nm biomimetic polymer surface coatings. Specifically, two ultrathin zwitterionic coatings, poly(sulfobetaine methacrylate) (pSBMA) and poly(2-methacryloyloxyethyl phosphorylcholine) (pMPC), were developed and characterized via x-ray photoelectron spectroscopy, contact angle, atomic force microscopy and ellipsometry. The coatings were tested under biological shear conditions and after exposure to five standard sterilization methods. Anti-fouling and hemocompatible characteristics of the coatings were

evaluated by measuring protein adsorption from single protein solutions of human serum albumin and fibrinogen, and examining platelet activation after exposure to fresh human blood and implantation in porcine model for up to 26 days.

Characterization results showed successful sub-5 nm pSBMA and pMPC surface modifications. In this thickness range, SNMs remained patent and modified silicon substrates resisted bio-fouling from single protein solutions of human albumin and fibrinogen, with pSBMA reducing protein adsorption by >80% compared to uncoated silicon. Shear data suggests the coatings are robust and functional following shear rates up to 2000/s over 24 hours. Additionally, they withstood sterilization procedures, with best performance of pSBMA and pMPC after electron-beam sterilization and ethylene oxide gas treatment, respectively. Scanning electron microscopy and immunohistochemistry following exposure to fresh human blood flow demonstrated pSBMA-silicon reduced platelet adhesion and activation by >97%. Porcine implants with pSBMA-silicon substrates remained patent over 26 days, with no gross clots in the flow path and minimal presence of blood activation. These promising *in vitro* and *in vivo* results will lead to further studies coupling SNM filtration and surface coatings, as well as clinical testing to determine the human response for use in bioartificial kidney and pancreas device applications.

TABLE OF CONTENTS

Chapter VI: Ultrathin Polybetaine Methacrylate Surface Modification on Silicon: Study

LIST OF TABLES

LIST OF FIGURES

Surface Modifications to Improve Hemocompatibility for Implantable Bioartificial Organs

1.1 Introduction

Over the past 50 years, the electronics industry has led the way in designing semiconductor-based integrated circuits, miniaturizing transistors down to nanoscale features. Leveraging this technology, microelectromechanical systems (MEMS) was developed, allowing for the production of intricate micro- and nanoscale silicon devices with precision and speed. From MEMS, "bioMEMS" was born, utilizing these devices for biological and healthcare applications. In addition to incorporating nanoscale features, these devices can also be integrated with electronics to produce biosensing instruments. Advancement in bioMEMS has allowed for the development of novel tools, paving the way for personalized medicine and point-of-care diagnostic tools such as DNA sequencing,[1] rapid protein analysis,[2,3] and drug delivery.[4]

The semiconductor used in bioMEMS is silicon, which is a relatively inexpensive material widely used in electronics. Silicon is attractive for biological and implant applications because it has been shown to be non-cytotoxic.[5,6] Additionally, various materials pertinent to implantable bioMEMS including silicon, polysilicon and silicon dioxide have been tested against a battery of tests laid out in ISO 10993, and were found to be non-leaching and non-irritant.[7] With these added benefits, a growing number of implants are being designed using silicon as a substrate such as neuroelectrodes,[8,9] drug delivery systems,[4,10,11] biosensors, and diagnostic devices.[12–14]

One such device is the silicon nanopore membrane (SNM), currently being used to develop bioartificial organs for renal replacement[15] and islet therapy.[16] The following section describes SNM and its uses.

1.2 Silicon Nanopore Membrane (SNM)
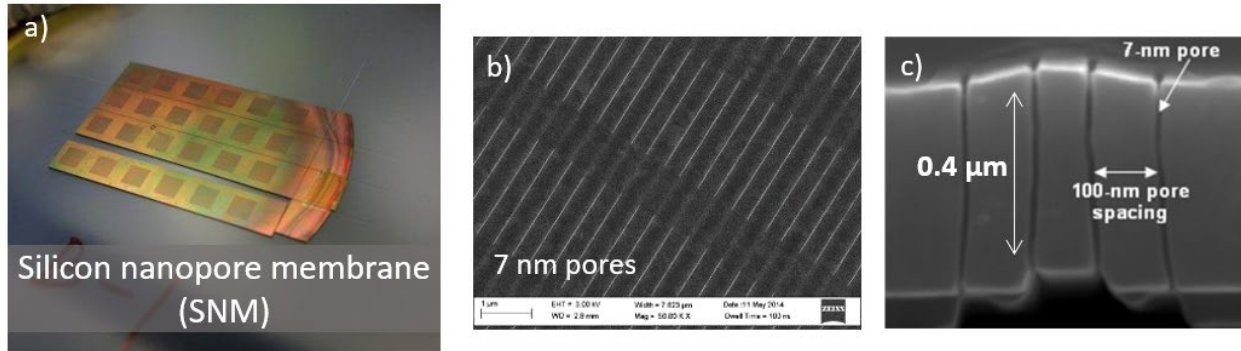
Figure 1.1: Silicon nanopore membrane (SNM). a) Diced as part of a wafer, b) top view under scanning electron microscopy (SEM) showing uniform 7 nm pores, and c) membrane cross-section showing pore height of 0.4 µm with 100 nm pore spacing.

Using MEMS technology, our lab has developed silicon nanopore membranes (SNMs), shown in Figure 1.1. Compared to conventional membranes, SNMs have highly uniform slit-pores that can be controllably tuned down to 5 nm width with less than 1% variation over a 100-mm diameter wafer.[17] The fabrication process is briefly described below (Figure 1.2):[18,19]

a) 500 nm of silicon dioxide (SiO_2) is thermally grown on 400 µm-thick monocrystalline double-side polished silicon substrate (Figure 1.2(a)).

b) 500 nm of undoped polysilicon is deposited at 580 °C using low pressure chemical vapor deposition (LPCVD) and annealed at 1075 °C for an hour (Figure 1.2(b)).

c) Using photolithography, an array of 400 nm wide slits with 400 nm spacing is patterned and dry etched using reactive ion etching (RIE) (Figure 1.2(c)).

d) Based on the desired pore size, x nm, a conformal layer of SiO_2 of x nm thickness is thermally grown at 800 °C (Figure 1.2(d)).

e) A second polysilicon layer of 800 nm thickness is deposited by LPCVD (Figure 1.2(e)).

f) The polysilicon and the top film of the thin oxide layer is blanket-etched until 450 nm of polysilicon remained, and the thin SiO_2 vertical sidewall is exposed (Figure 1.2(f)).

g) Polysilicon and thin layer of SiO_2 is removed from the backside of the wafer and 1 μm of low temperature oxide (LTO) is deposited by LPCVD for protection of membrane features for next steps (Figure 1.2(g)).

h) LTO on the backside of the wafer is used as a hard mask and an array of windows is patterned to create an etch mask for an array of windows.

i) Windows are etched back using deep reactive ion etching (DRIE) (Figure 1.2(h)), and the pores are released in using concentrated hydrofluoric acid (Figure 1.2(i)).
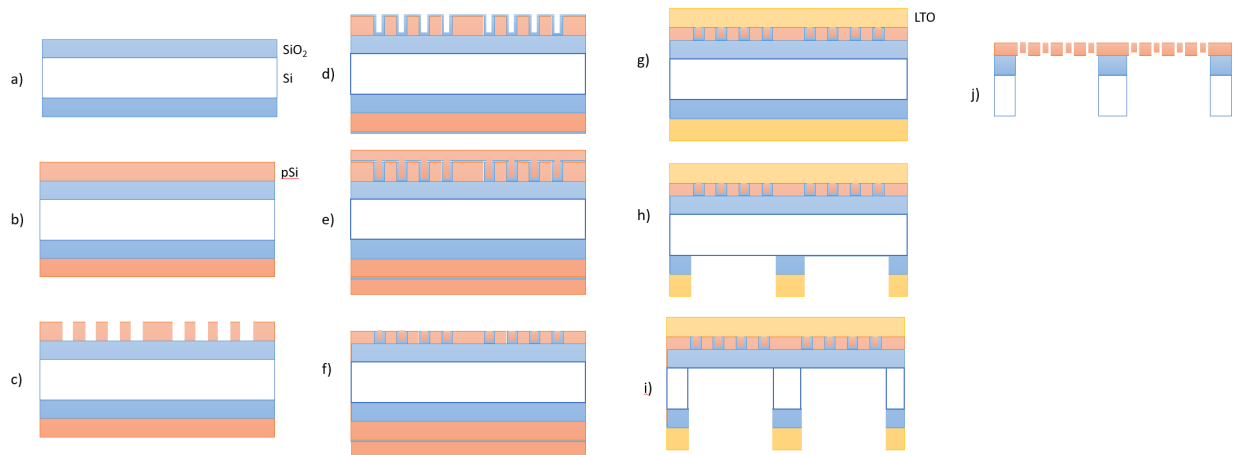
Figure 1.2: Step-wise fabrication process of SNM, with cross-section views shown. Figure not drawn to scale.

Using this process, reproducible, 450 nm-thin nanopore membranes can be produced with tight pore size distribution and minimally tortuous pores. The resulting membrane is highly selective and low resistance to fluid flow. Selectivity is further enhanced by the slit pore design in

3

comparison to cylindrical pores.[20] Because the pores are defined by a thin oxide layer,

controlling the time and temperature during oxide growth can tune the pore size for various

sieving applications. Additionally, the silicon surface can be readily functionalized to alter the

surface chemistry. These traits make SNMs attractive for biological applications such as

filtration and immunoisolation for bioartificial organs.

1.2.1 SNM for Bioartificial Kidney

The kidney is an essential organ whose key function is to filter out excess fluid, electrolytes, and

metabolic waste products from blood. Mainly caused by diabetes and hypertension, end stage

renal disease (ESRD) occurs when kidney function drops below 10% of its normal function.

ESRD has become a major medical concern in the United States due to its increasing incidence

rate, high mortality rate, and management expense. As of 2015, there were >700,000 Americans

suffering from ESRD. However, only ~17,000 patients receive a kidney transplant annually.[21]

Most of these patients rely of hemodialysis, where they are treated in dialysis centers thrice-

weekly in 3-4 hour sessions, resulting in yearly expense of >$88,000 per person.[22] This

treatment regimen allows for toxins to build up periodically between dialysis session, which are

at least two days apart, leading to poor quality of life for patients. Daily-extended hemodialysis,

such as at-home nocturnal hemodialysis, allows patients access to dialysis for at least 6 hours

daily. This increased blood filtration treatment has been linked to improved quality-of-life

indicators and patient outcomes.[23,24]

a)

The Denver Post, 2009

b)
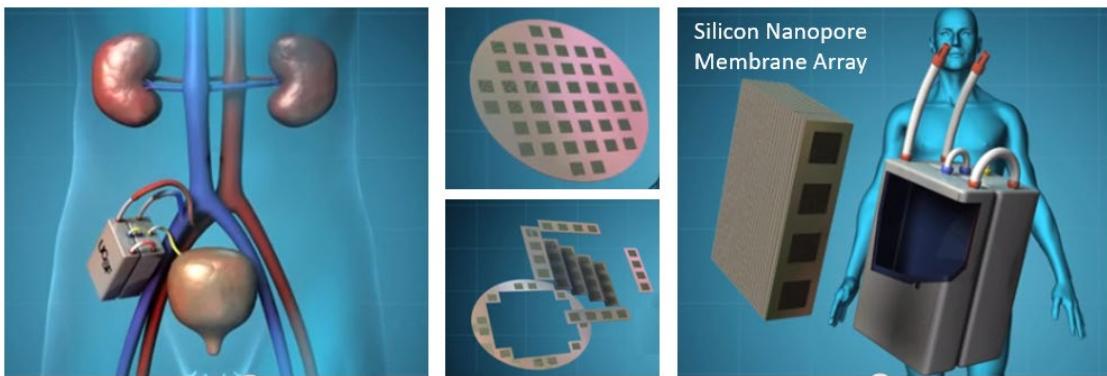
Figure 1.3: *a) Dialysis conducted at dialysis center. b) SNM-based bioartificial kidney: implantable model and housing (left), SNM patterned and diced on silicon wafer (middle), and diced SNMs stacked into implantable bioartificial kidney.*

While daily-extended hemodialysis leads to better patient outcomes compared to the standard-of-care,[24,25] the current healthcare infrastructure cannot support daily-extended hemodialysis as a viable option. Therefore, there is a need to develop novel technologies that can give rise to portable or implantable renal replacement therapy. Polymer membranes used in hemodialysis treatment have wide pore size distribution and require large pressures to drive filtration, limiting permeability and selectivity, as well as possibility of miniaturization.[19] SNMs, on the other hand, offer uniform pores at low resistance for efficient blood filtration, and its use advances the

technology toward the possibility of continuous renal replacement therapy through a portable or implantable device (Figure 1.3). [15,18,26]

1.2.2 SNM for Bioaritificial Pancreas

Type 1 diabetes (T1D), typically diagnosed due to an absolute insulin deficiency, is caused by the destruction of pancreatic β-cells located in the islets of Langerhans.[27] Current treatments of T1D include insulin infusion therapy and pancreas transplant. For insulin infusion therapy, patients are responsible for measuring blood glucose and injecting insulin based on the glucose reading. This method leaves a lot to be desired; usually given in a bolus, the pattern of insulin secretion does not mimic biological insulin release in the body. Additionally, patients are responsible for calculating and setting the amount of insulin needed and human errors can lead to hypo- or hyperglycemia, which can be fatal. Pancreatic transplants, on the other hand, are limited by donor availability. Furthermore, patients with transplant must remain on global immunosuppression to protect the pancreas from the host's immune response.

One approach to overcome immune response is by protecting the graft islets using a semi-permeable membrane. This membrane must allow the passage of glucose, insulin, and nutrients, while blocking cells, proteins, and cytokines associated with immune response. Immune cells— on the order of 10 μm, and large proteins such as antibodies can be blocked by membranes with a molecular cutoff size in the range of 30 nm. However, blocking cytokines such as Tumor Necrosis Factor-alpha (TNF-α), Interferon-gamma (IFN-γ) and Interleukin-1 beta (IL-1β) are also critical as they have been shown to be cytotoxic to islets.[28,29] However, these cytokines have Stokes diameters of ~3-4 nm, making it difficult to separate them from small molecules such as glucose (0.82 nm) and insulin (2.64 nm) using polymeric membranes with broad pore

size distribution.[30] Therefore, to design an implantable bioartificial pancreas, utilizing SNMs is attractive due to their high selectivity (Figure 1.4).
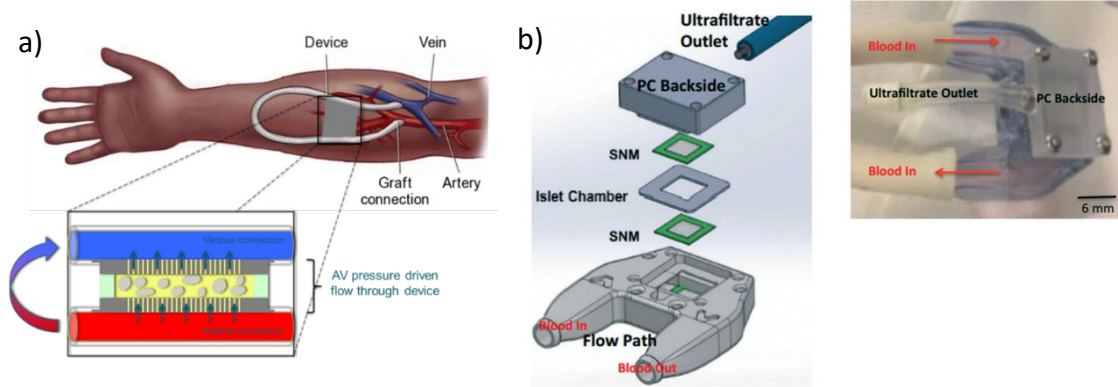
Figure 1.4: *SNM-based bioartificial pancreas. a) Schematic of implantable immunoisolation chamber for islet therapy; b) exploded (left) and assembled (right) view of intravascular bioartificial pancreas.*[16]

1.2.3 Challenges Facing Use of SNMs

While SNMs have physical attributes that can make bioartificial organs such as the kidney and pancreas possible, thrombosis on implanted silicon in contact with blood remains a challenge.[31] Although previous research has shown silicon to be non-cytotoxic[5,6] and non-leaching, [7] hemocompatibility of silicon is still a concern as cells and proteins attach to the surface, fouling the membranes, reducing their functionality, and inciting coagulation. Coagulation and thrombus formation can cause further complications leading to embolism.

1.3 Hemocompatibility Concerns for Foreign Material

The human body has built-in mechanism to protect itself from foreign invaders and implants must evade this defense. Averting these defenses require a solid understanding of the immunological and coagulation processes. The host reaction to an implant placed in tissue includes blood-material interaction, inflammation, foreign body reaction, and fibrous encapsulation. These processes entail the activation of various inter-related protein cascades

found in blood such as the coagulation system and the complement system, as well as activation

of leukocytes and platelets, leading to clotting and inflammation.[32–34] For SNMs that are

exposed to blood flow, minimizing reactions from blood-material interactions is critical.

Therefore, a brief discussion on the blood-material interaction follows.

1.3.1   Blood-Material Interaction
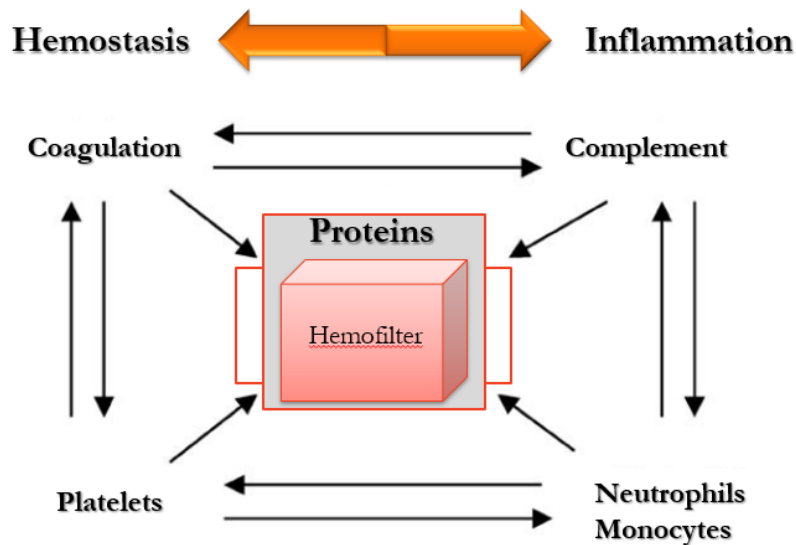
Figure 1.5: *Interaction of proteins, protein cascades, platelets and leukocytes with each other and biomaterial. Adapted from M.B. Gorbet, M.V. Sefton, Biomaterials 25 (2004) 5681-5703.[35]*

Within nanoseconds of contact with blood, plasma proteins adsorb to the implant surface. The

protein type, amount, and conformation determine further activation of coagulation system,

complement system, platelets and leukocytes (Figure 1.5).[35]

As shown in Figure 1.6, contact with negative charges on a biomaterial can activate Factor XII

(FXII) of the coagulation system.[35] Activated Factor XII (FXIIa), in turn, sets off a cascade of

enzymatic reactions leading to the production of thrombin from prothrombin.[36] Thrombin plays

a critical role in the coagulation system; it not only directly activates platelets but also converts

fibrinogen to fibrin, which polymerizes to start clot formation on the surface.[36] Fibrin interacts with leukocytes that leads to an inflammatory response and expression of tissue factor on the cell surface. Tissue factor further activates platelets as well as setting off the extrinsic coagulation cascade, increasing clot formation.[37,38] Activated platelets also expose negatively charged phospholipids that interact with FXII and propagate the coagulation cascade.[39–41]

In addition to directly catalyzing the reaction of converting prothrombin to thrombin, Factor Xa of the coagulation system assembles with Factor Va on the surface of activated platelets to increase thrombin production, which further promotes platelet activation.[39,41]

Aside from fibrin, fibrinogen itself also interacts with the foreign surface. Previous literature has shown that fibrinogen adhered to the surface exposes binding sites that allow for the activation of phagocytes and provides a substrate for platelets to attach to the biomaterial.[42–45]

The complement system acts alongside the coagulation system, and the goal of the complement system is to tag a pathogen so it can be more readily destroyed by phagocytes. Usually these proteins circulate the blood in inactive form, but in the presence of an antigen, or an antibody bound to an antigen, complement can get activated through three different pathways—classical, alternative, and lectin pathways.[36]

For biomaterials, complement activation begins with a layer of adsorbed protein to the biomaterial surface.[33] The classical complement pathway can be activated by the binding of C1q to IgG in the adsorbed protein layer on the biomaterial.[46] C1q forms C1 by creating a complex with C1s and C1r. Activated C1s cleaves C4 to produce C4a and C4b. C4b binds to the biomaterial surface and also binds a molecule of C2, which is then cleaved by C1s to produce C2a and C2b. C2a remains bound to C4b to produce C4b2a which is a C3 convertase, which

catalyzes the reaction that converts C3 to C3a and C3b. C3b binds to the surface and tags the surface for phagocytes, while C3a remains free floating and activates phagocytes. Surface-bound C3b can also start the alternative pathway by binding Factor B to itself. Bound Factor B is then cleaved by factor D into Ba and Bb. Bb remains attached to C3b, producing C3bBb, which is also a C3 convertase, producing more C3a and C3b, to initiate an amplification loop of the alternative pathway.[36,47] Research has also shown that C3 itself can bind to the biomaterial surface and mimic C3b conformation which can set off the alternative pathway.[48] Additionally, thrombin and FXIIa of the coagulation pathway are also able to convert C3 to C3a and C3b, leading to an inflammatory response via the alternative pathway.[33,35]

The complement pathway also produces the anaphylatoxin, C5a by activating the C5 convertase, which is a C3 convertase with an additional C3b bound to it (C4b2a3b and $C3b_2Bb$).[36] C5a and C3a both activate leukocytes to incite an immune response and activated leukocytes express tissue factor which in turn activates platelets and promotes coagulation.

Activation of coagulation and the inflammatory response not only causes attachment of proteins and cells to the surface, but can also cause clots further down the blood flow path of the device or beyond the device and into the bloodstream.
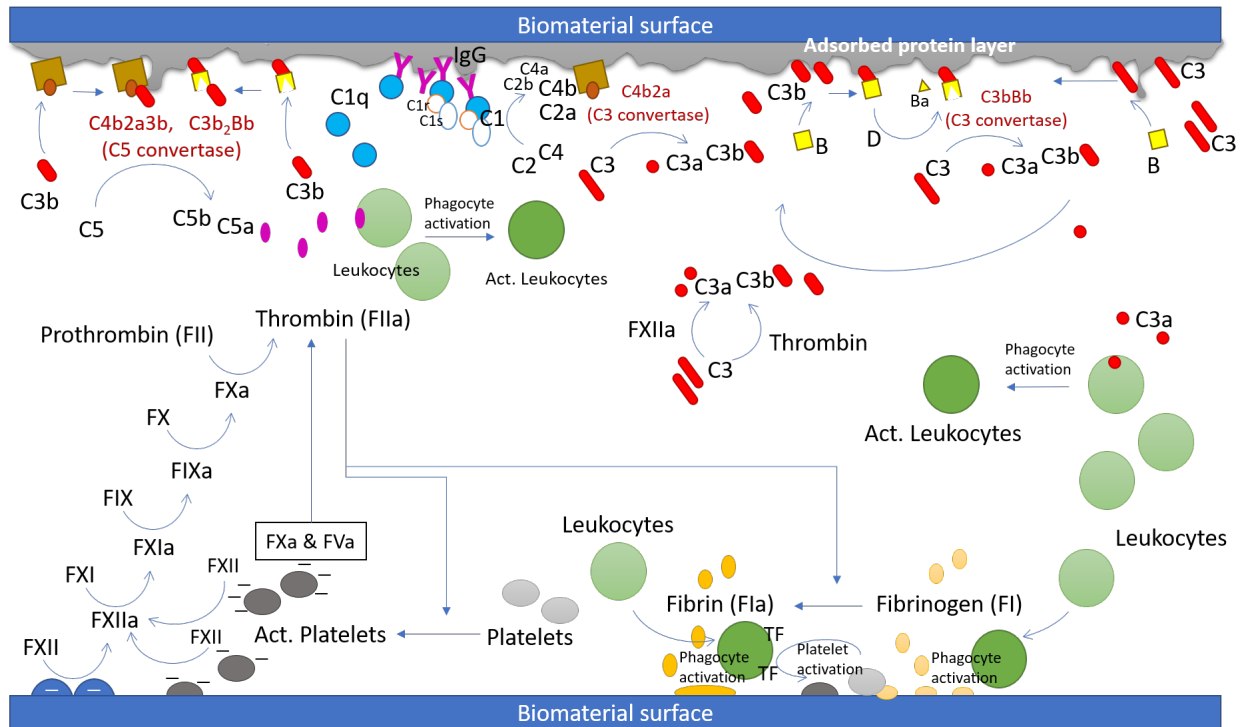
Figure 1.6: *A simplified schematic of complement and coagulation activation when in contact with biomaterial.*

1.3.2   Hemocompatibility Testing Considerations for Biomaterials

When testing hemocompatibility of biomaterials, there are two primary aspects to observe:

degradation and leaching of harmful materials that may lead to cytotoxicity or inflammation and

adhesion and activation of cells and platelets that can lead to inflammation and thrombosis. To

study these factors in detail, experiments are conducted *in vivo* and *in vitro*. If run properly,

preliminary *in vitro* testing can eliminate samples that are likely to fail *in vivo*. "Proper" *in vitro*

experimental setup, however, can vary. Although basic guidelines of experimental setup are

outlined in ISO 10993-4,[49] adjustments must be made based on the implant and the conditions it

will be exposed to. Therefore, when designing *in vitro* blood experiments, it is recommended

that the settings reflect the final implant conditions as much as possible.

11

For *in vitro* hemocompatibility experiments, the experimental fluid to be used requires careful consideration. While whole blood is the closest to implant conditions, researchers often use fractionated blood components,[50] such as plasma (platelet-rich-plasma, platelet-poor-plasma)[51–53] or serum. Doing so allows for better control over length of experiment, as well as interference from other blood variables. Blood can be sourced from humans,[50,54,55] pigs,[55] sheep,[55] dogs,[51] rats,[54] etc. Although human blood is ideal, in some cases, it may be easier to access and run experiments using other types of animal blood.

If fresh whole blood is used, the time length of experiments is critical. Many proteins in whole blood can curdle ~4 hours after collection.[49] Therefore, fresh whole blood experiments are not run for >4 hours. Additionally, because pooling blood from different subjects can activate the blood, for hemocompatibility experiments, it is important to use blood from one individual for one set of experiments. Finally, for fresh blood experiments, the blood must be collected in a non-activating manner and anticoagulated as described in the methods in Chapter 5, as well as in other previous literature.[56] The type and amount of anticoagulant should be chosen based on experimental conditions.

Aside from the experimental fluid itself, the testing conditions and platform used is also important. To mimic biological conditions, blood experiments should be conducted at 37 °C. In addition, the testing platform should be as close to the final condition as possible. In previous research, some experiments are conducted under static conditions.[50–52] However, flow conditions need to be analyzed for biomaterials that will be exposed to blood flow, in order to better understand the effect of shear stress through the device and how it may contribute to hemolysis and activation.[57] In designing a dynamic blood flow system, the variables to consider include the ratio of contact time with biomaterial surface compared to other materials used in the

system and flow rates that set the shear rates. Additionally, how the dynamic condition is set must also be well thought-out. Many researchers use agitators to ensure the blood does not settle,[58,59] while others use flow chambers[56,60] and loops (i.e. circulation models)[54,57,61] that are powered by a peristaltic pump. Finally, the presence of a blood reservoir in a flow system can affect the outcome of the experiments, since blood settling in a reservoir can get auto-activated.

Compared to *in vitro* experiments with whole blood, *in vivo* experiments allow for longer length of experiments. Choosing the correct animal model for an implant is critical, since that determines the activation level of the blood.[55] The location of the implant is also important because it defines the blood volume and the flow rate the implant experiences. Introducing the implant in the body is an interesting challenge; biomaterials have been placed in the muscle[62] as well as in shards in the artery or in anastomosis/arteriovenous shunts between the artery and vein.[63,64] While some implants are placed in the muscle for ease of experimentation, implants that are meant for exposure to blood flow should be tested under blood flow conditions.

Following both *in vitro* and *in vivo* experiments, post analysis of the biomaterial as well the experimental fluids need to be conducted. Aside from visual thrombus formation, microscopy[56,58,59] or radiolabeling[64] can be used to examine clot formation or attachment and activation of cells and platelets. For *in vitro* experiments, complement and coagulation cascade activation in the blood can also be analyzed using enzyme-linked immunosorbent assay (ELISA),[58,59] and hemolysis can be tested using spectroscopy.[65] For *in vivo* testing, histological testing can be done by taking sections, and leukocytes, collagen, and fibrosis buildup can be visualized.[62,66]

1.4 Methods of Surface Modifications to Improve Hemocompatibility

Once a foreign material is introduced to blood, it initially interacts with plasma proteins. This interaction defines the further reaction by the body such as activation of immune response, inflammation and coagulation. Therefore, many researchers have taken the approach of creating a surface that will not allow interaction with proteins.[67–69] This can be done by producing non-fouling surfaces through steric hindrance, controlling surface wettability, or promoting adhesion of specific proteins.[70] Often, researchers have attempted to mimic biological surfaces that already exist in nature, from producing a cellular wall such as endothelialization, to coatings of specific non-immunogenic, non-thrombotic materials such as phosphorylcholine and albumin passivation. Changes in surface topography and roughness can also affect protein adhesion to the surface.[71] In the section below, several leading approaches in surface modification to improve hemocompatibility are discussed, and their advantages and disadvantages are summarized in Table 1.1.

1.4.1 Endothelialization

Blood vessels are lined with a monolayer of endothelial cells that naturally prevent coagulation through cell surface components and cell secretions. In addition to regulating platelet adhesion and activation, endothelial cells express several thrombin inhibitory glycoproteins such as heparan sulfate proteoglycan and thrombomodulin, and release fibrin degrading agents such as tissue-type plasminogen activator and urokinase.[72] Typically used in cardiovascular implants such as synthetic grafts and stents, one approach to reaching hemocompatibility is by covering the surface of the implant with endothelial cells.[72–75] Endothelialization can either be achieved pre-implantation *in vitro*[76–79] or *in situ,*[80,81] where cells are recruited from the bloodstream post-implant. However, the cells must remain confluent since any break in cell coverage can start

14

thrombus formation, and seeding cells *in vitro* often leads to cellular detachment when exposed to physiological shear stress.[82] To address this issue, researchers have attempted to precondition endothelial cells with shear stress to strengthen their adhesion strength,[83–85] in addition to modifying the biomaterial surface with peptides found in extracellular matrix such as fibronectin-derived RGD[75,82] and laminin-derived YIGSR.[75,86]

Because endothelial cells are immunogenic, autologous cells are often used. However, harvesting and producing confluent autologous cells on implants can take ~3-24 months.[72,74] Therefore, *in situ* endothelialization—induction of self-endothelialization *in vivo* via transanastomotic migration, is also an approach being investigated.[80,81] Endothelial cells are slow to proliferate. Hence, endothelial progenitor cells (EPCs) can be seeded to create a rapid growth of endothelial cells. This approach has been previously shown to improve long-term patency.[87–89] Additional approaches for encouraging EPC growth include micropatterning the biomedical surface,[90,91] transfusion of additional EPCs,[92,93] and surface modification with antibodies such as CD34.[80,94]

While endothelialization may be applied to the grafts leading to an SNM-containing implant, this approach cannot be applied for the membranes itself: nanopore membranes require open pores and presence of confluent cells would restrict filtration.

1.4.2   Albumin Passivation

Albumin is the most abundant protein in blood and does not play any direct role in immune response or hemostasis. It is considered a "sticky" protein, and adsorbs to both hydrophilic and hydrophobic surfaces, although it has a much greater affinity for hydrophobic surfaces.[50,95] Albumin is typically applied by simple adsorption process to a foreign surface, and when a

surface is fully covered by albumin, it has been shown to reduce platelet adhesion and activation.[50,54,57] To make albumin more adherent to a material, the substrate surface can be modified by grafting long alkane chains.[50]

While albumin passivation works well for short-term blood contact applications, this method is highly susceptible to denaturation, degradation and replacement. These challenges make it difficult to use for long-term implants. Once adsorbed to the surface, albumin can alter its conformation, which can encourage adsorption of more activating proteins such as fibrinogen. When an albumin passivated surface is exposed to a cocktail of proteins, as is present in blood, it can often be displaced by larger, less abundant proteins such as IgM and fibrinogen, via a process called the Vroman effect.[96,97] These proteins can then initiate activation of blood. To eliminate the Vroman effect, researchers have covalently bonded albumin to the surfaces.[98] However, this still does not address the possibility of denaturation and degradation.

1.4.3 Bioactive Surface Modifications

Unlike albumin passivation, bioactive surface modifications rely on blood component interactions with the surface. For example, surface coatings such as lysine, urokinase, heparin and hirudin, as well as coatings that release nitric oxide (NO), expect interaction with the surface and actively attempt to deactivate clot formation.

Plasminogen, a protein that is converted to plasmin in the fibrinolytic pathway in order to degrade fibrin, has lysine binding sites. Tissue plasminogen activator (t-PA), which is needed for fibrinolysis, also binds lysine.[70,99] Therefore, by incorporating lysine into a biomaterial, it has been shown to selectively capture plasminogen and t-PA, and convert plasminogen to plasmin, which in turn can dissolve nascent clots on the surface.[100,101] This process is further

improved with the presence of polyethylene glycol (PEG)[102,103] and poly(2-hydroxyethyl methacrylate) (polyHEMA) spacers.[52,104]

Other bioactive coatings that attempt to dissolve clots include surfaces incorporating urokinase and thrombomodulin. Urokinase, which also converts plasminogen to plasmin, thus breaking down fibrin, has been shown to reduce clot formation *in vitro*[105] and *in vivo*.[62,106,107] However, *in vivo* experiments showed urokinase degradation after one month modified-catheter implantation in rabbit muscles.[62] Thrombomodulin, biologically present on endothelial cell surfaces, converts thrombin from its procoagulant form to anticoagulant form and activates protein C, which inactivates factors Va and VIIIa of the coagulation pathway.[108] When covalently immobilized onto a material, thrombomodulin has been shown to increase fibrinogen clotting time[109] and reduce blood activation *in vitro*,[59] as well as decrease platelet deposition over one hour *in vivo*.[63,64] However, further studies need to be conducted to show long term stability and functionality under flow conditions.

Heparin and hirudin are biomolecular drugs that are administered as anticoagulants. Heparin, a glycosaminoglycan (GAG) similar to endothelial cell surface proteoglycan heparan sulfate, is found in the human body sequestered in the granules of mast cells. It binds and alters the conformation of antithrombin (AT) to increase its inhibitory properties by a factor of 100-1000.[110] Aside from thrombin itself, AT binds and inhibits several other coagulation cascade proteins such as FXa, FIXa, FXIa, and FXIIa.[111] Heparin is widely used in the medical device industry and research: immobilized onto catheters, stents and ventricular assist devices as well as extracorporeal devices such as oxygenators.[110,112,113] While heparin is applied by ionic bonding, physical adsorption,[56] bulk material incorporation,[114] it can have increased lifetime when covalently bonded onto the surface via its many available carboxyl and hydroxyl groups.[115]

However, covalent bonding requires careful consideration to ensure that the thrombin binding site remain available.[110] Therefore, end-point-attached heparin has shown improved performance.[116] In addition to *in vitro* studies demonstrating the efficacy of heparin coatings, many *in vivo* studies have also illustrated that heparin-coated surfaces significantly decrease clot formation.[110,115] A one year study with heparin-modified PTFE graft implanted in humans demonstrated a reduction in graft failure by 37%.[117] By using PEG as a spacer, further improvements are made to heparin activity.[118] However, more studies need to be conducted to find out if the use of heparin causes other complications in the human body. Since heparin naturally remains sequestered in granules of mast cells and its full functionality there is yet to be determined, long-term exposure of heparin in blood may have side effects. Also, heparin binds other bioactive molecules such as growth factors, the effects of which are unknown.[119] An additional setback of heparin is that it is unable to bind complexed thrombin (i.e. thrombin bound to fibrin or another thrombin molecule), allowing clot formation to stem from these molecules.[120]

Unlike heparin, which inhibits thrombin indirectly via AT activation, hirudin, a small peptide derived from the salivary glands of medicinal leeches, inhibits thrombin by directly binding to its active site.[121,122] It is able to inhibit free-floating thrombin molecules, as well as thrombin bound to fibrin.[123] Additionally, upon binding thrombin, hirudin interferes with the active site of thrombin that interacts with platelets.[124] Recombinant hirudin can be applied such that its bioactivity is fully preserved,[125] and has been shown to reduce thrombus formation and platelet adhesion, and increase clotting time *in vitro* on several biomaterials such as nitinol,[126] Dacron[©],[127] polyester,[128] and silk fiber films.[129,130] A 2-hour *in vivo* study using a canine model also showed reduced thrombus formation, with lower plasma protein adsorption and platelet adhesion on hirudin-modified surfaces of Dacron[©] grafts.[131] One of the major limitations of

using hirudin is that the bond between hirudin and thrombin is very strong, and has a dissociation constant of only 1.98e-14 M.[132] Therefore, the bond is practically irreversible, reducing the lifetime and effectiveness of hirudin for long term applications. To overcome this problem, hirudin derivatives are being developed and they are in the preliminary testing phase.[125,126]

Nitric Oxide (NO) is a gas naturally released by endothelial cells that plays a role in regulating inflammation in the body. Released at a slow rate (0.5e-10 to 4e-10 mol/cm^2/min), NO prevents platelet and leukocyte adhesion and activation.[133] Therefore, unlike the anticoagulants previously discussed, utilizing this biomimetic approach would eliminate side effects. Modification of biomaterials using NO donors such as N -diazeniumdiolates and S -nitrosothiols has been widely studied and have been shown to be very effective.[134–136] These molecules can be blended into the polymeric biomaterial, covalently bonded to the biomaterial surfaces, or covalently bonded to the backbone of a polymeric biomaterial. These compounds are solid and stable under normal conditions and decompose through hydrolysis at physiological conditions (37 °C and pH 7.4). The major limitation of this surface modification is that it relies on a reservoir of NO donors. Therefore, long term application (>2 months) is yet to be demonstrated. Additionally, there will be an accumulation of by-products, which could be toxic and must be contained. Further improvements of the coatings are being investigated by combining NO-release with other anti-inflammatory coating approaches, such as thrombomodulin, heparin, and PEG.[137–139]

1.4.4   Inorganic Coatings

Among the metal oxide coatings, titanium oxides have been widely studied. Titanium forms an inert oxide layer on its surface when exposed to air. Although inert and stable in physiological conditions, natural titanium oxide adsorbs fibrinogen, and has been shown to adhere and spread

platelets within 5 s of blood exposure *in vitro*.[140] However, there are many factors that play a role in the hemocompatibility of titanium oxides and nitrides such as coating thickness, surface roughness, crystallinity (anatase, rutile, amorphous, polycrystalline), contamination and doping. These properties can be controlled by applying the oxide/nitride films via methods such as sputtering, ion beam enhanced deposition, and metal plasma immersion ion implantation.[141–144] These approaches show improved hemocompatibility of biomaterials with titanium oxides and nitride coatings both *in vitro* and *in vivo*.[143–146] Overall, trend shows that platelet adhesion and fibrinogen adsorption is decreased for TiN_xO_y compared to TiO_2, which points towards a surface that is lower in hydrophobicity and contains increased polar components.[147]

Diamond-like carbon (DLC) coating is a low friction, inert surface modification that is highly corrosion and wear resistant, utilized in load bearing implants such as for hip/knee joints, as well as for stents.[148,149] Typically deposited using chemical or physical vapor deposition (CVD or PVD),[148,150] the DLC films have high residual stress, which often causes delamination.[148,151] However, residual stress can be reduced by doping DLC with elements such as silver, nitrogen or titanium, as well as by adding metal interlayers.[148,151,152] Although DLC coatings improve biomaterials (i.e. stainless steel), they are known to adsorb plasma proteins such as albumin and fibrinogen, as well as adhere and spread platelets.[153,154] Structure and chemical bonding, surface roughness, and surface energy can influence interactions with blood and biological components,[154,155] and increased polar components help improve hemocompatibility.[150,156]

Pyrolytic carbon, a material resembling graphite, has demonstrated excellent thromboresistant properties.[157] This material has revolutionized the heart valve industry: St. Jude bileaflet valves (since 1977) as well Carbomedics bileaflet valves (since 1986) are fully fabricated of pyrolytic carbon, and have been implanted in more than 1.8 million patients over the years.[158] The success

rate for these heart valves are high, with <2% of operative risk worldwide and negligible thromboembolism and endocarditis.[158] Goodman, et al has demonstrated that pyrolytic carbon significantly adheres and activates human platelets *in vitro*, which may result in thromboembolism.[159] For this reason, patients receiving pyrolytic carbon mechanical heart valves are required to take anticoagulants for life.[145,159] Other researchers, are investigating surface modifications on pyrolytic carbon in order to improve its hemocompatibility and reduce the need for the use of anticoagulants.[145]

1.4.5   Hydrophobic/Omniphobic Coatings

Silicone materials, i.e. polydimethylsiloxane (PDMS), is known for its flexibility, durability, inertness and nontoxicity.[160] These properties lend themselves towards implant applications. Silicone is used in the medical industry as a direct biomaterial as well as a surface coating for applications such as breast implant, pacemaker leads, catheters etc. Additionally, small-diameter vascular poly(ether) urethane graft with PDMS incorporated in has shown improved hemocompatibility *in vitro* with human anticoagulated blood.[161] However, PDMS is naturally hydrophobic, making it more susceptible to platelet activation and increased plasma protein adsorption.[162] Additionally, PDMS elicits a high level of foreign body response, which can lead to thrombogenesis. Therefore, in order to increase hemocompatibility, there is ongoing work to modify PDMS surfaces with more hydrophilic polymers, such as polyethylene glycol and poly(sulfobetaine methacrylate).[163–165]

Many hydrophobic coatings are generated using fluorinated carbon. Polytetrafluoroethylene (PTFE), and expanded polytetrafluoroethylene (ePTFE) are fluoropolymers commonly utilized in implant applications ranging from vascular grafts to soft tissue augmentations.[166] Although relatively successful, it is also known to cause thrombosis, especially in implants with small

21

cross-sectional (<5mm) flow paths. Therefore, a significant amount of research is dedicated to improving the compatibility of this material.[167–169] Nonetheless, they are inert, stable and chemical resistant, which makes fluorocarbons very attractive for implants. Aside from PTFE, other fluorinated carbon coatings used for biological applications include, but are not limited to: vinylidene fluoride (VDF),[170] chlorotrifluoroethylene (CTFE),[170] perfluorohexane,[171] trifluoroehyl methacrylate (TFEMA).[172] These fluorocarbon surface modifications have shown reduced platelet activation compared to untreated surface[170,173,174] when applied to a variety of materials, such as polyester, polysulfone, polyethylene, polyurethanes via plasma deposition or graft polymerization.[170,171,173,175]

There are several approaches taken to improve hemocompatibility of fluorinated carbon coatings. For example, TFEMA was copolymerized with vinylphosphonic acid (VPA), which resulted in a surface contact angle greater than 110° and has led to reduced platelet adhesion.[172] In another approach, combining hydrophilic and hydrophobic elements in one coating to create amphiphilic surface has also improved its non-fouling properties.[176] Co-polymerization of perfluorodecyl acrylate (PFDA) and diethylene glycol dimethyl ether (DEGDME) via plasma deposition has shown to further increase the hemocompatibility and protein fouling resistance compared to fluorinated surfaces.[175]

Recently, slippery liquid-infused porous surface (SLIPS) has attracted a lot of attention. A biomimetic coating inspired by *Nepenthes* pitcher plant, it consists of a nano/microstructured surface infused by a lubricating fluid. This coating is truly unique because it can utilize any combination of solid nanostructured surface and liquid layer to resist target fouling.[69,177,178] One classic example is a fluorinated porous substrate (e.g. Teflon nanofibers) with perfluorinated liquid layer (e.g. 3M Fluorinert FC-70). This coating is omniphobic, and is able to resist fouling

from blood very effectively.[179] *In vivo* work in a porcine model demonstrated efficacy of the coating for 8 hours in catheters.[180] Over time, however, the lubricant layer slips away with the flowing fluid. Therefore, long term application using SLIPS would require large reservoirs of the lubricant built into the system, as well as a method to get the lubricant to the surface.

1.4.6 Hydrophilic Polymer Coatings

Polyethylene glycol (PEG) is a hydrophilic surface coating considered to be the "state-of-the-art." Its brush structures are thought to resist protein fouling and platelet adhesion by coordinating water molecules around itself and producing steric hindrance.[164,181–183] When PEG (length of 6-9 monomers) is applied on SNMs, the membranes remain patent and functional.[184] Additionally, PEG-coupled silicon implanted in a rat femoral artery for 28 days showed significant reduction in thrombus formation in comparison with uncoated silicon.[31] However, PEG is susceptible to oxidative degradation under physiological conditions,[185–187] and extending implant lifetime (>1 month) remains a challenge. Nonetheless, PEG is often used in conjunction with other coatings as a spacer or as part of a co-polymer to lend its non-fouling properties.[102,103,118]

Over the last several decades, many researchers have focused their attention on zwitterionic coatings. Biomimetic zwitterions of phosphorylcholine, sulfobetaine and carboxybetaine have excellent non-fouling properties. These coatings are highly hydrophilic and can resist protein adsorption and cell adhesion by strongly interacting and coordinating water molecules.

2-methacryloy-loxyethylphosphorylcholine (MPC), originally designed by Nakabayashi, et al., mimics the polar heads of the phospholipid bilayer that make up the cell membrane.[188–191] Polymers and hydrogels of MPC (pMPC) have demonstrated reduction in protein adsorption, as

well as platelet and leukocyte adhesion and activation,[192–196] while showing no cytotoxic effects.[197] Therefore, thromboresistant pMPC coating was applied to various implants, such as glucose sensors,[189] blood filtration,[198] ePTFE grafts, and stents.[199,200] Additionally, the non-fouling functionality of pMPC coating has been verified over coating thickness ranging from 20 to 110 nm.[201] MPC was also shown to be highly durable, even under load bearing conditions.[202] However, one major drawback of pMPC is that the monomer is difficult to synthesize and results in low yield, making it expensive to produce.

Over the last decade, Jiang et al. have developed polysulfobetaine methacrylate (pSBMA) and polycarboxybetaine methacrylate (pCBMA).[203,204] Both polymers are non-cytotoxic,[205] and have demonstrated ultra-low protein fouling (i.e. <0.3 ng/cm^2 of fibrinogen) with a significant reduction in platelet adhesion and activation.[53,203,206–213] Additionally, pSBMA and pCBMA are highly resistant to bacterial adhesion and biofilm formation.[208,209,214–216] These properties make them well-suited for implant applications.

pSBMA is biomimetic of taurine, a compound commonly found in animal tissue and bile. Surfaces have been successfully modified with pSBMA using various methods ranging from ATRP,[53,212,214,217] reverse ATRP,[218] plasma-induced polymerization,[219] as well as simple grafting-to method via use of a catechol[208] or click chemistry.[220] Utilizing these methods, pSBMA has been used to modify gold,[207,214] graphene,[218] glass,[212] silica nanoparticles,[221] silicon,[58,213] as well as other polymers such as PDMS,[163,165,222] cellulose,[53,210] polyurethane,[206] poly(vinylidene fluoride) (PVDF),[219] for use in a wide range of applications from blood purification,[210] glucose sensors,[223] and non-adherent wound dressing[215] to waste water purification.[218]

For many of these applications, long term stability is required. pSBMA was shown to be stable *in vitro* in various static aqueous solutions, such as phosphate buffered saline (PBS), human blood plasma, and distilled water over 28 days or less.[205,206,213,223] *In vitro* experimentation with static fresh human blood over 2 hours also demonstrate that pSBMA-coupled silicon significantly reduces platelet adhesion compared to silicon.[58] *In vitro* human blood flow experiments with sulfobetaine-modified vascular catheters showed a significant difference in blood activation after only 5 min of blood flow.[224] *In vivo* work with pSBMA include hydrogels of pSBMA that have been implanted subcutaneously in mice over 4 weeks. However this resulted in a capsule thickness and foreign body giant cell count that is comparable to control polyHEMA hydrogels.[205] Smith et al. also conducted *in vivo* experiments using sulfobetaine modified catheters in a canine model that show significantly reduced thrombus formation. However, the experiments only spanned 4 hours. Therefore, to our knowledge, there is very limited data of pSBMA performance in *in vivo* long-term blood flow conditions. Another aspect that requires further study is the effect of polymerization conditions and coating thickness since there are mixed results reported in literature: While some studies have demonstrated that varying polymerization time for 5 min to 480 min (yielding varying coating thicknesses) does not result in a difference in protein adsorption and platelet adhesion,[53] others have shown that for pSBMA a coating thickness of 62 nm results in optimal protein fouling resistance.[217]

While pCBMA, a biomimetic of glycine betaine, has demonstrated similar fouling-resistive behavior compared to pSBMA, one advantage of pCBMA is that it offers ease of functionalization through its carboxylate groups. Photopolymerized pCBMA hydrogels with high mechanical strength and stability have been shown to withstand degradation in oxidative, acidic and basic environments.[225] Additionally, when pCBMA hydrogel (created using a CBMA

cross-linker) was implanted subcutaneously in mice for 3 months, it produced significantly reduced collagen density and foreign body reaction compared to control polyHEMA hydrogel.[66] However, in order to synthesize the monomer CBMA, the precursor β-propiolactone is required, which is a carcinogen, making CBMA difficult to produce in-house.

There are many ways to graft zwitterionic coatings on to a surface. Grafting on the surface as opposed to grafting to the surface makes a big difference in the properties of the surface coating. Zwitterionic polymers can be grafted onto the surface (grown on the surface) using atom transfer radical polymerization (ATRP). Using a halogenated initiator covalently bonded to a surface, radical polymerization can propagate from the initiator using methacrylate backbone of the monomer.[226] Graft-to methods, such as click chemistry[220] or utilizing self-assembled monolayers typically leads to lower grafting density. The methods and conditions of grafting make a difference in the packing density, polymer chain configuration/crosslinking as well as the polymer chain length. These factors in turn play a crucial role in how the surface is hydrated and how water molecules are arranged, and therefore, the performance of the coating.[227–229]

Table 1.1: Surface modification approaches, and their pros and cons for application on silicon nanopore membranes.

Coating Type	Coating Description	Advantages	Disadvantages
Endothelialization	-endothelial cells (which make up the outer walls of blood vessels) line in surface of implant	-ideal biomimetic condition -no systemic effect	-cell viability/cell adhesion to foreign material remain a challenge -months/years for harvesting and growing -difficult to attain full coverage for >2 cm² surface area -to achieve best results cells must be harvested from host system -break in coverage is highly thrombogenic

Coating Type	Coating Description	Advantages	Disadvantages
Albumin Passivation	-albumin is the most abundant protein in blood -adsorption or covalent bonding of albumin to implant surface	-works well for short term applications -adsorbs to all types of surface, especially hydrophobic surfaces	-covalent bonded albumin does not work as well -susceptible to denaturation, degradation, and replacement (Vroman effect)
Lysine	-lysine binds plasminogen and tissue plasminogen activator, converting plasminogen to plasmin; plasmin dissolves fibrin -immobilize lysine to implant surface	-does not bind other proteins -breaks down clots only at implant surface and has no systemic effect	-% activity decreases rapidly in the first hours of exposure to blood flow -long-term application has yet to be proven
Urokinase	-urokinase converts plasminogen to plasmin; plasmin dissolves fibrin -immobilize urokinase to implant surface	-no systemic effect -works well for short term implants	-degrades in <1 month when implanted in muscle
Thrombomodulin	-binds thrombin and converts it to anticoagulant form; Activates protein C, which regulates proteins in coagulation cascade -immobilize thrombomodulin to implant surface	-amplifies regulation of coagulation pathway via activation of protein C	-long term *in vivo* data >1 hour yet to be collected
Heparin/Heparin Derivatives	-binds and increases the functionality of antithrombin, which inhibits thrombin and other factors in the coagulation cascade -immobilize heparin to the implant surface	-shown to reduce clot formation *in vitro* and *in vivo* for stents and catheters -already in use in industry	-may have unknown physiological effects -resistant to fibrin-bound thrombin -relies on the presence of antithrombin -risk of heparin-induced thrombocytopenia
Hirudin	-derived from medicinal leeches, directly binds and inhibits thrombin -immobilize hirudin to the implant surface	-directly blocks thrombin, including thrombin bound to fibrin -binds to active site of thrombin that interacts with platelets	-thrombin-hirudin interaction has very low dissociation constant; therefore, irreversible interaction leads to one-time interaction with thrombin for each hirudin molecule

Coating Type	Coating Description	Advantages	Disadvantages
Nitric Oxide (NO)	-NO donors blended/covalently bonded to implant surface attempt to mimic natural release of NO by endothelial cells to prevent adhesion and activation of platelets and leukocytes	-biomimetic -unlike other anticoagulants, NO released at physiological rate will not have additional side effects -shown to reduce adhesion and activation of platelets and leukocytes	-short lifetime (based on size of NO reservoir) -possibility of toxicity from accumulation of byproducts
Titanium Oxide/Nitrides coating	-oxides and nitrides are deposited on surfaces via ion beam enhanced deposition, sputtering etc.	-naturally inert -polarity, hydrophobicity, crystallinity, thickness etc. can be controlled via deposition method -utilized in industry on artificial heart valves	-thick coating is required for hemocompatibility -natural oxide adheres platelets and adsorbs fibrinogen
Diamond Like Carbon (DLC) coating	-amorphous carbon of sp^2 bonded matrix with sp^3 nodules, sometimes hydrogenated -typically deposited on substrates using chemical or physical vapor deposition	-low friction -high corrosion and wear resistance -low toxicity -utilized in industry on joints and load-bearing implants	-adsorbs large amounts of plasma proteins -adheres platelets -has structurally high residual stress leading to delamination
Pyrolytic Carbon	-graphite-like carbon	-utilized in industry for mechanical heart valves	-without the use of anticoagulants adheres and activates platelets
Silicone/ Polydimethylsiloxiane	-polymers based alternating silicon and oxygen atoms	-inert and nontoxic -durable -flexible	-hydrophobic -high level of foreign body reaction
Fluorinated/Teflon coatings	-hydrophobic surface created by fluorinated carbon	-resists thrombus formation -coatings currently utilized for large grafts and catheter	-hydrophobic -adsorbs plasma proteins -high failure rate and thrombosis formation for grafts/channels less than 5 mm diameter

Coating Type	Coating Description	Advantages	Disadvantages
Slippery liquid-infused porous surface (SLIPS)	-biomimetic of *Nepenthes* pitcher plants -nano/microstructured substrates with infused lubricating fluid	-surface repels proteins and cells very efficiently -liquid layer already FDA approved	-very hydrophobic -reservoir of fluid layer required
Oligo/Polyethylene glycol	-applied as a brush-structure to create steric hindrance/produce water coordination to resist fouling -regarded as "gold standard"	-hydrophilic -uniform ultrathin coatings can be achieved -shown to work *in vivo* to resist fouling over 1 month	-susceptible to oxidation; known to degrade under biological conditions in applications >1 month
Phosphorylcholine brush polymer	-very hydrophilic zwitterion-based molecule mimicking the polar heads of phospholipids -coordinates water molecules—hydration layer resists fouling	-biomimetic -hydrophilic -resists fouling and thrombus formation via hydration layer -utilized in industry (BTG)	-monomer difficult to synthesize, expensive
Sulfobetaine brush polymer	-very hydrophilic zwitterion-based molecule mimicking taurine -coordinates water molecules—hydration layer resists fouling	-biomimetic -hydrophilic -resists fouling and thrombus formation via hydration layer -low cost of monomer -easy to synthesize monomer	-long term stability under blood flow conditions not yet demonstrated in previous literature -not optimized for ultra-thin (sub-5 nm) thickness
Carboxybetaine brush polymer	-very hydrophilic zwitterion-based molecule mimicking glycine betaine -coordinates water molecules—hydration layer resists fouling	-biomimetic -hydrophilic --resists fouling and thrombus formation via hydration layer -easily functionalizable through carboxylate groups	-carcinogenic precursor for monomer synthesis reaction

1.5 Research Objective

While many approaches are attempted to achieve hemocompatibility, there is no one method that fits all applications. For use on SNMs in bioartificial organs, a coating must meet several

criteria: the coating must not only be non-fouling and non-activating, but also needs to be ultrathin and uniform to maintain pore patency and tight pore size distribution of the membranes. Additionally, it must be hydrophilic in order to preserve the low resistance of SNMs. Finally, it must remain stable over the implant lifetime. Given these conditions, zwitterionic pSBMA and pMPC were investigated as possible surface modifications for SNMs. Preliminary work with pSBMA on SNMs has demonstrated successful surface modification and SNM pore patency.[213] However, as the zwitterionic coatings are reduced in coating thickness to meet the "ultrathin" criteria, further exploration of zwitterionic coatings on SNM was needed prior to determining the suitability of these coatings for bioartificial organs.

In this study, pSBMA and pMPC coating methods was optimized to be ultrathin and functional. They were then characterized via x-ray photoelectron spectroscopy, contact angle, atomic force microscopy and ellipsometry. The coatings were tested under biological shear conditions, and against five standard sterilization methods. Non-fouling and hemocompatible properties of the coatings were evaluated by measuring protein adsorption from single protein solutions and examining platelet activation after exposure to fresh human blood. Control PEG-coupled silicon was used as a comparison. In addition, pSBMA-silicon was implanted in a porcine model for up to 26 days and evaluated for hemocompatibility. These experiments demonstrate the possibility of utilizing ultrathin zwitterionic pSBMA and pMPC coatings for implant applications.

1.6 References

1.   Merriman, B., Torrent, I. & Rothberg, J. M. Progress in Ion Torrent semiconductor chip based sequencing. *Electrophoresis* **33,** 3397–3417 (2012).

2.   Tia, S. Q., He, M., Kim, D. & Herr, A. E. Multianalyte on-chip native western blotting. *Anal. Chem.* **83,** 3581–3588 (2011).

3.   Tia, S. & Herr, A. E. On-chip technologies for multidimensional separations. *Lab Chip* **9,** 2524–2536 (2009).

4.   Shawgo, R. S., Grayson, A. C. R., Li, Y. & Cima, M. J. BioMEMS for drug delivery. *Curr. Opin. Solid State Mater. Sci.* **6,** 329–334 (2002).

5.   Fernández-Rosas, E. *et al.* Internalization and cytotoxicity analysis of silicon-based microparticles in macrophages and embryos. *Biomed. Microdevices* **12,** 371–379 (2010).

6.   Agrawal, a. a. *et al.* Porous nanocrystalline silicon membranes as highly permeable and molecularly thin substrates for cell culture. *Biomaterials* **31,** 5408–5417 (2010).

7.   Kotzar, G. *et al.* Evaluation of MEMS materials of construction for implantable medical devices. *Biomaterials* **23,** 2737–50 (2002).

8.   Cheung, K. C. & Renaud, P. BioMEMS for medicine: On-chip cell characterization and implantable microelectrodes. *Solid. State. Electron.* **50,** 551–557 (2006).

9.   Scholvin, J. *et al.* Close-packed silicon microelectrodes for scalable spatially oversampled neural recording. *IEEE Trans. Biomed. Eng.* **63,** 120–130 (2016).

10.   Desai, T. *et al.* Nanoporous Implants for Controlled Drug Delivery. *Ther. Micro/Nano Technol. - BioMEMS Biomed. Nanotechnol.* 263–286 (2007). doi:10.1007/978-0-387-

25844-7_15

11. Lesinski, G. B. *et al.* Release of biologically functional interferon-alpha from a nanochannel delivery system. *Biomed. Microdevices* **7,** 71–79 (2005).

12. Kang, S. *et al.* Bioresorbable silicon electronic sensors for the brain. *Nature* **530,** 71–76 (2016).

13. Lueke, J. & Moussa, W. A. MEMS-based power generation techniques for implantable biosensing applications. *Sensors* **11,** 1433–1460 (2011).

14. Acquaroli, L. N., Kuchel, T. & Voelcker, N. H. Towards implantable porous silicon biosensors. *RSC Adv.* **4,** 34768 (2014).

15. Fissell, W. H. & Roy, S. The implantable artificial kidney. *Semin. Dial.* **22,** 665–70 (2009).

16. Song, S. *et al.* An intravascular bioartificial pancreas device (iBAP) with silicon nanopore membranes (SNM) for islet encapsulation under convective mass transport. *Lab Chip* (2017). doi:10.1039/C7LC00096K

17. Fissell, W. H. *et al.* High-performance silicon nanopore hemofiltration membranes. *J. Memb. Sci.* **326,** 58–63 (2009).

18. Roy, S. *et al.* Silicon nanopore membrane technology for an implantable artificial kidney. *TRANSDUCERS 2009 - 15th Int. Conf. Solid-State Sensors, Actuators Microsystems* 755–760 (2009). doi:10.1109/SENSOR.2009.5285603

19. Kim, S. *et al.* Diffusive silicon nanopore membranes for hemodialysis applications. *PLoS One* **11,** 1–20 (2016).

20.   Kanani, D. M. *et al.* Permeability - Selectivity Analysis for Ultrafiltration: Effect of Pore Geometry. *J. Memb. Sci.* **349,** 405 (2010).

21.   *Chapter 1: Incidence, Prevalence, Patient Characteristics, and Treatment Modalities. United States Renal Data System* (2016). doi:10.1053/j.ajkd.2016.02.012

22.   *Chapter 9: Healthcare Expenditures for Persons With ESRD. United States Renal Data System* (2018). doi:10.1053/j.ajkd.2018.01.022

23.   Weinhandl, E. D., Nieman, K. M., Gilbertson, D. T. & Collins, A. J. Hospitalization in Daily Home Hemodialysis and Matched Thrice-Weekly In-Center Hemodialysis Patients. *Am. J. Kidney Dis.* (2014). doi:10.1053/j.ajkd.2014.06.015

24.   Culleton, B. *et al.* Effect of frequent nocturnal hemodialysis vs conventional hemodialysis. *J. Am. Med. Assoc.* **298,** 1291–1299 (2007).

25.   Song, J. J. *et al.* Regeneration and experimental orthotopic transplantation of a bioengineered kidney. *Nat. Med.* **19,** 646–51 (2013).

26.   Fissell, W. H., Roy, S. & Davenport, A. Achieving more frequent and longer dialysis for the majority: wearable dialysis and implantable artificial kidney devices. *Kidney Int.* **84,** 256–64 (2013).

27.   Daneman, D. Type 1 diabetes. *Lancet* **367,** 847–858 (2006).

28.   Cnop, M., Welsh, N., Jonas, J., Jo, A. & Lenzen, S. Mechanisms of Pancreatic Beta-cell Death in Type 1 and Type 2 Diabetes: Many Differences, Few Similarities. **54,** 97–107 (2005).

29.   Ammendrup, A. *et al.* The c-Jun amino-terminal kinase pathway is preferentially activated

by interleukin-1 and controls apoptosis in differentiating pancreatic β-cells. *Diabetes* **49,** 1468–1476 (2000).

30. Song, S. *et al.* Silicon nanopore membrane (SNM) for islet encapsulation and immunoisolation under convective transport. *Sci. Rep.* **6,** 23679 (2016).

31. Melvin, M. E., Fissell, W. H., Roy, S. & Brown, D. L. Silicon induces minimal thromboinflammatory response during 28-day intravascular implant testing. *ASAIO J.* **56,** 344–8 (2010).

32. Anderson, J. M., Rodriguez, A. & Chang, D. T. Foreign body reaction to biomaterials. *Semin. Immunol.* **20,** 86–100 (2008).

33. Franz, S., Rammelt, S., Scharnweber, D. & Simon, J. C. Immune responses to implants - A review of the implications for the design of immunomodulatory biomaterials. *Biomaterials* **32,** 6692–6709 (2011).

34. Tang, L. & Eaton, J. W. Natural responses to unnatural materials: A molecular mechanism for foreign body reactions. *Mol. Med.* **5,** 351–358 (1999).

35. Gorbet, M. B. & Sefton, M. V. Biomaterial-associated thrombosis: roles of coagulation factors, complement, platelets and leukocytes. *Biomaterials* **25,** 5681–703 (2004).

36. Murphy, K. & Weaver, C. *Janeway's Immunobiology*. (Garland Science, Taylor & Francis Group, 2017).

37. Parham, P. *The Immune System*. (Garland Science, Taylor & Francis Group, 2009).

38. Fischer, M., Sperling, C., Tengvall, P. & Werner, C. The ability of surface characteristics of materials to trigger leukocyte tissue factor expression. *Biomaterials* **31,** 2498–2507

(2010).

39.   Johne, J. *et al.* Platelets promote coagulation factor XII-mediated proteolytic cascade systems in plasma. *Biol. Chem.* **387,** 173–178 (2006).

40.   Sperling, C., Fischer, M., Maitz, M. F. & Werner, C. Blood coagulation on biomaterials requires the combination of distinct activation processes. *Biomaterials* **30,** 4447–4456 (2009).

41.   Heemskerk, J. W. M., Bevers, E. M. & Lindhout, T. Platelet activation and blood coagulation. *Thromb. Haemost.* **88,** 186–193 (2002).

42.   Hu, W. J., Eaton, J. W., Ugarova, T. P. & Tang, L. P. Molecular basis of biomaterial-mediated foreign body reactions (vol 98, pg 1231, 2001). *Blood* **99,** 3908 (2002).

43.   Tang, L. Mechanisms of fibrinogen domains : Biomaterial interactions. *J. Biomater. Sci. Polym. Ed.* **9,** 1257–1266 (1998).

44.   Savage, B., Bottini, E. & Ruggeri, Z. M. Interaction of integrin alpha-IIb-beta-3 with multiple fibrinigen domains during platelet adhesion. *J. Biol. Chem.* **270,** 28812–28817 (1995).

45.   Rodrigues, S. N., Gonçalves, I. C., Martins, M. C. L., Barbosa, M. A. & Ratner, B. D. Fibrinogen adsorption, platelet adhesion and activation on mixed hydroxyl-/methyl-terminated self-assembled monolayers. *Biomaterials* **27,** 5357–5367 (2006).

46.   Tengvall, P., Askendal, A. & Lundström, I. Ellipsometric in vitro studies on the activation of complement by human immunoglobulins M and G after adsorption to methylated silicon. *Colloids Surfaces B Biointerfaces* **20,** 51–62 (2001).

47. Nilsson, B., Ekdahl, K. N., Mollnes, T. E. & Lambris, J. D. The role of complement in biomaterial-induced inflammation. *Mol. Immunol.* **44,** 82–94 (2007).

48. Andersson, J., Ekdahl, K. N., Larsson, R., Nilsson, U. R. & Nilsson, B. C3 Adsorbed to a Polymer Surface Can Form an Initiating Alternative Pathway Convertase. *J. Immunol.* **168,** 5786–5791 (2002).

49. Seyfert, U. T., Biehl, V. & Schenk, J. In vitro hemocompatibility testing of biomaterials according to the ISO 10993-4. *Biomol. Eng.* **19,** 91–96 (2002).

50. Amiji, M., Park, H. & Park, K. Study on the prevention of surface-induced platelet activation by albumin coating. *J. Biomater. Sci. Polym. Ed.* **3,** 375–388 (1992).

51. Ito, Y., Sisido, M. & Imanishi, Y. Adsorption of plasma proteins and adhesion of platelets onto novel polyetherurethaneureas—relationship between denaturation of adsorbed proteins and platelet adhesion. *J. Biomed. Mater. Res.* **24,** 227–242 (1990).

52. Zhan, W. *et al.* Bioinspired Blood Compatible Surface Having Combined Fibrinolytic and Vascular Endothelium-Like Properties via a Sequential Coimmobilization Strategy. *Adv. Funct. Mater.* **25,** 5206–5213 (2015).

53. Liu, P.-S. *et al.* Grafting of zwitterion from cellulose membranes via ATRP for improving blood compatibility. *Biomacromolecules* **10,** 2809–16 (2009).

54. Borgdorff, P., Van den Berg, R. H., Vis, M. A., Van den Bos, G. C. & Tangelder, G. J. Pump-induced platelet aggregation in albumin-coated extracorporeal systems. *J. Thorac. Cardiovasc. Surg.* **118,** 946–952 (1999).

55. Goodman, S. L. Sheep , pig , and human platelet – material interactions with model

cardiovascular biomaterials. (1998).

56.   Sperling, C., Houska, M., Brynda, E., Streller, U. & Werner, C. In vitro
       hemocompatibility of albumin-heparin multilayer coatings on polyethersulfone prepared
       by the layer-by-layer technique. *J. Biomed. Mater. Res. - Part A* **76,** 681–689 (2006).

57.   Adrian, K. *et al.* The effect of albumin priming solution on platelet activation during
       experimental long-term perfusion. *Perfusion* **13,** 187–191 (1998).

58.   Muthusubramaniam, L. *et al.* Hemocompatibility of silicon-based substrates for
       biomedical implant applications. *Ann. Biomed. Eng.* **39,** 1296–305 (2011).

59.   Sperling, C., Salchert, K., Streller, U. & Werner, C. Covalently immobilized
       thrombomodulin inhibits coagulation and complement activation of artificial surfaces in
       vitro. *Biomaterials* **25,** 5101–5113 (2004).

60.   Streller, U., Sperling, C., Hübner, J., Hanke, R. & Werner, C. Design and evaluation of
       novel blood incubation systems for in vitro hemocompatibility assessment of planar solid
       surfaces. *J. Biomed. Mater. Res. B. Appl. Biomater.* **66,** 379–90 (2003).

61.   Nguyen, K. T. *et al.* In vitro hemocompatibility studies of drug-loaded poly-(L-lactic acid)
       fibers. *Biomaterials* **24,** 5191–5201 (2003).

62.   Lai, Z. F., Imamura, T., Koike, N. & Kitamoto, Y. Urokinase-immobilization suppresses
       inflammatory responses to polyurethane tubes implanted in rabbit muscles. *J. Biomed.
       Mater. Res. - Part A* **76,** 81–85 (2006).

63.   Qu, Z. *et al.* A biologically active surface enzyme assembly that attenuates thrombus
       formation. *Adv. Funct. Mater.* **21,** 4736–4743 (2011).

64. Qu, Z. *et al.* Immobilization of Actively Thromboresistant Assemblies on Sterile Blood-Contacting Surfaces. *Adv. Healthc. Mater.* **3,** 30–35 (2014).

65. Helms, C. C. *et al.* Mechanisms of hemolysis-associated platelet activation. *J. Thromb. Haemost.* **11,** 2148–2154 (2013).

66. Zhang, L. *et al.* Zwitterionic hydrogels implanted in mice resist the foreign-body reaction. *Nat. Biotechnol.* **31,** 553–6 (2013).

67. Sharma, S., Johnson, R. W. & Desai, T. a. XPS and AFM analysis of antifouling PEG interfaces for microfabricated silicon biosensors. *Biosens. Bioelectron.* **20,** 227–239 (2004).

68. Jiang, S. & Cao, Z. Z. Ultralow-fouling, functionalizable, and hydrolyzable zwitterionic materials and their derivatives for biological applications. *Adv. Mater.* **22,** 920–932 (2010).

69. Li, J. *et al.* Hydrophobic liquid-infused porous polymer surfaces for antibacterial applications. *ACS Appl. Mater. Interfaces* **5,** 6704–6711 (2013).

70. Brash, J. L. Exploiting the current paradigm of blood-material interactions for the rational design of blood-compatible materials. *J. Biomater. Sci. Polym. Ed.* **11,** 1135–1146 (2000).

71. Rechendorff, K., Hovgaard, M. B., Foss, M., Zhdanov, V. P. & Besenbacher, F. Enhancement of protein adsorption induced by surface roughness. *Langmuir* **22,** 10885–10888 (2006).

72. Li, S. & Henry, J. J. D. Nonthrombogenic approaches to cardiovascular bioengineering. *Annu. Rev. Biomed. Eng.* **13,** 451–475 (2011).

73. Butruk, B., Bąbik, P., Marczak, B. & Ciach, T. Surface endothelialization of polyurethanes. *Procedia Eng.* **59,** 126–132 (2013).

74. Liu, T., Liu, S., Zhang, K., Chen, J. & Huang, N. Endothelialization of implanted cardiovascular biomaterial surfaces: The development from in vitro to in vivo. *J. Biomed. Mater. Res. - Part A* **102,** 3754–3772 (2014).

75. Ren, X. *et al.* Surface modification and endothelialization of biomaterials as potential scaffolds for vascular tissue engineering applications. *Chem. Soc. Rev.* **44,** 5680–5742 (2015).

76. Lin, Y. S. *et al.* Growth of endothelial cells on different concentrations of Gly-Arg-Gly-Asp photochemically grafted in polyethylene glycol modified polyurethane. *Artif. Organs* **25,** 617–621 (2001).

77. Larsen, C. C., Kligman, F., Kottke-Marchant, K. & Marchant, R. E. The effect of RGD fluorosurfactant polymer modification of ePTFE on endothelial cell adhesion, growth, and function. *Biomaterials* **27,** 4846–4855 (2006).

78. Feugier, P., Black, R. A., Hunt, J. A. & How, T. V. Attachment, morphology and adherence of human endothelial cells to vascular prosthesis materials under the action of shear stress. *Biomaterials* **26,** 1457–1466 (2005).

79. Keselowsky, B. G., Collard, D. M. & García, A. J. Surface chemistry modulates fibronectin conformation and directs integrin binding and specificity to control cell adhesion. *J. Biomed. Mater. Res. Part A* **66A,** 247–259 (2003).

80. Lin, Q. *et al.* In situ endothelialization of intravascular stents coated with an anti-CD34

antibody functionalized heparin-collagen multilayer. *Biomaterials* **31,** 4017–4025 (2010).

81. Park, K. M., Lee, Y., Son, J. Y., Bae, J. W. & Park, K. D. In situ SVVYGLR peptide conjugation into injectable gelatin-poly(ethylene glycol)-tyramine hydrogel via enzyme-mediated reaction for enhancement of endothelial cell activity and neo-vascularization. *Bioconjug. Chem.* **23,** 2042–2050 (2012).

82. Walluscheck, K. P., Steinhoff, G., Kelm, S. & Haverich, A. Improved endothelial cell attachment on ePTFE vascular grafts pretreated with synthetic RGD-containing peptides. *Eur. J. Vasc. Endovasc. Surg.* **12,** 321–330 (1996).

83. Ott, M. J. & Ballermann, B. J. Shear stress-conditioned, endothelial cell-seeded vascular grafts: Improved cell adherence in response to in vitro shear stress. *Surgery* **117,** 334–339 (1995).

84. Baguneid, M. *et al.* Shear-stress preconditioning and tissue-engineering-based paradigms for generating arterial substitutes. *Biotechnol. Appl. Biochem.* **39,** 151–7 (2004).

85. Meinhart, J. G. *et al.* Enhanced Endothelial Cell Retention on Shear-Stressed Synthetic Vascular Grafts Precoated with RDG-Cross-Linked Fibrin. *Tissue Eng.* **11,** (2005).

86. Fittkau, M. H. *et al.* The selective modulation of endothelial cell mobility on RGD peptide containing surfaces by YIGSR peptides. *Biomaterials* **26,** 167–174 (2005).

87. Shirota, T., Yasui, H., Shimokawa, H. & Matsuda, T. Fabrication of endothelial progenitor cell (EPC)-seeded intravascular stent devices and in vitro endothelialization on hybrid vascular tissue. *Biomaterials* **24,** 2295–2302 (2003).

88. Griese, D. P. *et al.* Isolation and Transplantation of Autologous Circulating Endothelial

Cells into Denuded Vessels and Prosthetic Grafts: Implications for Cell-Based Vascular Therapy. *Circulation* **108,** 2710–2715 (2003).

89.   Shirota, T., He, H., Yasui, H. & Matsuda, T. Human Endothelial Progenitor Cell-Seeded Hybrid Graft: Proliferative and Antithrombogenic Potentials in Vitro and Fabrication Processing. *Tissue Eng.* **9,** (2003).

90.   Uttayarat, P. *et al.* Micropatterning of three-dimensional electrospun polyurethane vascular grafts. *Acta Biomater.* **6,** 4229–4237 (2010).

91.   Thakar, R. G., Ho, F., Huang, N. F., Liepmann, D. & Li, S. Regulation of vascular smooth muscle cells by micropatterning. *Biochem. Biophys. Res. Commun.* **307,** 883–890 (2003).

92.   Werner, N. *et al.* Intravenous Transfusion of Endothelial Progenitor Cells Reduces Neointima Formation After Vascular Injury. *Circ. Res.* **93,** 17e–24 (2003).

93.   Zhao, X., Huang, L., Yin, Y., Fang, Y. & Zhou, Y. Autologous endothelial progenitor cells transplantation promoting endothelial recovery in mice. *Transpl. Int.* **20,** 712–721 (2007).

94.   Liu, S. *et al.* Influence of a layer-by-layer-assembled multilayer of anti-CD34 antibody, vascular endothelial growth factor, and heparin on the endothelialization and anticoagulation of titanium surface. *J. Biomed. Mater. Res. - Part A* **101 A,** 1144–1157 (2013).

95.   Sweryda-Krawiec, B., Devaraj, H., Jacob, G. & Hickman, J. J. A New Interpretation of Serum Albumin Surface Passivation. *Langmuir* **20,** 2054–2056 (2004).

96.   Krishnan, A., Siedlecki, C. A. & Vogler, E. A. Mixology of protein solutions and the

Vroman effect. *Langmuir* **20,** 5071–5078 (2004).

97. Hirsh, S. L. *et al.* The Vroman effect: Competitive protein exchange with dynamic
     multilayer protein aggregates. *Colloids Surfaces B Biointerfaces* **103,** 395–404 (2013).

98. Matsuda, T. & Inoue, K. Novel Photoreactive Surface Modification Technology for
     Fabricated Devices. *ASAIO Trans.* (1990).

99. Tanzi, M. C. Bioactive technologies for hemocompatibility. *Expert Rev. Med. Devices* **2,**
     473–492 (2005).

100. McClung, W. G., Clapper, D. L., Hu, S. P. & Brash, J. L. Lysine-derivatized polyurethane
     as a clot lysing surface: Conversion of adsorbed plasminogen to plasmin and clot lysis in
     vitro. *Biomaterials* **22,** 1919–1924 (2001).

101. McClung, W. G., Clapper, D. L., Hu, S. P. & Brash, J. L. Adsorption of plasminogen from
     human plasma to lysine-containing surfaces. *J. Biomed. Mater. Res.* **49,** 409–414 (2000).

102. Chen, H. *et al.* Surfaces having dual fibrinolytic and protein resistant properties by
     immobilization of lysine on polyurethane through a PEG spacer. *J. Biomed. Mater. Res. A*
     90, 940–946 (2009).

103. Li, D., Chen, H., Glenn McClung, W. & Brash, J. L. Lysine-PEG-modified polyurethane
     as a fibrinolytic surface: Effect of PEG chain length on protein interactions, platelet
     interactions and clot lysis. *Acta Biomater.* **5,** 1864–1871 (2009).

104. Li, D., Chen, H., Wang, S., Wu, Z. & Brash, J. L. Lysine-poly(2-hydroxyethyl
     methacrylate) modified polyurethane surface with high lysine density and fibrinolytic
     activity. *Acta Biomater.* **7,** 954–958 (2011).

105. Lin-Shu, L., Ito, Y. & Imanishi, Y. Biological activity of urokinase immobilized to cross-linked poly(2-hydroxyethyl methacrylate). *Biomaterials* **12,** 545–549 (1991).

106. Khamoio, Y. *et al.* A Femoral Vein Catheter with Immobilized Urokinase (UKFC) as an Antithrombotic Blood Access. *ASAIO Trans.* **33,** 136–139 (1987).

107. Ohshiro, T. & Kosaki, G. Urokinase Immobilized on Medical Polymeric Materials: Fundamental and Clinical Studies. *Artif. Organs* **4,** 58–64 (1980).

108. Sperling, C. *et al.* Immobilization of human thrombomodulin onto PTFE. *J. Mater. Sci. Mater. Med.* **8,** 789–791 (1997).

109. Kishida, A., Ueno, Y., Maruyama, I. & Akashi, M. Immobilization of human thrombomodulin on biomaterials: evaluation of the activity of immobilized human thrombomodulin. *Biomaterials* **15,** 1170–1174 (1994).

110. Biran, R. & Pond, D. Heparin coatings for improving blood compatibility of medical devices. *Adv. Drug Deliv. Rev.* **112,** 12–23 (2017).

111. Holmer, E., Kurachit, K. & Soderstrom, G. S. The molecular-weight dependence of the rate-enhancing effect of heparin on the inhibition of thrombin , Factor Xa , Factor IXa , Factor XIa , Factor XIIa and kallikrein by antithrombin. *Biochem. J.* 395–400 (1981).

112. Zimmermann, A. K., Weber, N., Aebert, H., Ziemer, G. & Wendel, H. P. Effect of Biopassive and Bioactive Surface-Coatings on the Hemocompatibility of Membrane Oxygenators. *J. Biomed. Mater. Res. B. Appl. Biomater.* **80B,** 433–439 (2007).

113. Wendel, H. P. & Ziemer, G. Coating-techniques to improve the hemocompatibility of artificial devices used for extracorporeal circulation. *Eur. J. Cardio-Thoracic Surg.* **16,**

342–350 (2011).

114. Ma, L. *et al.* Toward highly blood compatible hemodialysis membranes via blending with heparin-mimicking polyurethane: Study in vitro and in vivo. *J. Memb. Sci.* **470,** 90–101 (2014).

115. Cheng, C., Sun, S. & Zhao, C. Progress in heparin and heparin-like/mimicking polymer-functionalized biomedical membranes. *J. Mater. Chem. B* **00,** 1–24 (2014).

116. Olsson, P., Sanchez, J., Mollnes, T. E. & Riesenfeld, J. On the blood compatibility of end-point immobilized heparin. *J. Biomater. Sci. Polym. Ed.* **11,** 1261–1273 (2000).

117. Lindholt, J. S. *et al.* The Scandinavian Propaten®Trial - 1-Year patency of PTFE vascular prostheses with heparin-bonded luminal surfaces compared to ordinary pure PTFE vascular prostheses - A randomised clinical controlled multi-centre trial. *Eur. J. Vasc. Endovasc. Surg.* **41,** 668–673 (2011).

118. Chen, H., Chen, Y., Sheardown, H. & Brook, M. A. Immobilization of heparin on a silicone surface through a heterobifunctional PEG spacer. *Biomaterials* **26,** 7418–7424 (2005).

119. Sakiyama-Elbert, S. E. & Hubbell, J. a. Development of fibrin derivatives for controlled release of heparin-binding growth factors. *J. Control. Release* **65,** 389–402 (2000).

120. Liaw, P. C. Y., Becker, D. L., Stafford, A. R., Fredenburgh, J. C. & Weitz, J. I. Molecular Basis for the Susceptibility of Fibrin-bound Thrombin to Inactivation by Heparin Cofactor II in the Presence of Dermatan Sulfate but Not Heparin. *J. Biol. Chem.* **276,** 20959–20965 (2001).

121. Alibeik, S., Zhu, S. & Brash, J. L. Surface modification with PEG and hirudin for protein resistance and thrombin neutralization in blood contact. *Colloids Surfaces B Biointerfaces* **81,** 389–396 (2010).

122. Grütter, M. G. *et al.* Crystal structure of the thrombin-hirudin complex: a novel mode of serine protease inhibition. *EMBO J.* **9,** 2361–2365 (1990).

123. Phaneuf, M. D. *et al.* Covalent linkage of recombinant hirudin to a novel ionic poly(carbonate) urethane polymer with protein binding sites: Determination of surface antithrombin activity. *Artif. Organs* **22,** 657–665 (1998).

124. Dong, J., Liu, J., Kang, G., Xie, J. & Wang, Y. Pushing the resolution of photolithography down to 15nm by surface plasmon interference. *Sci. Rep.* **4,** 5618 (2014).

125. Lahann, J., Plüster, W., Klee, D., Gattner, H. G. & Höcker, H. Immobilization of the thrombin inhibitor r-hirudin conserving its biological activity. *J. Mater. Sci. Mater. Med.* **12,** 807–810 (2001).

126. Lahann, J., Klee, D., Pluester, W. & Hoecker, H. Bioactive immobilization of r-hirudin on CVD-coated metallic implant devices. *Biomaterials* **22,** 817–826 (2001).

127. Phaneuf, M. D., Berceli, S. A., Bide, M. J., Quist, W. C. & LoGerfo, F. W. Covalent linkage of recombinant hirudin to poly(ethylene terephthalate) (Dacron): Creation of a novel antithrombin surface. *Biomaterials* **18,** 755–765 (1997).

128. Berceli, S. A., Phaneuf, M. D., LoGerfo, F. W. & Patterson, R. B. Evaluation of a novel hirudin-coated polyester graft to physiologic flow conditions: Hirudin bioavailability and thrombin uptake. *J. Vasc. Surg.* **27,** 1117–1127 (1998).

129. Wang, Q. *et al.* The effect of hirudin modification of silk fibroin on cell growth and antithrombogenicity. *Mater. Sci. Eng. C* **75,** 237–246 (2017).

130. Sun, D., Hao, Y., Yang, G. & Wang, J. Hemocompatibility and cytocompatibility of the hirudin-modified silk fibroin. *J. Biomed. Mater. Res. - Part B Appl. Biomater.* **103,** 556–562 (2015).

131. Wyers, M. C. *et al.* In vivo assessment of a novel Dacron surface with covalently bound recombinant hirudin. *Cardiovasc. Pathol.* **8,** 153–159 (1999).

132. Stone, S. R. & Hofsteenge, J. Kinetics of the Inhibition of Thrombin by Hirudin. *Biochemistry* **25,** 4622–4628 (1986).

133. Naghavi, N., De Mel, A., Alavijeh, O. S., Cousins, B. G. & Seifalian, A. M. Nitric oxide donors for cardiovascular implant applications. *Small* **9,** 22–35 (2013).

134. Brisbois, E. J. *et al.* Reduction in Thrombosis and Bacterial Adhesion with 7 Day Implantation of S-Nitroso-N-acetylpenicillamine (SNAP)-Doped Elast-eon E2As Catheters in Sheep. *J. Mater. Chem. B* **3,** 1639–1645 (2015).

135. Jun, H. W., Taite, L. J. & West, J. L. Nitric oxide-producing polyurethanes. *Biomacromolecules* **6,** 838–844 (2005).

136. Carpenter, A. W., Slomberg, D. L., Rao, K. S. & Schoenfisch, M. H. Influence of scaffold size on bactericidal activity of nitric oxide-releasing silica nanoparticles. *ACS Nano* **5,** 7235–7244 (2011).

137. Wu, B., Gerlitz, B., Grinnell, B. W. & Meyerhoff, M. E. Polymeric coatings that mimic the endothelium: Combining nitric oxide release with surface-bound active

thrombomodulin and heparin. *Biomaterials* **28,** 4047–4055 (2007).

138. Taite, L. J. & West, J. L. Sustained Delivery of Nitric Oxide from Poly(ethylene glycol) Hydrogels Enhances Endothelialization in a Rat Carotid Balloon Injury Model. *Cardiovasc. Eng. Technol.* **2,** 113–123 (2011).

139. Lipke, E. A. & West, J. L. Localized delivery of nitric oxide from hydrogels inhibits neointima formation in a rat carotid balloon injury model. *Acta Biomater.* **1,** 597–606 (2005).

140. Nygren, H., Tengvall, P. & Lundstrom, I. The initial reactions of TiO2 with blood. *J. Biomed. Mater. Res.* **34,** 487–492 (1997).

141. Tsyganov, I., Maitz, M. F. & Wieser, E. Blood compatibility of titanium-based coatings prepared by metal plasma immersion ion implantation and deposition. *Appl. Surf. Sci.* **235,** 156–163 (2004).

142. Nan, H. *et al.* Blood compatibility of amorphous titanium oxide films synthesized by ion beam enhanced deposition. *Biomaterials* **19,** 771–776 (1998).

143. Huang, N. *et al.* Hemocompatibility of titanium oxide films. *Biomaterials* **24,** 2177–2187 (2003).

144. Zhang, F., Zheng, Z. & Chen, Y. In vivo investigation of blood compatibility of titanium oxide films. *J. Biomed. Mater. Res.* **42,** 128–133 (1998).

145. Wang, X. *et al.* Improvement of blood compatibility of artificial heart valves via titanium oxide film coated on low temperature isotropic carbon. *Surf. Coatings Technol.* **128–129,** 36–42 (2000).

146. Hung, W. C. *et al.* Oxygen-implanted induced formation of oxide layer enhances blood compatibility on titanium for biomedical applications. *Mater. Sci. Eng. C* **68,** 523–529 (2016).

147. Tsyganov, I., Maitz, M. F., Wieser, E., Richter, E. & Reuther, H. Correlation between blood compatibility and physical surface properties of titanium-based coatings. *Surf. Coatings Technol.* **200,** 1041–1044 (2005).

148. Love, C. A., Cook, R. B., Harvey, T. J., Dearnley, P. A. & Wood, R. J. K. Diamond like carbon coatings for potential application in biological implants - A review. *Tribol. Int.* **63,** 141–150 (2013).

149. Dearnaley, G. & Arps, J. H. Biomedical applications of diamond-like carbon (DLC) coatings: A review. *Surf. Coatings Technol.* **200,** 2518–2524 (2005).

150. Roy, R. K. *et al.* Hemocompatibility of surface-modified, silicon-incorporated, diamond-like carbon films. *Acta Biomater.* **5,** 249–256 (2009).

151. Hauert, R., Thorwarth, K. & Thorwarth, G. An overview on diamond-like carbon coatings in medical applications. *Surf. Coatings Technol.* **233,** 119–130 (2013).

152. Bewilogua, K. & Hofmann, D. History of diamond-like carbon films - From first experiments to worldwide applications. *Surf. Coatings Technol.* **242,** 214–225 (2014).

153. Chen, J. Y. *et al.* Blood compatibility and sp3/sp2 contents of diamond-like carbon (DLC) synthesized by plasma immersion ion implantation-deposition. *Surf. Coatings Technol.* **156,** 289–294 (2002).

154. Yang, P. *et al.* Activation of platelets adhered on amorphous hydrogenated carbon (a-C :

H) films synthesized by plasma immersion ion implantation-deposition (PIII-D). *Biomaterials* **24,** 2821–2829 (2003).

155. Liao, T. T. *et al.* Biological responses of diamond-like carbon (DLC) films with different structures in biomedical application. *Mater. Sci. Eng. C* **69,** 751–759 (2016).

156. Kwok, S. C. H., Wang, J. & Chu, P. K. Surface energy, wettability, and blood compatibility phosphorus doped diamond-like carbon films. *Diam. Relat. Mater.* **14,** 78–85 (2005).

157. Bokros, J. C. Carbon in medical devices. *Ceram. Int.* **9,** 3–7 (1983).

158. Gott, V. L., Alejo, D. E. & Cameron, D. E. Mechanical Heart Valves: 50 Years of Evolution. *Ann. Thorac. Surg.* **76,** (2003).

159. Goodman, S. L., Tweden, K. S. & Albrecht, R. M. Platelet interaction with pyrolytic carbon heart-valve leaflets. *J. Biomed. Mater. Res.* **32,** 249–258 (1996).

160. Marois, Y. & Bélanger, M. C. Studies of Primary Reference Materials Low-Density Polyethylene and Polydimethylsiloxane : A Review. *J. Biomed. Mater. Res.* **58,** 467–477 (2001).

161. Spiller, D. *et al.* PDMS content affects in vitro hemocompatibility of synthetic vascular grafts. *J. Mater. Sci. Mater. Med.* **18,** 1097–1104 (2007).

162. Elam, J. H. & Nygren, H. Adsorption of coagulation proteins from whole blood on to polymer materials: relation to platelet activation. *Biomaterials* **13,** 3–8 (1992).

163. Plegue, T. J., Kovach, K. M., Thompson, A. J. & Potkay, J. A. Stability of Polyethylene Glycol and Zwitterionic Surface Modifications in PDMS Microfluidic Flow Chambers.

Langmuir **34,** 492–502 (2018).

164. Kovach, K. M., Capadona, J. R., Gupta, A. Sen & Potkay, J. A. The effects of PEG-based surface modification of PDMS microchannels on long-term hemocompatibility. *J. Biomed. Mater. Res. - Part A* **102,** 4195–4205 (2014).

165. Zhang, Z. *et al.* Polybetaine modification of PDMS microfluidic devices to resist thrombus formation in whole blood. *Lab Chip* **13,** 1963–1968 (2013).

166. Khan, W., Muntimadugu, E., Jaffe, M. & Domb, A. J. *Focal Controlled Drug Delivery*. (2014). doi:10.1007/978-1-4614-9434-8

167. Chandy, T., Das, G. S., Wilson, R. F. & Rao, G. H. R. Use of plasma glow for surface-engineering biomolecules to enhance bloodcompatibility of Dacron and PTFE vascular prosthesis. *Biomaterials* **21,** 699–712 (2000).

168. Hoshi, R. A. *et al.* The blood and vascular cell compatibility of heparin-modified ePTFE vascular grafts. *Biomaterials* **34,** 30–41 (2013).

169. Wang, S. *et al.* Biomimetic fluorocarbon surfactant polymers reduce platelet adhesion on PTFE/ePTFE surfaces. *J. Biomater. Sci. Polym. Ed.* **20,** 619–635 (2009).

170. Lin, J. C., Tiong, S. L. & Chen, C. Y. Surface characterization and platelet adhesion studies on fluorocarbons prepared by plasma-induced graft polymerization. *J. Biomater. Sci. Polym. Ed.* **11,** 701–714 (2000).

171. Clarotti, G. *et al.* Plasma deposition of thin fluorocarbon films for increased membrane hemocompatibility. *J. Memb. Sci.* **61,** 289–301 (1991).

172. Huang, S. C. W., Cheng, C. H., Chiu, Y., Lin, Y. C. & Lin, J. C. A facile novel

fluorocarbon copolymer solution coating process for improving platelet compatibility of titanium. *Mater. Sci. Eng. C* **80,** 584–593 (2017).

173. Chen, K. Y. & Kuo, J. F. Surface characterization and platelet adhesion studies of aliphatic polyurethanes grafted by fluorocarbon oligomers: Effect of fluorocarbon chain length and carboxylic acid group. *J. Mater. Sci. Mater. Med.* **13,** 37–45 (2002).

174. Tsai, W. B., Shi, Q., Grunkemeier, J. M., McFarland, C. & Horbett, T. A. Platelet adhesion to radiofrequency glow-discharge-deposited fluorocarbon polymers preadsorbed with selectively depleted plasmas show the primary role of fibrinogen. *J. Biomater. Sci. Polym. Ed.* **15,** 817–840 (2004).

175. Kumar, V. *et al.* Low surface energy fluorocarbon coatings via plasma polymerization process : process optimization and protein repellent study. *Proc. 19th Int. Symp. Plasma Chem. ISPC-19* **19,** 1–4 (2009).

176. Riess, J. G. Highly fluorinated amphiphilic molecules and self-assemblies with biomedical potential. *Curr. Opin. Colloid Interface Sci.* **14,** 294–304 (2009).

177. Wilson, P. W. *et al.* Inhibition of ice nucleation by slippery liquid-infused porous surfaces (SLIPS). *Phys. Chem. Chem. Phys.* **15,** 581–5 (2013).

178. Kim, P., Kreder, M. J., Alvarenga, J. & Aizenberg, J. Hierarchical or Not? Effect of the Length Scale and Hierarchy of the Surface Roughness on Omniphobicity of Lubricant-Infused Substrates. *Nano Lett.* 1793–1799 (2013).

179. Wong, T.-S. *et al.* Bioinspired self-repairing slippery surfaces with pressure-stable omniphobicity. *Nature* **477,** 443–7 (2011).

180.   Leslie, D. C. *et al.* A bioinspired omniphobic surface coating on medical devices prevents thrombosis and biofouling. *Nat. Biotechnol.* 1–10 (2014). doi:10.1038/nbt.3020

181.   Zhang, M., Desai, T. & Ferrari, M. Proteins and cells on PEG immobilized silicon surfaces. *Biomaterials* **19,** 953–960 (1998).

182.   Sharma, S., Popat, K. C. & Desai, T. a. Controlling nonspecific protein interactions in silicon biomicrosystems with nanostructured poly(ethylene glycol) films. *Langmuir* **18,** 8728–8731 (2002).

183.   Popat, K. C., Mor, G., Grimes, C. a & Desai, T. a. Surface modification of nanoporous alumina surfaces with poly(ethylene glycol). *Langmuir* **20,** 8035–41 (2004).

184.   Fissell, W. H. *et al.* High-performance silicon nanopore hemofiltration membranes. *J. Memb. Sci.* **326,** 58–63 (2009).

185.   Sharma, S., Johnson, R. W. & Desai, T. A. Evaluation of the Stability of Nonfouling Ultrathin Poly (ethylene glycol) Films for Silicon-Based Microdevices. *Langmuir* **20,** 348–356 (2004).

186.   Han, S., Kim, C. & Kwon, D. Thermal/oxidative degradation and stabilization of polyethylene glycol. *Polymer (Guildf).* **38,** 317–323 (1997).

187.   Branch, D. W., Wheeler, B. C., Brewer, G. J. & Leckband, D. E. Long-term stability of grafted polyethylene glycol surfaces for use with microstamped substrates in neuronal cell culture. *Biomaterials* **22,** 1035–1047 (2001).

188.   Ishihara, K. *et al.* Hemocompatibility of human whole blood on polymers with a phospholipid polar group and its mechanism. *J. Biomed. Mater. Res.* **26,** 1543–1552

(1992).

189. Nakabayashi, N. & Williams, D. F. Preparation of non-thrombogenic materials using 2-methacryloyloxyethyl phosphorylcholine. *Biomaterials* **24,** 2431–2435 (2003).

190. Ueda, T., Oshida, H., Kurita, K., Ishihara, K. & Nakabayashi, N. Preparation of 2-Methacryloyloxyethyl Phosphorylcholine Copolymers with Alkyl Methacrylates and Their Blood Compatibility. *Polym. J.* **24,** 1259–1269 (1992).

191. Kobayashi, M. *et al.* Wettability and antifouling behavior on the surfaces of superhydrophilic polymer brushes. *Langmuir* **28,** 7212–7222 (2012).

192. Chen, S., Liu, L. & Jiang, S. Strong resistance of oligo(phosphorylcholine) self-assembled monolayers to protein adsorption. *Langmuir* **22,** 2418–21 (2006).

193. Nagahashi, K., Teramura, Y. & Takai, M. Stable surface coating of silicone elastomer with phosphorylcholine and organosilane copolymer with cross-linking for repelling proteins. *Colloids Surfaces B Biointerfaces* **134,** 384–391 (2015).

194. Xu, Y., Takai, M. & Ishihara, K. Protein adsorption and cell adhesion on cationic, neutral, and anionic 2-methacryloyloxyethyl phosphorylcholine copolymer surfaces. *Biomaterials* **30,** 4930–4938 (2009).

195. Tegoulia, V. A., Rao, W., Kalambur, A. T., Rabolt, J. F. & Cooper, S. L. Surface properties, fibrinogen adsorption, and cellular interactions of a novel phosphorylcholine-containing self-assembled monolayer on gold. *Langmuir* **17,** 4396–4404 (2001).

196. Gao, B. *et al.* Grafting of phosphorylcholine functional groups on polycarbonate urethane surface for resisting platelet adhesion. *Mater. Sci. Eng. C* **33,** 2871–2878 (2013).

197. Sun, X. Y., Yu, S. S., Wan, J. Q. & Chen, K. Z. Facile graft of poly(2-methacryloyloxyethyl phosphorylcholine) onto Fe 3O4 nanoparticles by ATRP: Synthesis, properties, and biocompatibility. *J. Biomed. Mater. Res. - Part A* **101 A,** 607–612 (2013).

198. Lewis, A. L. *et al.* Synthesis and characterisation of phosphorylcholine-based polymers useful for coating blood filtration devices. *Biomaterials* **21,** 1847–1859 (2000).

199. Lewis, A. L., Tolhurst, L. A. & Stratford, P. W. Analysis of a phosphorylcholine-based polymer coating on a coronary stent pre- and post-implantation. *Biomaterials* **23,** 1697–1706 (2002).

200. Goda, T., Ishihara, K. & Miyahara, Y. Critical update on 2-methacryloyloxyethyl phosphorylcholine (MPC) polymer science. *J. Appl. Polym. Sci.* **132,** 1–10 (2015).

201. Inoue, Y., Onodera, Y. & Ishihara, K. Preparation of a thick polymer brush layer composed of poly(2-methacryloyloxyethyl phosphorylcholine) by surface-initiated atom transfer radical polymerization and analysis of protein adsorption resistance. *Colloids Surfaces B Biointerfaces* **141,** 507–512 (2016).

202. Yamane, S. *et al.* Wear resistance of poly(2-methacryloyloxyethyl phosphorylcholine)-grafted carbon fiber reinforced poly(ether ether ketone) liners against metal and ceramic femoral heads. *J. Biomed. Mater. Res. - Part B Appl. Biomater.* **106,** 1028–1037 (2018).

203. Zhang, Z. *et al.* Blood compatibility of surfaces with superlow protein adsorption. *Biomaterials* **29,** 4285–4291 (2008).

204. Zhang, Z., Chao, T., Chen, S. & Jiang, S. Superlow fouling sulfobetaine and carboxybetaine polymers on glass slides. *Langmuir* **22,** 10072–10077 (2006).

205. Zhang, Z. *et al.* Zwitterionic hydrogels: an in vivo implantation study. *J. Biomater. Sci. Polym. Ed.* **20,** 1845–1859 (2009).

206. Lee, S. Y., Lee, Y., Le Thi, P., Oh, D. H. & Park, K. D. Sulfobetaine methacrylate hydrogel-coated anti-fouling surfaces for implantable biomedical devices. *Biomater. Res.* **22,** 3 (2018).

207. Zhang, Z., Chen, S., Chang, Y. & Jiang, S. Surface grafted sulfobetaine polymers via atom transfer radical polymerization as superlow fouling coatings. *J. Phys. Chem. B* **110,** 10799–10804 (2006).

208. Dizon, G. V. *et al.* Bio-inert interfaces via biomimetic anchoring of a zwitterionic copolymer on versatile substrates. *J. Colloid Interface Sci.* **529,** 77–89 (2018).

209. Cheng, G. *et al.* Zwitterionic carboxybetaine polymer surfaces and their resistance to long-term biofilm formation. *Biomaterials* **30,** 5234–5240 (2009).

210. Liu, P.-S., Chen, Q., Wu, S.-S., Shen, J. & Lin, S.-C. Surface modification of cellulose membranes with zwitterionic polymers for resistance to protein adsorption and platelet adhesion. *J. Memb. Sci.* **350,** 387–394 (2010).

211. Ladd, J., Zhang, Z., Chen, S., Hower, J. C. & Jiang, S. Zwitterionic polymers exhibiting high resistance to nonspecific protein adsorption from human serum and plasma. *Biomacromolecules* **9,** 1357–1361 (2008).

212. Zhang, L. *et al.* Facile surface modification of glass with zwitterionic polymers for improving the blood compatibility. *Mater. Res. Express* **5,** (2018).

213. Li, L., Marchant, R. E., Dubnisheva, A., Roy, S. & Fissell, W. H. Anti-biofouling

Sulfobetaine Polymer Thin Films on Silicon and Silicon Nanopore Membranes. *J. Biomater. Sci.* **22,** 91–106 (2011).

214.   Cheng, G., Zhang, Z., Chen, S., Bryers, J. D. & Jiang, S. Inhibition of bacterial adhesion and biofilm formation on zwitterionic surfaces. *Biomaterials* **28,** 4192–9 (2007).

215.   Lalani, R. & Liu, L. Electrospun zwitterionic poly(sulfobetaine methacrylate) for nonadherent, superabsorbent, and antimicrobial wound dressing applications. *Biomacromolecules* **13,** 1853–1863 (2012).

216.   Yang, R., Xu, J., Ozaydin-Ince, G., Wong, S. Y. & Gleason, K. K. Surface-Tethered Zwitterionic Ultrathin Antifouling Coatings on Reverse Osmosis Membranes by Initiated Chemical Vapor Deposition. *Chem. Mater.* **23,** 1263–1272 (2011).

217.   Yang, W. *et al.* Film thickness dependence of protein adsorption from blood serum and plasma onto poly(sulfobetaine)-grafted surfaces. *Langmuir* **24,** 9211–9214 (2008).

218.   Zhu, J. *et al.* Surface zwitterionic functionalized graphene oxide for a novel loose nanofiltration membrane. *J. Mater. Chem. A* **4,** 1980–1990 (2016).

219.   Chang, Y., Chang, W., Shih, Y., Wei, T. & Hsiue, G. Zwitterionic Sulfobetaine-Grafted Poly (vinylidene fluoride) Membrane with Highly Effective Blood Compatibility via Atmospheric Plasma-induced Surface Copolymerization. *Appl. Mater. Interfaces* 1228–1237 (2011).

220.   Yu, H.-Y., Kang, Y., Liu, Y. & Mi, B. Grafting polyzwitterions onto polyamide by click chemistry and nucleophilic substitution on nitrogen: A novel approach to enhance membrane fouling resistance. *J. Memb. Sci.* **449,** 50–57 (2014).

221. Dong, Z. *et al.* Phase behavior of poly(sulfobetaine methacrylate)-grafted silica nanoparticles and their stability in protein solutions. *Langmuir* **27,** 15282–15291 (2011).

222. Zhang, H. & Chiao, M. Anti-fouling coatings of poly(dimethylsiloxane) devices for biological and biomedical applications. *J. Med. Biol. Eng.* **35,** 143–155 (2015).

223. Wu, H. *et al.* Highly sensitive and stable zwitterionic poly(sulfobetaine-3,4-ethylenedioxythiophene) (PSBEDOT) glucose biosensor. *Chem. Sci.* **9,** 2540–2546 (2018).

224. Smith, R. S. *et al.* Vascular Catheters with a Nonleaching Poly-Sulfobetaine Surface Modification Reduce Thrombus Formation and Microbial Attachment. *Sci. Transl. Med.* **4,** 153ra132-153ra132 (2012).

225. Carr, L. R., Zhou, Y., Krause, J. E., Xue, H. & Jiang, S. Uniform zwitterionic polymer hydrogels with a nonfouling and functionalizable crosslinker using photopolymerization. *Biomaterials* **32,** 6893–6899 (2011).

226. Matyjaszewski, K. & Xia, J. Atom transfer radical polymerization. *Chem. Rev.* **101,** 2921–2990 (2001).

227. Sin, M.-C., Chen, S.-H. & Chang, Y. Hemocompatibility of zwitterionic interfaces and membranes. *Polym. J.* **46,** 436–443 (2014).

228. Chen, S., Li, L., Zhao, C. & Zheng, J. Surface hydration: Principles and applications toward low-fouling/nonfouling biomaterials. *Polymer (Guildf).* **51,** 5283–5293 (2010).

229. Azzaroni, O., Brown, A. A. & Huck, W. T. S. UCST wetting transitions of polyzwitterionic brushes driven by self-association. *Angew. Chemie - Int. Ed.* **45,** 1770–

1774 (2006).

Development, Optimization and Characterization of Ultrathin Zwitterionic Surface Modifications

2.1 Introduction

With advancements in bio-microelectromechanical systems (bioMEMS), silicon has become a common substrate for novel implant devices, such as neuroelectrodes,[1,2] drug delivery systems,[3–5] biosensors and diagnostic devices,[6–8] and artificial organs.[9–12] One such device is the silicon nanopore membrane (SNM): these membranes are highly uniform in geometry and low in fluidic resistance, making them attractive for blood filtration and immunoisolation in renal replacement[9,13,14] and islet therapy.[11,15] These applications require SNMs to come in direct contact with blood flow. While silicon has been shown to be non-cytotoxic, non-leaching and non-irritant,[16–18] the surfaces must also be non-activating and non-fouling for use as membranes in biological applications.

To attain desired interfacial properties, rather than using alternative materials, the surface of the substrate is often modified.[19] For SNMs, there are specific surface traits that are desired: a) the surface must be non-fouling and non-activating; b) the surface must be hydrophilic to lower the resistance of the membranes; c) the applied surface coatings must be durable, ultrathin and uniform to maintain pore patency and tight pore size distribution; and d) the surface modification must be applicable to silicon. Based on these requirements, two zwitterionic coatings were

chosen for investigation with SNMs: sulfobetaine methacrylate (SBMA) and 2-methacryloyloxyethyl phosphorylcholine (MPC).

Zwitterionic polymeric brush structures are extremely hydrophilic and have shown enhanced hemocompatibility. Using a methacrylate backbone, polymer brushes and hydrogels can be controllably grown with atom-transfer radical polymerization (ATRP).[20–22] The zwitterions branch off from the methacrylate backbone and electrostatically interact with each other. More importantly, they create a hydration layer on the surface by coordinating water molecules through hydrogen bonding and electrostatic interactions.[21,23] This hydration layer resists protein fouling[24–28] and thrombus formation.[20,23,29]

As a control, polyethylene glycol (PEG) surface modification was used, which has previously demonstrated excellent resistance to protein adsorption and platelet adhesion.[30,31] Our previous research shows PEG-modified silicon significantly reduced thrombus formation and inflammation following 4-week implantation in rat veins.[32] However, PEG is also known to autoxidize under biological conditions, making it impractical for long term implant applications.[33]

We coated silicon substrates with PEG, polymerized SBMA (pSBMA), and polymerized MPC (pMPC). Each of the coatings was applied at sub-5 nm thickness, and characterized using various surface characterization methods: elemental composition was determined using x-ray photoelectron spectroscopy (XPS), which captures ~10 nm of the surface; static water contact angle was measured using goniometry to evaluate the changes in wettability; ellipsometry was used to determine the change in coating thickness; and atomic force microscopy (AFM) was used to examine the surface roughness after coating. Additionally, the coatings were applied to SNMs

and the hydraulic permeability was measured. Based on hydraulic permeability, the effective pore size of the membranes was determined.

To our knowledge, surface modification using pSBMA and pMPC at sub-5 nm scale has not previously been utilized or well characterized. Therefore, for best results at this scale, protocol optimization was conducted. During ATRP, there are many parameters that can change the polymer properties. For example, altering the concentration of reagents, time and temperature of polymerization, and/or washing conditions post-polymerization can affect the length of polymers grown as well as the grafting density of the polymers. To optimize the coating protocol, these variables were changed, and the coating performance was evaluated. This chapter presents two such experiments where polymerization time and post-polymerization washing conditions were tested. Based on experiments such as these, the optimal conditions were selected for future experiments presented in this thesis.

The first of the two optimization experiments presented shows the effect of variation in reaction time. Polymerization reaction time plays a critical role in the length of the polymer chain. While desired coating thickness must be sub-5 nm, polymer coating that is too thin can also be ineffective since it may expose the substrate surface underneath.

The second optimization experiment presented shows variation in washing conditions. After polymerization, it is important to remove excess reagents so they do not interfere with polymer performance. One example is the ATRP catalyst, copper (I) bromide (CuBr), which is difficult to remove from silicon surfaces. Therefore, a rigorous washing regimen was developed that includes organic as well as aqueous solvents. For this optimization experiment, four organic solvents were tested: methanol, ethanol, toluene, and chloroform.

Each of the optimization experiments was followed by characterization by ellipsometry and goniometry. Additionally, the performance of the coatings were evaluated using adsorption of proteins on the surface. Specifically, human fibrinogen and bovine serum albumin (BSA) were used, as reported in previous literature.[26,31,33–35] BSA was chosen as model protein for non-specific surface binding, while fibrinogen was chosen for its role in thrombus formation.[30,36,37]

2.2 Materials and Methods

2.2.1 Silicon Surface Modification

Unless otherwise stated, chemicals were purchased from Sigma-Aldrich (St. Louis, MO, USA).

2.2.1.1 Synthesis of ATRP Initiator, BrTMOS

ATRP initiator, 2-bromo-2-methyl-N-3[(trimethoxysilyl)propyl]-propanamide (BrTMOS) was synthesized as previously reported.[26,33] Briefly, under nitrogen (N_2) protection, 11 mmol of σ-bromoisobutyryl bromide (98%) was added dropwise to a mixture of 10 mmol (3-aminopropyl)trimethoxysilane (97%) and 10 mmol trimethylamine in 50 mL of anhydrous tetrahydrofuran (THF) over 30 minutes. The exothermic reaction was kept on ice to reduce heating, and allowed to continue overnight. After removing the precipitate, THF was evaporated from the filtrate using a rotary evaporator (Buchi, Flawil, Switzerland) and the concentrated oil was dissolved in 20 mL of dichloromethane. The solution was then washed with 10% potassium bisulfate (2 x 20 mL), cold deionized (DI) water (1 x 20 mL), and saturated sodium chloride solution (2 x 20 mL), respectively, using a separation funnel. Finally, the organic phase was collected and dried using anhydrous magnesium sulfate ($MgSO_4$). After filtering out the $MgSO_4$, dichloromethane was evaporated off, yielding the final product, BrTMOS. ^{1}H NMR (400MHz, $CHCl_3$) was conducted on the colorless oil to verify BrTMOS formation: δ 6.90 (s, 1H, NH),

3.49 (s, 9H, SiOCH$_3$), 3.26 (t, 2H, CH$_2$N), 1.95 (s, 6H, CH$_3$), 1.66 (m, 2H, CH$_2$), 0.66 (t, 2H,

SiCH$_2$). NMR spectrum is included in Appendix A. Chemical structure of BrTMOS is shown

below:
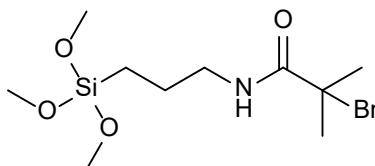
2.2.1.2 Sample Preparation

Sulfuric acid (H$_2$SO$_4$, 96%), hydrogen peroxide (H$_2$O$_2$, 30%), and hydrofluoric acid (HF, 49%)

were purchased from Avantor Performance Materials, (Center Valley, PA, USA). Double-side-

polished, 400 μm thick, p-type silicon wafers (Ultrasil Corporation, Hayward, CA, USA) were

diced in 1 x 1 cm^2 chips. SNMs were fabricated following procedures previously described.[9,38]

All samples were rinsed in acetone, methanol, isopropanol and water (1 x 5 min, each). To

remove residual organics, the substrates were cleaned using a freshly made solution of

"piranha"—a 3:1 ratio of H$_2$SO$_4$ to H$_2$O$_2$ for 20 min. After rinsing in DI water (2 x 10 min) all

samples were placed in HF for 2 min to etch away silicon dioxide (SiO$_2$, thermally grown to

produce slit pores for SNMs). The substrates were rinsed again with DI water (3 x 10 min) and

placed back in a fresh "piranha" solution for 20 min to activate the surface. Following a final

rinse with DI water (3x 10 min), all substrates were dried on the hot plate at 60 °C for 1 hour.

2.2.1.3 Surface Polymerization
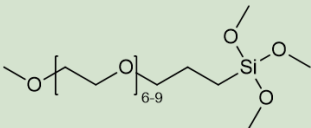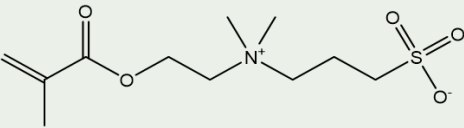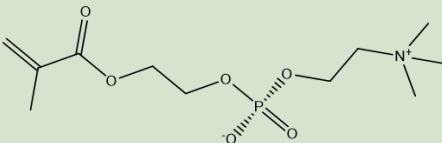
2.2.1.3.1 Zwitterionic Surface Modification

The following zwitterionic surface modifications protocol presented are the ultimate conditions

based on the optimization experiments. The substrates were placed in a 1% (v/v) BrTMOS

solution in bicyclohexyl for 2 hours. The surfaces were then rinsed with chloroform, ethanol, and water, respectively, to remove excess BrTMOS.

The chemical structures of zwitterionic monomers, 2-(methacryloyloxy)ethyl]dimethyl-(3-sulfopropyl)ammonium hydroxide (SBMA), and 2-methacryloyloxyethyl phosphorylcholine (MPC), are shown in Table 2.1. A degassed solution of 468 mg (3 mmol) of 2,2'-bipyridyl ($\geq$98%) and individual monomers—SBMA: 1.06g (3.8 mmol), and MPC: 506 mg (1.9 mmol)—and 22.3 mg (0.1 mmol) of copper (II) bromide (99%) was prepared in 5:5 mL of methanol:water. This mixture was added to a reaction chamber housing four substrates and 143 mg (1 mmol) of copper (I) bromide (99.999%) under nitrogen protection, and polymerization ran for 15 min for pSBMA and 7 min for pMPC. The substrates were then rinsed with chloroform, ethanol, Dulbecco's phosphate buffered saline (D-PBS, UCSF Cell Culture Facility, San Francisco, CA, USA), and water, respectively, and dried using a stream of nitrogen gas.

Table 2.1: Chemical structure of PEG-silane, SBMA and MPC monomer.

1, 2-[methoxy(polyethyleneoxy)propyl]trimethoxysilane (PEG-silane)	
2-(methacryloyloxy)ethyl]dimethyl-(3-sulfopropyl)ammonium hydroxide, sulfobetaine methacrylate (SBMA)	
2-methacryloyloxyethyl phosphorylcholine (MPC)	

2.2.1.3.2 PEG Surface Modification

Silicon surfaces were modified with PEG as previously described.[10,11] Briefly, 2-[methoxy(polyethyleneoxy)$_{6-9}$propyl]trimethoxysilane (PEG-silane), as shown in Table 2.1, was purchased from Gelest (Morrisville, PA, USA) and covalently bonded to silicon by immersing the substrates in a solution of 285 µl PEG-silane in 25 mL of toluene for 2 hours at 70 °C. The substrates were then rinsed three times at 10 min intervals with toluene, ethanol, and water, respectively, to remove excess PEG, and stored dry under ambient condition until use.

2.2.2 Surface Coating Characterization

2.2.2.1 X-ray Photoelectron Spectroscopy (XPS)

XPS was conducted using a Surface Science Instruments S-probe spectrometer with a monochromatized Al Kα x-ray source (serviced by Service Physics, Bend, OR, USA). Data was collected under a vacuum of pressure less than 5e10^{-9} torr, with an x-ray spot size of 800 µm. To calculate the composition, survey spectra used a pass energy of 150 eV, while high resolution scans used a pass energy of 50 eV. The take-off angle was 0°, yielding a sampling depth of ~10 nm. Data was analyzed using the Hawk Data Analysis Software (Service Physics). The binding energy scales were calibrated by setting C1s peak to 285.0 eV. Three measurements were taken per sample group for survey spectra, and one spot was analyzed for high resolution.

2.2.2.2 Goniometry

Static contact angle measurements were taken using Attension Theta Lite from Biolin Scientific (Stockholm, Sweden). A droplet size of ~3.5 µl of water placed on the substrate and the angle between the droplet and substrate was measured in air over 10 s at 0.1 s interval. A minimum of 3 measurements were taken for each sample set.

2.2.2.3 Ellipsometry

Ellipsometry was conducted using Gaertner Stokes Ellipsometer using a 6328 Å HeNe laser at 70° incidence angle. A refractive index of 1.403 was used for PEG and 1.45 was used for pSBMA and pMPC, respectively. As was previously done for transparent films with known index of refraction,[33] coating thickness was iteratively solved for by entering in measured reflection and transmission data into Fresnel equations. A minimum of 3 locations on individual substrate was collected and averaged over each sample set.

2.2.2.4 Atomic Force Microscopy (AFM)

Atomic force microscopy (AFM) was conducted using NanoScope Scanning Probe Microscope (Bruker, Santa Barbara, CA, USA), running on tapping mode with the triangular ScanAsyst-fluid+ tip (Bruker) with a spring constant of 0.7 N/m. A scan rate of 0.977 Hz, with 512 samples/line sampling rate was used to generate AFM images. At least three different locations on each type of surface were scanned and the root mean square roughness (R_q) values were averaged over three 1 μm^2 areas. NanoScope Analysis Software (Bruker) was used to process images and determine roughness values.

2.2.2.5 Hydraulic Permeability Measurement

Surface modifications on SNMs with porous area of 36 mm^2 were conducted, and change in pore size was calculated based on membrane permeability. Hydraulic permeability of the membrane was measured before and after surface modification using the setup shown in Figure 2.1. An SNM sits on the chip seat in the two-chamber filtration manifold, and a gasket creates a seal between the feed and the filtrate side. A peristaltic pump draws water from the reservoir to maintain a constant cross flow rate. A pressure gauge measures the pressure right before the

flow reaches the manifold. Finally, a resistor is placed in series following the manifold to control the transmembrane pressure before the feed is returned to the reservoir. The filtrate is collected into a syringe open to ambient air and the volume is measured.

Given the rectangular geometry of the pores, where the width (w) of the pore is much smaller than its length (L) and height (h), resistance (R) through the membrane can be characterized by the following equation:

$$R = \frac{\Delta P}{Q} = \frac{12\mu h}{w^3 Ln} \qquad \text{Eqn. 2.1}$$

where ΔP is the transmembrane pressure, Q is the volumetric flow rate, μ is the viscosity of water, and n is the number of pores. Using the hydraulic permeability setup to set the resistance, the transmembrane pressure was controlled and the filtration rate was measured. With these two values, and knowing the viscosity of water, number of pores (1.56e7 pores), length (2.325 μm) and height (400 nm) of the pores, the width of the pores (the nominal feature) was calculated.
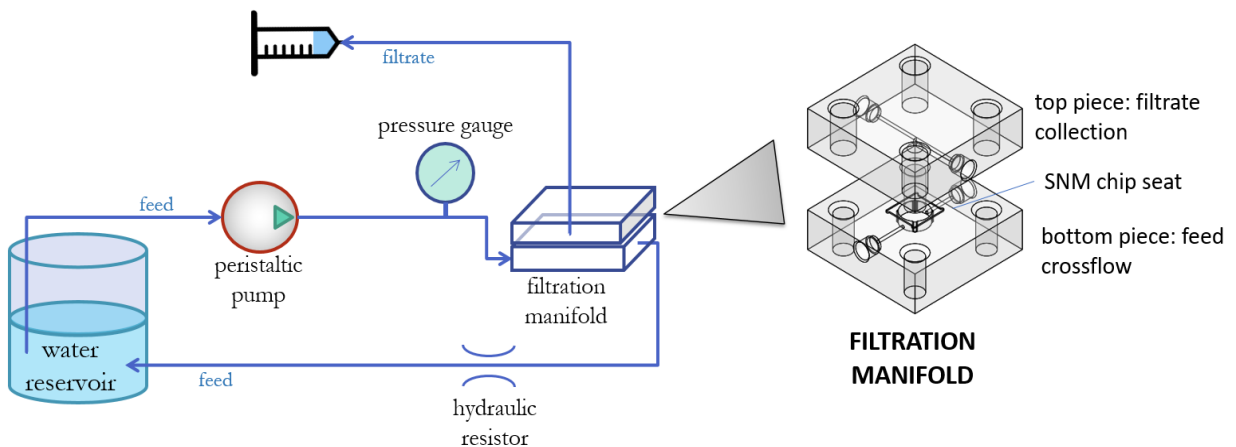
Figure 2.1: *Hydraulic permeability setup. A peristaltic pump draws water from the reservoir and maintains a constant flow rate. A pressure gauge measures the pressure immediately before flow reaches filtration manifold, where SNM is positioned for filtration. The feed crossflow is returned to the water reservoir, while the filtrate volume is measured using a syringe over time.*

2.2.3 In Vitro *Protein Adsorption*

2.2.3.1 Human Fibrinogen Enzyme-Linked Immunosorbent Assay (ELISA)

Human fibrinogen adsorption on the surfaces of the substrates was determined by conducting enzyme-linked immunosorbent assay (ELISA) following protocol published previously.[33] Substrates were placed in 24-well tissue-culture polystyrene (TCPS) plates and incubated with D-PBS for 1.5 hours. D-PBS was replaced with 0.5 mL of single protein solution: 1 mg/mL concentration of human fibrinogen was added and allowed to incubate at 37 °C for 1.5 hours. All substrates were rinsed five times with D-PBS. Surfaces were then blocked with bovine serum albumin (BSA, ≥98%) using 1 mg/mL BSA solution for 1.5 hours. The substrates were rinsed five times with D-PBS, and transferred to new 24-well TCPS wells. Next, the samples were incubated with 10 µg/mL anti-human fibrinogen conjugated with horseradish peroxidase (HRP) (coagulation factor I) (HRP) (USBiological, Salem, MA, USA) for 1.5 hours. The substrates were washed with D-PBS five times and transferred to a new well. A reaction mixture was made in 0.05 M citrate phosphate buffer (pH 5.0, Sigma-Aldrich) with 0.5 mg/mL of o-phenylenediamine (OPD, VWR Inc. Visalia, CA, USA) and 0.03% hydrogen peroxide. Reaction mixture (0.5 mL) was added to each well, and the reaction was allowed to run at 37 °C for 20 minutes. The reaction was stopped by adding 0.5 mL sulfuric acid (1 M). The solution was transferred to 96 well plates, and light absorbance at 490 nm was determined using a microplate reader. A minimum of 3 substrates were analyzed for each sample set, and light absorbance reading was normalized to tissue culture polystyrene (TCPS) control.

2.2.3.2 Bovine Serum Albumin (BSA) Adsorption

BSA adsorption was evaluated following protocol previously published.[39] A 0.5 mg/mL of fluorescein isothiocyanate conjugated bovine serum albumin (FITC-BSA) was well mixed in D-PBS, and protected from light using aluminum foil. Samples were placed into a 24-well plate, and 1 mL of FITC-BSA solution was added to each sample. The samples were protected from light and incubated at 37 °C for 1 hour. Each chip was rinsed three times using D-PBS to remove unadsorbed proteins, and placed in a new well with 1 mL of D-PBS. Imaging was done using a Nikon TI-E Microscope (Nikon Instruments, Melville, NY, USA) at 100x magnification. Five representative locations (top left, top right, center, bottom left and bottom right) were imaged per chip and three chips were imaged per sample group. One representative image is presented in this chapter. The images were then quantified for fluorescence from FITC-BSA using ImageJ software (National Institutes of Health), and the average and standard deviation values are reported.

2.3 Results

2.3.1 Optimization of Polymerization Time

The effect of reaction time on pSBMA polymerization on silicon is presented in Figures 2.2-2.5. In this experiment, two time-points were evaluated: 10 min and 20 min. Figure 2.2 represents the effect of polymerization time on the coating thickness and the contact angle. Results show that a 10 min reaction time yields an average thickness of 4.4 nm and a contact angle of 18.5°. With 20 polymerization time, pSBMA coating thickness increases to an average of 5.7 nm and contact angle decreases to 5.5°.
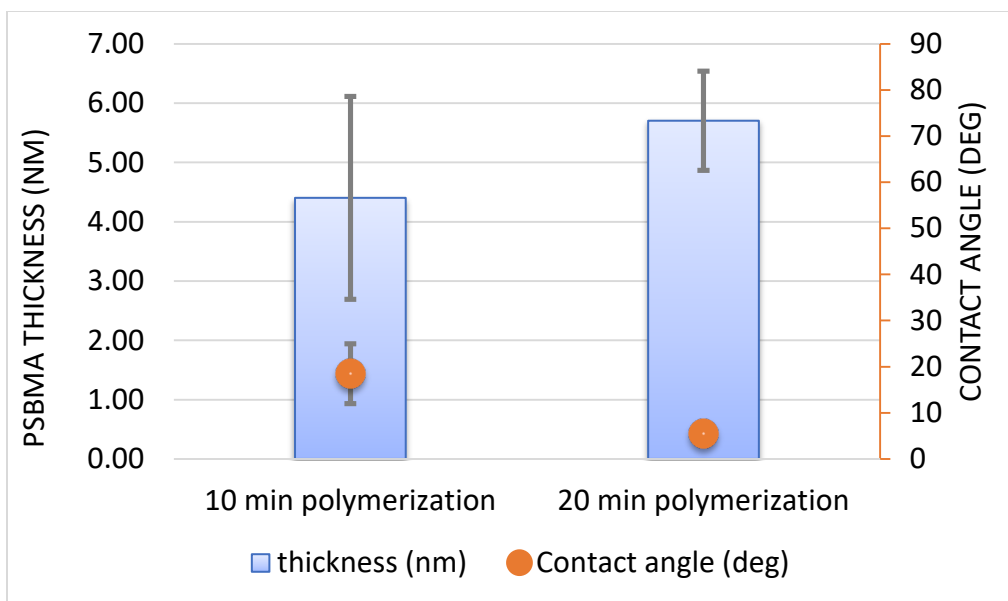
Figure 2.2: *Effect of polymerization time variation (10 and 20 min) on pSBMA coating thickness and surface contact angle.*

Following characterization, coating performance was evaluated using adsorption from single protein solutions as a metric. Adsorption of human fibrinogen is quantified using ELISA in Figure 2.3 and adsorption of BSA is depicted and quantified based on imaging in Figures 2.4 and 2.5, respectively. Results show pSBMA with 20 min polymerization had the least fibrinogen adsorption, reducing fibrinogen adsorption by ~71% compared to uncoated silicon. PEG and pSBMA with 10 min polymerization reduced fibrinogen adsorption by ~17% and ~23%, respectively, compared to uncoated silicon.
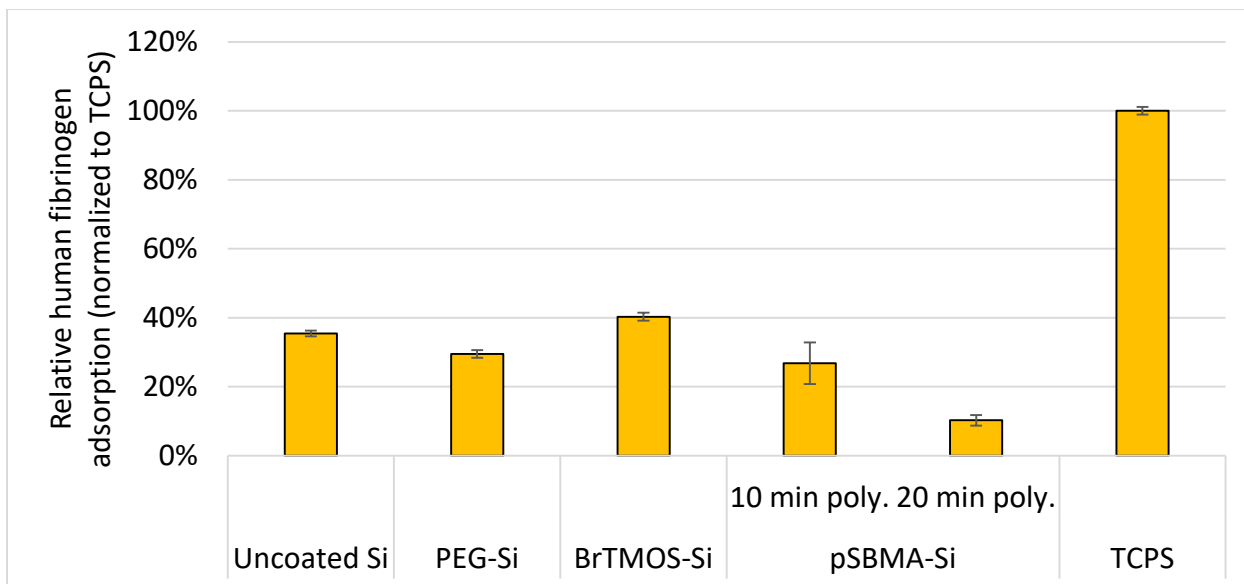
Figure 2.3: *Relative human fibrinogen adsorption before and after surface modification. Lowest adsorption was observed with 20 min polymerization of pSBMA. Data is normalized to tissue culture polystyrene (TCPS).*

Figure 2.4, depicting FITC-BSA adsorption on silicon surface before and after surface modification, demonstrates that surfaces are visually similar with and without coatings. When quantified, and normalized to uncoated silicon, it is evident that PEG-silicon demonstrates a significant reduction in BSA adsorption compared to silicon, reducing it by ~79%. pSBMA, regardless of polymerization time, has no significant difference in performance when compared to silicon.
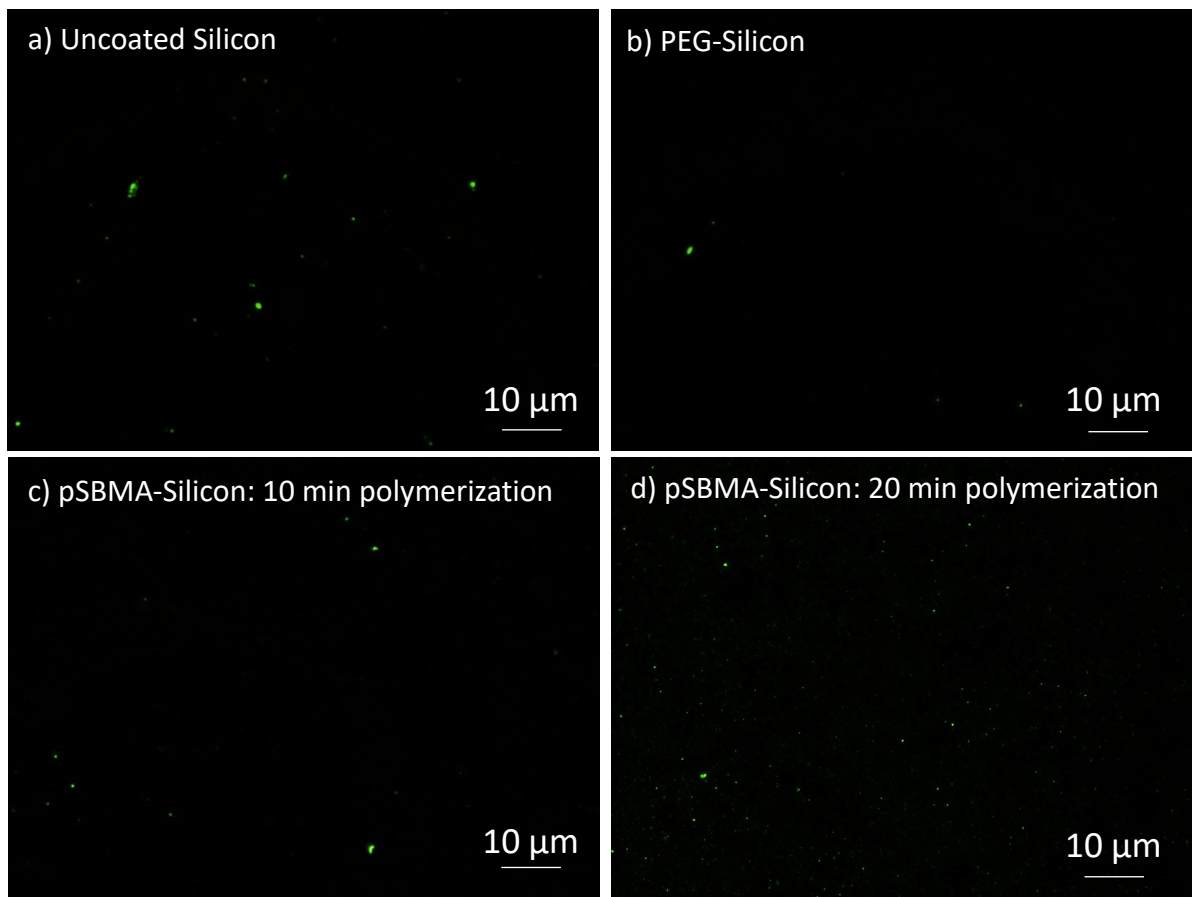
Figure 2.4: *FITC-BSA adsorption on silicon (a) before and (b-d) after surface modification with PEG and pSBMA (10 min and 20 min polymerization).*
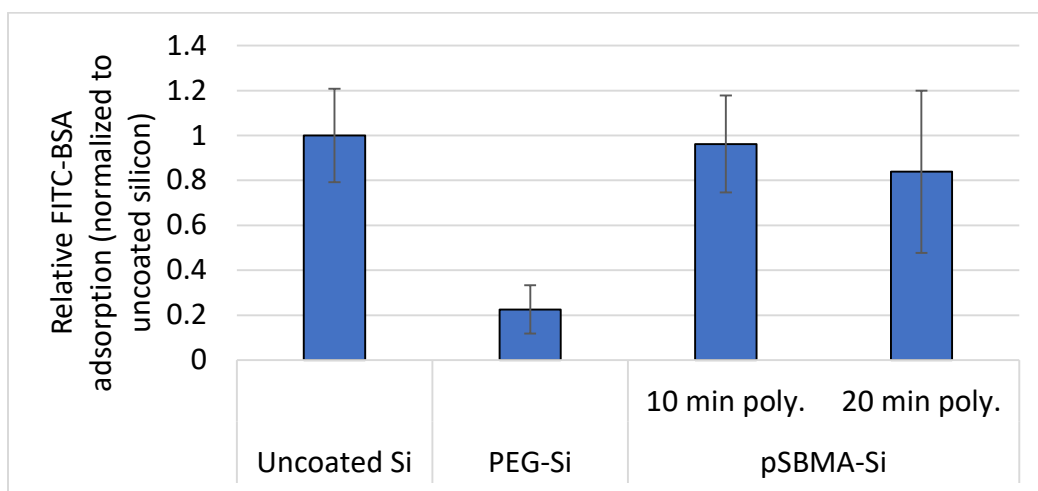
Figure 2.5: *FITC-BSA adsorption on silicon before and after surface modification with PEG and pSBMA (10 min and 20 min polymerization). Fluorescence has been quantified using 5 representative images per sample following substrate incubation with FITC-BSA.*

2.3.2 Optimization of Wash Conditions Following Polymerization

The effect of various wash conditions following pSBMA polymerization is presented in Figures 2.6-2.9. Post-polymerization washing entails wash steps using aqueous and organic solvents. In this optimization experiment, various organic solvents were tested to see which solvent best removed residues without harming the surface coating. Four organic solvents were tested for washing: ethanol, methanol, toluene, and chloroform. Figure 2.6 represents effect of the various washes on the coating thickness and the contact angle. Results show that with pSBMA coating, contact angle remained <11° for all washes, the lowest reaching 6.75° with chloroform washing. Coating thickness ranged from 3.7 to 4.8 nm, with the maximum thickness measured for methanol washing.
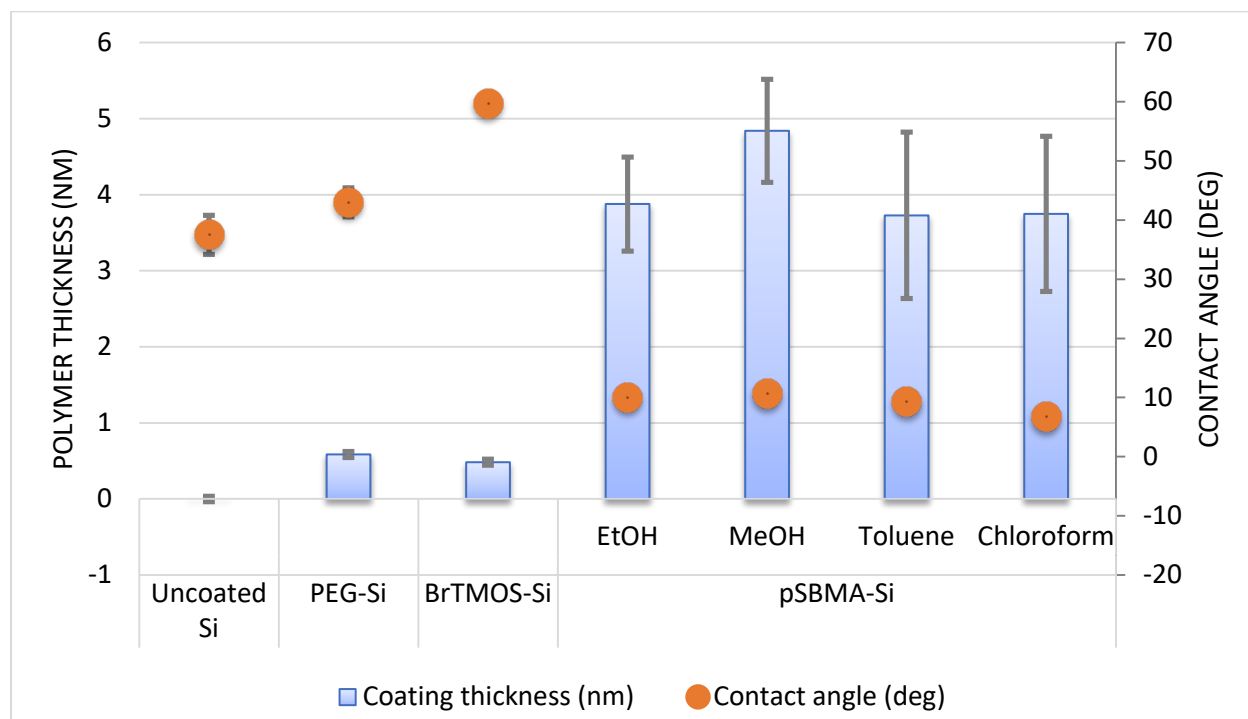
Figure 2.6: *Effect of post-polymerization wash conditions on polymer thickness and water contact angle. Four organic solvents were tested: ethanol (EtOH), methanol (MeOH), toluene and chloroform.*
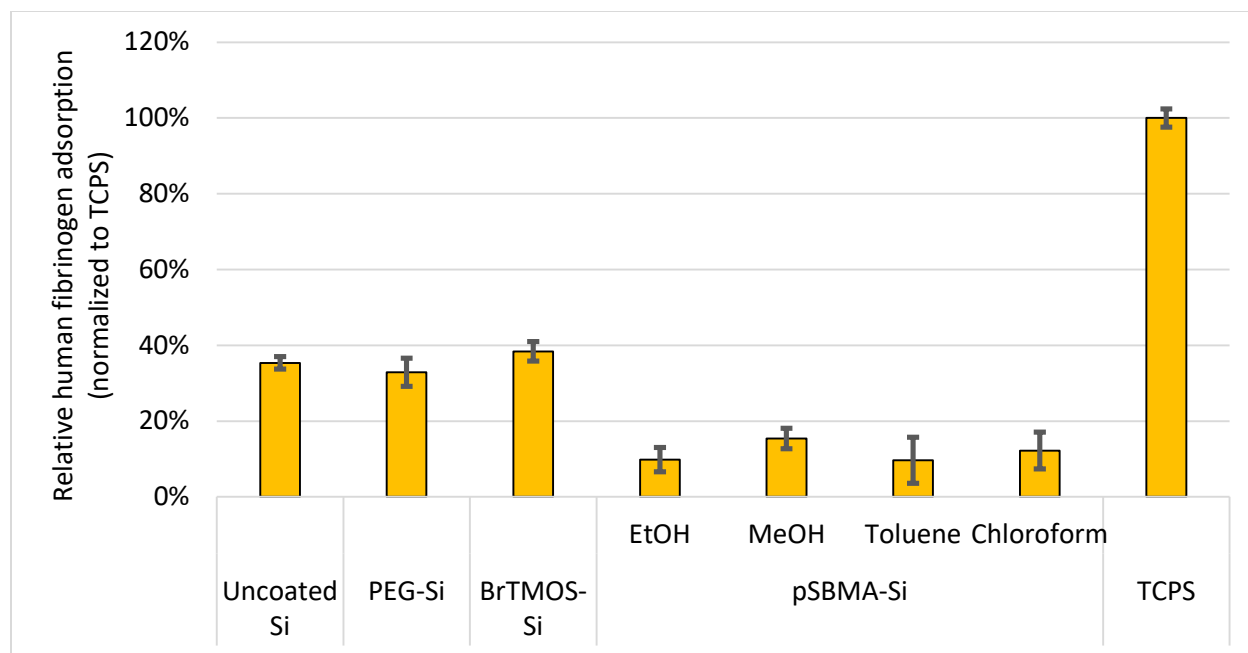
Figure 2.7: *Human fibrinogen adsorption quantified using ELISA before and after surface modification for varying organic solvent wash conditions. Data has been normalized to tissue culture polystyrene (TCPS).*

Human fibrinogen adsorption was measured using ELISA over the various wash conditions and presented in Figure 2.7. Results show that all pSBMA coating, regardless of wash conditions, reduce fibrinogen adsorption by at least 56% compared to uncoated silicon. Control PEG-coating, however, did not significantly reduce fibrinogen adsorption compared to uncoated silicon.

FITC-BSA adsorption was also evaluated and presented in Figure 2.8 and 2.9. Figure 2.8 shows that washing with methanol led to a considerably higher BSA adhesion compared to the rest of the substrates. Images were quantified based on fluorescence and normalized to uncoated silicon. Results show control PEG reduces protein adsorption by ~59%. Aside from pSBMA-silicon washed with methanol, all other groups lowered BSA adsorption. The lowest protein adsorption was observed with chloroform washes, reducing BSA adsorption by ~89% compared to uncoated silicon.

a) Uncoated Silicon
10 μm

b) PEG-Silicon
10 μm

c) BrTMOS-Silicon
10 μm
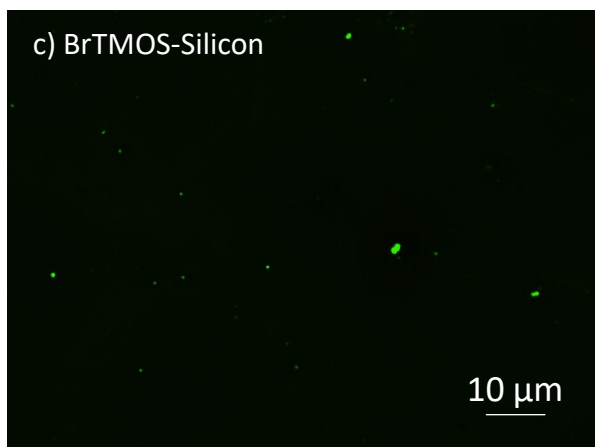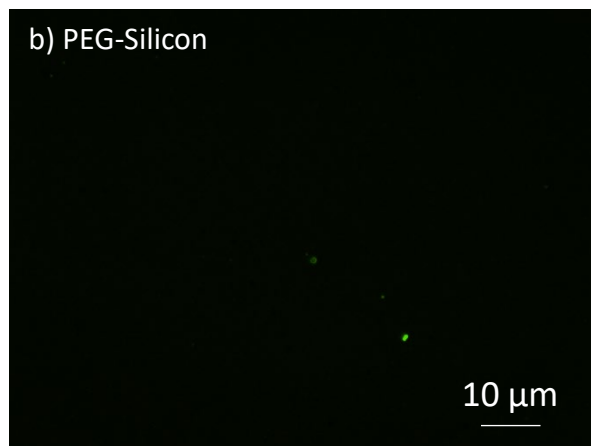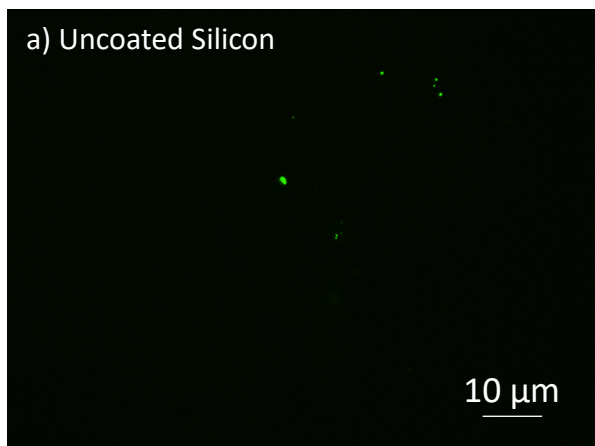
*figure continued on next page
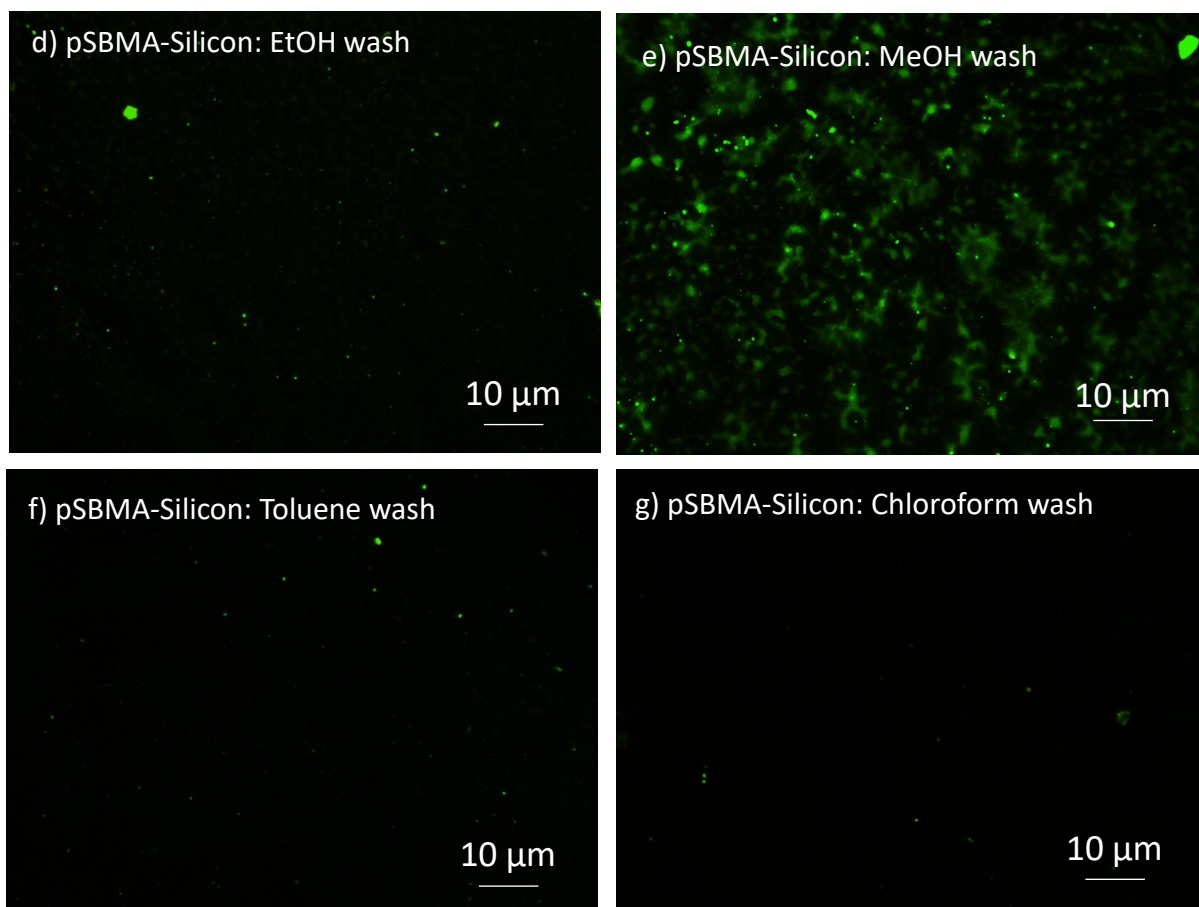
Figure 2.8: *Representative images of FITC-BSA adsorption on silicon surfaces before and after surface modification with varying wash conditions. Controls, (a) uncoated silicon, (b) PEG-silicon, and (c) BrTMOS-silicon and varying wash conditions after pSBMA polymerization of (d) ethanol (EtOH), (e) methanol (MeOH), (f) toluene, and (g) chloroform are presented.*
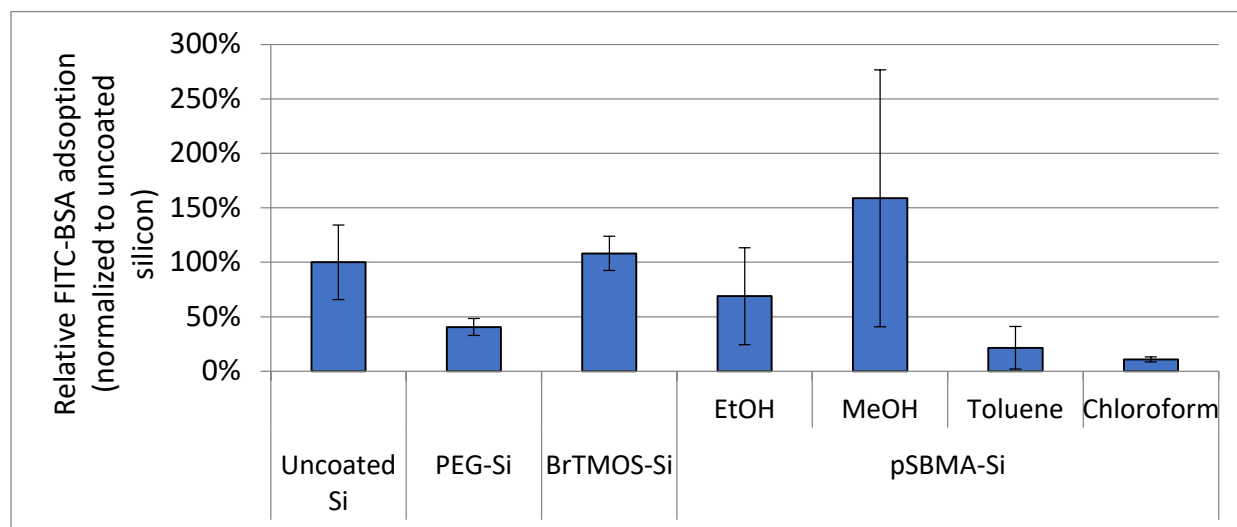
Figure 2.9: *Average FITC-BSA adsorption on surface quantified from representative images. Data is normalized to uncoated silicon.*

2.3.3 Final Surface Coating Characterization Following Optimization Experiments
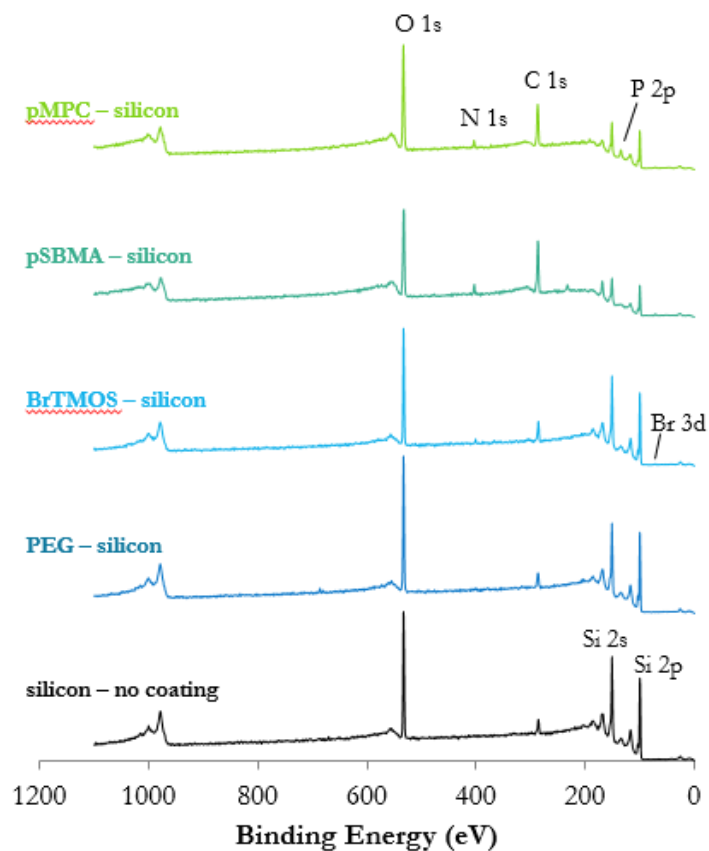
Figure 2.10: *XPS survey spectra of uncoated silicon, PEG-silicon, BrTMOS-silicon, pSBMA-silicon and pMPC-silicon.*

Table 2.2: *Change in contact angle, coating thickness and surface elemental composition between unmodified silicon, PEG-silicon, BrTMOS-silicon, pSBMA-silicon, pMPC-silicon. *Uncoated silicon contact angle increases based on increasing time interval between "piranha" treatment and when contact angle measurement is taken.*

		No Coating	**PEG-Silicon**	**BrTMOS-Si**	**pSBMA-Si**	**pMPC-Si**
Contact Angle (H_2O)		$52.8 \pm 2.6°*$	$43.8 \pm 1.0°$	$61.1 \pm 7.3°$	$8.5 \pm 2.4°$	$11.5 \pm 0.9°$
Thickness (nm)		--	0.8 ± 0.2	0.41 ± 0.18	3.46 ± 0.64	4.4 ± 0.59
Elemental Composition (%)	Si, 2p	56.8 ± 0.8	52.1 ± 3.1	53.3 ± 0.5	$20.6 \pm .4$	24.8 ± 0.8
	O, 1s	28.5 ± 1.8	32.2 ± 0.4	27.4 ± 1.5	27.6 ± 0.5	30.3 ± 0.6
	C, 1s	14.0 ± 2.2	15.6 ± 2.8	17.1 ± 1.1	44.9 ± 0.6	38.3 ± 0.4
	N, 1s	0.4 ± 0.1	0.2 ± 0.1	$1.5 \pm .1$	3.9 ± 0.1	3.0 ± 0.2
	Br, 3d			0.6 ± 0.4	0.2 ± 0.1	0.3 ± 0.0
	S, 2p				2.8 ± 0.1	
	P, 2p					3.4 ± 0.4

Figure 2.10 presents the XPS survey spectra of unmodified and modified silicon, and the contact angle, coating thickness and surface elemental composition is summarized in Table 2.2. All coatings are below 5 nm and hydrophilic as desired. For elemental composition, uncoated silicon samples mainly consist of silicon (Si 2p, 100 eV) and oxygen (O 1s, 532 eV), as expected. There is also a presence of adventitious carbon of ~14%. With PEG modification, there is a slight increase in carbon (C 1s, 285 eV), as well as O 1s, and decrease in Si 2p. BrTMOS-coupled silicon shows a 3.1% increase in C 1s and 3.5% decrease in Si 2p. There is also 1.1% and 0.6% increase in N 1s (~400 eV) and Br 3d (~69 eV), which are signature elements of BrTMOS. Based on the stoichiometric ratio, 1:1 ratio of bromine to nitrogen is expected. However, data shows a ratio of 1.8:1. This trend has been seen previously, and may be explained by the instability of C-Br bond under XPS.[26]

Following BrTMOS modification, pSBMA and pMPC are polymerized. With pSBMA polymerization, there is a 27.8% increase in C 1s and 32.7% decrease in Si 2p, as well as presence of signature elements, N 1s (2.4% increase) and sulfur, S 2p (2.8% increase). pMPC polymerization also shows increased presence of C 1s (24.3% increase) and a decrease in Si 2p (32.0% decrease). As expected, there is an increase in signature elements—2.6% increase in N 1s and 3.4% increase in phosphorus (P 2p, 133 eV).

Following successful modification on silicon, SNM surfaces were modified and hydraulic permeability was measured. Based on the permeability, the effective pore size was calculated to be 10.4, 9.5, 2.3 and 2.4 nm for uncoated SNM, PEG-SNM, pSBMA-SNM and pMPC-SNM.

Surface topography (2-D and 3-D) is illustrated in Figure 2.11. Average root mean square surface roughness (R_q) of uncoated silicon was measured to be 0.54 nm. Because higher surface roughness has been linked to increased protein adsorption in previous studies,[40] lower surface

roughness is preferred. All surfaces visually look different: Unmodified silicon is fairly smooth, with uniformly distributed nanocavities, and its roughness is on the same scale as noted previous literature.[41] Keeping unmodified silicon as baseline, PEG-silicon has more peaks, increasing surface roughness by 0.2 nm, while BrTMOS-silicon has slightly smaller features, with reduction in nanocavities that were present on bare silicon. Additionally, there is also an uneven distribution of tight peaks in BrTMOS-silicon sample, typically on the scale of sub-10 nm.

With pSBMA modification, the peaks that were present on BrTMOS-silicon surface is no longer visible. Rather, they are replaced by nanoscale broad peaks on the scale of 25 nm. Since AFM was conducted in dry, ambient conditions, these mushroom-like features could be formed by the interaction between adjacent polymer chains, or polymer chains curling in on itself. pMPC modification resulted in very uniform surface, lowering surface roughness by 0.1 nm compared to BrTMOS-silicon. With zwitterionic surface modifications, there were no significant increase in surface roughness.
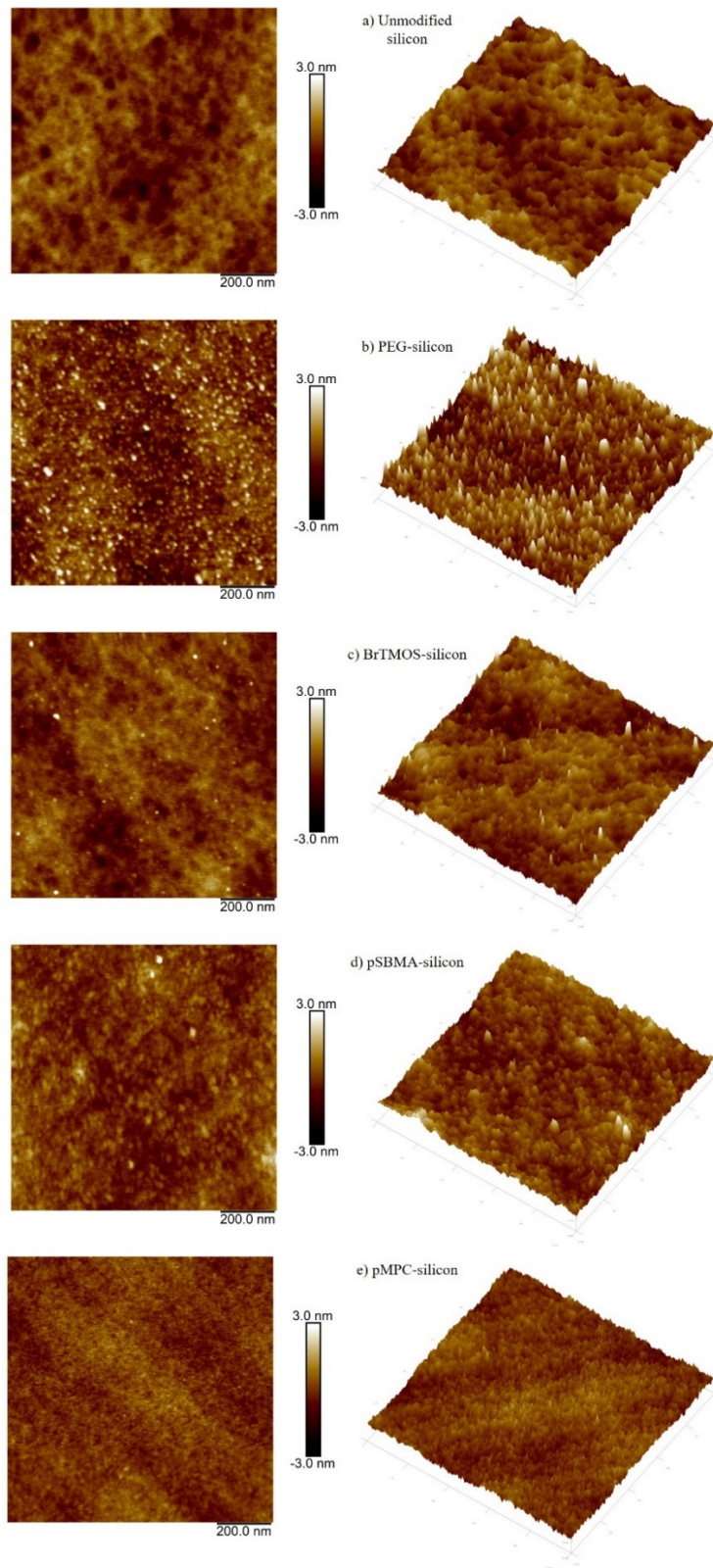
Figure 2.11: *(Left) 2-D and (right) 3-D surface topography of (a) uncoated silicon ($R_q = 0.54\pm0.03$ nm), (b) PEG-silicon ($R_q = 0.70\pm0.04$), (c) BrTMOS-silicon ($R_q = 0.52\pm0.02$), (d) pSBMA-silicon ($R_q = 0.54\pm0.10$) and (e) pMPC-silicon ($R_q = 0.40\pm0.02$).*

80
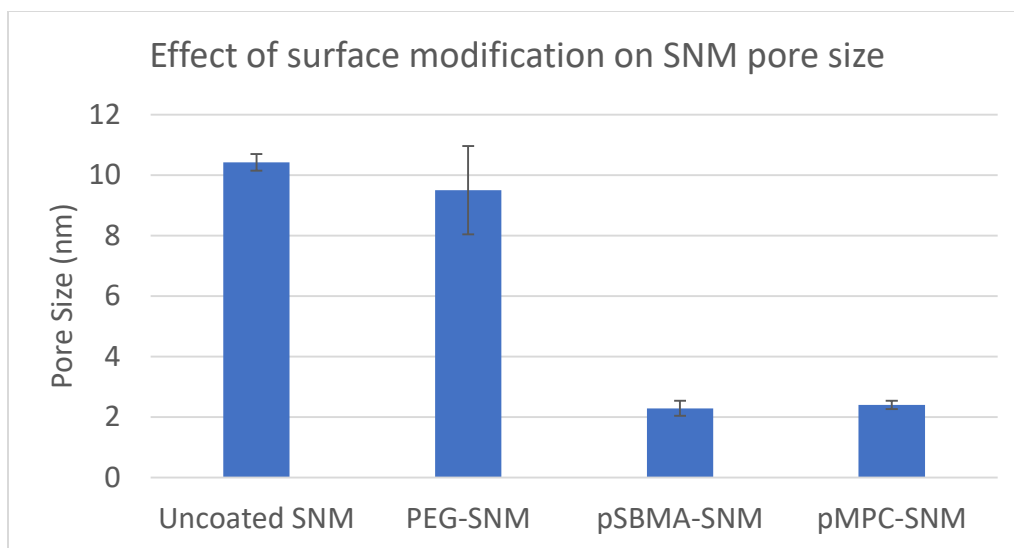
Figure 2.12: *Effective pore size of silicon nanopore membrane (SNM) before and after surface modification.*

2.4 Discussion

Ultrathin film pSBMA and pMPC zwitterionic polymers were evaluated for application on silicon membranes. Surface grafting protocols were optimized to meet the desired thickness of sub-5 nm while still retaining non-fouling properties. This chapter presents two such optimization experiments and the final characterization of the coatings after optimal conditions were reached.

Polymerization time, as well as concentration of reagents and catalysts in ATRP reaction can affect grafting density and length of polymer.[42] The first optimization experiment presented evaluated 10 min and 20 min polymerization time for pSBMA. In both cases, the contact angle decreased to below 20° and coating thickness was at least 4.4 nm, indicating successful polymerization. With increased polymerization time from 10 min to 20 min, contact angle decreased and average thickness increased, suggesting higher degree of polymerization with 20 min reaction time. However, 20 min polymerization led to >5 nm coating thickness, which is beyond the acceptable range for application on ~10 nm-pore SNMs.

The effect of coating thickness on performance was assessed by conducting protein adsorption. Results show human fibrinogen resistance is 1.7 times lower with 20 min polymerization compared to 10 min polymerization. Average BSA adsorption with 20 min polymerization time was ~14% lower than 10 min polymerization. However, the change in BSA adsorption was not statistically significant. The results indicate that 20 min polymerization leads to better performance than 10 min polymerization. Further experiments with variation in time demonstrated that a polymerization time of 15 min yields a coating thickness below 5 nm and is able to reduce protein adsorption significantly compared to uncoated silicon (data presented in Chapter 5).

The second optimization experiment presented tested varying organic solvents for washes following polymerization. Once polymerization is complete, it is critical to wash away excess reagents without harming the polymers. Since zwitterions are highly soluble in water, excess zwitterionic monomers can be easily washed away by rinsing with aqueous solution. However, CuBr is insoluble in water. Previous literature has utilized methanol or ethanol rinses to wash ATRP-polymerized surfaces.[33,43,44] In this optimization experiment, four organic solvents were tested: methanol, ethanol, toluene and chloroform. However, in contrary to previous literature, results imply that rinses with methanol and ethanol are not enough to remove CuBr adhered to the silicon surface. Methanol wash led to the maximum coating thickness and the highest BSA adsorption, indicating that the elevated coating thickness could be from residues from the reaction. Ethanol showed improved performance of surface coating compared to methanol. Nonetheless, it also resulted in significantly higher BSA adsorption compared to toluene and chloroform.

While there was no significant difference between the wash groups for fibrinogen adsorption, based on BSA adsorption on the surfaces, substrates washed with chloroform outperformed substrates washed with the other tested solvents. This may be explained by the halogen-halogen interaction between the choline atom in chloroform and the bromine atom in copper (I) bromide.[45] This interaction may assist in dissolving CuBr and loosen attached molecules from the silicon substrates.

Results from the optimized coating protocol demonstrate successful polymerization of pSBMA and pMPC that meet the thickness, surface energy and performance requirements. While ellipsometry and goniometry data imply that the surface has been modified, XPS data, which provide the elements and their bonding, confirms the changes in surface chemistry. Further proof of surface modification can be seen in the physical changes at the surface represented in the AFM data. Surface roughness data collected from AFM show that pSBMA and pMPC coatings do not increase surface roughness compared to unmodified silicon. Moreover, the standard deviation in R_q is low. These properties allow us to maintain our uniformity of SNMs after their surface is modified.

The change in effective pore size (pore width) for SNMs due to surface modification was calculated based on the hydraulic permeability, as has been done previously.[46] Initially, the pore size is ~10.5 nm. Following pSBMA and pMPC coupling, the pore size of membranes decreased by 8.2 nm and 8.1 nm, respectively. Under these experimental conditions, pSBMA thickness on solid silicon chips was ~4.4 nm. Therefore, if the walls of the pores are conformally coated, we expect to see a change of ~8.8 nm in pore size. The discrepancy of ~0.4 nm indicates a slower rate of reaction inside the pores compared to the membrane surface. Because polymer grafting

on to silicon is diffusion-dependent and the space within a nanopore is narrow compared to the open surface, the diffusion rate is slower.

Although there is a difference in the coating thickness between the surface and the pore walls, data suggests that the coating within the pores is conformal. Using Equation 1, and assuming all else is constant, pore width is proportional to the cube root of the flow rate through the membrane: $w \propto Q^{\frac{1}{3}}$. Permeability measurements are based on at least three different pressure points. A nonconformal coating would render this equation inapplicable, and the calculated pore size would vary under different pressures. However, at each pressure point, ranging from 1 to 9 psi, the pore size remains approximately constant, implying conformal coating within the pores.

2.5 Conclusions

A growing number of silicon-based biomedical implants are being designed due to silicon's-precision and versatility in micro- and nanoscale features. For blood-contacting implants, the activation of blood needs to be limited to avert thrombus formation and retain device functionality. For devices with critical nanoscale features exposed to blood, ultrathin, zwitterionic pSBMA and pMPC coatings under 5 nm thickness are promising options. This chapter demonstrates that ultrathin zwitterionic coatings can be successfully applied onto silicon and SNMs. Further work testing robustness of the coatings, as well as their performance in biological conditions is presented in subsequent chapters.

2.6 References

1.   Cheung, K. C. & Renaud, P. BioMEMS for medicine: On-chip cell characterization and implantable microelectrodes. *Solid. State. Electron.* **50,** 551–557 (2006).

2.   Scholvin, J. *et al.* Close-packed silicon microelectrodes for scalable spatially oversampled neural recording. *IEEE Trans. Biomed. Eng.* **63,** 120–130 (2016).

3.   Shawgo, R. S., Grayson, A. C. R., Li, Y. & Cima, M. J. BioMEMS for drug delivery. *Curr. Opin. Solid State Mater. Sci.* **6,** 329–334 (2002).

4.   Desai, T. *et al.* Nanoporous Implants for Controlled Drug Delivery. *Ther. Micro/Nano Technol. - BioMEMS Biomed. Nanotechnol.* 263–286 (2007). doi:10.1007/978-0-387-25844-7_15

5.   Lesinski, G. B. *et al.* Release of biologically functional interferon-alpha from a nanochannel delivery system. *Biomed. Microdevices* **7,** 71–79 (2005).

6.   Kang, S. *et al.* Bioresorbable silicon electronic sensors for the brain. *Nature* **530,** 71–76 (2016).

7.   Lueke, J. & Moussa, W. A. MEMS-based power generation techniques for implantable biosensing applications. *Sensors* **11,** 1433–1460 (2011).

8.   Acquaroli, L. N., Kuchel, T. & Voelcker, N. H. Towards implantable porous silicon biosensors. *RSC Adv.* **4,** 34768 (2014).

9.   Fissell, W. H. *et al.* High-performance silicon nanopore hemofiltration membranes. *J. Memb. Sci.* **326,** 58–63 (2009).

10. Kim, S. *et al.* Diffusive silicon nanopore membranes for hemodialysis applications. *PLoS*

One **11,** 1–20 (2016).

11.   Song, S. *et al.* Silicon nanopore membrane (SNM) for islet encapsulation and

        immunoisolation under convective transport. *Sci. Rep.* **6,** 23679 (2016).

12.   Desai, T. a., Hansford, D. J. & Ferrari, M. Micromachined interfaces: New approaches in

        cell immunoisolation and biomolecular separation. *Biomol. Eng.* **17,** 23–36 (2000).

13.   Roy, S. *et al.* Silicon nanopore membrane technology for an implantable artificial kidney.

        TRANSDUCERS 2009 - 15th Int. Conf. Solid-State Sensors, Actuators Microsystems 755–

        760 (2009). doi:10.1109/SENSOR.2009.5285603

14.   Fissell, W. H., Fleischman, A. J., Humes, H. D. & Roy, S. Development of continuous

        implantable renal replacement: past and future. *Transl. Res.* **150,** 327–336 (2007).

15.   Song, S. *et al.* An intravascular bioartificial pancreas device (iBAP) with silicon nanopore

        membranes (SNM) for islet encapsulation under convective mass transport. *Lab Chip*

        (2017). doi:10.1039/C7LC00096K

16.   Fernández-Rosas, E. *et al.* Internalization and cytotoxicity analysis of silicon-based

        microparticles in macrophages and embryos. *Biomed. Microdevices* **12,** 371–379 (2010).

17.   Agrawal, a. a. *et al.* Porous nanocrystalline silicon membranes as highly permeable and

        molecularly thin substrates for cell culture. *Biomaterials* **31,** 5408–5417 (2010).

18.   Kotzar, G. *et al.* Evaluation of MEMS materials of construction for implantable medical

        devices. *Biomaterials* **23,** 2737–50 (2002).

19.   Werner, C., Maitz, M. F. & Sperling, C. Current strategies towards hemocompatible

        coatings. *J. Mater. Chem.* **17,** 3376 (2007).

20. Nakabayashi, N. & Williams, D. F. Preparation of non-thrombogenic materials using 2-methacryloyloxyethyl phosphorylcholine. *Biomaterials* **24,** 2431–2435 (2003).

21. Ladd, J., Zhang, Z., Chen, S., Hower, J. C. & Jiang, S. Zwitterionic polymers exhibiting high resistance to nonspecific protein adsorption from human serum and plasma. *Biomacromolecules* **9,** 1357–1361 (2008).

22. Zhang, L. *et al.* Zwitterionic hydrogels implanted in mice resist the foreign-body reaction. *Nat. Biotechnol.* **31,** 553–6 (2013).

23. Smith, R. S. *et al.* Vascular Catheters with a Nonleaching Poly-Sulfobetaine Surface Modification Reduce Thrombus Formation and Microbial Attachment. *Sci. Transl. Med.* **4,** 153ra132-153ra132 (2012).

24. Chen, S., Liu, L. & Jiang, S. Strong resistance of oligo(phosphorylcholine) self-assembled monolayers to protein adsorption. *Langmuir* **22,** 2418–21 (2006).

25. Jiang, S. & Cao, Z. Z. Ultralow-fouling, functionalizable, and hydrolyzable zwitterionic materials and their derivatives for biological applications. *Adv. Mater.* **22,** 920–932 (2010).

26. Zhang, Z., Chao, T., Chen, S. & Jiang, S. Superlow fouling sulfobetaine and carboxybetaine polymers on glass slides. *Langmuir* **22,** 10072–10077 (2006).

27. Muthusubramaniam, L. *et al.* Hemocompatibility of silicon-based substrates for biomedical implant applications. *Ann. Biomed. Eng.* **39,** 1296–305 (2011).

28. Carr, L. R., Zhou, Y., Krause, J. E., Xue, H. & Jiang, S. Uniform zwitterionic polymer hydrogels with a nonfouling and functionalizable crosslinker using photopolymerization.

Biomaterials **32,** 6893–6899 (2011).

29.   Zhang, Z. *et al.* Blood compatibility of surfaces with superlow protein adsorption. *Biomaterials* **29,** 4285–4291 (2008).

30.   Zhang, M. & Ferrari, M. Hemocompatible polyethylene glycol films on silicon. *Biomed. Microdevices* (1998).

31.   Popat, K. C. & Desai, T. a. Poly(ethylene glycol) interfaces: An approach for enhanced performance of microfluidic systems. *Biosens. Bioelectron.* **19,** 1037–1044 (2004).

32.   Melvin, M. E., Fissell, W. H., Roy, S. & Brown, D. L. Silicon induces minimal thromboinflammatory response during 28-day intravascular implant testing. *ASAIO J.* **56,** 344–8 (2010).

33.   Li, L., Marchant, R. E., Dubnisheva, A., Roy, S. & Fissell, W. H. Anti-biofouling Sulfobetaine Polymer Thin Films on Silicon and Silicon Nanopore Membranes. *J. Biomater. Sci.* **22,** 91–106 (2011).

34.   Li, J. *et al.* Preparation and characterization of nonfouling polymer brushes on poly(ethylene terephthalate) film surfaces. *Colloids Surf. B. Biointerfaces* **78,** 343–50 (2010).

35.   Iqbal, Z. *et al.* Sterilization effects on ultrathin film polymer coatings for silicon-based implantable medical devices. *J. Biomed. Mater. Res. Part B Appl. Biomater.* 1–10 (2017). doi:10.1002/jbm.b.34039

36.   Sharma, S., Johnson, R. W. & Desai, T. A. Evaluation of the Stability of Nonfouling Ultrathin Poly (ethylene glycol) Films for Silicon-Based Microdevices. *Langmuir* **20,**

348–356 (2004).

37.   Zhang, M., Desai, T. & Ferrari, M. Proteins and cells on PEG immobilized silicon surfaces. *Biomaterials* **19,** 953–960 (1998).

38.   Lopez, C. A., Fleischman, A. J., Roy, S. & Desai, T. A. Evaluation of silicon nanoporous membranes and ECM-based microenvironments on neurosecretory cells. *Biomaterials* **27,** 3075–3083 (2006).

39.   Sharma, S., Johnson, R. W. & Desai, T. a. Evaluation of the Stability of Nonfouling Ultrathin Poly (ethylene glycol) Films for Silicon-Based Microdevices. *Langmuir* 348– 356 (2004). doi:10.1021/la034753l

40.   Rechendorff, K., Hovgaard, M. B., Foss, M., Zhdanov, V. P. & Besenbacher, F. Enhancement of protein adsorption induced by surface roughness. *Langmuir* **22,** 10885– 10888 (2006).

41.   Sharma, S., Johnson, R. W. & Desai, T. a. XPS and AFM analysis of antifouling PEG interfaces for microfabricated silicon biosensors. *Biosens. Bioelectron.* **20,** 227–239 (2004).

42.   Matyjaszewski, K. & Xia, J. Atom transfer radical polymerization. *Chem. Rev.* **101,** 2921– 2990 (2001).

43.   Zhang, Z., Chen, S., Chang, Y. & Jiang, S. Surface grafted sulfobetaine polymers via atom transfer radical polymerization as superlow fouling coatings. *J. Phys. Chem. B* **110,** 10799–10804 (2006).

44.   Ma, H., Hyun, J., Stiller, P. & Chilkoti, A. "Non-Fouling" Oligo(ethylene glycol)-

Functionalized Polymer Brushes Synthesized by Surface-Initiated Atom Transfer Radical Polymerization. *Adv. Mater.* **16,** 338–341 (2004).

45. Desiraju, G. R. & Parthasarathy, R. The Nature of Halogen•••Halogen Interactions: Are Short Halogen Contacts Due to Specific Attractive Forces or Due to Close Packing of Nonspherical Atoms? *J. Am. Chem. Soc.* **111,** 8725–8726 (1989).

46. Fissell, W. H. *et al.* High-Performance Silicon Nanopore Hemofiltration Membranes. *J. Memb. Sci.* **326,** 58–63 (2009).

Stability of Ultrathin Film Polymer Coatings Under Shear Conditions

3.1 Introduction

Silicon-based bio-microelectromechanical systems (bioMEMS) are commonly utilized in a diverse set of implantable medical devices, such as neuroelectrodes,[1,2] drug delivery systems,[3–5] biosensors and diagnostic devices.[6–8] Our lab has developed a unique bioMEMS-based membrane, the silicon nanopore membrane (SNM), which offers highly uniform and controllable pores with variation <1% across the wafer.[9] As shown in Figure 3.1, low fluidic resistance SNMs with ~10 nm pore size have been developed for blood filtration and immunoisolation applications in renal replacement[9–11] and islet therapies.[12,13] These applications bring silicon in direct contact with blood flow, and therefore, biocompatibility and resistance to fouling is critical. Previous research has shown silicon to be non-cytotoxic.[14,15] Additionally, various materials pertinent to implantable bioMEMS including silicon, polysilicon and silicon dioxide have been tested against a battery of tests laid out in ISO 10993, and were found to be non-leaching and non-irritant.[16] However, the blood-contacting surfaces must also be non-activating and non-fouling over the lifetime of the implant.

To enhance the hemocompatibility, the substrate surface is often modified.[17] Polyethylene glycol and oligoethylene glycol (PEG and OEG, respectively) are hydrophilic surface modifications that have demonstrated excellent non-fouling properties, shown to lower protein
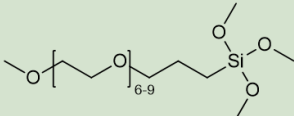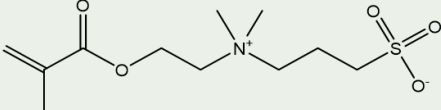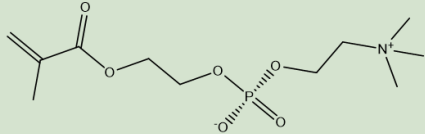
adsorption and platelet adhesion.[18,19] In our previous research, PEG-modified SNM has shown

functionality retention after 90 hours of an anticoagulated whole blood hemofiltration

experiment.[9] Additionally, PEG-silicon showed significantly reduced thrombus formation and

inflammation after 4 weeks of implantation in rat veins.[20] However, PEG is susceptible to

 oxidative degradation, making it impractical for long term implants.[21–23] Recently, hydrophilic

zwitterionic polymer surface modifications have demonstrated significantly reduced protein

fouling[24–28] and thrombosis formation.[29–31] Several biomimetic zwitterions, such as sulfobetaine,

carboxybetaine and phosphorylcholine, have been used with a methacrylate backbone to build

polymer brushes and hydrogels.[31–33] It is hypothesized that the zwitterions are able to coordinate
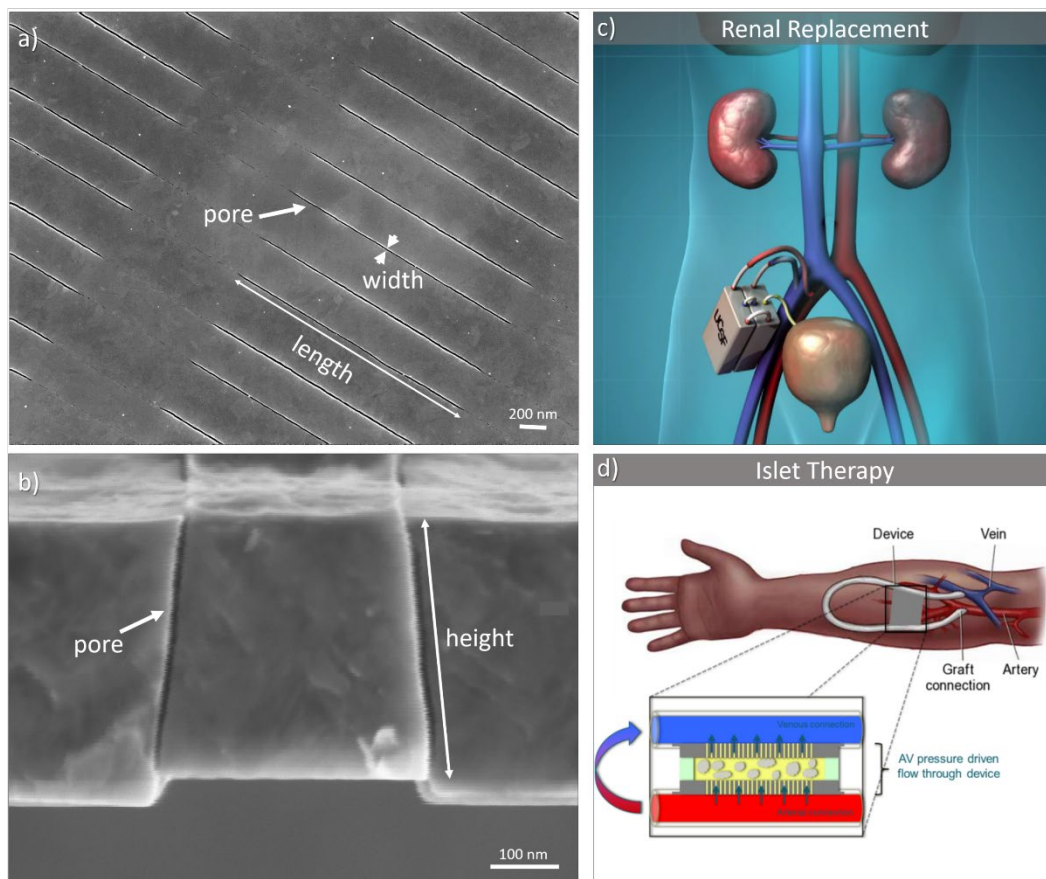
Figure 3.1: a) top view and b) side view of silicon nanopore membrane (SNM) with pore length of 2μm, width of 7 nm and height of 360 nm, developed for applications in (c) filtration during renal replacement therapy for artificial kidney and (d) immunoisolation chamber for islet therapy in bioartificial pancreas. Image (b) was reprinted from S. Song et al./ Scientific Reports, ©2016, with permission from Nature Publishing Groups.

water molecules and produce a stable hydration layer due to their hydrogen bonding and electrostatic interactions.[30,32] This hydration layer allows the surface to be in stealth mode and resist protein adsorption and cell adhesion. Additionally, due to the methacrylate backbone, these polymer brushes can be controllably grown on the surface to a desired thickness using atom-transfer radical polymerization (ATRP).[34]

Table 3.1: Chemical structure of PEG-silane, SBMA and MPC monomer.

1, 2-[methoxy(polyethyleneoxy)propyl]trimethoxysilane (PEG-silane)	
2-(methacryloyloxy)ethyl]dimethyl-(3-sulfopropyl)ammonium hydroxide, sulfobetaine methacrylate (SBMA)	
2-methacryloyloxyethyl phosphorylcholine (MPC)	

For surface-modified implants, it is critical that the polymer coatings are stable in physiological conditions. Previous work demonstrated that sulfobetaine coating is stable under static physiologic conditions mimicked by submersion in D-PBS at 37 °C for 30 days.[35] Smith, et al. showed that following exposure to serum for 60 days, sulfobetaine can still retain functionality.[36] Although coating thickness is affected, PEG was also shown to perform well after four weeks of incubation in PBS.[22] For implants that require contact with blood flow, coatings are subjected to shear, and the effect of physiological shear on ultrathin film polymer coatings has not been well-characterized. Therefore, in this chapter we investigate the effect of shear on three different ultrathin film surface modifications shown in Table 3.1: PEG, polysulfobetaine methacrylate

(pSBMA) and poly(2-methacryloyloxyethyl phosphorylcholine) (pMPC). In order to be applicable to SNMs, these coatings have been applied at ~5 nm or less in thickness. Fundamental changes in the coatings, such as surface chemistry, wettability and thickness were analyzed after they were subjected to physiological shear for 24 hours. Additionally, protein resistance of the surface modifications was also evaluated against human serum albumin.

3.2 Materials and Methods

3.2.1 Sample Preparation

Double side polished, 400 μm thick, p-type silicon wafers were obtained from Ultrasil Corporation (Hayward, CA, USA) and diced into 1 cm^2 chips. The chips were cleaned by "piranha," a solution of 3:1 ratio of sulfuric acid (96%) to hydrogen peroxide (30%) for 20 min. The chips were then rinsed with reverse osmosis purified water (RO water) at 5-minute intervals (3X). Afterwards, they were exposed to hydrofluoric acid for 5 min to remove the native silicon dioxide that spontaneously forms on silicon surfaces exposed to atmospheric oxygen. The chips were again rinsed with RO water at 5-min intervals (3X), followed by activation of the surface via a final piranha clean and RO water rinse as described above. The silicon chips were then dried under a stream of nitrogen gas and kept on a hotplate at 110 °C for 1 hour.

3.2.2 Surface Modification

3.2.2.1 PEG Surface Modification

Silicon surfaces were modified with PEG as described in previous literature.[13,37] Briefly, 2-[methoxy(polyethyleneoxy)propyl]trimethoxysilane (PEG-silane) was purchased from Gelest, Inc. (Morrisville, PA, USA) and covalently bonded to silicon by immersing the substrates in a solution of 285 μl PEG-silane in 25 mL of toluene for 2 hours at 70 °C. The substrates were then

rinsed three times at 10 min intervals with toluene, ethanol, and water, respectively, to remove excess PEG, and stored dry under ambient conditions until use.

3.2.2.2 Zwitterionic Surface Modification

All chemicals were purchased from Sigma-Aldrich (St. Louis, MO, USA), unless stated otherwise. Zwitterionic surface modifications were conducted as described in previous publication.[35] Briefly, a surface initiator, 2-bromo-2-methyl-N-3[(trimethoxysilyl)propyl]-propanamide (BrTMOS), was synthesized.[35] The substrates were placed in a 1% (v/v) BrTMOS solution in bicyclohexyl for 2 hours. The surfaces were then rinsed with chloroform, ethanol, and water, respectively, to remove excess BrTMOS.

Zwitterionic monomers, 2-(methacryloyloxy)ethyl]dimethyl-(3-sulfopropyl)ammonium hydroxide (SBMA) and 2-methacryloyloxyethyl phosphorylcholine (MPC), are shown in Table 3.1 respectively. A degassed solution of 468 mg (3 mmol) of 2,2'-bipyridyl (≥98%) and individual monomers—SBMA: 1.06g (3.8 mmol), and MPC: 506 mg (1.9 mmol)—and 22.3 mg (0.1 mmol) of copper (II) bromide (99%) was prepared in 5:5 mL of methanol:water. This mixture was added to a reaction chamber housing four substrates and 143 mg (1 mmol) of copper (I) bromide (99.999%) under nitrogen protection and polymerization ran for 15 min for pSBMA and 7 min for pMPC. The substrates were then rinsed with chloroform, ethanol, Dulbecco's phosphate buffered saline (D-PBS, UCSF Cell Culture Facility, San Francisco, CA, USA), and water respectively, and dried using a stream of nitrogen gas.

3.2.3 Flow Chamber Design and Fabrication

Shear flow cells were fabricated out of cast acrylic sheets and silicone. The top and bottom piece was laser cut from a 12x12 in^2, 5/16 in thick optically clear cast acrylic sheet (McMaster-Carr,

Santa Fe Springs, CA, USA). The channel was created from 0.01 in thick silicone rubber (high-purity silicone rubber sheet, 55A Durometer, McMaster-Carr).

Figure 3.2: a) device design for shear variation study, b) device made from cast acrylic, with silicone gasket setting channel height. c) setup for 24-hour shear rate variation study set in a 37°C incubator. Shear was varied by controlling the flow rate set by a peristaltic pump. Flow is driven from the reservoir by the peristaltic pump through the flow cells and back to the reservoir.
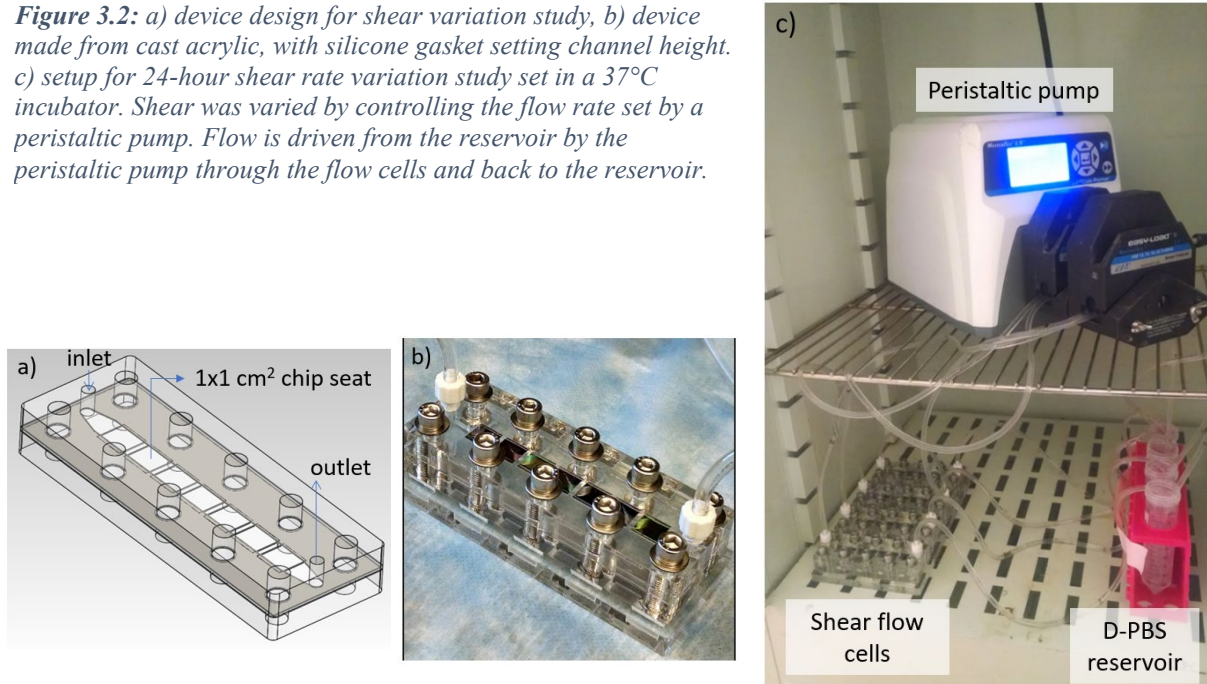
The device shown in Figure 3.2 (a) and (b) was designed to hold seven chips on the bottom piece with the inlet and outlet through-holes on the top piece. A gasket was used to create the flow path and set the channel height. The shear rates in human arterioles does not exceed 1650/s.[38] Therefore, for our experiments, we explored shear rates of 500/s, 1000/s, 1500/s and 2000/s to cover the range of shear rates experienced in the human body. As shown in Figure 3.2(c), the substrates were exposed to D-PBS flow at 37 °C for 24 hours at varying flow rates. A constant channel height of 220 μm was used and flow rate was varied to adjust the shear rate. Since the flow chamber creates a flat rectangular channel, the shear rate at the surface, $\dot{\gamma}_{wall}$ is given by:

$$\dot{\gamma}_{wall} = \frac{\tau_{wall}}{\mu} = \frac{\Delta P}{\mu L}\left(\frac{h}{2}\right) \qquad \text{Eqn. 1}$$

where L, h, τ_{wall}, μ and ΔP are the length and height of the flow path, shear stress at the wall, dynamic viscosity of the fluid, and pressure difference across the flow path, respectively. Wall shear rate based on the volumetric flow rate (Q) and dimensions of the flow path is given by:

$$\dot{\gamma}_{wall} = \frac{6}{h^2 w} Q \qquad \text{Eqn. 2}$$

where w and h are the width and height of the flow path. These equations were applied with the following assumptions: (a) the fluid is Newtonian and incompressible, (b) steady state is reached and the flow is fully developed, and (c) edge effects are negligible and the flow is laminar. Therefore, the flow rate was set to 1.6, 3.2, 4.8, and 6.4 ml/min to achieve a shear rate of 500, 1000, 1500, and 2000/s, respectively. Computational fluid dynamics (CFD) analysis using ANSYS Fluent v18.2 (Ozen Engineering, Inc, Sunnyvale, CA, USA) (Figure 3.3) demonstrates the flow is fully developed and velocity is constant throughout the channel.

Samples not exposed to D-PBS was used as controls for comparison. Following flow exposure, the samples were removed from the flow cells, and surface chemistry, contact angle, and coating thickness was analyzed. Finally, protein resistance of the substrates was evaluated via human serum albumin adsorption.

Figure 3.3: ANSYS simulation showing fully developed flow before substrates are reached, and uniform velocity across the length and width of the channel.

3.2.4 Surface Characterization

3.2.4.1 X-Ray Photoelectron Spectroscopy (XPS)

X-ray photoelectron spectroscopy (XPS) was conducted using a Surface Science Instruments S-Probe photoelectron spectrometer with a monochromatized Al Kα X-ray beam and a low energy electron flood gun for charge neutralization of non-conducting samples. A pass energy of 150 eV and 50 eV was used to generate the survey spectra and high resolution spectra, respectively. Samples were pressurized to <5e-9 torr and a 0° take-off angle was used, corresponding to sampling depth of ~10 nm. For each sample, XPS was measured at four locations with a spot size of ~800 μm. Elemental composition calculations were performed using Service Physics Hawk version 7 software (Bend, OR, USA).

3.2.4.2 Contact Angle

Change in surface hydrophilicity was measured using sessile drop contact angle goniometry (Attension Theta Lite, Biolin Scientific, Stockholm, Sweden). A ~3.5 μl water droplet was placed on the substrate in air and the contact angle between the droplet and the substrate was measured. Data points was collected every 0.1 s over 10 s, and averaged. A total of six data points was collected from each sample subset.

3.2.4.3 Ellipsometry

Surface coating thickness was measured using an LSE Stokes ellipsometer (Gaertner Scientific, Skokie, IL, USA) with a 6328 Å HeNe laser at an incidence angle of 70°. Measured reflection and transmission data was entered into Fresnel equations and with the known refractive index, the thickness of the transparent film was iteratively solved for. In the cases of both zwitterionic and PEG surface coatings, an index of refraction of 1.45 was used.[35] Although exposure to

higher temperature, saline solution, and shear flow may lead to degradation and/or

conformational changes within the polymers, the refractive index was assumed to be constant.

Spatial homogeneity was characterized by measuring three locations on three separate chips per

sample set. A total of nine measurements were averaged, and the mean and standard deviation

are reported.

3.2.4.4 Human Serum Albumin Adsorption

Protein adsorption on the substrates was quantified via enzyme linked immunosorbent assay

(ELISA). The substrates were incubated in a 1 mg/mL solution of human serum albumin (HSA)

in D-PBS for 90 minutes at 37°C. Surface protein concentrations were measured using ELISA

as described in published methods.[26,35] Briefly, all substrates were rinsed 5 times with 0.5 mL of

D-PBS following HSA incubation, and were blocked using bovine serum albumin[39] (BSA,

≥98%, Sigma-Aldrich) at 1 mg/mL concentration for 1.5 hours. The substrates were rinsed 5

times with 0.5 mL of D-PBS, and transferred to fresh chambers. The samples were then

incubated with 10 μg/mL anti-human serum albumin antibody conjugated with horseradish

peroxidase for 1.5 hours (Abcam, Cambridge, MA, USA). After another rinse (5 times with 0.5

mL of D-PBS), the substrates again rinsed and transferred to fresh chambers. A solution of 0.5

mg/mL of o-phenylenediamine (OPD, VWR Inc. Visalia, CA, USA) and 0.03% hydrogen

peroxide in 0.05 M citrate phosphate buffer (pH 5.0, Sigma-Aldrich). This reaction was

protected from light using aluminum foil for 20 min at 37 °C, and subsequently stopped by

adding 0.5 mL of 1M sulfuric acid. The light absorbance of the solutions was measured at 490

nm. Each sample type was tested in triplicate and the background (control with no HSA added)

was subtracted. All HSA protein adsorption data was normalized to tissue culture polystyrene

(TCPS) which was used as a positive control.

3.2.6 Statistical Analysis

A minimum of three measurements were collected for all samples in each analysis. Statistical significance was determined by ordinary one-way analysis of variance (ANOVA) since comparisons were drawn only within each coating subset. Significance was defined at $p < 0.05$. Level of significance is indicated by the number of asterisks: $p \leq 0.05 = *$; $p \leq 0.01 = **$; $p \leq 0.001 = ***$; $p \leq 0.0001 = ****$. Analysis was conducted using Graphpad Prism software (San Diego, CA, USA).

3.3 Results

3.3.1 XPS

Table 3.2 shows the elemental composition of unmodified silicon, PEG-, pSBMA-, and pMPC-modified silicon when not exposed to shear. These controls demonstrate that with increased polymer modification the carbon content, silicon content is decreased. Additionally, signature elements are present as expected—PEG shows increased C-O bonds, pSBMA has increased sulfur and nitrogen, and pMPC has increased phosphorus and nitrogen presence.

For unmodified silicon, XPS data is presented in Table 3.3. As expected, Si 2p (100 eV) and O 1s (528 eV) make up the majority of the elemental composition. This arises from the substrate monocrystalline silicon and native silicon dioxide that grows on the surface of silicon when exposed to ambient air. Additionally, in the unmodified silicon control, there is 9.8% C 1s and 0.4% N 1s adventitious carbon and nitrogen present, respectively. When exposed to shear, there is at least a 6.3% elevation in carbon concentration, with the maximum of 13.9% increase for 1500/s shear rate. Increase in C 1s is also coupled with an increase in O 1s and N 1s (~400 eV), indicating contamination.

XPS measurements on the effect of shear on PEG-coating is presented in Table 3.4. In comparison to control unmodified silicon, control PEG-silicon presents 27.4% increase in carbon concentration. Based on the high resolution data, it is evident that most of the additional carbon is from C-C/C-H and C-O/C-N bonds. C-N bonds can be ruled out since there is only 0.1% N 1s present, leaving mainly C-O bonds as is expected of PEG. With exposure to shear, carbon concentration decreases by more than 50% compared to control, and there is a slight increase in nitrogen content. Given the elemental make-up of PEG, it is difficult to determine whether the carbon expressed in XPS is due to contamination or PEG itself.

XPS data presented in Table 3.5 demonstrates that compared to control unmodified silicon, control pSBMA-silicon shows a 45.7% decrease in silicon and a 47.1% increase in carbon. In addition, with modification, there is a presence of N 1s, S 2s (~228 eV) and Br 3d (~69 eV). The ratio of sulfur to nitrogen is approximately 1:1.2. The additional nitrogen is likely due to a presence of adventitious nitrogen as well as nitrogen in the underlying BrTMOS initiator. With shear, there is ~18-20% increase in silicon, and ~20-23% decrease in carbon. Additionally, sulfur concentration slightly decreases by ~0.5% or less. It should also be noted that there is a trace amount of phosphorus contamination (<0.5%).

As shown in Table 3.6, control pMPC-silicon shows a 42.2% decrease in silicon and 42.9% increase in carbon compared to control unmodified silicon. There is also the presence of N 1s, P 2s (~190 eV), and Br 3d, which are the signature elements of pMPC. With shear, there is negligible to no decrease in phosphorus and nitrogen concentration. However, there is a ~19-26% decrease in carbon and ~16-24% increase in silicon. The lowest carbon concentration is observed for shear rate of 1000/s.

Table 3.2: XPS data for control unmodified silicon, PEG-silicon, pSBMA-silicon, and pMPC-silicon when not exposed to shear and D-PBS.

Sample	% Elemental Composition								Carbon Composition Breakdown (High Resolution)		
Dry, no PBS exposure	Si (2p)	O (1s)	C (1s)	N (1s)	S (2s)	P (2s)	Br (3d)	Contaminants (F)	C-C, C-H	C-O, C-N	O-C=O, C=O, O-C=O
Unmodified Silicon	58.3 ± 1.5	28.1 ± 0.3	9.8 ± 0.6	0.4 ± 0.1				3.4 ± 1.4	6.0 ± 0.2	2.9 ± 0.1	0.9 ± 0.1
PEG on Silicon	37.2 ± 7.3	29.3 ± 1.2	33.4 ± 8.4	0.1 ± 0.2					13.4 ± 1.4	18.2 ± 1.2	1.9 ± 0.2
pSBMA on Silicon	12.6 ± 0.8	25.0 ± 0.3	56.9 ± 0.6	2.6 ± 0.1	2.2 ± 0.2	0.3 ± 0.1	0.3 ± 0.0		23.8 ± 0.2	29.5 ± 0.0	3.7 ± 0.2
pMPC on Silicon	16.1 ± 1.2	26.9 ± 0.5	52.7 ± 2.6	2.4 ± 0.1		1.6 ± 0.1	0.4 ± 0.0		20.0 ± 0.9	29.4 ± 0.9	3.3 ± 0.0
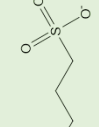
Table 3.3: XPS data for unmodified silicon when varying shear rate.

Sample	Shear	% Elemental Composition					Carbon Composition Breakdown (High Resolution)			
		Si (2p)	O (1s)	C (1s)	N (1s)	Contaminants (F, Cu)	C-C, C-H	C-O, C-N	O-C=O, C=O	O-C=O
Unmodified Silicon	500/s	47.6 ± 0.3	35.3 ± 0.2	16.3 ± 0.5	0.8 ± 0.1		8.7 ± 0.5	6.2 ± 0.2	1.0	0.9 ± 0.1
	1000/s	43.0 ± 0.2	38.2 ± 0.6	17.7 ± 0.8	1.2 ± 0.1		9.0 ± 0.1	7.1 ± 0.5	1.0	1.1 ± 0.3
	1500/s	44.2 ± 0.4	31.5 ± 0.2	23.7 ± 0.5	0.6 ± 0.1		14.4 ± 0.8	6.3 ± 0.1	1.2	2.4 ± 0.0
	2000/s	45.3 ± 0.9	34.5 ± 0.4	19.1 ± 1.0	1.1 ± 0.0		9.3 ± 0.2	7.4 ± 0.3	1.1 ± 0.2	1.3 ± 0.1
	Dry, No PBS	58.3 ± 1.5	28.1 ± 0.3	9.8 ± 0.6	0.4 ± 0.1	3.4 ± 1.4	6.0 ± 0.2	2.9 ± 0.1		0.9 ± 0.1
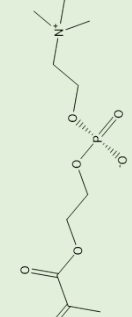
Table 3.5: *XPS data for PEG-modified silicon when varying shear rate.*

Sample	Shear	% Elemental Composition				Carbon Composition Breakdown (High Resolution)		
		Si (2p)	O (1s)	C (1s)	N (1s)	C-C, C-H	C-O, C-N	O-C=O, C=O, O-C=O
PEG on Silicon	500/s	52.0 ± 2.2	35.0 ± 0.9	12.5 ± 1.6	0.6 ± 0.0	3.5 ± 0.2	8.1 ± 0.2	0.9 ± 0.4
	1000/s	52.7 ± 1.2	34.4 ± 0.9	12.7 ± 0.6	0.4 ± 0.0	3.6 ± 0.1	8.4 ± 0.5	0.8 ± 0.4
	1500/s	46.6 ± 1.3	37.6 ± 0.9	15.1 ± 0.4	0.6 ± 0.1	6.2 ± 0.2	7.6 ± 0.5	1.4 ± 0.7
	2000/s	51.2 ± 1.2	36.0 ± 1.3	12.1 ± 0.2	0.8 ± 0.1	3.8 ± 0.5	7.4 ± 0.5	0.8 ± 0.0
	Dry, No PBS	37.2 ± 7.3	29.3 ± 1.2	33.4 ± 8.4	0.1 ± 0.2	13.4 ± 1.4	18.2 ± 1.2	1.9 ± 0.2

Table 3.4: *XPS data for pSBMA-modified silicon when varying shear rate.*

Sample	Shear	% Elemental Composition						Contaminants (P)	Carbon Composition Breakdown (High Resolution)		
		Si (2p)	O (1s)	C (1s)	N (1s)	S (2s)	Br (3d)		C-C, C-H	C-O, C-N	O-C=O
pSBMA on Silicon	500/s	33.0 ± 3.1	27.0 ± 0.4	34.4 ± 2.6	3.0 ± 0.3	1.7 ± 0.3	0.6 ± 0.0	0.4 ± 0.0	14.7 ± 0.3	16.7 ± 0.3	2.9 ± 0.0
	1000/s	30.8 ± 1.6	27.0 ± 0.4	36.2 ± 1.8	3.1 ± 0.0	1.9 ± 0.2	0.5 ± 0.0	0.3 ± 0.1	15.4 ± 0.5	17.9 ± 0.7	3.0 ± 0.2
	1500/s	31.1 ± 0.8	26.5 ± 0.6	36.9 ± 0.8	3.0 ± 0.2	1.7 ± 0.1	0.5 ± 0.0	0.3 ± 0.0	15.6 ± 1.2	17.9 ± 1.2	3.4 ± 0.0
	2000/s	32.1 ± 1.4	26.9 ± 0.2	35.4 ± 1.5	3.0 ± 0.2	1.7 ± 0.1	0.6 ± 0.0	0.3 ± 0.1	15.0 ± 0.3	17.6 ± 0.3	2.8 ± 0.0
	Dry, No PBS	12.6 ± 0.8	25.0 ± 0.3	56.9 ± 0.6	2.6 ± 0.1	2.2 ± 0.2	0.3 ± 0.0	0.3 ± 0.1	23.8 ± 0.2	29.5 ± 0.0	3.7 ± 0.2

Table 3.6: XPS data for pMPC-modified silicon when varying shear rate.

Sample	Shear	% Elemental Composition						Carbon Composition Breakdown (High Resolution)		
		Si (2p)	O (1s)	C (1s)	N (1s)	P (2s)	Br (3d)	C-C, C-H	C-O, C-N	O-C=O
pMPC on Silicon	500/s	34.5 ± 0.8	29.2 ± 0.7	31.2 ± 0.7	2.9 ± 0.3	1.5 ± 0.0	0.6 ± 0.0	11.0 ± 0.1	17.3 ± 0.1	2.8 ± 0.0
	1000/s	40.5 ± 1.7	28.7 ± 0.1	26.4 ± 1.3	2.5 ± 0.3	1.2 ± 0.1	0.7 ± 0.0	10.6 ± 0.4	12.8 ± 0.3	3.0 ± 0.1
	1500/s	34.6 ± 0.9	28.5 ± 0.6	32.3 ± 0.8	2.7 ± 0.2	1.4 ± 0.1	0.6 ± 0.0	12.3 ± 0.1	17.2 ± 0.0	2.9 ± 0.1
	2000/s	32.2 ± 1.0	28.8 ± 0.1	33.8 ± 1.0	3.0 ± 0.2	1.6 ± 0.0	0.6 ± 0.0	12.8 ± 0.6	17.8 ± 0.9	3.3 ± 0.3
	Dry, No PBS	16.1 ± 2.0	26.9 ± 0.5	52.7 ± 2.6	2.4 ± 0.1	1.6 ± 0.1	0.4 ± 0.0	20.0 ± 0.9	29.4 ± 0.9	3.3 ± 0.0

3.3.2 Contact Angle
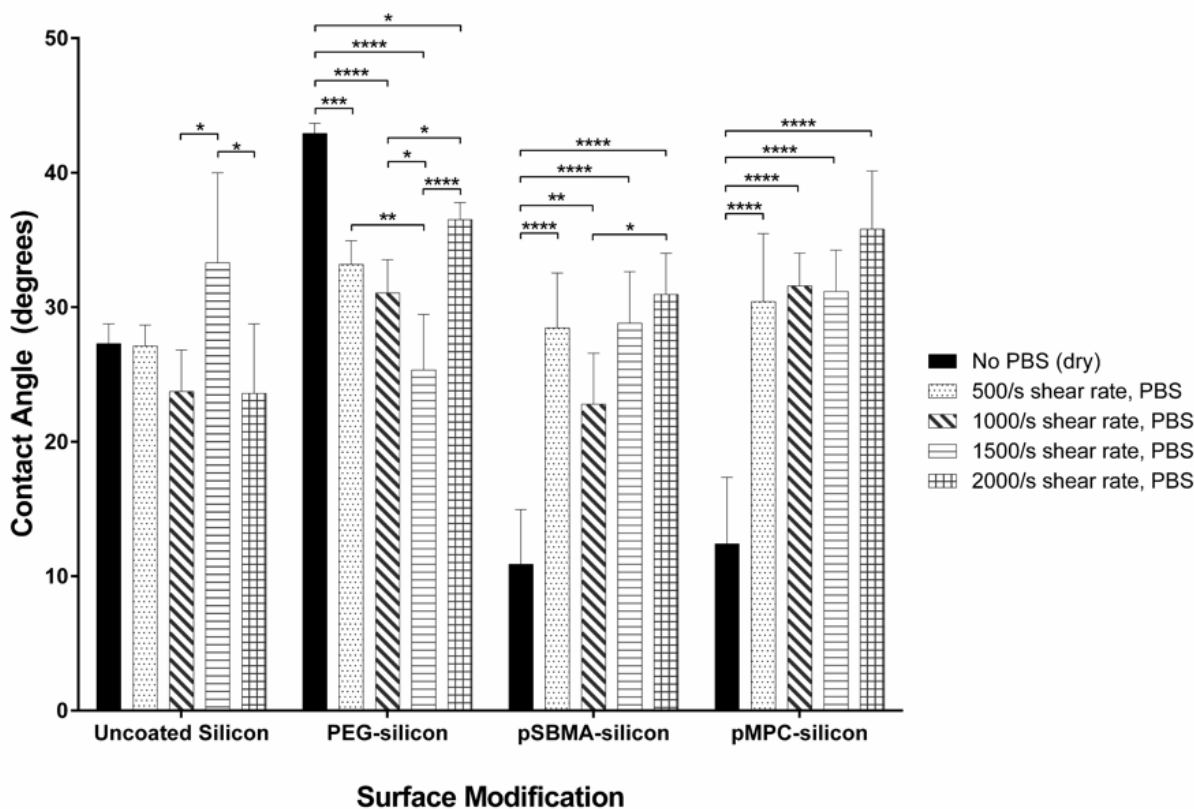
Figure 3.4: *Contact angle for each surface modification with varying shear rates. Significance was defined at p <0.05. Level of significance is indicated by the number of asterisks: p ≤ 0.05 = *; p ≤ 0.01 = **; p ≤ 0.001 = ***; p ≤ 0.0001 = ****.*

The effect of shear on the surface hydrophilicity is represented in Figure 3.4. Following surface cleaning with piranha, contact angle was below 10° due to the hydroxylation of silicon. However, with time, the contact angle increases as the surface loses the hydrophilicity. The contact angle for unmodified silicon was measured at 27.3° one week following piranha treatment. There is no significant difference found between the control unmodified silicon and silicon substrates exposed to shear. The maximum difference in the uncoated silicon subset from control was due to 1500/s shear rate, yielding a difference of 6.0° from control unmodified silicon.

With PEG modification, contact angle increases to 42.9°. Although no trend could be elucidated with varying shear, there was a significant decrease in contact angle for PEG-silicon when exposed to shear. The lowest angle measured was 25.3° for a shear rate of 1500/s.

pSBMA and pMPC both contain zwitterionic moieties, and as such, they are very hydrophilic. Control substrates of pSBMA-silicon and pMPC-silicon are 10.9°, and 12.4°, respectively. With shear, the contact angle significantly increases for both coatings. However, in general, there are no significant differences between any of the shear groups within each subset with the exception of shear rates of 1000/s and 2000/s for pSBMA-silicon. For both zwitterionic coatings, following exposure to shear, the contact angle settled at ~30°. The highest contact angle of 30.9° and 35.8° was measured at 2000/s shear rate for pSBMA and pMPC, respectively.

3.3.3 Ellipsometry

Change in coating thickness was measured using ellipsometry and data is presented in Figure 3.5. Uncoated silicon, without exposure shear, was used as baseline control for native oxide thickness measurement. With shear, "thickness" is increased, which may be due to contamination and/or native oxide growth under these conditions. Initial thickness of PEG is 0.95 nm. With shear, the coating thickness measurements appears to increase, but is only significant for 1000/s and 1500/s shear rates. Although there is no trend evident with shear, 1500/s shear rate leads to the largest increase in thickness for both PEG, and unmodified silicon.

Zwitterionic polymers pSBMA and pMPC started out with thickness of 4.7 and 5.2 nm, respectively. In both cases, exposure to shear led to a decrease in thickness. However, with varying shear, there is no significant difference noted. Following shear, coating thickness was ~2.5-2.8 nm for pSBMA and ~2.2-2.3 nm for pMPC.
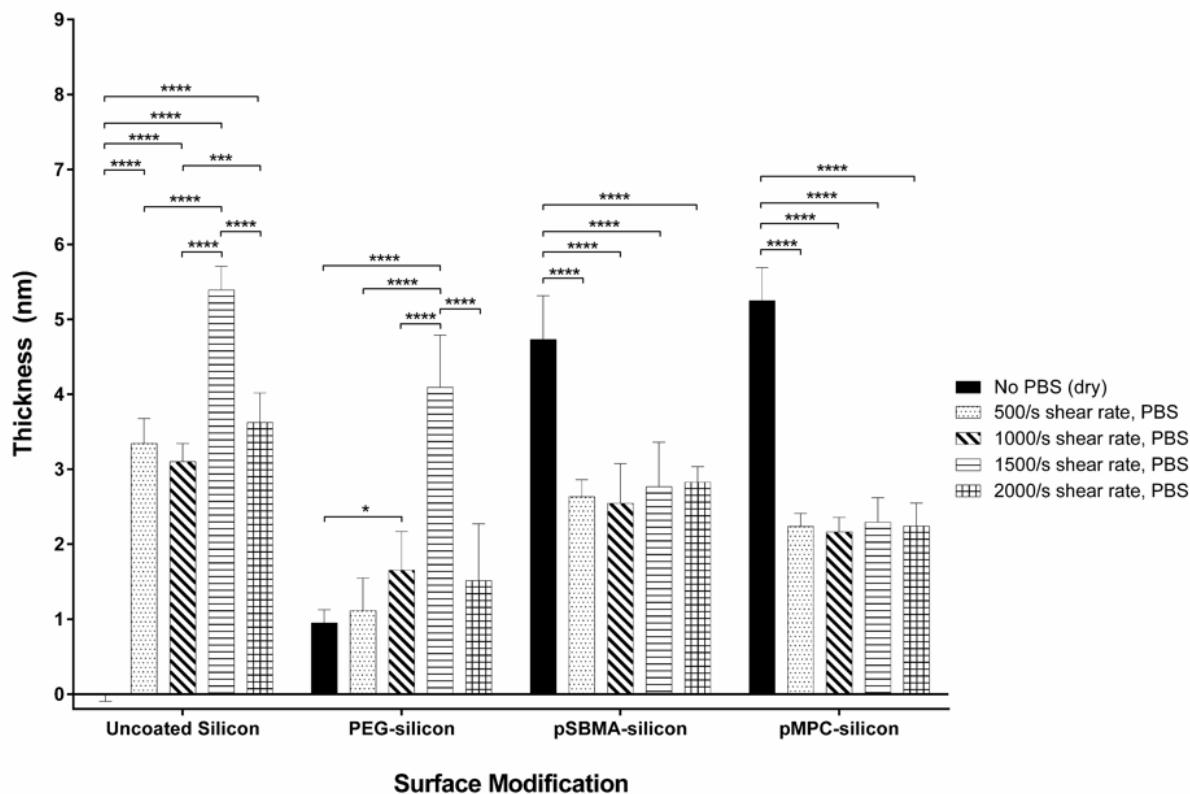
Figure 3.5: *Change in thickness with varying shear rates for each surface modifications. Data has been normalized to native oxide measured in uncoated silicon that has not been exposed to D-PBS. Significance was defined at p <0.05. Level of significance is indicated by the number of asterisks: $p \leq 0.05 = *$; $p \leq 0.01 = **$; $p \leq 0.001 = ***$; $p \leq 0.0001 = ****$.*

3.3.4 ELISA

Following exposure to shear, coating functionality was characterized by measuring protein resistance against human serum albumin. The amount of protein adsorption for each surface coating before and after shear is plotted in Figure 3.6. All data has been normalized to positive control tissue culture polystyrene. For unmodified silicon, there was no significant difference in protein adsorption between control and substrates exposed to shear. PEG modification yielded little difference in protein resistance from unmodified silicon. Biological shear of PEG-silicon did not increase the protein adsorption.

Control pSBMA and pMPC coated silicon improved protein resistance by ~71% and ~93%, respectively, compared to uncoated silicon. Like PEG, exposure to shear did not lead to increased protein adsorption for pSBMA-silicon. For pMPC-silicon, shear of 1000/s and above led to increased protein adsorption by a factor of ~2.3. Nonetheless, all pSBMA and pMPC-coated substrates reduced protein adsorption by greater than 70% compared to unmodified silicon.
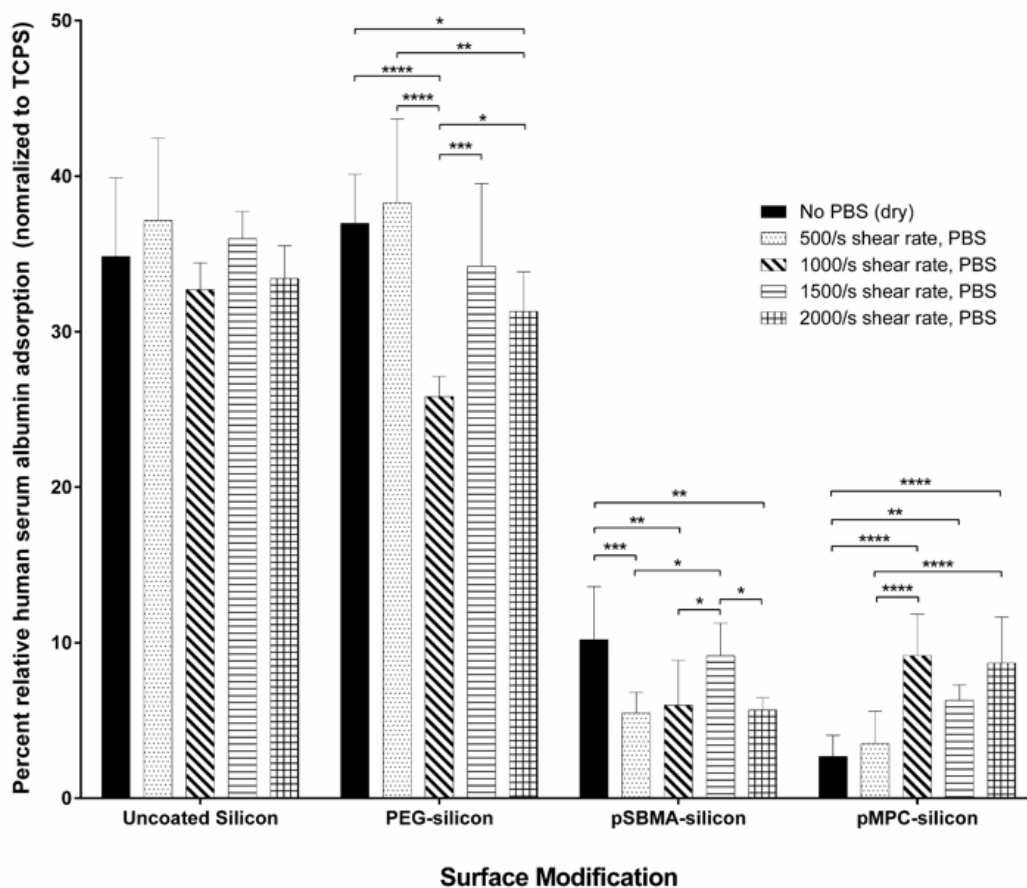
Figure 3.6: *Protein adsorption for uncoated, PEG-, pSBMA-, and pMPC-silicon before and after exposure to shear rates of 500-2000/s. Data is normalized to positive control tissue culture polystyrene (TCPS). Significance was defined at p <0.05. Level of significance is indicated by the number of asterisks: $p \leq 0.05$ = *; $p \leq 0.01$ = **; $p \leq 0.001$ = ***; $p \leq 0.0001$ = ****.*

3.4 Discussion

For implantable devices in contact with blood flow, the effect of shear rate must be investigated. Our implantable organs require ultrathin film polymer surface coatings to be subjected to biological shear. Shear rates in the human body can be can be as high as 1650/s.[38] Increasing shear leads to faster removal of solutes from the surface, which may lead to increased degradation of surface coatings. Previously, isolated studies of coating degradation were conducted under static conditions.[22,35] This chapter explores the effect of biological shear on ultrathin polymer surface modifications. Specifically, three hydrophilic, brush-structure coatings that are of ~5 nm or less in thickness were examined: PEG, pSBMA and pMPC. The experiment was run for 24 hours in physiological temperature of 37 °C and shear rates of 500-2000/s were achieved over these surfaces using varying flow rates of D-PBS. Using D-PBS has its drawbacks when compared to blood or serum: there are no enzymes, proteins, or cells present in D-PBS. Hence, the effect of these biological components will not be reflected via these experiments. Nonetheless, PBS is often used in previous literature in place of blood due to its similarity in pH and saline content,[22,35] and for this study, it allows us to do sensitive surface analysis that would be compromised by proteins and cells attached on the surface.
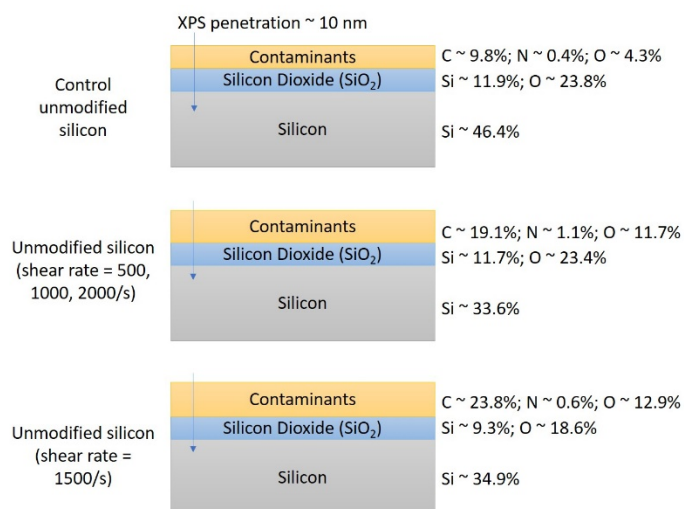
Figure 3.7: Schematic of elemental breakdown of unmodified silicon based on high resolution and spectral XPS data. Data illustrates change in oxygen found in XPS is due to contaminants, not silicon dioxide. Image not drawn to scale.

Due to shear and exposure to D-PBS, uncoated silicon gathered organic contamination over 24 hours of flow. Both XPS and ellipsometry data

109

indicated a change in surface chemistry with shear. Since both C 1s and O 1s concentration increased, the change in thickness may be due to contamination and/or increase in native oxide growth on the surface. However, as illustrated in Figure 3.7, calculations based on the high-resolution and spectral XPS data indicate that the additional oxygen arising in shear exposed surfaces is bound to carbon rather than silicon. Therefore, with shear, the elevated thickness found using ellipsometry is likely due to contamination and not due to oxide growth. The experiment was conducted in a clean, but not sterile, environment, which may have led to bacterial growth on the surface over time. The highest level of contamination was found with 1500/s shear rate. Overall, despite additional contamination, ELISA results did not indicate a significant difference in protein resistance with shear compared to control.

While all three surface analyses confirmed successful surface modification, there was no change in protein resistance for PEG-coupled silicon compared to uncoated silicon. Initially, ~1 nm thick PEG coating is present on the control. However, PEG-coated silicon did not improve protein resistance over unmodified silicon. Although previous literature shows a significant decrease in bacterial growth and biofilm formation following PEG modification,[40,41] our data suggests attachment of organic contaminants, possibly due to bacterial growth on the surface. Based on data provided by the manufacturer (Gelest), the PEG chains should be 6-9 monomer units in length. However, mass spectrometry of Gelest PEG solution (data presented in Appendix B) shows a variety of chain lengths present. Therefore, chains grafted to silicon may be smaller than expected and/or the grafting density may be low, leading to lower protein resistive function.

Based on the three surface analyses conducted, PEG degradation is difficult to explain due to its similarity to carbon contamination in elemental signature. With shear, there is an increase in the

apparent thickness, up to 3 nm higher with 1500/s shear rate than control PEG coating. We see a similar pattern in uncoated silicon, suggesting there may be optimal conditions leading to higher biological burden for the 1500/s shear rate. Increase in carbon content, specifically C-O bonds, is typically indicative of PEG.[42] When compared to control, with shear, we see a decrease in C 1s concentration, which is reflected in decreased C-C/C-H and C-O bonds. There is also <1% increase in N 1s concentration, which may be due to contamination. Because these same bonds are present in organic contamination, there could be three possibilities: PEG degraded completely and surface contaminants are resulting in elevated thickness; PEG degraded partially, enough to allow surface contaminants to attach to the surface; or none of the PEG degraded, but initial PEG grafting density was not enough to resist contaminants. The last option is highly unlikely because it would lead to greater C 1s concentration than PEG control. However, partial or full degradation of PEG from the surface cannot be differentiated.

For pSBMA-silicon, while there was no significant difference in surface chemistry and thickness between 500-2000/s shear rates, exposure to shear and D-PBS led to changes in surface characteristics. Control pSBMA coating had a starting contact angle of ~10.9° and thickness of ~4.7 nm. These results, combined with the elemental signature of nitrogen, sulfur and an ester group (O-C=O), indicated pSBMA was successfully grafted to the silicon. With shear, decrease in C 1s was evident. For example, for a shear rate of 2000/s, there was a 40% reduction in C 1s, 23% reduction in S 2s and 25% reduction in O-C=O groups. However, since both carbon and ester groups are present in control unsterilized, unmodified substrates, and sulfur is unique to SBMA, change in surface chemistry is best determined on the change in sulfur content. Ellipsometry data presented ~40% decrease in coating thickness following exposure to shear. This change appears to be due to removal of SBMA from the surface, as well as conformational

change in pSBMA chains. Despite these alterations at the surface, there was no increase in protein adsorption with shear and functionality of the coating was preserved.

pMPC followed similar trend as pSBMA: while there were changes in the surface characteristics with shear, their nonfouling properties were still retained. With an initial thickness of ~5.2, XPS of pMPC-silicon showed the presence of signature elements and bonds, such as N 1s, P 2s, and O-C=O. Like pSBMA, there was a significant decrease in carbon concentration following exposure to shear and D-PBS. A shear rate of 1000/s yielded the least thickness and concentration of elemental signature. Under this condition, C 1s shows a 50%, P 2s shows a 25% and O-C=O shows a 10% decrease. Additionally, there was a ~62% decrease in coating thickness. Because phosphorus is the unique signature element in pMPC, tracking its change indicates that there was approximately 25% removal of MPC from the surface, while about 37% change in thickness is due to conformational change in the pMPC chains. While ELISA result shows that shear affected the performance of pMPC coatings, all pMPC samples still led to a >75% decrease in protein adsorption compared to unmodified silicon. Therefore, exposure to shear did not change functionality.

For the zwitterion-coated samples, removal of SBMA and MPC could originate from either uncrosslinked monomers present at the surface or breakdown of pSBMA monomer chains. If, over time, further removal of monomer chemical signature takes place, especially at the same rate, it is likely due to the degradation of the polymer. However, if the chemical signature stabilizes over time, uncrosslinked polymers are likely washed away with exposure to shear stress. Therefore, there is a need for future study that incorporates shear rate over time.

3.5 Conclusions

While surface modified implants are often exposed to blood flow, isolated studies of the effect of shear, especially on ultrathin polymer coatings, have not been examined. The results presented in this chapter demonstrate that between the range of biological shear rates from 500-2000/s, ~5 nm zwitterionic surface modifications retain their functionality. However, exposure to shear for 24 hours using D-PBS increased contact angle, and reduced surface polymer concentration and coating thickness. These changes may be due to removal of uncrosslinked monomers or partial polymer degradation. However, further studies of shear coupled with time must be conducted to separate the differences.

3.6 References

1.   Cheung, K. C. & Renaud, P. BioMEMS for medicine: On-chip cell characterization and implantable microelectrodes. *Solid. State. Electron.* **50,** 551–557 (2006).

2.   Scholvin, J. *et al.* Close-packed silicon microelectrodes for scalable spatially oversampled neural recording. *IEEE Trans. Biomed. Eng.* **63,** 120–130 (2016).

3.   Desai, T. *et al.* Nanoporous Implants for Controlled Drug Delivery. *Ther. Micro/Nano Technol. - BioMEMS Biomed. Nanotechnol.* 263–286 (2007). doi:10.1007/978-0-387-25844-7_15

4.   Lesinski, G. B. *et al.* Release of biologically functional interferon-alpha from a nanochannel delivery system. *Biomed. Microdevices* **7,** 71–79 (2005).

5.   Shawgo, R. S., Grayson, A. C. R., Li, Y. & Cima, M. J. BioMEMS for drug delivery. *Curr. Opin. Solid State Mater. Sci.* **6,** 329–334 (2002).

6.   Kang, S. *et al.* Bioresorbable silicon electronic sensors for the brain. *Nature* **530,** 71–76 (2016).

7.   Lueke, J. & Moussa, W. A. MEMS-based power generation techniques for implantable biosensing applications. *Sensors* **11,** 1433–1460 (2011).

8.   Acquaroli, L. N., Kuchel, T. & Voelcker, N. H. Towards implantable porous silicon biosensors. *RSC Adv.* **4,** 34768 (2014).

9.   Fissell, W. H. *et al.* High-performance silicon nanopore hemofiltration membranes. *J. Memb. Sci.* **326,** 58–63 (2009).

10.   Roy, S. *et al.* Silicon nanopore membrane technology for an implantable artificial kidney.

TRANSDUCERS 2009 - 15th Int. Conf. Solid-State Sensors, Actuators Microsystems 755–760 (2009). doi:10.1109/SENSOR.2009.5285603

11.   Fissell, W. H., Fleischman, A. J., Humes, H. D. & Roy, S. Development of continuous implantable renal replacement: past and future. *Transl. Res.* **150,** 327–336 (2007).

12.   Song, S. *et al.* An intravascular bioartificial pancreas device (iBAP) with silicon nanopore membranes (SNM) for islet encapsulation under convective mass transport. *Lab Chip* (2017). doi:10.1039/C7LC00096K

13.   Song, S. *et al.* Silicon nanopore membrane (SNM) for islet encapsulation and immunoisolation under convective transport. *Sci. Rep.* **6,** 23679 (2016).

14.   Fernández-Rosas, E. *et al.* Internalization and cytotoxicity analysis of silicon-based microparticles in macrophages and embryos. *Biomed. Microdevices* **12,** 371–379 (2010).

15.   Agrawal, a. a. *et al.* Porous nanocrystalline silicon membranes as highly permeable and molecularly thin substrates for cell culture. *Biomaterials* **31,** 5408–5417 (2010).

16.   Kotzar, G. *et al.* Evaluation of MEMS materials of construction for implantable medical devices. *Biomaterials* **23,** 2737–50 (2002).

17.   Werner, C., Maitz, M. F. & Sperling, C. Current strategies towards hemocompatible coatings. *J. Mater. Chem.* **17,** 3376 (2007).

18.   Zhang, M. & Ferrari, M. Hemocompatible polyethylene glycol films on silicon. *Biomed. Microdevices* (1998). at <http://www.springerlink.com/index/H6K15PK44618078T.pdf>

19.   Popat, K. C. & Desai, T. a. Poly(ethylene glycol) interfaces: An approach for enhanced performance of microfluidic systems. *Biosens. Bioelectron.* **19,** 1037–1044 (2004).

20.   Melvin, M. E., Fissell, W. H., Roy, S. & Brown, D. L. Silicon induces minimal thromboinflammatory response during 28-day intravascular implant testing. *ASAIO J.* **56,** 344–8 (2010).

21.   Han, S., Kim, C. & Kwon, D. Thermal/oxidative degradation and stabilization of polyethylene glycol. *Polymer (Guildf).* **38,** 317–323 (1997).

22.   Sharma, S., Johnson, R. W. & Desai, T. a. Evaluation of the Stability of Nonfouling Ultrathin Poly (ethylene glycol) Films for Silicon-Based Microdevices. *Langmuir* 348–356 (2004). doi:10.1021/la034753l

23.   Cerruti, M. *et al.* Poly(ethylene glycol) monolayer formation and stability on gold and silicon nitride substrates. *Langmuir* **24,** 10646–10653 (2008).

24.   Chen, S., Liu, L. & Jiang, S. Strong resistance of oligo(phosphorylcholine) self-assembled monolayers to protein adsorption. *Langmuir* **22,** 2418–21 (2006).

25.   Jiang, S. & Cao, Z. Ultralow-fouling, functionalizable, and hydrolyzable zwitterionic materials and their derivatives for biological applications. *Adv. Mater.* **22,** 920–932 (2010).

26.   Zhang, Z., Chao, T., Chen, S. & Jiang, S. Superlow fouling sulfobetaine and carboxybetaine polymers on glass slides. *Langmuir* **22,** 10072–10077 (2006).

27.   Muthusubramaniam, L. *et al.* Hemocompatibility of silicon-based substrates for biomedical implant applications. *Ann. Biomed. Eng.* **39,** 1296–305 (2011).

28.   Carr, L. R., Zhou, Y., Krause, J. E., Xue, H. & Jiang, S. Uniform zwitterionic polymer hydrogels with a nonfouling and functionalizable crosslinker using photopolymerization.

Biomaterials **32,** 6893–6899 (2011).

29.   Zhang, Z. *et al.* Blood compatibility of surfaces with superlow protein adsorption. *Biomaterials* **29,** 4285–4291 (2008).

30.   Smith, R. S. *et al.* Vascular Catheters with a Nonleaching Poly-Sulfobetaine Surface Modification Reduce Thrombus Formation and Microbial Attachment. *Sci. Transl. Med.* **4,** 153ra132-153ra132 (2012).

31.   Nakabayashi, N. & Williams, D. F. Preparation of non-thrombogenic materials using 2-methacryloyloxyethyl phosphorylcholine. *Biomaterials* **24,** 2431–2435 (2003).

32.   Ladd, J., Zhang, Z., Chen, S., Hower, J. C. & Jiang, S. Zwitterionic polymers exhibiting high resistance to nonspecific protein adsorption from human serum and plasma. *Biomacromolecules* **9,** 1357–1361 (2008).

33.   Zhang, L. *et al.* Zwitterionic hydrogels implanted in mice resist the foreign-body reaction. *Nat. Biotechnol.* **31,** 553–6 (2013).

34.   Yang, W. *et al.* Film thickness dependence of protein adsorption from blood serum and plasma onto poly(sulfobetaine)-grafted surfaces. *Langmuir* **24,** 9211–9214 (2008).

35.   Li, L., Marchant, R. E., Dubnisheva, A., Roy, S. & Fissell, W. H. Anti-biofouling Sulfobetaine Polymer Thin Films on Silicon and Silicon Nanopore Membranes. *J. Biomater. Sci. Polym. Ed.* **22,** 91–106 (2011).

36.   Smith, R. S. *et al.* Vascular Catheters with a Nonleaching Poly-Sulfobetaine Surface Modification Reduce Thrombus Formation and Microbial Attachment. *Sci. Transl. Med.* **4,** 1–10 (2012).

37.   Kim, S. *et al.* Diffusive silicon nanopore membranes for hemodialysis applications. *PLoS One* **11,** 1–20 (2016).

38.   Papaioannou, T. G. & Stefanadis, C. Vascular Wall Shear Stress : Basic Principles and Methods. *Hell. J. Cardiol.* **46,** 9–15 (2005).

39.   Huang, Y., Lü, X., Qian, W., Tang, Z. & Zhong, Y. Competitive protein adsorption on biomaterial surface studied with reflectometric interference spectroscopy. *Acta Biomater.* **6,** 2083–2090 (2010).

40.   Dong, B., Manolache, S., Somers, E. B., Wong, A. C. L. & Denes, F. S. Generation of antifouling layers on stainless steel surfaces by plasma-enhanced crosslinking of polyethylene glycol. *J. Appl. Polym. Sci.* **97,** 485–497 (2005).

41.   Shimotoyodome, A. *et al.* Reduction of Streptococcus mutans adherence and dental biofilm formation by surface treatment with phosphorylated polyethylene glycol. *Antimicrob. Agents Chemother.* **51,** 3634–3641 (2007).

42.   Sharma, S., Johnson, R. W. & Desai, T. a. XPS and AFM analysis of antifouling PEG interfaces for microfabricated silicon biosensors. *Biosens. Bioelectron.* **20,** 227–239 (2004).

Sterilization Effects on Ultrathin Film Polymer Coatings for Silicon-based Implants

Substantial portions of this chapter have been published in Journal of Biomedical Materials Research Part B: Applied Biomaterials, 2017:00B:000-000.

4.1 Introduction

Implantable medical devices based on silicon are increasingly attractive due to their precisely-defined micro- and nanoscale features which can be produced at low cost and integrated with microelectronics. These devices include microelectrodes for neuroprosthetics,[1] controlled drug delivery systems,[2,3] immunoisolation chambers for cell transplants,[4–8] and nanofilters for renal replacement therapy.[9,10] Such applications bring silicon in direct contact with body fluids, including blood. According to the US Centers for Disease Control and Prevention (CDC), any medical device in contact with sterile biological fluids is categorized as a "critical item" and must be sterilized. For implants, the sterility assurance level (SAL) must be at least 10^{-6}, which is equivalent to the probability of one in a million spores surviving the sterilization process. This SAL level is reached by a number of physical and chemical processes: high temperature exposure, chemical and chemical plasma exposure, and irradiation.[11] These treatments eradicate microbes and spores. However, their harsh characteristics can cause cross-linking, bond disruption, and/or oxidation of the medical device components, possibly causing undesirable damage to functionalized surfaces.

Our lab has developed silicon nanopore membrane (SNM) technology for use in bioartificial

organs, including implantable bioartificial kidney,[9,12,13] and bioartificial pancreas,[7] as shown in

Figure 4.1. SNMs consist of uniform, sub-10 nm slit shaped pores produced on silicon

substrates. This highly permeable and selective membrane allows for convective clearance of

solutes similar to a functioning glomerulus in a healthy kidney. In the bioartificial pancreas, the

SNM provides protects encapsulated islets from the host's immune factors, while allowing the

passage of glucose, insulin, and other small molecules.
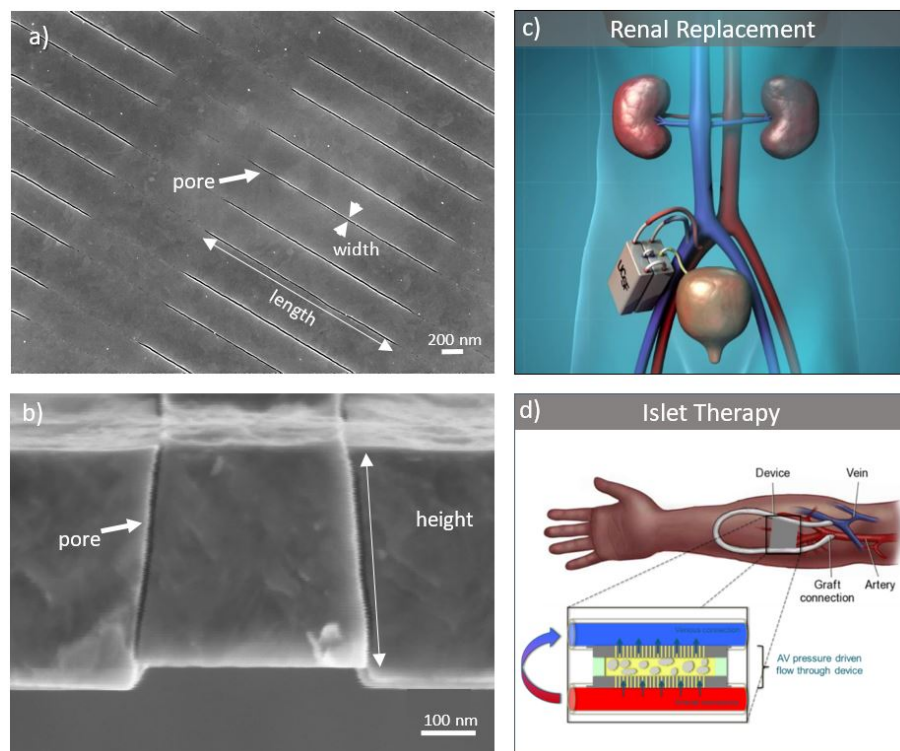
Figure 4.1: *Silicon nanopore membrane (SNM) developed for bioartificial organs. SNM (a) top view depicting pore length of 2 μm and pore width of 7 nm, and (b) side view depicting 360 nm pore height, reprinted from S. Song et al./ Scientific Reports (6), ©2016, with permission from Nature Publishing Group (c) Concept of an artificial kidney based on SNM renal replacement therapy. (d) Immunoisolation chamber for encapsulated islets in a bioartificial pancreas.*

In order to successfully create bioartificial organs, biocompatibility of the SNM is essential. To

this end, the biocompatibility of silicon is enhanced by the application of ultrathin polymer

coatings that minimize biofouling and degradation of the underlying substrate.[14–17] For our

bioartificial kidney and pancreas, we are investigating three surface modifications. These

coatings were selected for their hydrophilicity and controllable degree of polymerization:

polyethylene glycol (PEG), polysulfobetaine methacrylate (pSBMA) and poly(2-

methacryloyloxyethyl phosphorylcholine) (pMPC). PEG is a widely used non-fouling surface

modification.[16,18–24] The surface remains hydrated and brush-like PEG chains creates steric

repulsion to resist fouling.[14,25] pSBMA and pMPC are zwitterionic polymer brushes that have

also previously demonstrated excellent non-fouling properties.[15,26–29] These biomimetic

polymers coordinate water molecules in a manner that resists protein and cell adhesion.[30]

Silicon itself is not known to be affected by conventional sterilization techniques such as

autoclave and gamma radiation.[31] However, the effect of sterilization on thin-film polymeric

surface coatings applied to silicon is not well characterized. Previous studies have shown effects

of sterilization on hydrogels, crosslinked polymers, and surface modifications that are orders of

magnitude thicker.[32–34] However, effect of sterilization on sub-10 nm thick brush-like polymer

structures of PEG, pSBMA and pMPC have not been reported. Therefore, the work presented in

this chapter focuses on the effect of common sterilization modalities on silicon coated with PEG,

pSBMA, and pMPC. The modified substrates were sterilized using five techniques approved by

the CDC: autoclave, dry heat, hydrogen peroxide (H_2O_2) plasma, ethylene oxide (EtO) gas, and

electron beam (E-beam) irradiation. We utilized various surface characterization techniques to

examine the physical and chemical effects of sterilization. X-ray photoelectron spectroscopy

(XPS) was conducted to determine the changes in chemical composition at the surface. Contact

angle measurements were taken to determine the change in surface wettability, and change in

polymer thickness was measured using ellipsometry. Together, these three tests give us insight

into the conformation change and/or degradation of the polymer chains. Finally, protein fouling capacity with and without sterilization was measured using enzyme-linked immunosorbent assays (ELISA).

4.2 Materials and Methods

4.2.1 Sample Preparation

Double side polished, 400 µm thick, p-type silicon wafers from Ultrasil Corporation (Hayward, CA, USA) were diced into 1 cm^2 chips. The chips were cleaned by "piranha," a solution of 3:1 ratio of sulfuric acid (96%) to hydrogen peroxide (30%) for 20 min. Next, they were exposed to hydrofluoric acid for 5 min to remove native silicon dioxide that spontaneously forms on silicon surfaces exposed to atmospheric oxygen. The silicon was then activated by another piranha treatment. The substrates were dried under a stream of nitrogen gas and used immediately for surface modification.

4.2.2 Surface Modification

4.2.2.1 PEG Surface Modification

Silicon surfaces were modified with PEG as previously described.[7,13] Briefly, substrates were dried on a hotplate at 110 °C for 1 hour. PEG-silane, 2-[methoxy(polyethyleneoxy)propyl]trimethoxysilane (shown in Table 4.1), purchased from Gelest (Morrisville, PA, USA), were covalently bonded to silicon by immersing the substrates in a solution of 285 µl PEG-silane in 25 mL of toluene for 2 hours at 70 °C. Excess PEG was removed by rinsing the substrates three times at 10 min intervals with toluene, ethanol, and water respectively.

4.2.2.2 Zwitterionic Surface Modification

All chemicals were purchased from Sigma-Aldrich (St. Louis, MO, USA), unless stated otherwise. Zwitterionic surface modifications were conducted as described in previously published literature.[35] Detailed description of surface modifications can be found in Chapter 2, Materials and Methods. Briefly, a surface initiator 2-bromo-2-methyl-N-3[(trimethoxysilyl)propyl]-propanamide (BrTMOS) as shown in Table 4.1, was synthesized.[35] The substrates were placed in a 1% (v/v) BrTMOS solution in bicyclohexyl for 2 hours. Excess BrTMOS was removed from the surfaces by rinsing them with chloroform, ethanol, and water respectively.

Table 4.1: *Chemical structures of PEG-silane, BrTMOS-silane linker for zwitterioinic coatings, SBMA monomer and MPC monomer.*

1, 2-[methoxy(polyethyleneoxy)propyl]trimethoxysilane (PEG-silane)	
2-bromo-2-methyl-N-3[(trimethoxysilyl)propyl]-propanamide (BrTMOS)	
2-(methacryloyloxy)ethyl]dimethyl-(3-sulfopropyl)ammonium hydroxide, sulfobetaine methacrylate (SBMA)	
2-methacryloyloxyethyl phosphorylcholine (MPC)	

SBMA monomer, 2-(methacryloyloxy)ethyl]dimethyl-(3-sulfopropyl)ammonium hydroxide, and

MPC monomer, 2-methacryloyloxyethyl phosphorylcholine, are shown in Table 4.1. Degassed

solution of 468 mg (3 mmol) of 2,2'-bipyridyl (≥98%) and individual monomers—SBMA: 1.06g

(3.8 mmol), and MPC: 506 mg (1.9 mmol)—and 22.3 mg (0.1 mmol) of copper (II) bromide

(99%) was prepared in 5:5 mL of methanol:water. This mixture was added to a nitrogen

protected reaction chamber containing four substrates modified with BrTMOS and 143 mg (1

mmol) of copper (I) bromide (99.999%). Polymerization ran for 15 min for pSBMA and 7 min

for pMPC. The substrates were then rinsed with chloroform, ethanol, Dulbecco's phosphate

buffered saline (D-PBS, UCSF Cell Culture Facility, San Francisco, CA, USA), and water

respectively, and dried using a stream of nitrogen gas.

4.2.3   Sterilization Processes

Five sterilization processes were evaluated: autoclave, dry heat, H_2O_2 plasma treatment, EtO gas

treatment and E-beam sterilization. Autoclave was conducted using STERIS Amsco Century,

SV-120 Scientific Prevacuum Sterilizer (Mentor, OH, USA), where substrates were exposed to

high pressure steam for 30 minutes at 121 °C. For dry heat sterilization, substrates were placed

in a 160 °C oven for 2 hours.[36] H_2O_2 plasma treatment was conducted using STERRAD® 100S

Sterilization System (standard cycle). EtO gas treatment was conducted with a 2-hour exposure

time at 132 mBar and 55°C by D2EO (San Jose, CA, USA). Lastly, E-beam sterilization was

performed by STERIS (Petaluma, CA, USA), at an applied dosage range of 21.0 to 21.9 kGy.

4.2.4   Surface Characterization

4.2.4.1 X-ray Photoelectron Spectroscopy (XPS)

XPS was conducted using a Surface Science Instruments S-Probe spectrometer with a

monochromatized Al Kα X-ray beam. A pass energy of 150 eV was used to generate the survey

and high resolution spectra. Samples were placed in a vacuum of <5e-9 torr and a 0° take-off

angle was used, corresponding to sampling depth of ~10 nm. XPS readings were measured at

three locations with a spot size of ~800 μm for each sample. Elemental composition calculations

were performed using Service Physics Hawk version 7 software (Bend, OR, USA).

4.2.4.2 Goniometry (Contact Angle)

Surface hydrophilicity was measured using sessile drop contact angle goniometry (Attension

Theta Lite, Biolin Scientific, Stockholm, Sweden). A ~3.5 µl water droplet was placed on the

substrate in ambient air and the contact angle between the droplet and the substrate was

measured. Data points was collected every 0.1 s over 10 s, and averaged. Six data points was

collected from each sample subset group.

4.2.4.3 Ellipsometry

Surface coating thickness was measured using LSE Stokes ellipsometer (Gaertner Scientific,

Skokie, IL, USA) with a 6328 Å HeNe laser at an incidence angle of 70°. With known refracting

index, and measured reflection and transmission data, Fresnel equations were used to iteratively

solve for thickness of the transparent film. An index of refraction of 1.45 was used for both

zwitterionic and PEG surface coatings.[35] Although sterilization processes may lead to

conformational changes and cross-linking within the polymers, refractive index was assumed to

be constant. Measurements on three locations on three separate chips per sample set were taken

to characterize spatial homogeneity. A total of nine measurements were averaged, and the mean

and standard deviation is reported.

4.2.4.4 ELISA

Resistance to protein fouling was determined using ELISA using published methods.[27,35]

Substrates were hydrated in D-PBS for 90 minutes. D-PBS was replaced with 1 mg/mL solution

of human serum albumin (HSA) in D-PBS for 90 minutes and the samples were incubated at 37°C. All substrates were rinsed 5 times with 0.5 mL of D-PBS following HSA incubation, and were blocked using bovine serum albumin[37] (BSA, ≥98%, Sigma-Aldrich) at 1 mg/mL concentration for 1.5 hours. The substrates were rinsed 5 times with 0.5 mL of D-PBS, and transferred to fresh chambers. The samples were incubated with 10 µg/mL anti-human serum albumin antibody conjugated with horseradish peroxidase for 1.5 hours (Abcam, Cambridge, MA, USA). After another rinse (5 times with 0.5 mL of D-PBS), the substrates again rinsed and transferred to fresh chambers. A solution of 0.5 mg/mL of o-phenylenediamine (OPD, VWR Inc. Visalia, CA, USA) and 0.03% hydrogen peroxide in 0.05 M citrate phosphate buffer (pH 5.0, Sigma-Aldrich). This reaction was protected from light using aluminum foil for 20 min at 37 °C, and subsequently stopped by adding 0.5 mL of 1M sulfuric acid. The light absorbance of the solutions was measured at 490 nm. Each sample type was tested in triplicate and the background (control with no HSA added) was subtracted. All HSA protein adsorption data was normalized to tissue culture polystyrene (TCPS) which was used as a positive control.

4.2.5 Statistical Analysis

A minimum of three measurements were collected for all samples in each analysis. Statistical significance was determined by ordinary one-way analysis of variance (ANOVA) since comparisons were drawn only within each coating subset. Significance was defined at $p < 0.05$. Level of significance is indicated by the number of asterisks: $p \leq 0.05 = *$; $p \leq 0.01 = **$; $p \leq 0.001 = ***$; $p \leq 0.0001 = ****$. Analysis was conducted using Graphpad Prism software (San Diego, CA, USA).

4.3 Results

4.3.1   X-ray Photoelectron Spectroscopy (XPS)

A comparison of survey XPS spectra for each of the unsterilized substrate types is shown in Figure 4.2. Figure 4.3(a) - (d) present the corresponding spectra after the various sterilization methods for each of the surface modifications, and the elemental composition is summarized in Table 4.2. An example of high resolution XPS data is presented in Table 4.3. Measurements show there is a presence of Si 2p (100 eV) and O 1s (528 eV) peaks from the monocrystalline silicon substrate and native silicon dioxide in all substrates. The unmodified (uncoated) silicon shows a presence of ~8% adventitious carbon, with the exception of H_2O_2 plasma treated substrates, where the carbon content was ~16%. With H_2O_2 plasma treatment, the unmodified silicon exhibits an elevated level of oxygen and a presence of nitrogen, sodium and fluorine. Since these elements are not significantly present on the other substrates, it is possible that they are contaminants arising from sample mishandling. Besides H_2O_2 treated samples, high resolution data shows less than 5% change in crystalline silicon and silicon dioxide content between sterilized and unsterilized silicon substrates.
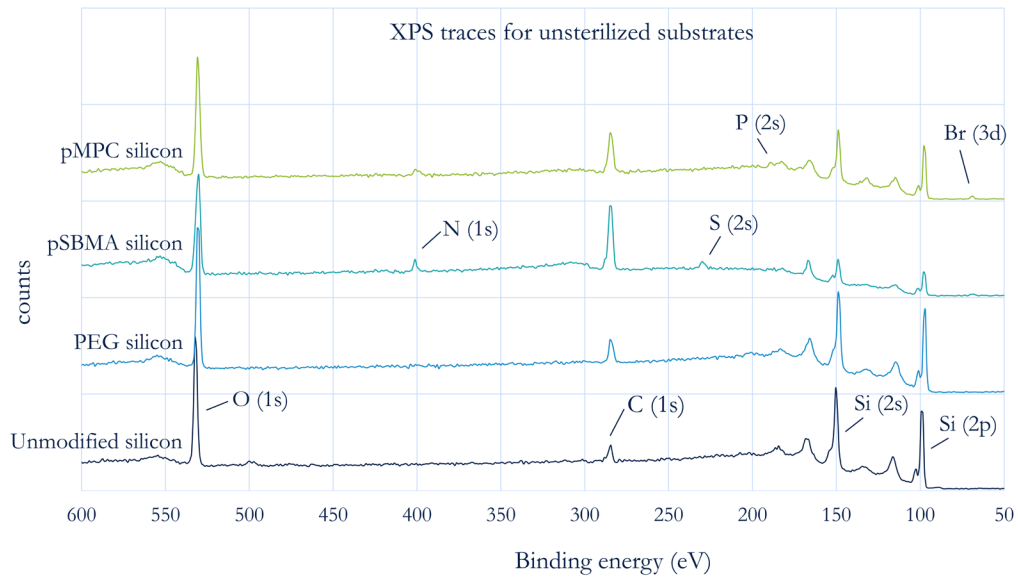
Figure 4.2: *XPS traces of control unsterilized unmodified silicon, PEG-silicon, pSBMA-silicon, and pMPC-silicon demonstrating successful surface modification of silicon.*
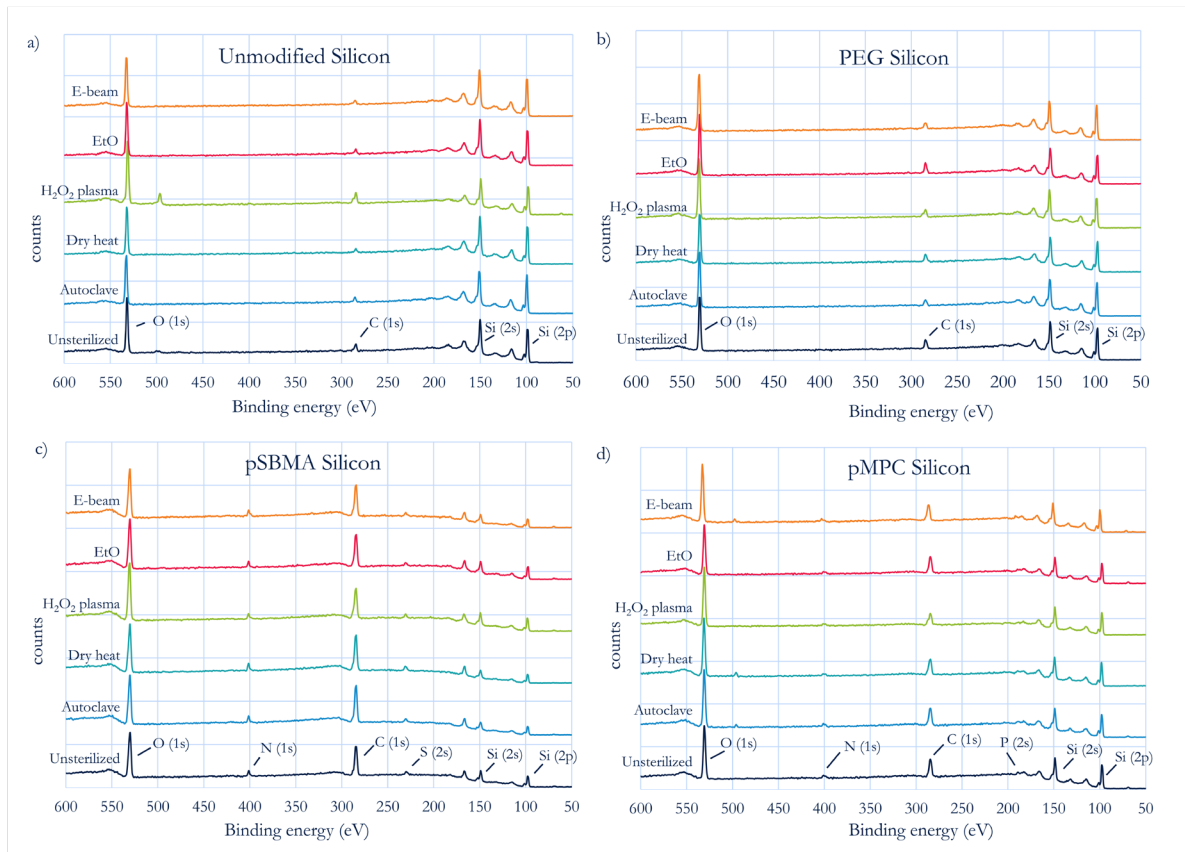
Figure 4.3: *XPS traces of (a) unmodified silicon, (b) PEG-silicon, (c) pSBMA-silicon, and (d) pMPC-silicon over varying sterilization conditions demonstrating the survival of surface coatings on silicon following sterilization.*

Table 4.2: *Percent of elemental composition following sterilization processes for each surface modification and control unmodified silicon. Unmodified silicon results demonstrate the level of adventitious carbon to be between 7-9%. PEG, pSBMA, and pMPC signature elements are present following sterilization, indicating that the polymers remain on the surface despite harsh sterilization treatments.*

Sample	Sterilization	% Elemental Composition							
		Si (2p)	O (1s)	C (1s)	N (1s)	S (2s)	P (2s)	Br (3d)	Contaminants (Na, F, Zn)
Unmodified Silicon	Autoclave	62.4 ± 0.8	28.6 ± 1.1	9.0 ± 1.0					
	Dry Heat	66.4 ± 0.6	27.6 ± 0.2	6.0 ± 0.5					
	H_2O_2 plasma	46.9 ± 4.4	31.9 ± 0.3	16.3 ± 2.1	1.2 ± 0.2				3.7 ± 3.0
	EtO	62.8 ± 1.9	29.6 ± 0.4	6.8 ± 1.4					0.8 ± 0.8
	E-beam	63.3 ± 1.8	28.8 ± 0.9	7.2 ± 1.8					0.7 ± 0.6
	No Sterilization	61.5 ± 4.5	29.3 ± 1.4	7.8 ± 2.2					1.4 ± 1.5
PEG on Silicon	Autoclave	52.1 ± 10.0	33.0 ± 0.8	15.0 ± 9.9					
	Dry Heat	52.4 ± 3.1	31.3 ± 0.3	16.3 ± 2.8					
	H_2O_2 plasma	52.1 ± 1.6	32.4 ± 0.6	14.3 ± 1.9	1.2 ± 0.2				
	EtO	52.5 ± 2.0	32.1 ± 2.0	15.2 ± 2.8	0.2 ± 0.3				
	E-beam	55.6 ± 2.0	32.9 ± 1.6	11.4 ± 0.6					
	No Sterilization	49.7 ± 3.0	31.8 ± 1.3	18.4 ± 1.8	0.1 ± 0.1				
pSBMA on Silicon	Autoclave	12.3 ± 1.4	26.1 ± 0.4	53.3 ± 1.1	4.3 ± 0.1	3.7 ± 0.1		0.3 ± 0.0	
	Dry Heat	12.2 ± 0.8	25.7 ± 0.3	53.6 ± 0.7	4.7 ± 0.1	3.8 ± 0.1		0.1 ± 0.0	
	H_2O_2 plasma	14.6 ± 2.5	29.9 ± 0.7	47.9 ± 1.3	4.3 ± 0.4	3.1 ± 0.4		0.3 ± 0.0	
	EtO	16.7 ± 1.3	26.5 ± 0.5	49.4 ± 0.6	4.1 ± 0.2	3.0 ± 0.4		0.3 ± 0.0	
	E-beam	10.8 ± 1.0	28.2 ± 0.5	51.6 ± 0.9	5.1 ± 0.4	3.7 ± 0.3	0.3 ± 0.1	0.3 ± 0.0	
	No Sterilization	20.0 ± 3.0	27.1 ± 0.2	45.6 ± 2.7	3.8 ± 0.3	2.9 ± 0.2	0.2 ± 0.1	0.4 ± 0.0	

Sample	Sterilization	% Elemental Composition							
		Si (2p)	O (1s)	C (1s)	N (1s)	S (2s)	P (2s)	Br (3d)	Contaminants (Na, F, Zn)
pMPC on Silicon	Autoclave	32.9 ± 0.1	29.9 ± 1.2	32.0 ± 1.7	3.1 ± 0.2		1.3 ± 0.1	0.5 ± 0.1	0.3 ± 0.5
	Dry Heat	34.4 ± 1.5	31.6 ± 1.1	29.4 ± 0.4	2.8 ± 0.1		1.0 ± 0.1	0.1 ± 0.0	0.7 ± 1.2
	H_2O_2 plasma	37.6 ± 0.6	34.3 ± 0.4	25.2 ±0.6	2.2 ± 0.2		0.7 ± 0.1		
	EtO	30.5 ± 2.1	30.3 ± 0.5	33.2 ± 1.1	3.0 ± 0.3		1.6 ± 0.1	0.8 ± 0.0	0.4 ± 0.7
	E-beam	34.7 ± 1.4	31.2 ± 0.6	28.9 ± 1.0	2.7 ± 0.4		1.4 ± 0.1	0.5 ± 0.1	0.5 ± 0.5
	No Sterilization	34.6 ± 0.7	29.5 ± 0.2	31.2 ± 0.6	2.7 ± 0.2		1.4 ± 0.1	0.6 ± 0.1	

Table 4.3: *XPS high resolution data with breakdown of high resolution bond composition for Si (2p), C (1s), and N (1s). Despite changes in chemical content, presence of signature elements and bonds demonstrate surface modification survival post-sterilization.*

Sample	Sterilization	% Elemental Composition												
		Si_{cryst}	Si (SiO_2)	O	C-C,H	C-O,N	O-C=O	N-C	NR_3^+	NO_x	S	P	Br	Contaminants
Unmodified Silicon	Autoclave	52.7	9.0	28.3	7.9	1.6	0.6							
	Dry Heat	57.0	9.3	27.8	4.5	0.8	0.6							
	H_2O_2 plasma	37.0	8.5	31.9	10.7	3.1	3.2							5.6
	EtO	54.0	9.1	29.9	4.9	1.0	0.4							0.8
	E-beam	53.4	8.3	29.8	5.7	1.3	0.4							1.0
	No Sterilization	52.0	9.5	30.4	4.7	1.4	0.6							1.4
PEG on Silicon	Autoclave	48.9	9.4	33.6	3.1	4.7	0.4							
	Dry Heat	40.5	8.3	31.6	4.1	14.9	0.6							
	H_2O_2 plasma	42.3	8.8	31.7	8.4	4.4	3.1							1.2
	EtO	45.6	9.1	33.3	4.3	6.8	0.9							
	E-beam	45.7	9.2	34.0	5.3	4.8	1.0							
	No Sterilization	39.5	8.3	32.0	5.12	14.0	0.9							0.2

Sample	Sterilization	% Elemental Composition												
		Si_{cryst}	Si (SiO$_2$)	O	C-C,H	C-O,N	O-C=O	N-C	NR$_3^+$	NO$_x$	S	P	Br	Contaminants
pSBMA on Silicon	Autoclave	11.3	2.7	25.7	20.9	28.0	3.2	0.7	3.6		3.8		0.4	
	Dry Heat	10.5	2.6	25.5	23.6	25.1	4.3	0.5	4.2		3.9			
	H$_2$O$_2$ plasma	12.5	2.9	29.4	19.1	22.9	5.4	0.9	3.7		3.0		0.3	
	EtO	12.6	2.6	27.1	21.0	25.4	3.3	0.5	3.5	0.3	3.4		0.3	
	E-beam	8.4	2.3	27.7	22.1	25.4	4.6	0.5	4.3	0.3	3.9		0.2	0.4
	No Sterilization	17.5	4.0	27.2	17.7	23.0	3.3	0.5	3.1	0.1	2.9		0.3	0.4
pMPC on Silicon	Autoclave	26.8	6.1	28.6	15.0	16.3	2.6	1.2	1.6	0.2		1.2	0.5	
	Dry Heat	27.9	6.3	32.4	10.8	15.4	3.2	1.4	1.6			0.9	0.1	
	H$_2$O$_2$ plasma	31.2	6.3	33.8	10.3	10.5	4.7	0.8	1.6			0.8		
	EtO	22.6	5.9	30.6	14.8	15.9	3.3	1.2	1.4	0.7		1.6	0.8	1.3
	E-beam	29.8	6.4	31.7	10.4	14.5	3.0	0.8	1.6			1.3	0.5	
	No Sterilization	29.2	5.6	29.5	11.1	17.8	2.2	0.9	1.7	0.1		1.3	0.6	

With PEG-coupled to silicon, the concentration of Si 2p decreased by ~12% and O 1s and C 1s increased by ~3% and ~11%, respectively. High resolution data (Table 4.3) shows the increase in carbon is mainly due to an increase in C-O bonds, which is expected in PEG coatings.[25] After sterilization, a slight decrease in carbon content was observed. Percentage of carbon content ranged between ~11% and ~16% compared to ~18% seen in the unsterilized counterpart. Except for dry heat-treated samples, this decrease in carbon is mainly due to reduced C-O bonds. Overall, for sterilized samples, maximum presence of C-O bonds are found after dry heat treatment, while H$_2$O$_2$ plasma sterilization exhibited the minimum C-O bonds. Nonetheless, percent of C-O bonds are greater in sterilized samples compared to unmodified silicon, indicating presence of some PEG on all sterilized substrates.

Compared to unmodified silicon, control pSBMA-coupled silicon exhibited a sharp decrease in Si 2p concentration (by >40%), and an increase in C 1s content (by >37%). There is also a presence of signature elements, N 1s (~400 eV) and S 2s (~228 eV), as well as Br 3d (~69 eV), indicating successful pSBMA surface modification. High resolution XPS data (Table 4.3) shows a 3.1% NR_3^+ concentration and a 2.9% sulfur concentration, which is a ratio of ~1:1, and matches stoichiometric pSBMA elemental ratio. After sterilization, silicon concentration of these samples slightly decreased. Sterilized samples had Si 2p concentration ranging from ~11% to ~17% compared to the 20% silicon content of the unsterilized pSBMA substrates. However, concentration of C 1s, O 1s, N 1s and S 2s on sterilized pSBMA-silicon surfaces remained comparable or higher than the unsterilized counterparts. It should also be noted that there is a negligible amount of phosphorus contaminant present (<1%) for E-beam sterilized and non-sterilized substrates.

Unsterilized control pMPC-coupled silicon shows a decrease in Si 2p and an increase in C 1s content, as expected. Signature elements for pMPC, phosphorus P 2s (~190 eV) and N 1s, are also present, suggesting successful polymerization of pMPC on the silicon surface. High resolution XPS data (Table 4.3) shows a 1.7% NR_3^+ concentration and a 1.2% phosphorus concentration, yielding a ratio of ~1:1, which is consistent with pMPC stoichiometric ratio. Overall, except for H_2O_2 treatment, sterilization of pMPC-silicon did not result in a large change in elemental composition. With H_2O_2 plasma sterilization, the largest drop in carbon concentration was observed compared to the other sterilization techniques, as well as the lowest level of phosphorus and nitrogen. It should also be noted that the starting concentration of carbon is lower and silicon is higher in pMPC substrates compared to pSBMA substrates, indicating a lower degree of polymerization for starting pMPC than for pSBMA.

4.3.2   Contact Angle
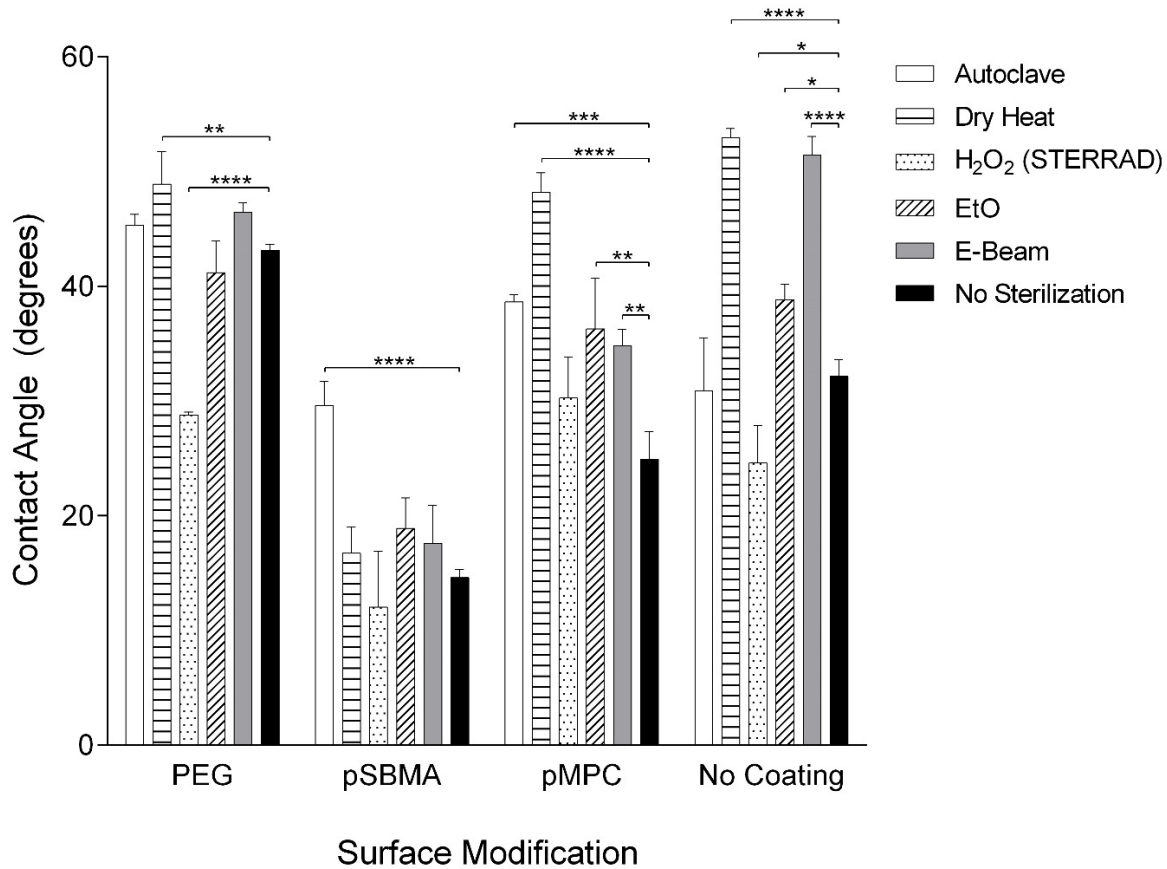
Figure 4.4: *Contact angle measurements before and after sterilization for surface modifications and unmodified silicon. Hydrophilicity—a fundamental property of the surface modification—of PEG was most affected by H_2O_2 plasma, pSBMA by autoclave, and pMPC by dry heat. Level of significance is indicated by the number of asterisks: $p \leq 0.05 = *$; $p \leq 0.01 = **$; $p \leq 0.001 = ***$; $p \leq 0.0001 = ****$.*

Contact angle data are presented in Figure 4.4. The sessile water droplet was stable over 10 seconds. For control unmodified silicon substrate has a contact angle of 32°. With PEG surface modification, the contact angle increased to 43°. Zwitterionic coatings decreased the contact angle to 15° and 25° for pSBMA and pMPC, respectively. The contact angle measurements are all below 90° and demonstrate that all three surface modifications are hydrophilic. However, significant changes in surface wettability are observed with sterilization treatments, especially for uncoated and pMPC-coated substrates. The contact angle for pSBMA-silicon was most

affected by autoclave, increasing by 15°. PEG-silicon was most affected by peroxide treatment, decreasing by 14°.

4.3.3 Ellipsometry
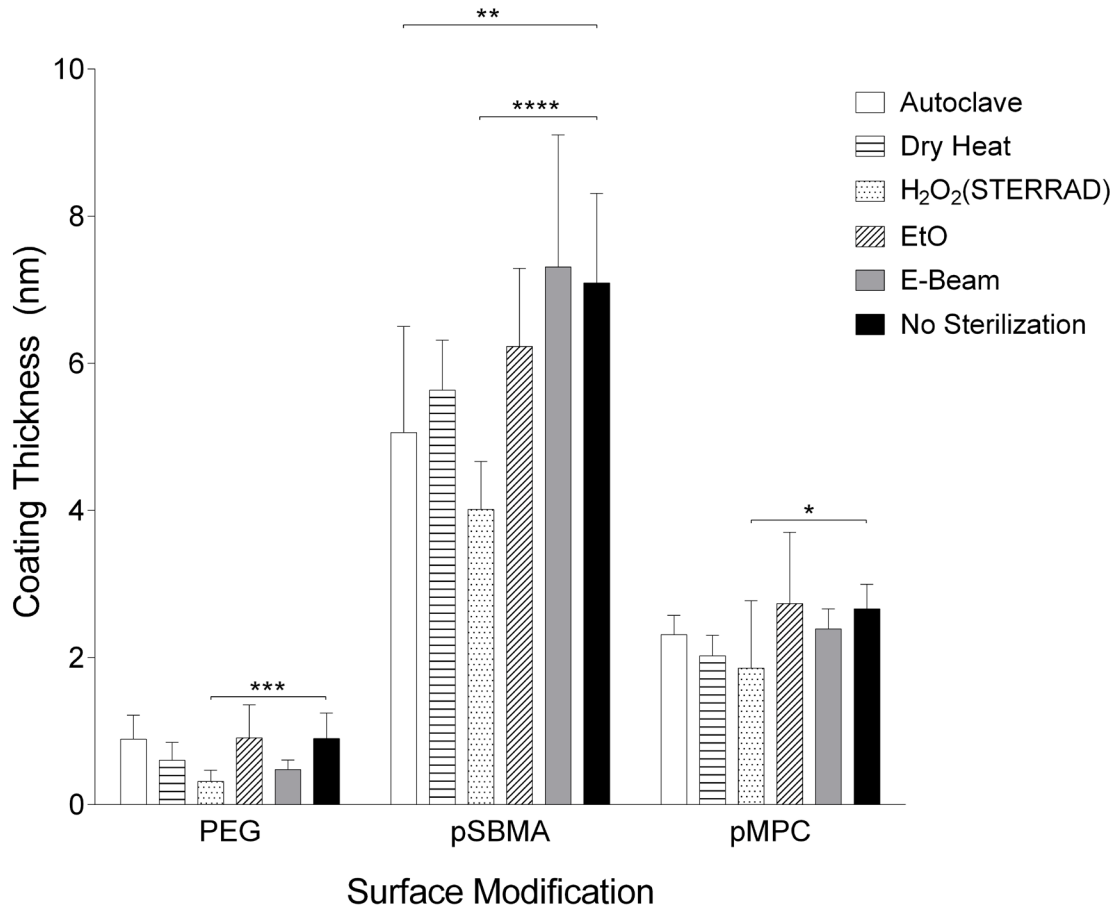
Figure 4.5: *Coating thickness measured by ellipsometry for PEG, pSBMA, and pMPC. Change in coating thickness could be due to chain scission or polymer conformation change. Largest decrease in thickness for all three coatings was due to peroxide treatment. Level of significance is indicated by the number of asterisks: $p \leq 0.05 = *$; $p \leq 0.01 = **$; $p \leq 0.001 = ***$; $p \leq 0.0001 = ****$.*

Surface coating thickness was determined using ellipsometry, and the data is reported in Figure 4.5. The thickness for each of the unsterilized control coatings are 0.9, 7.1 and 2.7 nm for PEG, pSBMA and pMPC, respectively. Sterilization with H_2O_2 plasma led to statistically significant differences for all coatings. Table 4.4 presents the change in thickness relative to the unsterilized

control samples, revealing substantial reduction in coating thickness following several of the sterilization processes tested. Thickness of PEG decreased by >30% when treated with dry heat, peroxide and E-beam irradiation, while pSBMA and pMPC exhibited >20% thickness change with dry heat and peroxide treatment. pSBMA was also greatly affected by steam treatment in the autoclave, decreasing in thickness by 29%.

Table 4.4: Relative change in coating thickness following sterilization treatments. Data is normalized to unsterilized surface modified counterparts.

	PEG	pSBMA	pMPC
Autoclave	-1%	-29%	-13%
Dry Heat	-32%	-21%	-24%
H_2O_2	-64%	-43%	-30%
EtO	1%	-12%	3%
E-beam	-46%	3%	-10%

4.3.4 ELISA

HSA protein adsorption data is shown in Figure 4.6. It illustrates that both unsterilized pSBMA and pMPC coated silicon chips display excellent non-fouling properties, and reduce protein adsorption by 90% and 95%, respectively compared with unmodified silicon. In contrast, PEG-coated chips only yielded a 10% reduction compared to unmodified silicon.

Overall, the sterilization processes tested did not cause a significant change in protein adsorption for unmodified silicon. For the surface-modified silicon, sterilization seemed to adversely affect the coatings as evidenced by increased protein fouling. For PEG on silicon, E-beam radiation caused a significant increase in HSA adsorption compared to its unsterilized counterpart. Dry heat and EtO treatment significantly increased HSA adsorption on pSBMA-silicon. Lastly, all tested sterilization methods caused a significant increase in HSA adsorption for the pMPC-silicon surfaces.
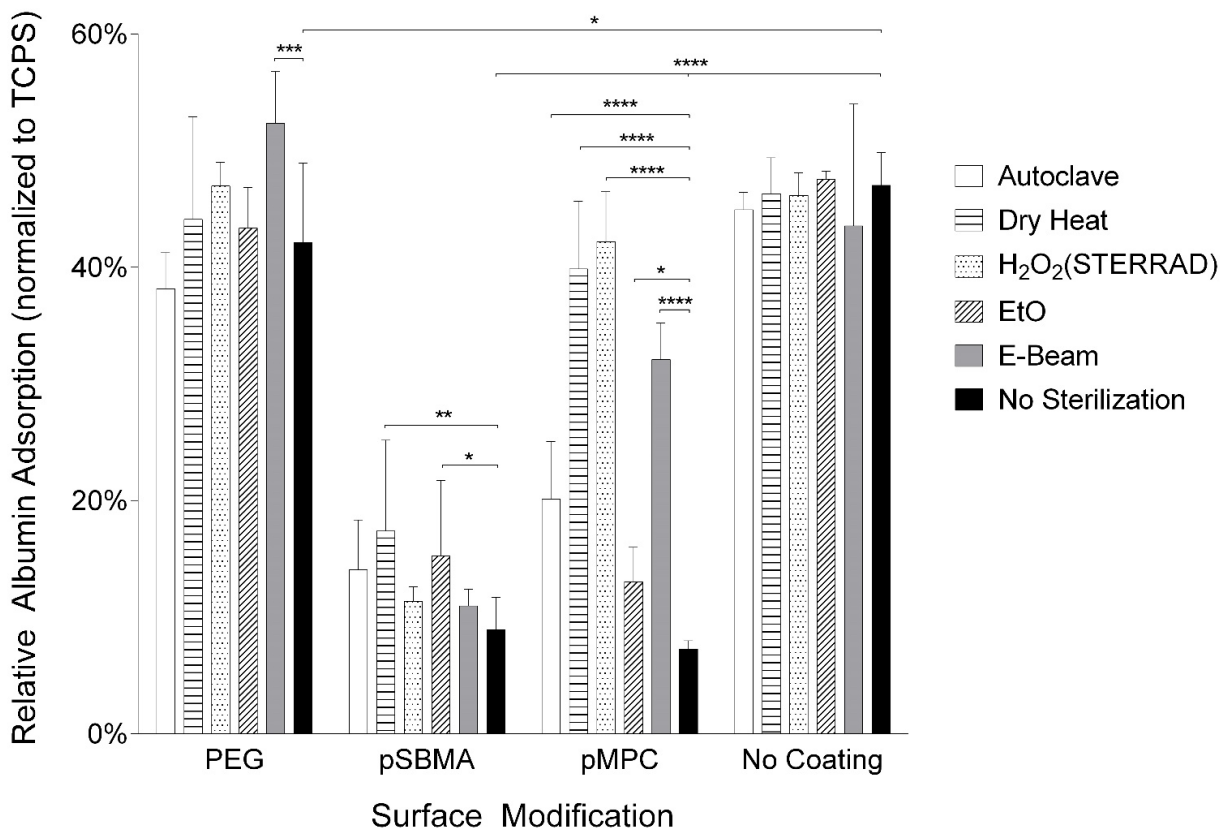
Figure 4.6: *Relative human serum albumin (HSA) adsorption on PEG, pSBMA and pMPC-modified and unmodified silicon surfaces. Data has been normalized to tissue culture polystyrene (TCPS). There is a statistically significant reduction in protein adsorption with surface modification. Following sterilization, protein adsorption generally increases. Level of significance is indicated by the number of asterisks: $p \leq 0.05$ = *; $p \leq 0.01$ = **; $p \leq 0.001$ = ***; $p \leq 0.0001$ = ****.*

4.4 Discussion

For development of implantable medical devices, the effect of sterilization on the device and its surface modifications must be considered. This chapter evaluated the effects of five common sterilization modalities for three ultrathin surface modifications on silicon—PEG, pSBMA and pMPC.[7,9,35] These polymer films are grafted to/from the surface in brush-like structures at less than 10 nm thickness. Zwitterionic polymers, pSBMA and pMPC, have a presence of charged moieties, but are overall charge neutral. Since sterilization processes are harsh treatments that

are destructive to living organisms, it is anticipated that they could adversely affect the chemical and physical characteristics of the polymers and therefore, affect their functionality.

A total of five sterilization techniques were examined and the data is presented in this chapter: Autoclave and dry heat are the two high-temperature sterilization processes tested. For polymers, exposure to high temperature can lead to thermal degradation via oxidation, as well as molecular rearrangement and cross-linking, affecting chemical properties.[38,39] Autoclave is the most widely used sterilization method for medical instruments. However, steam is known to affect the surface energy of many polymers through spontaneous rearrangement, leading to a change in their hydrophilicity.[40]

In contrast, H_2O_2, EtO and E-beam sterilization are all room temperature treatments. Nonetheless, H_2O_2 plasma sterilization is a fairly corrosive process where reactive free radicals bombard the surfaces to kill microbes. Additionally, it has also been shown to modify exposed surfaces, reducing polymer strength, and changing morphology, composition and wettability.[40] Toxic EtO gas sterilization is often used in the medical field for devices that cannot withstand steam, dry heat or irradiation. However, it can leave behind dissolved residues in polymers, requiring long aeration periods post-sterilization.[41] Lastly, E-beam sterilization uses a beam of charged electrons to alter the chemical bonds in biological materials such as DNA strands, leading to chain scission and crosslinking.[42]

Because these sterilization processes denature, crosslink, and degrade chemical structures in living things, they can also bring about significant changes in the properties of polymers, especially ultrathin surface coatings. Therefore, to evaluate alterations in these polymers caused by sterilization, the change in their hydrophilicity, elemental composition, thickness and non-

fouling capacity was measured. Table 4.5 summarizes the effect of sterilization on each surface

modification based on hydrophilicity, coating thickness, and protein resistance.

PEG-silicon: Compared to unsterilized silicon, unsterilized control PEG-silicon only exhibited a

11% reduction in protein adsorption. This is in contrast to previous literature, which has

demonstrated that PEG on silicon can reduce albumin adsorption by 75% compared to uncoated

silicon.[19,43] We examined and confirmed PEG surface modification on silicon via its surface

chemical composition, contact angle, and coating thickness prior to sterilization. However, it

should be noted that PEG chain length and surface grafting density can affect protein resistance,

and the "graft to" method used in this dissertation for PEG surface modification generally yields

poor surface density compared to "graft from" method.[44] Therefore, our low reduction in protein

adsorption could be due to low grafting density.

PEG on silicon was least affected by autoclave and EtO treatments, while dry heat, H_2O_2, and E-

beam treatments affected its properties and protein resistance. Within the PEG subset, dry heat,

H_2O_2, and E-beam treatments caused 32, 64, and 47% decrease in coating thickness,

respectively. Additionally, except for dry heat treatment, all other sterilization processes show a

decrease in C-O bonds via XPS analysis. The adverse effect on physical and chemical surface

properties correlate with ELISA data, which exhibit a corresponding increase in protein

adsorption. H_2O_2 plasma treatment also significantly decreased surface wettability, which may

be indicative of chain scission and ionization of PEG polymers after treatment. Despite having

decreased C-O bonds compared to unsterilized controls, when all metrics are considered, EtO

and autoclave appeared to have minimal effects on PEG coatings.

pSBMA-silicon: Differences in surface elemental composition and coating thickness of pSBMA-

silicon reflect a possible change in pSBMA polymer chain conformation or crosslinking after

sterilization. XPS data shows an increase in carbon and a decrease in silicon following all five

sterilization processes. Increase in nitrogen and sulfur content is also evident, which are the

signature elements of pSBMA. Except in the case of e-beam sterilization, there was a decrease

in coating thickness for the sterilized substrates. While part of the decrease in coating thickness

could be due to chain scission of the polymers, the lower thickness measurements coupled with

the increased pSBMA signature elements measured via XPS demonstrates a compression of the

polymer layer from crosslinking or conformational change. To examine crosslinking in more

detail, polymer swelling behavior may be the subject of a future study. However, these

alterations in polymer layer did not lead to a significant negative impact in protein resistance.

Of the three surface coatings examined, pSBMA had the highest initial coating thickness,

measuring 7.1 nm for the unsterilized control samples. It may be that the relatively higher

polymer chain length allowed conformational and crosslinking changes to occur without

compromising its effectiveness at protein resistance.

E-beam sterilization led to the lowest impact on pSBMA coating, while autoclave, dry heat,

H_2O_2 or EtO treatments exhibited mixed low, moderate and severe impacts on various properties.

When comparing within the subset of sterilized pSBMA samples, XPS showed the lowest carbon

concentration for H_2O_2 plasma treated samples, followed by EtO. H_2O_2 exposure also caused the

lowest contact angle and the greatest change in thickness, a decrease of over 43%, on pSBMA-

silicon substrates. This alteration indicates possible chain scission. However, since the original

polymer coating thickness was greater than the damage caused by these sterilization processes,

the non-fouling property of pSBMA was still preserved.

pMPC-silicon: All five sterilization methods tested adversely affected pMPC-coatings. Aside

from EtO treatment, all sterilization methods resulted in at least 10% change in pMPC coating

thickness, with a maximum change of 30% decrease using H_2O_2 treatment. However, compared to unsterilized samples, XPS results show minor change in carbon concentration. Unlike the pSBMA coating, the starting pMPC chains are shorter (2.7 nm thick for unsterilized substrates) and their resulting lower degree of freedom limits alterations in chain conformation. H_2O_2 treated pMPC samples resulted in significant drop in carbon concentration (31% to 25%), indicating possible chain scission and polymer degradation. Overall, all sterilization methods tested led to substantial increase in contact angle and protein adsorption for pMPC-silicon substrates. However, it is possible that the damage done by sterilization may have been more tolerable with a thicker brush coating. These results indicate that EtO treatment had the least adverse effects on pMPC samples.

Table 4.5: Summarization of the effect of sterilization on hydrophilicity (H), coating thickness (CT), and the protein resistance (PR) of surface modifications.

Surface Modification	Impact	Autoclave			Dry Heat			H_2O_2			EtO			E-beam		
		H	CT	PR	H	CT	PR	H	CT	PR	H	CT	PR	H	CT	PR
PEG	Low	🟢	🟢	🟢	🟢						🟢	🟢	🟢	🟢		
	Moderate						⚪			⚪						
	Severe					🔴		🔴	🔴							🔴	🔴
pSBMA	Low				🟢			🟢		🟢	🟢			🟢	🟢	🟢
	Moderate			⚪								⚪				
	Severe	🔴	🔴			🔴	🔴		🔴				🔴			
pMPC	Low										🟢					
	Moderate		⚪					⚪				⚪			⚪	
	Severe	🔴		🔴	🔴	🔴	🔴		🔴	🔴	🔴			🔴		🔴

4.5 Conclusions

Sterilization treatments can be especially harsh on polymer surface modifications on implantable medical devices. Therefore, this chapter presented data examining the effects of various sterilization processes on thin-film polymeric brushes on silicon. Results show H_2O_2 plasma

treatment adversely affected all three polymer coatings. In contrast, autoclave and EtO treatment appear to be well suited to PEG, E-beam sterilization to pSBMA, and EtO treatment for pMPC coatings. These findings will be useful for any silicon medical devices that utilizes ultrathin zwitterionic or PEG coatings for their applications.

As the use of novel polymers and functional surfaces become more prevalent in medical devices, effect of sterilization treatment on them must be carefully assessed. Our results illustrate that these effects are unique to the various surface coating chemical and physical properties.

4.6 References

1. Cheung KC, Renaud P. BioMEMS for medicine: On-chip cell characterization and implantable microelectrodes. *Solid State Electron*. 2006;50(4):551-557. doi:10.1016/j.sse.2006.03.023.

2. Shawgo RS, Grayson ACR, Li Y, Cima MJ. BioMEMS for drug delivery. *Curr Opin Solid State Mater Sci*. 2002;6(4):329-334. doi:10.1016/S1359-0286(02)00032-3.

3. Desai T, Sharma S, Walczak R, et al. Nanoporous Implants for Controlled Drug Delivery. *Ther Micro/Nano Technol - BioMEMS Biomed Nanotechnol*. 2007:263-286. doi:10.1007/978-0-387-25844-7_15.

4. Desai T a., Hansford DJ, Ferrari M. Micromachined interfaces: New approaches in cell immunoisolation and biomolecular separation. *Biomol Eng*. 2000;17:23-36. doi:10.1016/S1389-0344(00)00063-0.

5. Smith C, Kirk R, West T, et al. Diffusion characteristics of microfabricated silicon nanopore membranes as immunoisolation membranes for use in cellular therapeutics. *Diabetes Technol Ther*. 2005;7(1):151-162. doi:10.1089/dia.2005.7.151.

6. Desai T a., Hansford D, Ferrari M. Characterization of micromachined silicon membranes for immunoisolation and bioseparation applications. *J Memb Sci*. 1999;159:221-231. doi:10.1016/S0376-7388(99)00062-9.

7. Song S, Faleo G, Yeung R, et al. Silicon nanopore membrane (SNM) for islet encapsulation and immunoisolation under convective transport. *Sci Rep*. 2016;6(January):23679. doi:10.1038/srep23679.

8. Song S, Blaha C, Moses W, et al. An intravascular bioartificial pancreas device (iBAP) with silicon nanopore membranes (SNM) for islet encapsulation under convective mass

transport. *Lab Chip*. 2017. doi:10.1039/C7LC00096K.

9.   Roy S, Dubnisheva A, Eldridge A, et al. Silicon nanopore membrane technology for an implantable artificial kidney. *TRANSDUCERS 2009 - 15th Int Conf Solid-State Sensors, Actuators Microsystems*. 2009:755-760. doi:10.1109/SENSOR.2009.5285603.

10.   Striemer CC, Gaborski TR, McGrath JL, Fauchet PM. Charge- and size-based separation of macromolecules using ultrathin silicon membranes. *Nature*. 2007;445(February):749-753. doi:10.1038/nature05532.

11.   Rutala WA, Weber DJ. Guideline for Disinfection and Sterilization in Healthcare Facilities, 2008. *Clin Infect Dis*. 2008:1-158. doi:10.1086/423182.

12.   Fissell WH, Roy S. The implantable artificial kidney. *Semin Dial*. 2009;22(6):665-670. doi:10.1111/j.1525-139X.2009.00662.x.

13.   Kim S, Feinberg B, Kant R, et al. Diffusive silicon nanopore membranes for hemodialysis applications. *PLoS One*. 2016;11(7):1-20. doi:10.1371/journal.pone.0159526.

14.   Muthusubramaniam L, Lowe R, Fissell WH, et al. Hemocompatibility of silicon-based substrates for biomedical implant applications. *Ann Biomed Eng*. 2011;39(4):1296-1305. doi:10.1007/s10439-011-0256-y.

15.   Nakabayashi N, Williams DF. Preparation of non-thrombogenic materials using 2-methacryloyloxyethyl phosphorylcholine. *Biomaterials*. 2003;24:2431-2435. doi:10.1016/S0142-9612(03)00113-3.

16.   Fissell WH, Dubnisheva A, Eldridge AN, Fleischman AJ, Zydney AL, Roy S. High-performance silicon nanopore hemofiltration membranes. *J Memb Sci*. 2009;326:58-63. doi:10.1016/j.memsci.2008.09.039.

17.   Melvin ME, Fissell WH, Roy S, Brown DL. Silicon induces minimal

thromboinflammatory response during 28-day intravascular implant testing. *ASAIO J.* 2010;56(4):344-348. doi:10.1097/MAT.0b013e3181d98cf8.

18. Popat KC, Desai T a. Poly(ethylene glycol) interfaces: An approach for enhanced performance of microfluidic systems. *Biosens Bioelectron*. 2004;19:1037-1044. doi:10.1016/j.bios.2003.10.007.

19. Zhang M, Desai T, Ferrari M. Proteins and cells on PEG immobilized silicon surfaces. *Biomaterials*. 1998;19:953-960. doi:10.1016/S0142-9612(98)00026-X.

20. Li J, Tan D, Zhang X, et al. Preparation and characterization of nonfouling polymer brushes on poly(ethylene terephthalate) film surfaces. *Colloids Surf B Biointerfaces*. 2010;78(2):343-350. doi:10.1016/j.colsurfb.2010.03.027.

21. Hanein Y, Pan YV, Ratner BD, Boèhringer KF, Denton DD. Micromachining of non-fouling coatings for bio - MEMS applications. 2001;81:2001.

22. Ma H, Hyun J, Stiller P, Chilkoti A. "Non-Fouling" Oligo(ethylene glycol)-Functionalized Polymer Brushes Synthesized by Surface-Initiated Atom Transfer Radical Polymerization. *Adv Mater*. 2004;16(4):338-341. doi:10.1002/adma.200305830.

23. Zhu X, Loo HE, Bai R. A novel membrane showing both hydrophilic and oleophobic surface properties and its non-fouling performances for potential water treatment applications. *J Memb Sci*. 2013;436:47-56. doi:10.1016/j.memsci.2013.02.019.

24. Wagner VE, Koberstein JT, Bryers JD. Protein and bacterial fouling characteristics of peptide and antibody decorated surfaces of PEG-poly(acrylic acid) co-polymers. *Biomaterials*. 2004;25(12):2247-2263. doi:10.1016/j.biomaterials.2003.09.020.

25. Sharma S, Johnson RW, Desai T a. XPS and AFM analysis of antifouling PEG interfaces for microfabricated silicon biosensors. *Biosens Bioelectron*. 2004;20(2):227-239.

doi:10.1016/j.bios.2004.01.034.

26.   Zhang Z, Zhang M, Chen S, Horbett T a., Ratner BD, Jiang S. Blood compatibility of surfaces with superlow protein adsorption. *Biomaterials*. 2008;29:4285-4291. doi:10.1016/j.biomaterials.2008.07.039.

27.   Zhang Z, Chao T, Chen S, Jiang S. Superlow fouling sulfobetaine and carboxybetaine polymers on glass slides. *Langmuir*. 2006;22(12):10072-10077. doi:10.1021/la062175d.

28.   Chen S, Liu L, Jiang S. Strong resistance of oligo(phosphorylcholine) self-assembled monolayers to protein adsorption. *Langmuir*. 2006;22(6):2418-2421. doi:10.1021/la052851w.

29.   Zhang Z, Chao T, Liu L, Cheng G, Ratner BD, Jiang S. Zwitterionic hydrogels: an in vivo implantation study. *J Biomater Sci Polym Ed*. 2009;20(13):1845-1859. doi:10.1163/156856208X386444.

30.   Smith RS, Zhang Z, Bouchard M, et al. Vascular catheters with a nonleaching poly-sulfobetaine surface modification reduce thrombus formation and microbial attachment. *Sci Transl Med*. 2012;4(153):153ra132. doi:10.1126/scitranslmed.3004120.

31.   Kotzar G, Freas M, Abel P, et al. Evaluation of MEMS materials of construction for implantable medical devices. *Biomaterials*. 2002;23(13):2737-2750. http://www.ncbi.nlm.nih.gov/pubmed/12059024.

32.   Brétagnol F, Rauscher H, Hasiwa M, et al. The effect of sterilization processes on the bioadhesive properties and surface chemistry of a plasma-polymerized polyethylene glycol film: XPS characterization and L929 cell proliferation tests. *Acta Biomater*. 2008;4(6):1745-1751. doi:10.1016/j.actbio.2008.06.013.

33.   Kyomoto M, Moro T, Miyaji F, et al. Enhanced Wear Resistance of Orthopaedic Bearing

Due to the Cross-Linking of Poly(MPC) Graft Chains Induced by Gamma-Ray Irradiation. *J Biomed Mater Res B Appl Biomater*. 2007;84B:320-327. doi:10.1002/jbmb.

34.   Kanjickal D, Lopina S, Evancho-Chapman MM, Schmidt S, Donovan D. Effects of sterilization on poly(ethylene glycol) hydrogels. *J Biomed Mater Res - Part A*. 2008;87(3):608-617. doi:10.1002/jbm.a.31811.

35.   Li L, Marchant RE, Dubnisheva A, Roy S, Fissell WH. Anti-biofouling Sulfobetaine Polymer Thin Films on Silicon and Silicon Nanopore Membranes. *J Biomater Sci Polym Ed*. 2011;22:91-106. doi:10.1163/092050609X12578498982998.

36.   Centers for Disease Control and Prevention-Guidelines for Disinfection and Sterilization in Healthcare Facilities (Other Sterilization Methods). https://www.cdc.gov/infectioncontrol/guidelines/disinfection/sterilization/other-methods.html. Published 2016. Accessed May 6, 2017.

37.   Huang Y, Lü X, Qian W, Tang Z, Zhong Y. Competitive protein adsorption on biomaterial surface studied with reflectometric interference spectroscopy. *Acta Biomater*. 2010;6(6):2083-2090. doi:10.1016/j.actbio.2009.12.035.

38.   Krzysztof P, James N. *Thermal Degradation of Polymeric Materials*. 1st ed. Shawbury, UK: iSmithers Rapra Publishing; 2005.

39.   Han S, Kim C, Kwon D. Thermal/oxidative degradation and stabilization of polyethylene glycol. *Polymer (Guildf)*. 1997;38(2):317-323. doi:10.1016/S0032-3861(97)88175-X.

40.   Kubyshkina G, Zupančič B, Štukelj M, Grošelj D, Marion L, Emri I. The influence of different sterilization techniques on the time-dependent behavior of polyamides.". *J Biomater Nanobiotechnol*. 2011;2(4):361-368. doi:10.4236/jbnb.2011.24045.

41.   Gilding DK, Reed AM, Baskett SA. Ethylene oxide sterilization: effect of polymer

structure and sterilization conditions on residue levels. *Biomaterials*. 1980;1(3):145-148. doi:10.1016/0142-9612(80)90037-X.

42. Silindir M, Özer AY. Sterilization methods and the comparison of E-beam sterilization with gamma radiation sterilization. *Fabad J Pharm Sci*. 2009;34(1):43-53.

43. Zhang M, Ferrari M. Hemocompatible polyethylene glycol films on silicon. *Biomed Microdevices*. 1998. http://www.springerlink.com/index/H6K15PK44618078T.pdf.

44. Yeh P-Y, Kizhakkedathu JN, Chiao M. A Novel Method to Attenuate Protein Adsorption Using Combinations of Polyethylene Glycol (PEG) Grafts and Piezoelectric Actuation. *J Nanotechnol Eng Med*. 2010;1(November 2010):41010. doi:10.1115/1.4002532.

Hemocompatible Ultrathin Film Surface Modifications on Silicon: Study *In Vitro*

5.1 Introduction
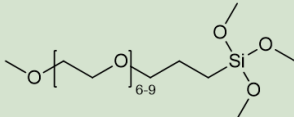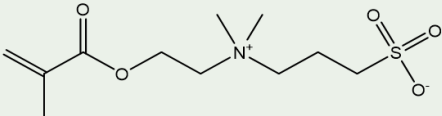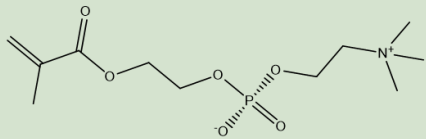
Due to the precision and versatility of micro- and nanoscale features it offers, silicon has become a common substrate material for novel biomedical devices. Many of these devices are often in direct contact with blood, such as neuroelectrodes,[1,2] drug delivery systems,[3–5] biosensors and diagnostic devices,[6–8] and artificial organs.[9–12] To advance the area of bioartificial organs, our lab has developed silicon nanopore membranes (SNMs) for blood filtration in renal replacement[9,13,14] and immunoisolation in islet therapy. [11,15] SNMs are highly uniform and low resistance membranes with controllable pore size on the order of ~10 nm and variation of <1% across the wafer.[9] Because their applications require SNMs to come in direct contact with blood flow, hemocompatibility and non-fouling properties are essential. While silicon has been shown to be non-cytotoxic, non-leaching and non-irritant,[16–18] the surfaces must also be non-activating and non-fouling for implant applications.

To improve hemocompatibility of a substrate, the surface is often modified.[19] Specifically, hydrophilic, polymeric brush structures on the surface have shown enhanced hemocompatibility. One such coating is polyethylene glycol and oligoethylene glycol (PEG and OEG, respectively), which has demonstrated excellent resistance to protein adsorption and platelet adhesion.[20,21] Our

previous research shows PEG-modified silicon significantly reduced thrombus formation and inflammation following 4-week implantation in rat veins.[22]

Another group of hydrophilic polymer brush surface modifications is zwitterionic coatings. Using a methacrylate backbone, polymer brushes and hydrogels are built to a desired thickness with atom-transfer radical polymerization (ATRP).[23–25] These biomimetic zwitterions, such as sulfobetaine, carboxybetaine and phosphorylcholine, coordinate water molecules through hydrogen bonding and electrostatic interactions.[24,26] This hydration layer allows the coating to resist protein fouling[27–31] and thrombus formation.[23,26,32]

Table 5.1: *Chemical structure of PEG-silane, SBMA and MPC monomer.*

1, 2-[methoxy(polyethyleneoxy)propyl]trimethoxysilane (PEG-silane)	
2-(methacryloyloxy)ethyl]dimethyl-(3-sulfopropyl)ammonium hydroxide, sulfobetaine methacrylate (SBMA)	
2-methacryloyloxyethyl phosphorylcholine (MPC)	

To apply coatings on SNMs, several requirements must be met: in addition to being non-activating and non-fouling, the coatings must also be hydrophilic and sub-5 nm for pore patency. For this purpose, we have chosen to explore three different coatings presented in Table 5.1: PEG, zwitterionic poly(sulfobetaine methacrylate) (pSBMA), and poly(2-methacryloyloxyethyl phosphorylcholine) (pMPC). Zwitterionic surface coatings are relatively new, and sub-5 nm

thick pSBMA and pMPC need to be further characterized under physiological conditions. Since SNMs will be ultimately implanted, animal testing for compatibility and functionality is required. However, before delving into expensive animal testing, we conducted a series of *in vitro* experiments to narrow down our coating choices. Aside from the benefit of testing a variety of materials and conditions at lower cost, *in vitro* testing also allows for testing against fresh human blood. Examining surface chemistry compatibility against fresh human blood is critical because reactions to blood may vary from one species to another.[33]

In this chapter, we explore the hemocompatibility of PEG, pSBMA, and pMPC *in vitro*. Protein fouling from single protein solutions of fibrinogen and albumin was first tested as was done in previous literature.[29,34–36] However, where further *in vitro* testing of biomaterials and their blood interaction are concerned, it is difficult to utilize a standardized platform. Often, experiments are conducted with blood components, such as platelet rich plasma[37] or platelet poor plasma,[35] rather than whole blood. In some cases, static blood incubation[30,38] is used while others use perfusion platforms, such as modified Chandler's loop.[39–42] In perfusion experiments, there are many variable that can be set: flow rates, shear rates, presence of reservoir, time of material contact, time of experimental run, type and amount of anticoagulants used, type of pump and etc. Here, we conducted some preliminary static tests against standard materials such as polytetrafluoroethylene (PTFE) and titanium. However, to better mimic the final conditions, *in vitro* flow experiments were also run in implant housing, as well as an in-house designed polyether ether ketone (PEEK) flow cell designed specifically for *in vitro* studies. Following blood flow experiments, the surfaces were examined with scanning electron microscopy (SEM) and fluorescence microscopy for cellular and platelet adhesion and activation.

5.2 Materials and Methods

5.2.1 Sample Preparation

Double side polished, 400 µm thick, p-type silicon wafers were obtained from Ultrasil Corporation (Hayward, CA, USA) and diced into 1 cm^2 chips and 1 by 6.5 cm^2 long chips. The chips were cleaned by "piranha," a solution of 3:1 ratio of sulfuric acid (96%) to hydrogen peroxide (30%) for 20 min. The chips were then rinsed with reverse osmosis purified water (RO water) at 5-minute intervals (3X). Afterwards, they were exposed to hydrofluoric acid for 5 min to remove the layer of silicon dioxide that spontaneously forms on silicon surfaces exposed to atmospheric oxygen.   The chips were again rinsed with RO water at 5-min intervals (3X), followed by activation of the surface via a final piranha treatment and RO water rinse, as described above. The silicon chips were then dried under a stream of nitrogen gas and allowed to completely dry on a hotplate at 110 °C for 1 hour.

5.2.2 Surface Modification

5.2.2.1 PEG Surface Modification

Silicon surfaces were modified with PEG as previously described.[10,11] Briefly, 2-[methoxy(polyethyleneoxy)propyl]trimethoxysilane (PEG-silane) was purchased from Gelest, Inc. (Morrisville, PA, USA) and covalently bonded to silicon by immersing the substrates in a solution of 285 µl PEG-silane in 25 mL of toluene for 2 hours at 70 °C. The substrates were then rinsed three times at 10 min intervals with toluene, ethanol, and water, respectively, to remove excess PEG, and stored dry under ambient condition until use.

5.2.2.2 Zwitterionic Surface Modification

All chemicals were purchased from Sigma-Aldrich (St. Louis, MO, USA), unless stated otherwise. Zwitterionic surface modifications were conducted as described previously.[35] Briefly, a surface initiator, 2-bromo-2-methyl-N-3[(trimethoxysilyl)propyl]-propanamide (BrTMOS), was synthesized.[35] The substrates were placed in a 1% (v/v) BrTMOS solution in bicyclohexyl for 2 hours. The surfaces were then rinsed with chloroform, ethanol, and water, respectively, to remove excess BrTMOS.

Zwitterionic monomers, 2-(methacryloyloxy)ethyl]dimethyl-(3-sulfopropyl)ammonium hydroxide (SBMA), and 2-methacryloyloxyethyl phosphorylcholine (MPC), are shown in Table 5.1. A degassed solution of 468 mg (3 mmol) of 2,2'-bipyridyl ($\geq$98%) and individual monomers—SBMA: 1.06g (3.8 mmol), and MPC: 506 mg (1.9 mmol)—and 22.3 mg (0.1 mmol) of copper (II) bromide (99%) was prepared in 5:5 mL of methanol:water. This mixture was added to a reaction chamber housing four substrates and 143 mg (1 mmol) of copper (I) bromide (99.999%) under nitrogen protection, and polymerization was allowed to run for 15 min and 7 min for pSBMA and pMPC, respectively. The substrates were then rinsed with chloroform, ethanol, Dulbecco's phosphate buffered saline (D-PBS, UCSF Cell Culture Facility, San Francisco, CA, USA), and water respectively, and dried using a stream of nitrogen gas.

5.2.3 In Vitro *Protein Adsorption via Enzyme-Linked Immunosorbent Assay (ELISA)*

Protein adsorption on the surfaces of the substrates was determined by conducting enzyme-linked immunosorbent assay (ELISA) following protocol published previously.[35] Substrates were placed in 24-well tissue-culture polystyrene (TCPS) plates and incubated with D-PBS for 1.5 hours. D-PBS was replaced with 0.5 mL of single protein solution: 1 mg/mL concentration

of human fibrinogen (Sigma-Aldrich) or human albumin (Abcam, Cambridge, MA, USA) was added and allowed to incubate at 37 °C for 1.5 hours. All substrates were rinsed five times with D-PBS. Surfaces were then blocked using bovine serum albumin (BSA, ≥98%, Sigma-Aldrich) using 1 mg/mL BSA solution for 1.5 hours. The substrates were rinsed five times with D-PBS, and transferred to a new 24-well TCPS well. Next, the samples were incubated with 10 μg/mL anti-human proteins conjugated with horseradish peroxidase (HRP) for 1.5 hours: anti-human fibrinogen (coagulation factor I) (HRP) (USBiological, Salem, MA, USA) for fibrinogen ELISA and anti-human serum albumin antibody-HRP (Abcam) for albumin ELISA. The substrates were washed with D-PBS five times and transferred to a new well. A reaction mixture was made in 0.05 M citrate phosphate buffer (pH 5.0, Sigma-Aldrich) with 0.5 mg/mL of o-phenylenediamine (OPD, VWR Inc. Visalia, CA, USA) and 0.03% hydrogen peroxide. The reaction mixture (0.5 mL) was added to each well, and the reaction was allowed to run at 37 °C for 20 minutes. The reaction was stopped by adding 0.5 mL sulfuric acid (1 M). The solution was transferred to 96-well plates and light absorbance at 490 nm was determined using a microplate reader. A minimum of 3 substrates were analyzed for each sample set and light absorbance reading was normalized to TCPS control.

5.2.4 Blood Collection

Informed consent was obtained prior to blood collection and experiments in all cases. For static experiments, fresh blood was collected from a volunteer end stage renal disease patient (male, 37, on aspirin). Blood was collected into 8.5 mL BD Vacutainers with acid citrate dextrose (solution A, trisodium citrate 22g/L, citric acid 8g/L, and dextrose 24.5 g/L) (Thermo Fisher Scientific, Waltham, MA, USA).

For blood flow experiments, fresh blood was collected from a healthy human donor (male, 31) into 10 ml BD Vacutainers with 15.8 USP/mL lithium heparin (Thermo Fisher Scientific, Waltham, MA, USA). Initial 2 mL of blood collected was discarded to minimize blood activation from effect of blood collection process. Blood was stored on ice for approximately 15 min until use in experiments.

5.2.5 Fresh Blood Experiments Under Static Conditions

Samples were placed in 24-well polypropylene plates, and rinsed 3 times with D-PBS. After the final rinse, D-PBS was fully removed, and 1 mL of fresh human blood was added to each well, as shown in Figure 5.1. The samples were incubated with gentle shaking at 37 °C, with 5%
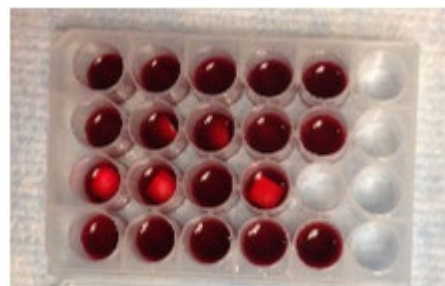
Figure 5.1: *Static blood experiment setup.*

CO_2. After 2 hours, the samples were removed and rinsed 3 times with D-PBS, and preserved for imaging.

5.2.6 Fresh Blood Experiments Under Flow Conditions

5.2.6.1 Blood Flow Experiments with Titanium Implant Device

The experimental setup of the blood flow experiments conducted using titanium implant device is shown in figure 2. The titanium housing consists of three 1 mm high blood channels. The fully assembled device is shown in Figure 5.2(b), while 5.2(c) and (d) shows the experimental setup. Two devices were run in parallel: device 1 contained only uncoated silicon chips, while device 2 contained only pSBMA-modified chips. Blood was circulated at a rate of 20 mL/min using a peristaltic pump for two hours. This flow rate results in a wall shear rate of 73.3/s. Given the space constraints, devices were incubated at 37 °C while the pump was housed

immediately next to the incubator. Approximately 50 cm of Masterflex, Tygon E-LFL L/S 14

Tubing (1.6 mm inner diameter tubing from Cole-Parmer, Vernon Hills, IL, USA) was used to

connect the inlet and outlet of the blood flow platform. After two hours, the blood was removed,

and D-PBS was circulated through the device until no trace of blood was visible (~200 mL of D-

PBS per device). Then, the devices were disassembled, and the chips removed and preserved for

imaging.
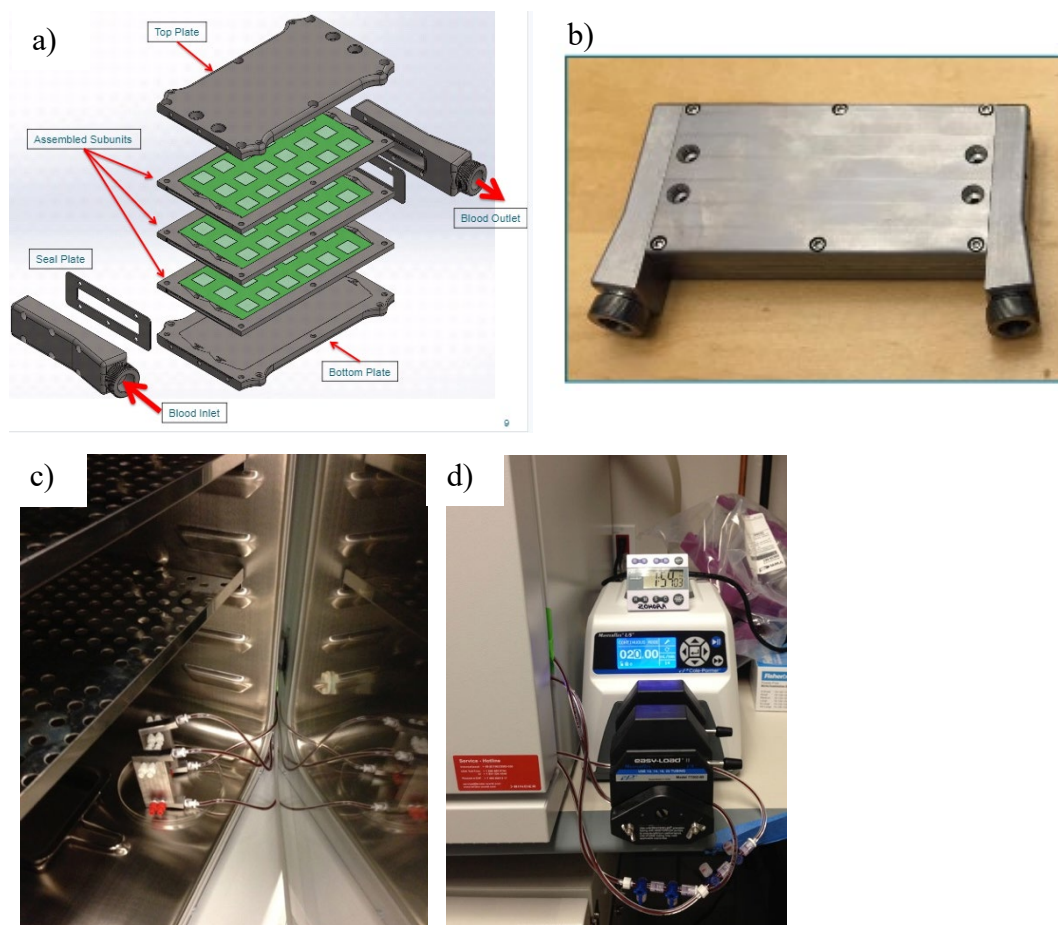
Figure 5.2: *a) exploded view of titanium implant device for blood flow experiment (b) titanium implant devcie, (c) and (d) experimental setup: titanium implant device was incubated at 37 °C and a peristaltic pump outside incubatro was used to circulate blood for 2 hours.*

5.2.6.2 Blood Flow Experiments with PEEK Housing

An *in vitro* blood flow platform was designed and fabricated out of PEEK as shown in Figure 5.3(a) and (b). Blood enters through the top PEEK piece inlet and flow is allowed to develop guided by 500 μm thick silicone gasket 1. Developed blood flow enters through the slit in middle PEEK piece, and the test substrate is exposed to the blood flow. Blood then leaves out the slit in middle PEEK piece and out the outlet of the top PEEK piece. The blood flow channel over the test substrate has a height of 200 μm. As shown in Figure 5.3(c), a peristaltic pump drives the blood flow at a rate of 4 mL/min, yielding a shear rate of 1000/s. To avoid stagnant blood, no reservoir was used. Rather, 100 cm of Tygon E-LFL L/S 14 tubing was used to connect the inlet and outlet of the blood flow platform. Prior to blood experiment, the tubing and experimental setup was circulated with D-PBS containing 50 USP/mL heparin for 30 minutes. The setup was then washed out with D-PBS and circulated with D-PBS for 30 minutes to remove residual heparin. The blood flow experiment was then conducted in a 37 °C, 5% CO_2 incubator for 2 hours.

After 2 hours, the blood was collected for activation assessment using flow cytometry. The setup was run with D-PBS until no trace of blood was detected in the tubing. The *in vitro* flow cells were then taken apart, and the blood channels were analyzed for gross clots. The 1 by 6.5 cm^2 substrates were rinsed 3 times with D-PBS and broken into ~1 cm pieces for surface analysis for cellular adhesion using scanning electron microscopy (SEM) and platelet adhesion and activation using immunohistochemistry (IHC).
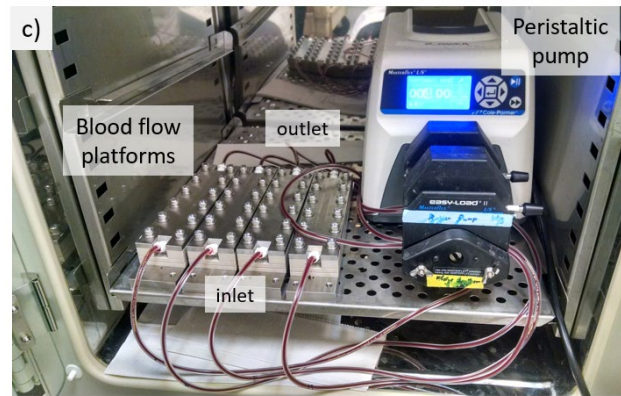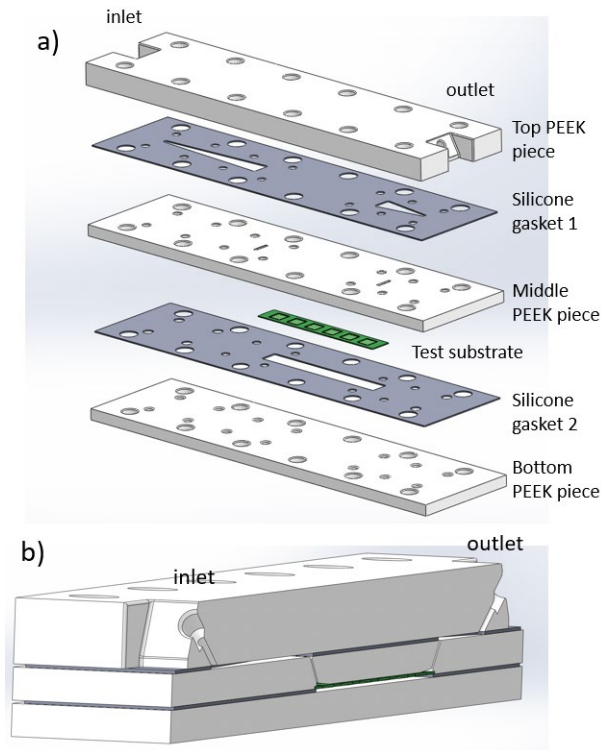
Figure 5.3: in vitro *blood flow platform a) exploded view, showing the top PEEK piece containing the inlet and outlet, silicone gasket 1, developing uniform blood flow and directing the blood flow through the slits in middle PEEK piece. Substrate surface is exposed to laminar blood flow with a channel height of 200 μm, and blood is directed out of the slit in middle PEEK piece and out the outlet on top PEEK piece. Silicone gasket 2 and bottom PEEK piece supports the substrate. b) cross section showing blood flow path through device. c) setup of 2-hour fresh human blood flow study in a 37° C incubator.*

5.2.5 Post-Analysis Following Blood Experiments

5.2.5.1 Scanning Electron Microscopy (SEM)

Cellular adhesion was visualized using SEM. Samples were fixed by incubation in a solution of 3% glutaraldehyde (Sigma-Aldrich), 0.1 M sodium cacodylate (VWR) and 0.1 M sucrose (Sigma-Aldrich) for 48 hours. Afterwards, the substrates were removed, washed two times with deionized water, and dehydrated in the following ethanol/water (v/v) solutions for 10 min in each: 35%, 50%, 70%, 95% and two times in 100%. Samples were allowed dry overnight and mounted on aluminum stubs for imaging using a Carl Zeiss Ultra 55 Field Emission Scanning Electron Microscope (Zeiss, Dublin, CA, USA). Prior to imaging, samples were sputter coated with gold-palladium.

5.2.5.2 Immunohistochemistry (IHC)

Immunohistochemistry (IHC) was used to image platelet adhesion and activation on the substrates. Samples were fixed with 4% paraformaldehyde (Thermo Fisher Scientific) at room temperature for 30 minutes and allowed to remain in 1% paraformaldehyde at 4 °C until they were imaged (~1 week). Before imaging, the samples were marked for human platelets and platelet activation using FITC-labeled anti-CD41 (Bioss Inc., Woburn, MA, USA)) and Cy3-labeled anti-CD62p (Bioss Inc.) markers, respectively. Samples were rinsed 3 times in D-PBS, and imaged using Nikon TI-E Microscope (Nikon Instruments, Melville, NY, USA). Imaging was conducted at 100x, in at least 5 separate representative locations per chip, and at least three different chips per sample group. A representative image per sample is reported. For *in vitro* flow experiments using PEEK flow cells, IHC images were quantified using ImageJ software (National Institutes of Health). To process an image, the threshold was first set, and the image were converted to binary format. Next, the area covered by platelets was calculated. This area was normalized by the average area taken by individual platelets in order to obtain a platelet count. Quantified data presented is averaged over approximately 20 different locations per sample.

5.2.5.3 Flow Cytometry

Platelet activation in blood was analyzed by flow cytometry. Positive and negative controls were prepared to realize maximum and minimum platelet activation. Positive control was produced by activating blood using thrombin receptor activating peptide (TRAP) following blood collection. Blood was activated for 20 min at room temperature without agitation with 200 μmol/L TRAP final blood concentration. The reaction was stopped with ice-cold paraformaldehyde (PFA), at a final concentration of 0.5% in the blood samples. The samples

were stored on ice for 20 min for the PFA to take effect. For negative control, samples were kept at room temperature for 20 min after blood collection without agitation and without activation. Ice-cold PFA was added to a final concentration of 0.5%, and the samples were placed on ice for 20 minutes before labeling with antibodies.

For each experimental sample, after 2-hour blood flow in PEEK flow cells, ~1-2 mL of blood was collected from each circuit. Aliquots of 100 µl of blood was set aside for antibody labeling. Further activation was stopped by adding ice-cold PFA to a final concentration of 0.5%. Samples were placed on ice for 20 minutes before labeling with antibodies.

Monoclonal anti-CD41-FITC specific to human was used for a platelet marker, and monoclonal anti-CD62P-APC specific to human was used as a platelet activation marker. Both antibodies were purchased from Sigma-Aldrich. The reaction was allowed to occur at 37 °C protected from light for 30 minutes, and stopped by adding 3 mL of cold 1% PFA. All samples were stored at 4 °C and cytometry was conducted within 6 hours of sample preparation.

Cytometry was conducted using BD FACSAria IIu (BD Biosciences, San Jose, CA, USA), and BD FACSDiva Software was utilized in order to collect data. Data analysis was conducted using FlowJo software (Ashland, OR, USA).

5.3 Results

5.3.1 In Vitro *Protein Adsorption via Enzyme-Linked Immunosorbent Assay (ELISA)*

Preliminary protein fouling experiments from single protein solutions was assessed. All data has been normalized to TCPS. As shown in Figure 5.4, both human serum albumin (HSA) and human fibrinogen adsorption data showed similar trend: silicon adsorbed ~37-38% of TCPS, while PEG, pSBMA and pMPC reduced protein adsorption by at least 50% compared to

159

unmodified silicon. pSBMA had the least protein adsorption, reducing protein adsorption by
>80% compared to unmodified silicon.
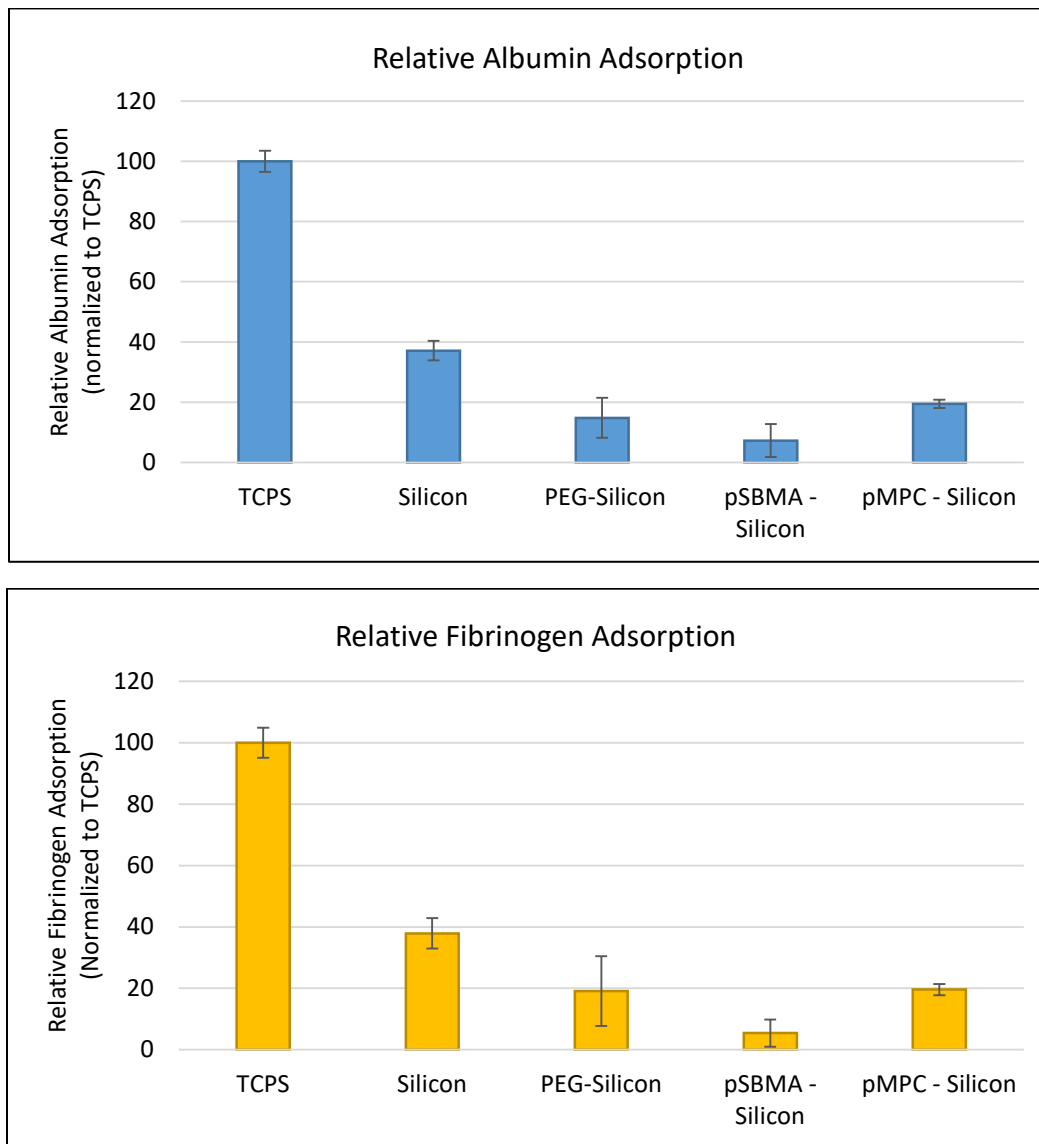
Figure 5.4: *(a) human serum albumin (b) human fibrinogen adsorption from single protein solution. All data is normalized to tissue culture polystyrene (TCPS).*

5.3.2 Fresh Blood Experiments Under Static Conditions

Following 2-hour incubation with fresh human blood, samples were analyzed for fibrinogen

adsorption. The adsorption data, normalized to unmodified silicon and presented in Figure 5.5,

demonstrates that PEG-coupled silicon had approximately the same level of protein adsorption as

unmodified silicon, while pSBMA-coupled silicon reduced adsorption by >50%. Titanium and

pSBMA-silicon performed similarly, while polytetrafluoroethylene (PTFE) had the highest

adsorption.

Samples were also analyzed for cellular adhesion using SEM. Figure 5.6 shows there was a

significant amount of leukocyte adhesion on PTFE, while titanium, PEG- and pSBMA-coated

silicon had significantly lower amount of blood cell adhesion. Some leukocyte spreading was

evident on PEG-silicon and titanium surfaces.
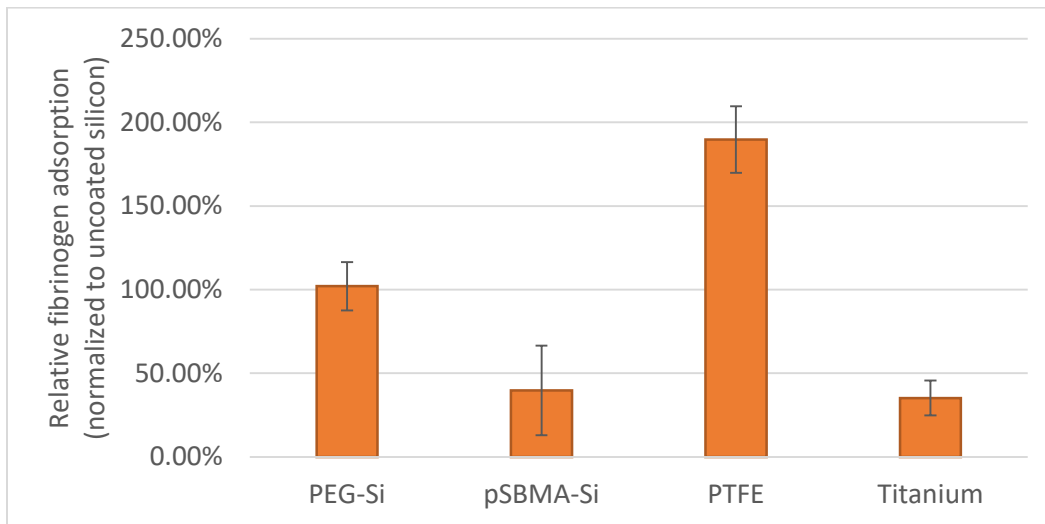
Figure 5.5: *Fibrinogen adsorption from whole human blood. Data is normalized to unmodified silicon.*
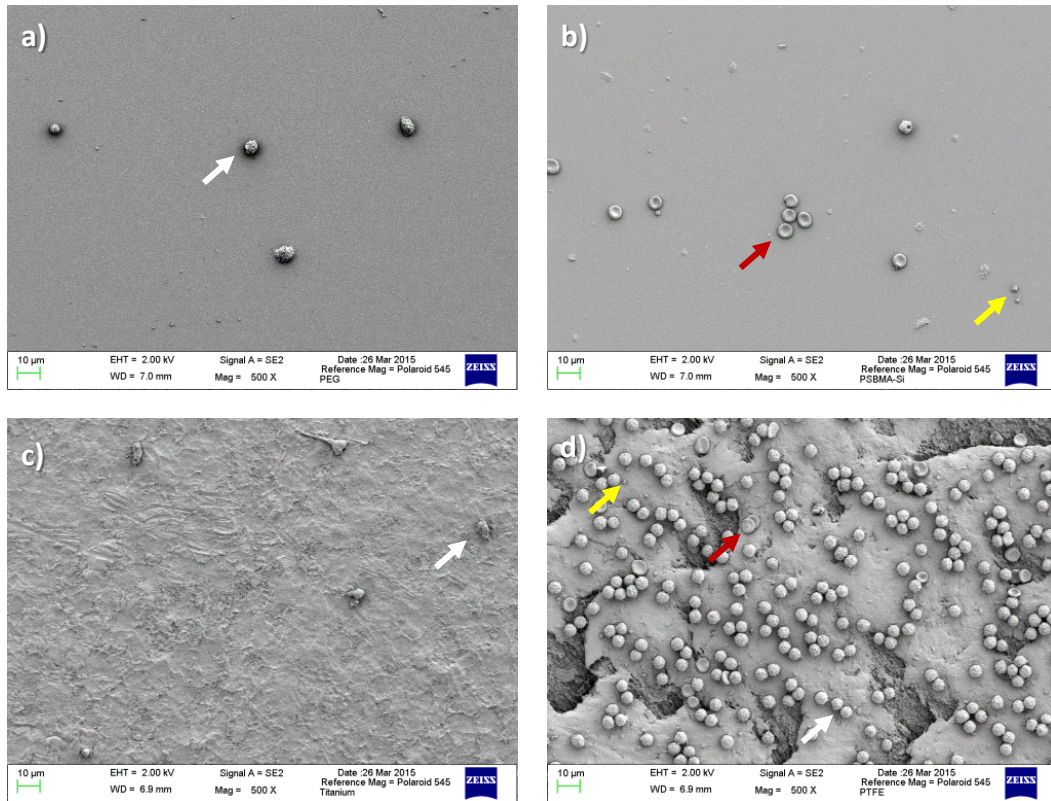
Figure 5.6: *Representative SEM images of surfaces following static fresh whole blood incubation. a) PEG-silicon, b) pSBMA-silicon, c) titanium, and d) PTFE. Examples of leukocytes, red blood cells, and platelets are annotated with white, red and yellow arrows, respectively.*

Figure 5.7 shows representative IHC images for a) PEG-silicon, b) pSBMA-silicon, c) titanium, and d) PTFE, where each sample is marked for presence of CD-62p, which indicates activation. PEG and pSBMA-modified silicon showed the least amount of activation, followed by titanium. PTFE showed the maximum amount of activation, with clots present on the surface.
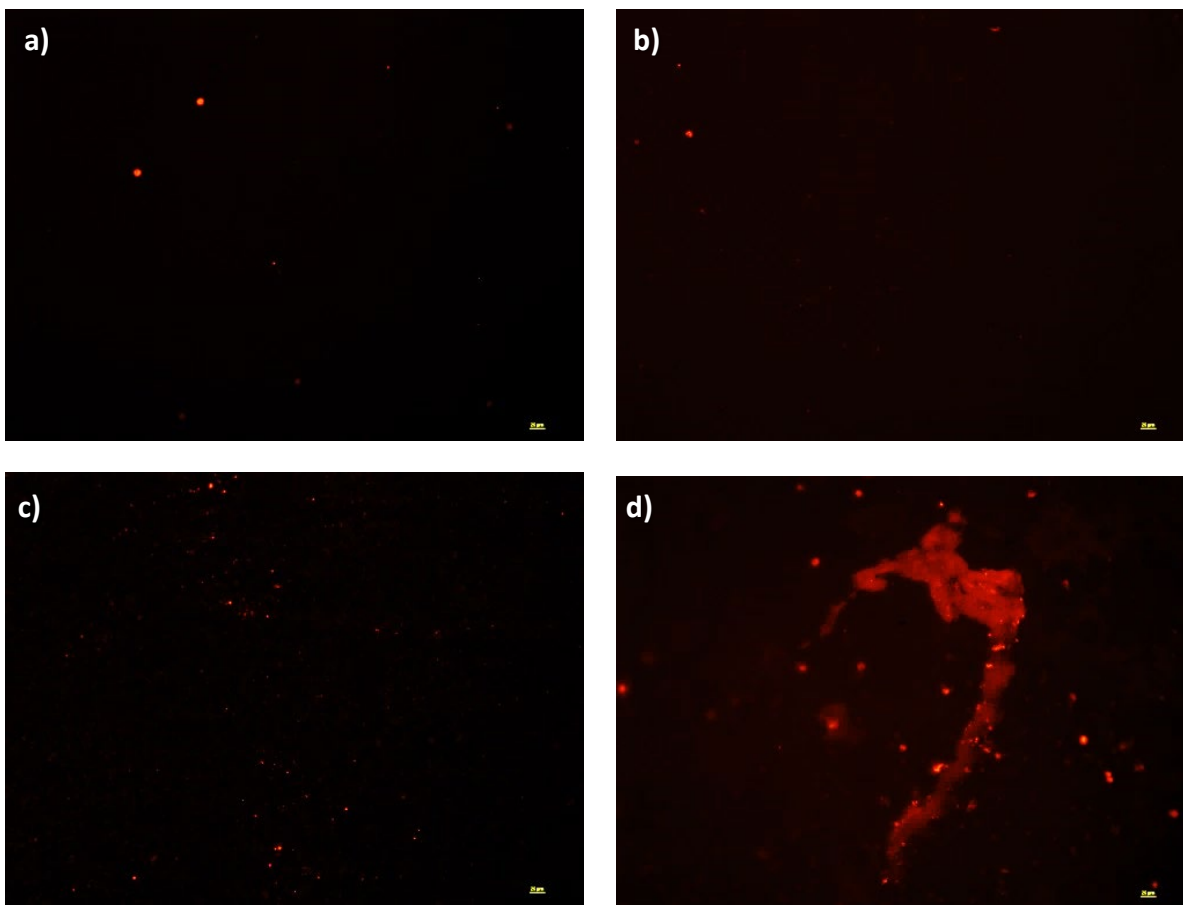
***Figure 5.7:** Representative IHC images of surfaces following static fresh whole blood incubation. Samples are marked for platelet activation (CD-62p). a) PEG-silicon, b) pSBMA-silicon, c) titanium, and d) PTFE. Scale bar represents 25μm.*

5.3.3 Fresh Blood Experiments Under Flow Conditions

5.3.3.1 Blood Flow Experiments in Titanium Implant Device

Images from disassembly following 2-hour blood flow in titanium implant device is presented in Figure 5.8. With the exception of one gross clot found in the flow path of uncoated silicon substrates, both flow paths for silicon and pSBMA-silicon were clear. Following disassembly, the chips were removed and surfaces were imaged. Representative SEM images, shown in Figure 5.9, demonstrates a significant amount of platelet adhesion as well as presence of platelet aggregates on unmodified silicon surfaces. pSBMA-coated silicon exhibited an overall clean

surface, with limited platelet and cell adhesion. The substrates were also marked for activated platelets, and images are presented in Figure 5.10. Here, as seen in the SEM images, there was significantly more platelet activation on unmodified silicon as compared to pSBMA-coated silicon.
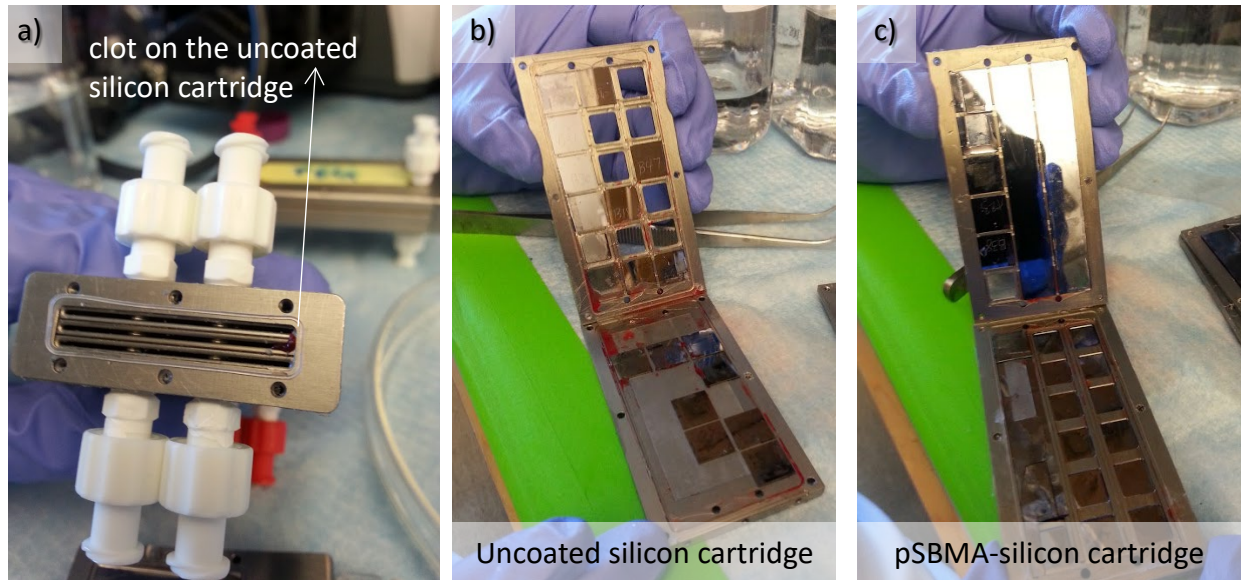
Figure 5.8: Images of titanium housing disassembly. (a) gross clot found in flow path of cartridge containing uncoated silicon chips. (b) uncoated silicon cartridge taken apart, and (c) pSBMA-silicon cartridge taken apart. No other gross clots were found.
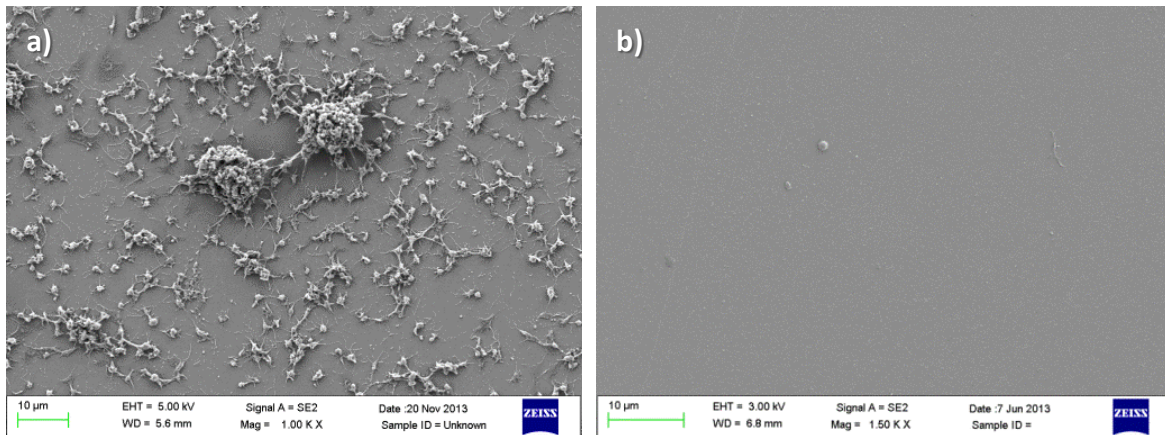
Figure 5.9: SEM images (a) unmodified silicon and (b) pSBMA-coated silicon following blood flow using fresh human blood for 2 hours.
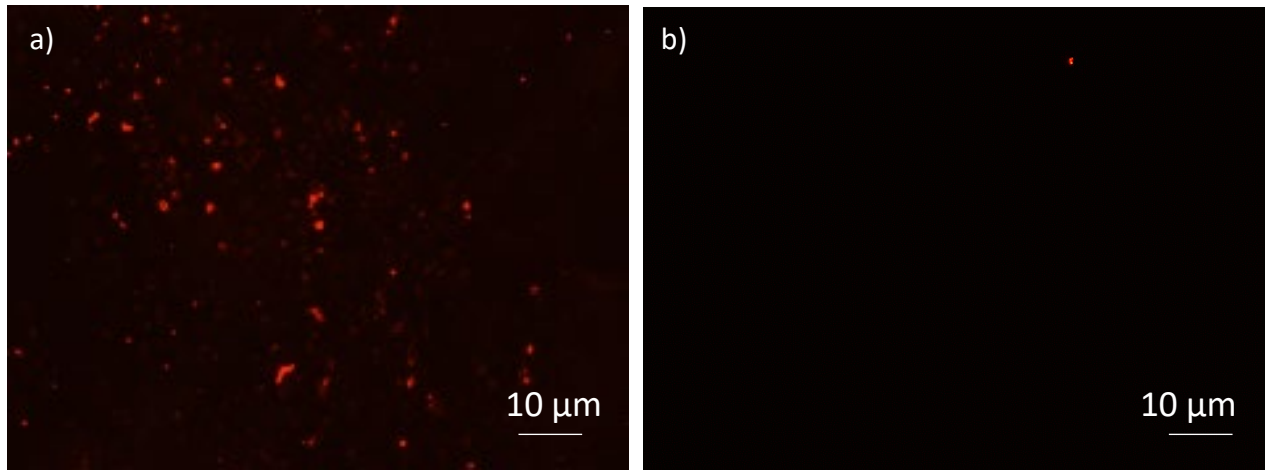
Figure 5.10: *Immunohistochemistry (IHC) showing platelet activation marked by CD-62p. (a) unmodified silicon and b) pSBMA-modified silicon after 2 hours exposure to fresh human blood flow.*

5.3.3.2 Blood Flow Experiments with PEEK Housing

Figure 5.11: *Disassembly of PEEK flow cell after 2-hour blood flow at a shear rate of 1000/s. There were some presence of white platelet clots on the flow path.*

After 2 hours of blood flow, the PEEK flow cells were disassembled. The flow paths were mainly clear, as shown in Figure 5.11. However, there was presence of white platelet clots adhered to the PEEK surface. These clots may have formed because of high shear blood flow conditions.[43] Silicon and modified silicon surfaces were analyzed using SEM (Figure 5.12) and IHC (Figure 5.13). SEM imaging demonstrates that both zwitterionic coatings had minimal cell and platelet adherence, while unmodified silicon exhibited a significantly higher number of adhered platelets and platelet aggregates. PEG-modified surfaces also had presence of adhered platelets on the surface. IHC imaging showed a similar trend: there is an increased amount of adhered and activated platelets for unmodified and PEG-modified silicon, compared to pSBMA-

and pMPC-modified silicon. Following IHC, the number of platelets adhered and activated was quantified, and the data is presented in Figure 5.14. pSBMA and pMPC-silicon had significantly lower platelet adhesion compared to unmodified silicon. pSBMA also showed significantly lower activation compared to unmodified silicon. However, modifying silicon with PEG did not improve platelet adhesion and activation compared to unmodified silicon. Because of the non-homogeneity of platelet adhesion to the surfaces, the error bars are high—for all sample sets, there are locations of high cell count and low cell counts.
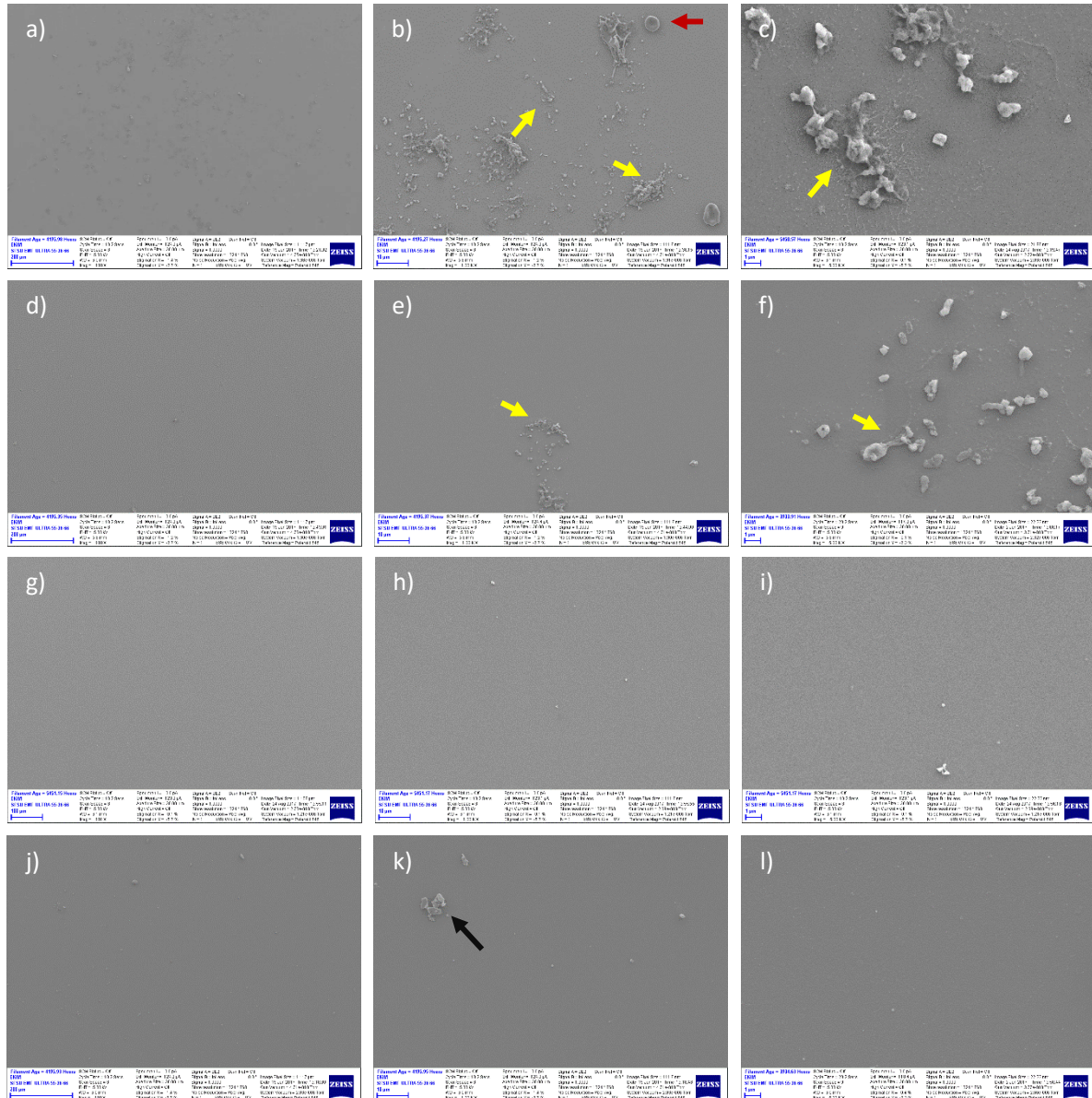
Figure 5.12: *SEM images following in vitro blood flow experiment. (a)-(c) Unmodified silicon; (d)-(f) PEG-silicon; (g)-(i) pSBMA-silicon; and (j)-(l) pMPC-silicon. Red arrow shows an example of red blood cell; yellow arrows show examples of adhered platelets and platelet aggregates, and black arrow represents an example of debris.*

167
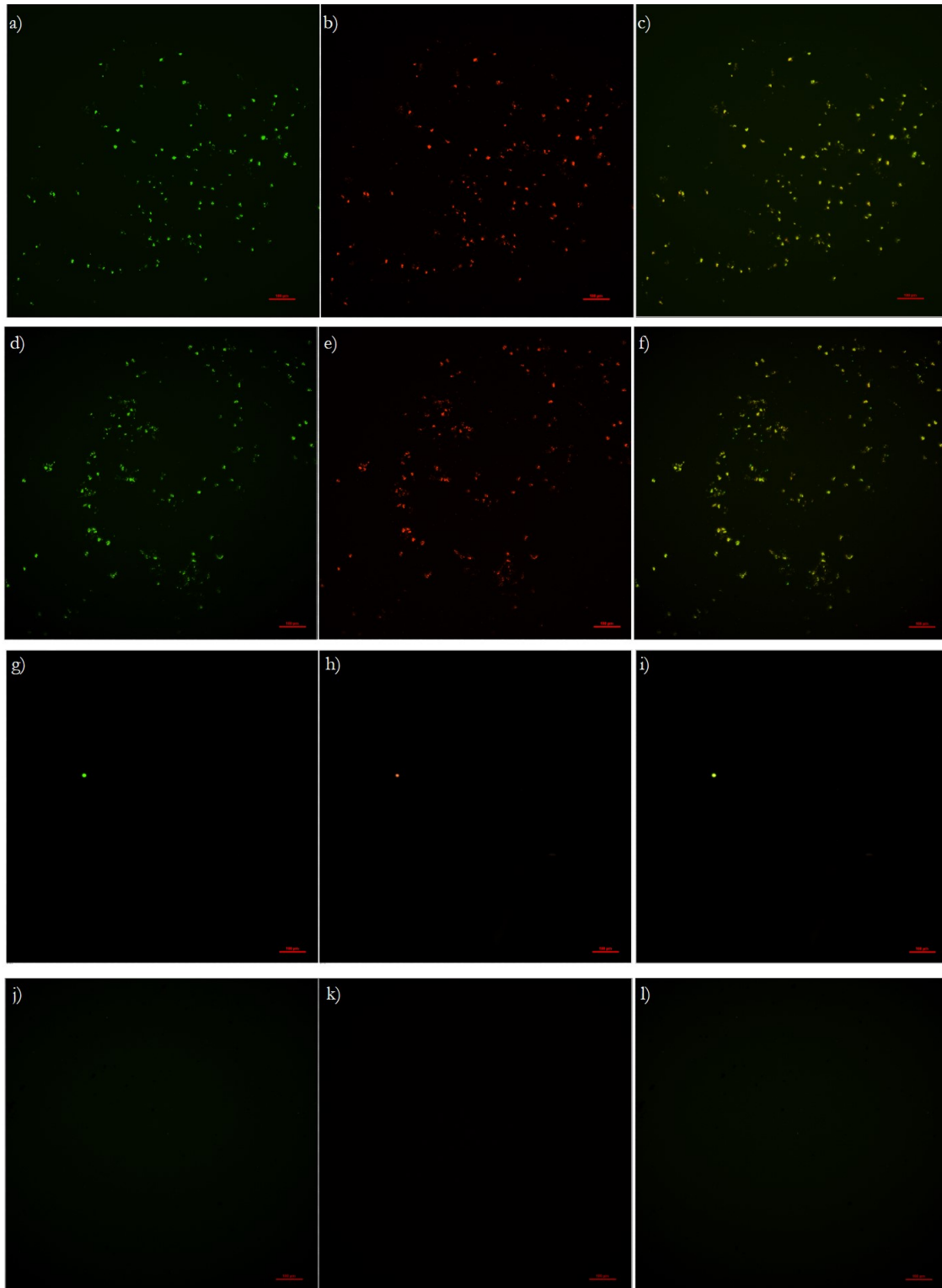
Figure 5.13: *IHC imaging demonstrating non-fouling behavior of pBSMA and pMPC compared to unmodified and PEG-modified silicon. (a)-(c) unmodified silicon; (d)-(f) PEG silicon; (g)-(i) pSBMA-silicon; (j)-(l) pMPC-silicon. Left image is marked with CD41-FITC, stained green, shows adhered platelets on the surface. Middle images is marked with CD62-Cy3, stained red, shows activated platelets marked with CD62p, and images on the right column shows overlap of the first two columns, stained yellow indicating platelets that are activated.*
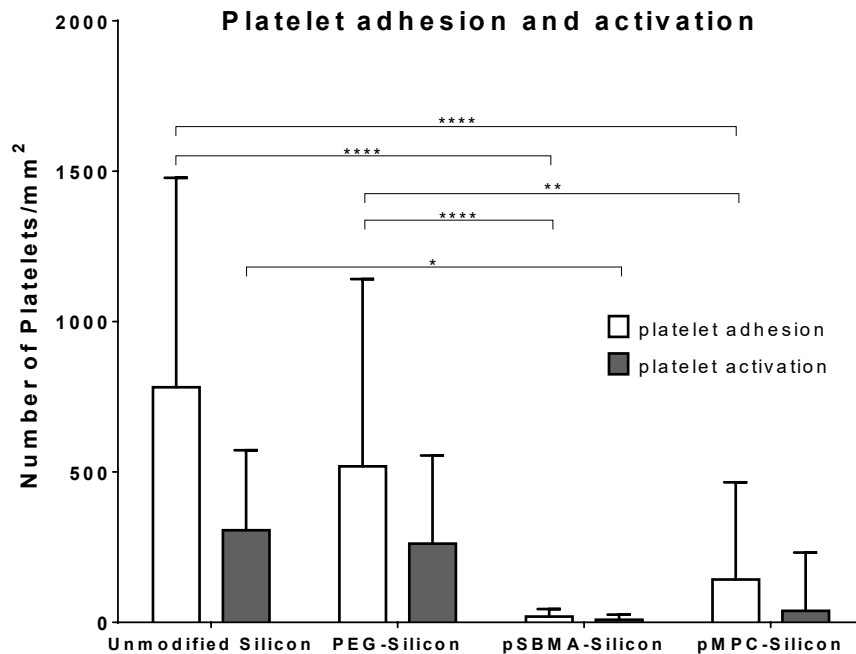
Figure 5.14: *IHC surface platelet adhesion and activation data quantified. pSBMA-silicon followed by pMPC-silicon had the least platelet adhesion and activation. Level of significance is indicated by the number of asterisks: $p \leq 0.05 = *$; $p \leq 0.01 = **$; $p \leq 0.001 = ***$; $p \leq 0.0001 = ****$.*

Amount of activation in the blood was quantified using whole blood flow cytometry. With forward scatter (FSC) as an indicator of size and side scatter (SSC) as an indicator of granularity, whole blood separated into two distinct populations. An example of this plot is presented in Figure 5.15: The smaller population was gated as single platelets, labeled "platelets," which consists of platelets and cellular debris. The larger population labeled "cells" consists of red blood cells, white blood cells, platelet aggregates, as well as platelet-leukocyte aggregates.

After gating based on size, as shown in Figure 5.15, the "platelet" and "cells" populations were individually analyzed for fluorescence. CD-41, also known as integrin alpha-IIb, is a protein that is located on all platelets. Therefore, platelets were marked with anti-CD41 labeled with fluorescein isothiocyanate (FITC) to isolate the platelet population. CD62p, also known as p-

selectin, is a protein that is only expressed on platelet surfaces following activation. Therefore, platelets were marked with anti-CD62p labeled allophycocyanin (APC) to isolate the activated platelet population.
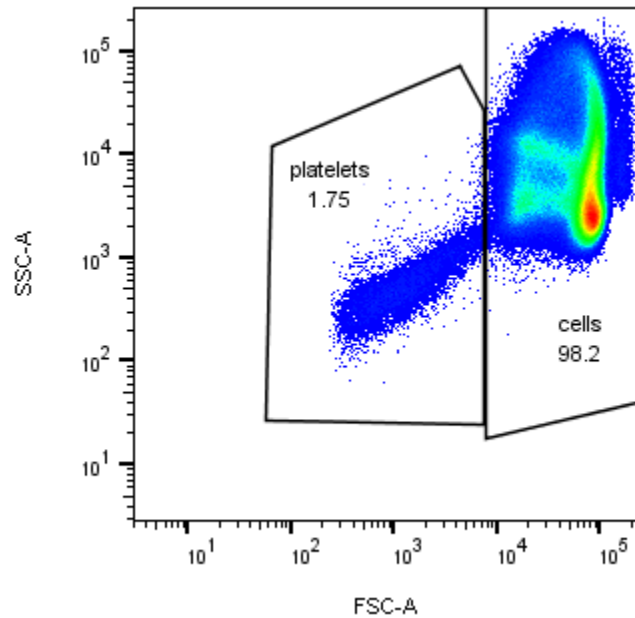
Figure 5.15: *Example of population separation based on size (forward scatter, FSC) and granularity (side scatter, SSC). Negative control (no activation) data is presented here.*

Figure 5.16 demonstrates how gates were set based on positive and negative control. As shown in Figure 5.16 (a), when CD41-FITC-labeled for platelets, it forms two distinct populations, separating out platelets from debris. The platelet-positive population (FITC-positive), was then further analyzed for activation (APC-positive) in Figure 5.16(b). Although the positive and negative control populations overlap, there is a distinct shift. Therefore, the gate was set at the intersection of positive and negative controls. As shown in Figure 5.16 (c) and (d), gates were set in a similar method for the "cells" group. When looked at the combined platelet population across the two populations, positive control had 85.8% activation, while negative control had 3.1% activation.
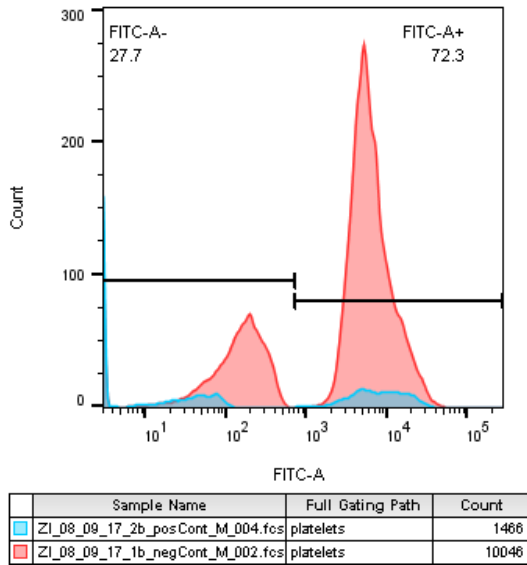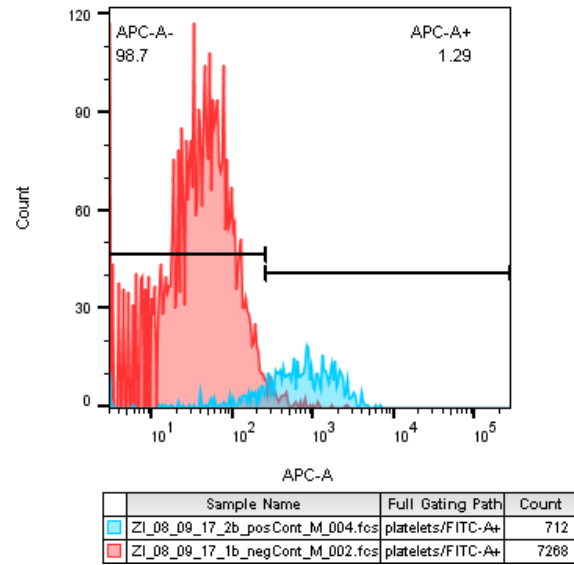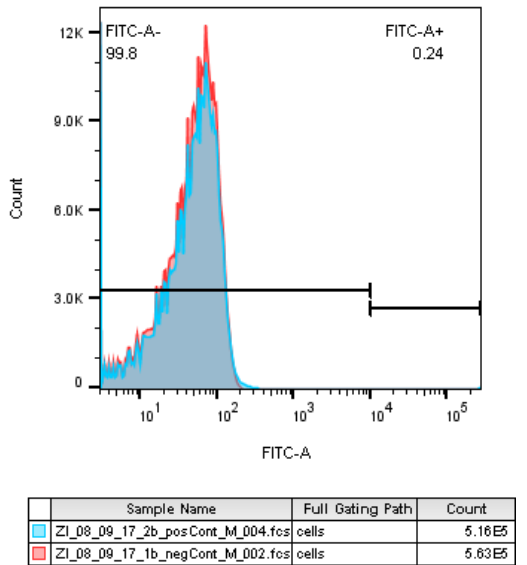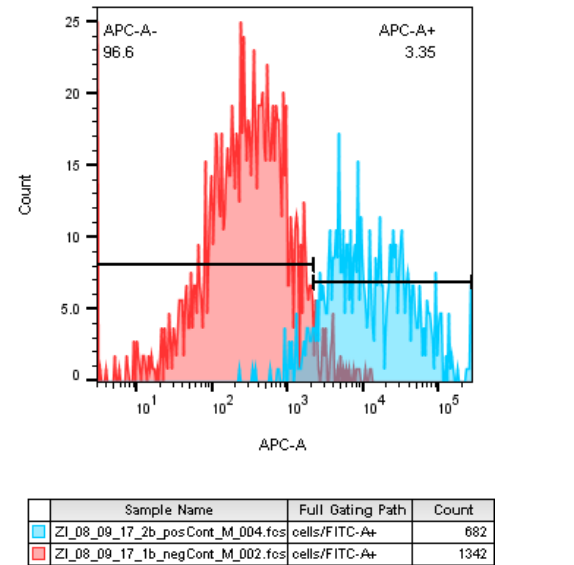
Figure 5.16: *a) positive and negative controls for "platelet" population as marked with anti-CD41-FITC; b) positive and negative controls for FITC-positive "platelet" population as marked with anti-CD62-APC; c) positive and negative controls for "cells" population as marked with anti-CD41-FITC; and d) positive and negative controls for FITC-positive "cells" population as marked with anti-CD62-APC.*

a)
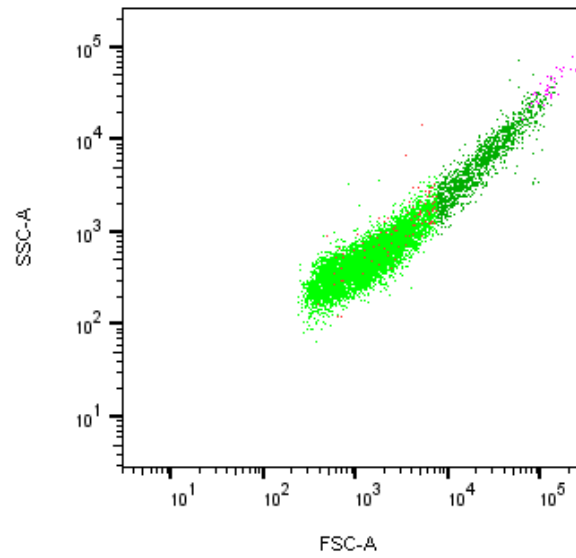
	Sample Name	Full Gating Path	Count
🟥	ZI_08_09_17_1b_negCont_M_002.fcs	platelets/FITC-A+/APC-A+	94.0
🟪	ZI_08_09_17_1b_negCont_M_002.fcs	cells/FITC-A+/APC-A+	45.0
🟩	ZI_08_09_17_1b_negCont_M_002.fcs	platelets/FITC-A+	7268
🟢	ZI_08_09_17_1b_negCont_M_002.fcs	cells/FITC-A+	1342

b)
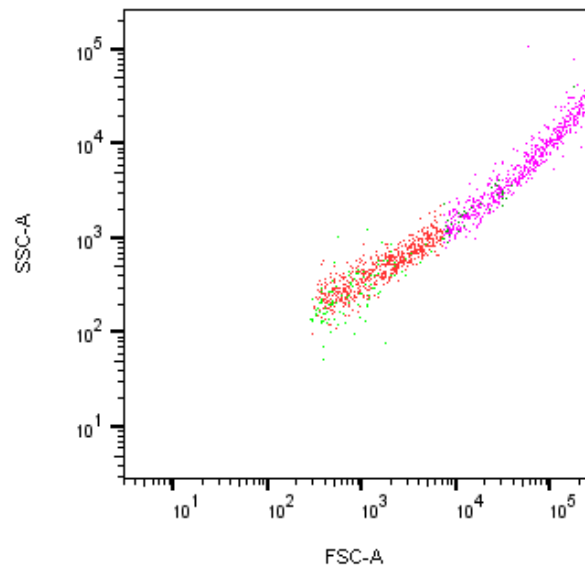
	Sample Name	Full Gating Path	Count
🟥	ZI_08_09_17_2b_posCont_M_004.fcs	platelets/FITC-A+/APC-A+	584
🟪	ZI_08_09_17_2b_posCont_M_004.fcs	cells/FITC-A+/APC-A+	630
🟩	ZI_08_09_17_2b_posCont_M_004.fcs	platelets/FITC-A+	712
🟢	ZI_08_09_17_2b_posCont_M_004.fcs	cells/FITC-A+	682

c)
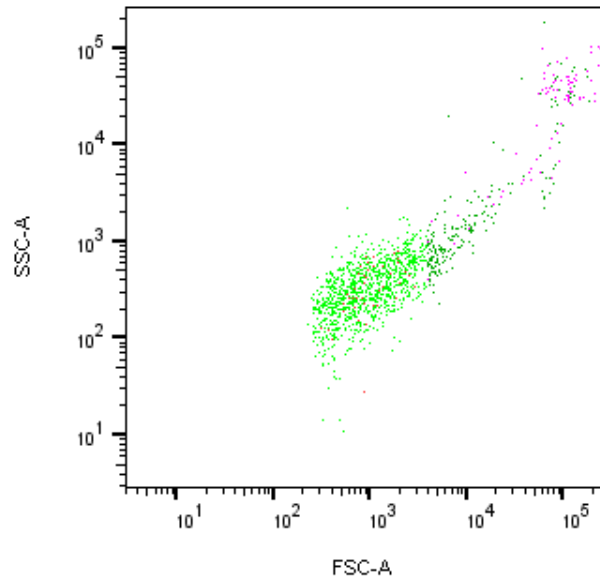
	Sample Name	Full Gating Path	Count
🟥	ZI_05_30_17_3b_bareSi_M_006.fcs	platelets/FITC-A+/APC-A+	41.0
🟪	ZI_05_30_17_3b_bareSi_M_006.fcs	cells/FITC-A+/APC-A+	89.0
🟩	ZI_05_30_17_3b_bareSi_M_006.fcs	platelets/FITC-A+	972
🟩	ZI_05_30_17_3b_bareSi_M_006.fcs	cells/FITC-A+	289

d)
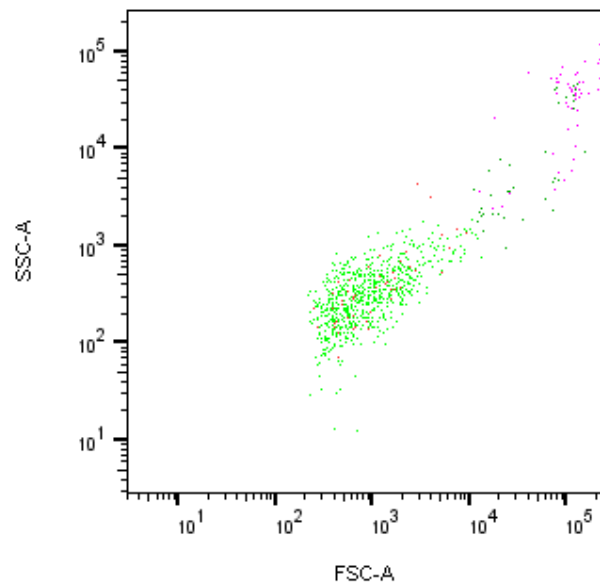
	Sample Name	Full Gating Path	Count
🟥	ZI_05_30_17_4b_PEG_M_008.fcs	platelets/FITC-A+/APC-A+	48.0
🟪	ZI_05_30_17_4b_PEG_M_008.fcs	cells/FITC-A+/APC-A+	60.0
🟩	ZI_05_30_17_4b_PEG_M_008.fcs	platelets/FITC-A+	716
🟩	ZI_05_30_17_4b_PEG_M_008.fcs	cells/FITC-A+	98.0

e)
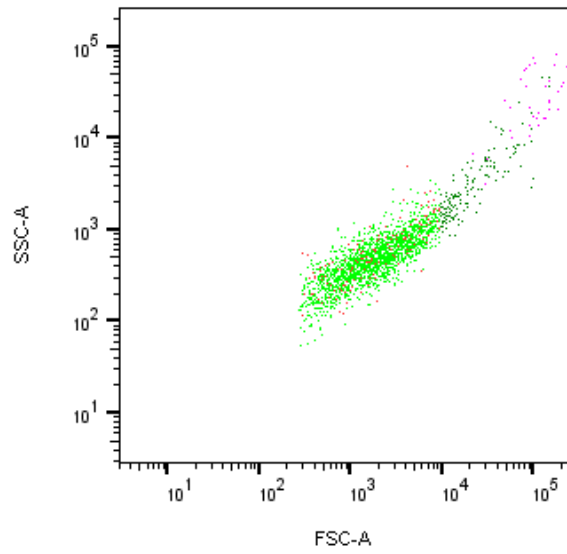
	Sample Name	Full Gating Path	Count
🟥	ZI_08_09_17_4b_SBMA1_M_006.fcs	platelets/FITC-A+/APC-A+	134
🟪	ZI_08_09_17_4b_SBMA1_M_006.fcs	cells/FITC-A+/APC-A+	58.0
🟩	ZI_08_09_17_4b_SBMA1_M_006.fcs	platelets/FITC-A+	1850
🟢	ZI_08_09_17_4b_SBMA1_M_006.fcs	cells/FITC-A+	211

f)
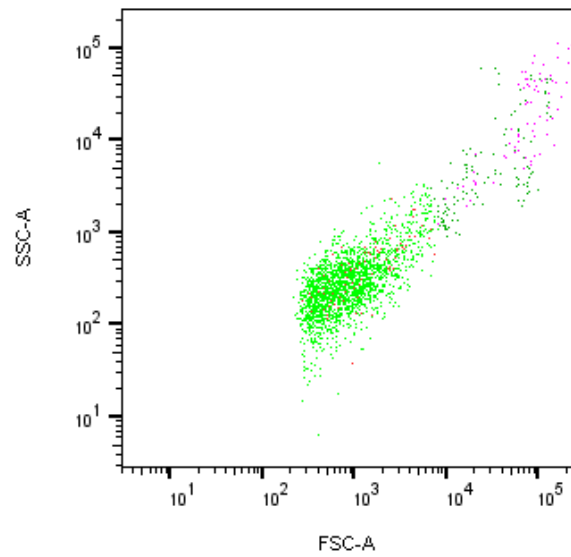
	Sample Name	Full Gating Path	Count
🟥	ZI_05_30_17_6b_MPC_M_012.fcs	platelets/FITC-A+/APC-A+	78.0
🟪	ZI_05_30_17_6b_MPC_M_012.fcs	cells/FITC-A+/APC-A+	76.0
🟩	ZI_05_30_17_6b_MPC_M_012.fcs	platelets/FITC-A+	2064
🟢	ZI_05_30_17_6b_MPC_M_012.fcs	cells/FITC-A+	194

174

g)
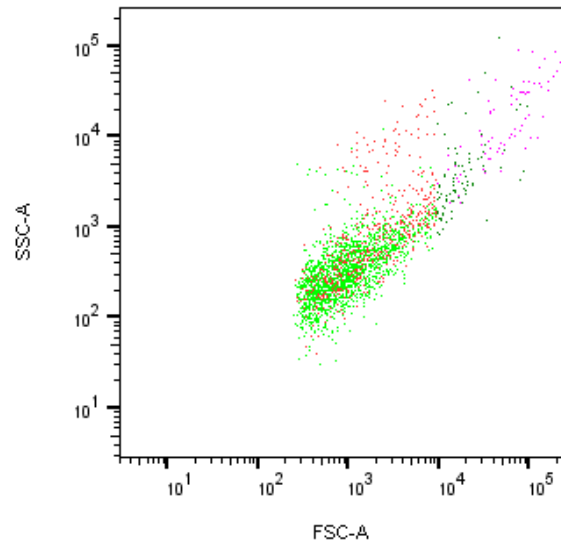
	Sample Name	Full Gating Path	Count
■ (red)	ZI_08_09_17_7b_tubing_M_009.fcs	platelets/FITC-A+/APC-A+	467
■ (magenta)	ZI_08_09_17_7b_tubing_M_009.fcs	cells/FITC-A+/APC-A+	78.0
■ (light green)	ZI_08_09_17_7b_tubing_M_009.fcs	platelets/FITC-A+	2144
■ (dark green)	ZI_08_09_17_7b_tubing_M_009.fcs	cells/FITC-A+	171

Figure 5.17: Representative dot plots from flow cytometry for each of the samples. Green dots represent particles that have a presence of CD41-FITC, indicating platelets. Light green dots fall in the "platelet" population while dark green dots fall in the "cells and aggregates" population. Red and magenta dots represent particles that are CD41-positive and have a presence of CD62-APC on the surface, indicating activation. Red dots fall in the "platelet" population while magenta dots fall in the "cells and aggregates" population0. a) negative control; b) positive control; c) unmodified silicon; d) PEG-silicon; e) pSBMA-silicon; f) pMPC-silicon; g) tubing only.

Figure 5.17(a) – (g) shows a representative dot plot for each of the sample group. Platelet population and activation of platelets are shown as a distribution of size and granularity. Negative and positive controls, where blood was not circulated for 2 hours, show a tighter distribution for granularity (SSC) of platelets compared to the other experimental groups. While distribution varies from sample to sample, when averaged, there is no significant differences in activation between each of the experimental group. Circulating blood through the tubing only at the same flow rate as the experimental groups shows no significant difference from any of the sample, as demonstrated in the summary plot of Figure 5.18.
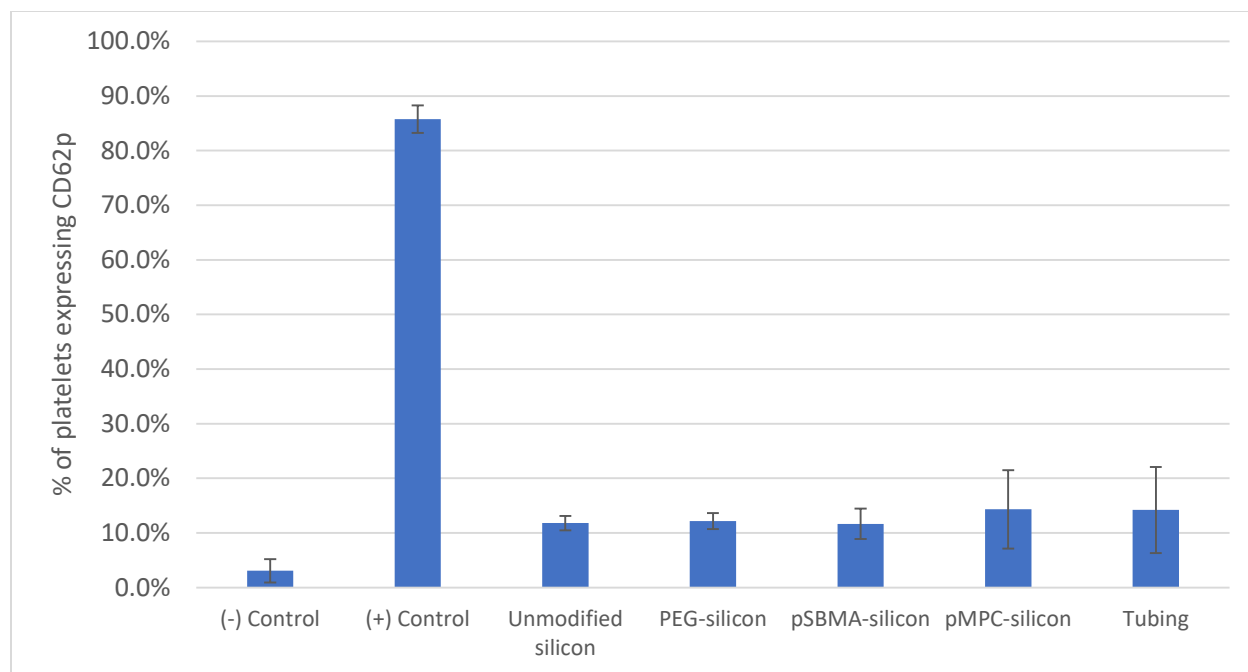
Figure 5.18: *Percent of platelets that are activated in controls and following 2-hour blood flow experiment at a shear rate of 1000/s over surfaces.*

5.4 Discussion

While animal testing is critical for any novel biomaterial or implant, preliminary *in vitro* testing can significantly reduce sample size, lowering the number of animal sacrifices required as well as cost. However, there are no standard methods for testing biomaterials *in vitro*. Therefore, this chapter looked at surfaces via several methods, including under static and blood flow conditions.

Protein Adsorption from Single Protein Solution:

Adsorption from two separate protein solutions were tested: HSA and human fibrinogen. HSA was chosen as model protein for non-specific surface binding, while fibrinogen was chosen for its role in thrombus formation.[20,44,45] Overall, adsorption from both HSA and fibrinogen showed similar trend: compared to control TCPS, all silicon and modified silicon surfaces have lowered protein adsorption by more than 60%. This may due to differences in surface chemistry and

surface roughness between the samples. Following piranha treatment, water contact angle for silicon is <10° due to newly introduced hydroxyl groups on the surface. Over time, silicon loses the hydroxyl groups and the contact angle slowly raises back up to ~43°.[46] In the time frame that ELISA is conducted after piranha treatment, measured contact angle is ~30°, while coated silicon is ~10° for zwitterionic coatings and ~40° for PEG-silicon. On the other hand, TCPS has a contact angle of ~55°.[47] Along with surface chemistry, surface roughness also can increase protein fouling,[48] and root mean square surface roughness (R_{RMS}) for polystyrene is ~4.5 nm,[47] while R_{RMS} for silicon is <0.2 nm.[49] These two factors would favor silicon surfaces to be less fouling compared to TCPS.

With surface modification protein adsorption decreased significantly. For both HSA and fibrinogen, protein adsorption was reduced by more than 50%, 80% and 45% for PEG, pSBMA and pMPC, respectively, compared to unmodified silicon. This demonstrates that at < 5 nm thickness, the surface coatings are able to maintain their non-fouling properties.

Static Fresh Human Blood Experiment:

Titanium and PTFE have been used for decades in implants such as hard tissue replacements in orthopedics and dentistry,[50] pulmonary valve replacements[51] and surface coatings.[52,53] In addition to mechanical strength and toughness, titanium offers biocompatibility and corrosion resistance due to its chemically inert surface oxide.[50,54–56] Hydrophobic PTFE is known to be non-toxic and stable under biological conditions.[57,58] Therefore, in this chapter we compared PEG- and pSBMA-modified silicon to titanium and PTFE.

Aside from imaging the substrates for cellular adhesion and activation, fibrinogen adsorption on the surfaces were also analyzed using ELISA. Previous literature shows that protein adsorption

can differ when it is from whole blood or plasma compared to single protein solutions.[35] Our results also show a poorer performance in fouling properties from whole blood compared to that from single protein solution. After two-hour incubation in fresh human blood from an ESRD patient, PEG-modified silicon did not lower fibrinogen adsorption compared to unmodified silicon. pSBMA and titanium reduced protein adsorption by only 50% compared to silicon, and PTFE almost doubled the protein adsorption. The high fibrinogen adsorption of PTFE compared to the other surfaces could once again be due to surface roughness. Among the surfaces tested, PTFE is also the most hydrophobic surface, which leads to increased fibrinogen adsorption.[59]

PTFE also shows a high amount of cellular adhesion and activation on the surface. Under SEM imaging, a large number of adhered leukocytes is evident on PTFE. In comparison, other three surfaces tested—titanium, PEG-silicon, and pSBMA-silicon, had negligible cellular adhesion and activation. However, PEG-silicon and titanium exhibit signs of leukocyte spreading. Spreading typically follows leukocyte adhesion, where cells rearrange their cytoskeleton and flatten to tightly adhere to the surface.[60] PEG brushes are meant to deter cells from adhering. However, low grafting density of PEG (discussed extensively in Ch 3 and 4), may allow regional islands on which cells are able to attach and spread.

Interestingly, although there are a large number of leukocytes on PTFE surface, they did not spread. It is difficult to ascertain whether the adhered cells are unable to spread on the PTFE surface or if they were fixed before they had a chance to spread. Nonetheless, when stained for p-selectin, which is only expressed when platelets are activated, clots were evident on PTFE surface. While PTFE is inert, previous literature shows its hydrophobic surface properties can lead to inflammation.[61]

Based on SEM and IHC imaging, pSBMA and PEG had the least amount of cell adherence and activation. Under SEM imaging, pSBMA surface shows some presence of red blood cells. However, red blood cells alone are not an indication of inflammation or activation. There is also presence of a few platelets on the pSBMA-silicon surface. However, as evident under IHC staining, they only negligible compared to titanium and PTFE controls.

Fresh Human Blood Flow Experiments:

To better mimic our implants *in vivo*, flow experiments were conducted in our current titanium implant device (Figure 5.2). However, unlike in the static experiment, we used fresh human blood from a healthy donor. At a blood shear rate of ~73/s over the surfaces, pSBMA was compared to unmodified silicon. Over two hours, pSBMA-coated silicon was able to resist platelet adhesion and activation, while unmodified silicon showed a significant amount of platelet adhesion and activation (Figures 5.9 and 5.10). This experiment demonstrated that <5 nm pSBMA brushes maintain their functionality under whole blood flow conditions.

The titanium housing has a channel height of 1 mm over test substrates. However, to generate sufficient filtrate, the final bioartificial kidney hemofilter will require blood channel height of ~200 nm in order to accommodate larger SNM area. Therefore, we designed a PEEK flow cell with 200 nm channel to test our coated substrates. This device allows us to test blood flow at high shear rate, unlike other *in vitro* flow testing devices used in previous literature.[62] The flow experiments done in PEEK flow cell had the wall shear rate of 1000/s, which is more than 10 times higher compared to the experiment in titanium implant device. With the PEEK experimental setup, however, we found formation and attachment of white clots on the PEEK surface (Figure 5.11). Closer examination under microscope revealed that these clots consist of mainly platelets, with very little to no presence of fibrin. White clots typically occur in high

shear conditions. Unlike red clots, which contain erythrocytes and are likely to form at low shear flow, high-shear thrombi do not follow the typical path of coagulation cascade. Rather, it relies of platelet accumulation and platelet interaction with Von Willebrand factor (vWF).[43] Although majority of the white clots were attached to the PEEK housing, the presence of these clots in the system may have elevated the total platelet adhesion and activation count.

Imaging was conducted for all test substrates using SEM and fluorescence microscopy. SEM images shows platelets and platelet aggregates attached to unmodified silicon and PEG-silicon, while pSBMA and pMPC had negligible attachment. IHC imaging also showed a similar trend. Once quantified, as reported in Figure 5.14, it is noticeable that PEG-silicon had lower amount of platelet attachment compared to unmodified silicon. Zwitterionic coatings had the least amount of platelet adhesion and activation, with pSBMA-silicon demonstrating the best performance. Although the quantified data agrees trend-wise with the visualized images and cell counting was done in similar method as was done before,[66] it should be noted that the number of platelets were calculated from 2-dimensional images. Therefore, overlapping platelets, for example, in a platelet aggregate, were under-counted using this method.

In addition to doing surface analysis, activation of platelets in blood was also examined using flow cytometry. While it is challenging to conduct flow cytometry on platelets due to their small size, fluorescent markers were used against CD41 to segregate platelets and platelet aggregates from the rest of the blood cells. Positive control activated with TRAP led to >80% activation, while negative control had <5% activation. These values are in agreement with positive and negative controls in previous literature,[67] confirming the platelet population was properly managed and analyzed.

In conducting flow cytometry, we attempted to determine the amount of activation in blood due to exposure to different surfaces. However, the amount of platelet activation in blood due to varying surface coatings could not be determined using flow cytometry because there was no significant difference in activation between any of the substrates. As a control, flow through tubing alone was also tested. Platelet activation in blood for control tubing was comparable to any of the samples run—~14%. Therefore, it is clear that the platelet activation seen in the substrates is likely due to the flow system and experimental setup such as tubing, peristaltic pump, time and amount of blood flow, and etc., rather than the substrates themselves. This is not unexpected, since blood in contact with other surfaces, such as tubing, connectors and PEEK flow cell, far outweighs the amount of time the blood is in contact with test surface: At any given moment, only ~2% of the blood is in the flow chamber over the test surface. Additionally, the effect of peristaltic pump on 5 mL of blood over 2 hours could be causing a significant amount of hemolysis. Therefore, further studies need to be conducted to determine the best conditions under which flow cytometry can be used to differentiate blood activation due to various surfaces. Static tests with lower hemolysis may be better suited for flow cytometry analysis. For flow cytometry analysis following blood flow experiments, a shorter time length of experiment or lower shear rate may be better suited.

5.5 Conclusions

With preliminary *in vitro* experiments, number of *in vivo* experiments can be reduced. Although there is no one standardized method of conducting *in vitro* testing, we looked at several methods, including static blood exposure and blood flow experiments. Through this set of experiments, we found that at <5 nm thickness, zwitterionic coatings grafted to the surface outperformed grafted on PEG coating. Among the zwitterionic coatings, pSBMA consistently reduces protein

181

adsorption, resists platelet and cellular adhesion and activation compared to pMPC. As a next step, *in vivo* experiments need to be conducted; based on the results presented in this chapter, attention will be focused on pSBMA-coated silicon.

5.6 References

1.   Cheung, K. C. & Renaud, P. BioMEMS for medicine: On-chip cell characterization and implantable microelectrodes. *Solid. State. Electron.* **50,** 551–557 (2006).

2.   Scholvin, J. *et al.* Close-packed silicon microelectrodes for scalable spatially oversampled neural recording. *IEEE Trans. Biomed. Eng.* **63,** 120–130 (2016).

3.   Shawgo, R. S., Grayson, A. C. R., Li, Y. & Cima, M. J. BioMEMS for drug delivery. *Curr. Opin. Solid State Mater. Sci.* **6,** 329–334 (2002).

4.   Desai, T. *et al.* Nanoporous Implants for Controlled Drug Delivery. *Ther. Micro/Nano Technol. - BioMEMS Biomed. Nanotechnol.* 263–286 (2007). doi:10.1007/978-0-387-25844-7_15

5.   Lesinski, G. B. *et al.* Release of biologically functional interferon-alpha from a nanochannel delivery system. *Biomed. Microdevices* **7,** 71–79 (2005).

6.   Kang, S. *et al.* Bioresorbable silicon electronic sensors for the brain. *Nature* **530,** 71–76 (2016).

7.   Lueke, J. & Moussa, W. A. MEMS-based power generation techniques for implantable biosensing applications. *Sensors* **11,** 1433–1460 (2011).

8.   Acquaroli, L. N., Kuchel, T. & Voelcker, N. H. Towards implantable porous silicon biosensors. *RSC Adv.* **4,** 34768 (2014).

9.   Fissell, W. H. *et al.* High-performance silicon nanopore hemofiltration membranes. *J. Memb. Sci.* **326,** 58–63 (2009).

10.   Kim, S. *et al.* Diffusive silicon nanopore membranes for hemodialysis applications. *PLoS*

One **11,** 1–20 (2016).

11.   Song, S. *et al.* Silicon nanopore membrane (SNM) for islet encapsulation and immunoisolation under convective transport. *Sci. Rep.* **6,** 23679 (2016).

12.   Desai, T. a., Hansford, D. J. & Ferrari, M. Micromachined interfaces: New approaches in cell immunoisolation and biomolecular separation. *Biomol. Eng.* **17,** 23–36 (2000).

13.   Roy, S. *et al.* Silicon nanopore membrane technology for an implantable artificial kidney. *TRANSDUCERS 2009 - 15th Int. Conf. Solid-State Sensors, Actuators Microsystems* 755–760 (2009). doi:10.1109/SENSOR.2009.5285603

14.   Fissell, W. H., Fleischman, A. J., Humes, H. D. & Roy, S. Development of continuous implantable renal replacement: past and future. *Transl. Res.* **150,** 327–336 (2007).

15.   Song, S. *et al.* An intravascular bioartificial pancreas device (iBAP) with silicon nanopore membranes (SNM) for islet encapsulation under convective mass transport. *Lab Chip* (2017). doi:10.1039/C7LC00096K

16.   Fernández-Rosas, E. *et al.* Internalization and cytotoxicity analysis of silicon-based microparticles in macrophages and embryos. *Biomed. Microdevices* **12,** 371–379 (2010).

17.   Agrawal, a. a. *et al.* Porous nanocrystalline silicon membranes as highly permeable and molecularly thin substrates for cell culture. *Biomaterials* **31,** 5408–5417 (2010).

18.   Kotzar, G. *et al.* Evaluation of MEMS materials of construction for implantable medical devices. *Biomaterials* **23,** 2737–50 (2002).

19.   Werner, C., Maitz, M. F. & Sperling, C. Current strategies towards hemocompatible coatings. *J. Mater. Chem.* **17,** 3376 (2007).

20.   Zhang, M. & Ferrari, M. Hemocompatible polyethylene glycol films on silicon. *Biomed. Microdevices* (1998). at <http://www.springerlink.com/index/H6K15PK44618078T.pdf>

21.   Popat, K. C. & Desai, T. a. Poly(ethylene glycol) interfaces: An approach for enhanced performance of microfluidic systems. *Biosens. Bioelectron.* **19,** 1037–1044 (2004).

22.   Melvin, M. E., Fissell, W. H., Roy, S. & Brown, D. L. Silicon induces minimal thromboinflammatory response during 28-day intravascular implant testing. *ASAIO J.* **56,** 344–8 (2010).

23.   Nakabayashi, N. & Williams, D. F. Preparation of non-thrombogenic materials using 2-methacryloyloxyethyl phosphorylcholine. *Biomaterials* **24,** 2431–2435 (2003).

24.   Ladd, J., Zhang, Z., Chen, S., Hower, J. C. & Jiang, S. Zwitterionic polymers exhibiting high resistance to nonspecific protein adsorption from human serum and plasma. *Biomacromolecules* **9,** 1357–1361 (2008).

25.   Zhang, L. *et al.* Zwitterionic hydrogels implanted in mice resist the foreign-body reaction. *Nat. Biotechnol.* **31,** 553–6 (2013).

26.   Smith, R. S. *et al.* Vascular Catheters with a Nonleaching Poly-Sulfobetaine Surface Modification Reduce Thrombus Formation and Microbial Attachment. *Sci. Transl. Med.* **4,** 153ra132-153ra132 (2012).

27.   Chen, S., Liu, L. & Jiang, S. Strong resistance of oligo(phosphorylcholine) self-assembled monolayers to protein adsorption. *Langmuir* **22,** 2418–21 (2006).

28.   Jiang, S. & Cao, Z. Z. Ultralow-fouling, functionalizable, and hydrolyzable zwitterionic materials and their derivatives for biological applications. *Adv. Mater.* **22,** 920–932

(2010).

29. Zhang, Z., Chao, T., Chen, S. & Jiang, S. Superlow fouling sulfobetaine and carboxybetaine polymers on glass slides. *Langmuir* **22,** 10072–10077 (2006).

30. Muthusubramaniam, L. *et al.* Hemocompatibility of silicon-based substrates for biomedical implant applications. *Ann. Biomed. Eng.* **39,** 1296–305 (2011).

31. Carr, L. R., Zhou, Y., Krause, J. E., Xue, H. & Jiang, S. Uniform zwitterionic polymer hydrogels with a nonfouling and functionalizable crosslinker using photopolymerization. *Biomaterials* **32,** 6893–6899 (2011).

32. Zhang, Z. *et al.* Blood compatibility of surfaces with superlow protein adsorption. *Biomaterials* **29,** 4285–4291 (2008).

33. Goodman, S. L. Sheep , pig , and human platelet – material interactions with model cardiovascular biomaterials. (1998).

34. Li, J. *et al.* Preparation and characterization of nonfouling polymer brushes on poly(ethylene terephthalate) film surfaces. *Colloids Surf. B. Biointerfaces* **78,** 343–50 (2010).

35. Li, L., Marchant, R. E., Dubnisheva, A., Roy, S. & Fissell, W. H. Anti-biofouling Sulfobetaine Polymer Thin Films on Silicon and Silicon Nanopore Membranes. *J. Biomater. Sci.* **22,** 91–106 (2011).

36. Iqbal, Z. *et al.* Sterilization effects on ultrathin film polymer coatings for silicon-based implantable medical devices. *J. Biomed. Mater. Res. Part B Appl. Biomater.* 1–10 (2017). doi:10.1002/jbm.b.34039

37. Mao, C. *et al.* Various approaches to modify biomaterial surfaces for improving hemocompatibility. *Adv. Colloid Interface Sci.* **110,** 5–17 (2004).

38. Eriksson, C., Lausmaa, J. & Nygren, H. Interactions between human whole blood and modified TiO2 -surfaces : Influence of surface topography and oxide thickness on leukocyte adhesion and activation. *Biomaterials* **22,** 1987–1996 (2001).

39. Haycox, C. L. & Ratner, B. D. In vitro platelet interactions in whole human blood exposed to biomaterial surfaces: insights on blood compatibility. *J. Biomed. Mater. Res.* **27,** 1181–93 (1993).

40. Nguyen, K. T. *et al.* In vitro hemocompatibility studies of drug-loaded poly-(L-lactic acid) fibers. *Biomaterials* **24,** 5191–5201 (2003).

41. Streller, U., Sperling, C., Hübner, J., Hanke, R. & Werner, C. Design and evaluation of novel blood incubation systems for in vitro hemocompatibility assessment of planar solid surfaces. *J. Biomed. Mater. Res. B. Appl. Biomater.* **66,** 379–390 (2003).

42. Sperling, C., Houska, M., Brynda, E., Streller, U. & Werner, C. In vitro hemocompatibility of albumin-heparin multilayer coatings on polyethersulfone prepared by the layer-by-layer technique. *J. Biomed. Mater. Res. - Part A* **76,** 681–689 (2006).

43. Casa, L. D. C. & Ku, D. N. Thrombus Formation at High Shear Rates. *Annu. Rev. Biomed. Eng.* **19,** 415–433 (2017).

44. Sharma, S., Johnson, R. W. & Desai, T. A. Evaluation of the Stability of Nonfouling Ultrathin Poly (ethylene glycol) Films for Silicon-Based Microdevices. *Langmuir* **20,** 348–356 (2004).

45. Zhang, M., Desai, T. & Ferrari, M. Proteins and cells on PEG immobilized silicon surfaces. *Biomaterials* **19,** 953–960 (1998).

46. Hermansson, K., Lindberg, U., Hok, B. & Palmskog, G. Wetting properties of silicon surfaces. *TRANSDUCERS '91 1991 Int. Conf. Solid-State Sensors Actuators. Dig. Tech. Pap.* 193–196 (1991). doi:10.1109/SENSOR.1991.148835

47. Zeiger, A. S., Hinton, B. & Van Vliet, K. J. Why the dish makes a difference: Quantitative comparison of polystyrene culture surfaces. *Acta Biomater.* **9,** 7354–7361 (2013).

48. Rechendorff, K., Hovgaard, M. B., Foss, M., Zhdanov, V. P. & Besenbacher, F. Enhancement of protein adsorption induced by surface roughness. *Langmuir* **22,** 10885–10888 (2006).

49. Sharma, S., Johnson, R. W. & Desai, T. a. XPS and AFM analysis of antifouling PEG interfaces for microfabricated silicon biosensors. *Biosens. Bioelectron.* **20,** 227–239 (2004).

50. Long, M. & Rack, H. J. Titanium alloys in total joint replacement--a materials science perspective. *Biomaterials* **19,** 1621–1639 (1998).

51. Quintessenza, J. A., Jacobs, J. P., Chai, P. J., Morell, V. O. & Lindberg, H. Polytetrafluoroethylene Bicuspid Pulmonary Valve Implantation: Experience With 126 Patients. *World J. Pediatr. Congenit. Hear. Surg.* **1,** 20–27 (2010).

52. Zhang, F. *et al.* Blood compatibility of titanium oxide prepared by ion-beam-enhanced deposition. *Surf. Coatings Technol.* **84,** 476–479 (1996).

53. Bureau, C. *et al.* Improved Clinical Outcome Using Polytetrafluoroethylene-Coated Stents

for TIPS: Results of a Randomized Study. *Gastroenterology* **126,** 469–475 (2004).

54.   Sidambe, A. T. Biocompatibility of advanced manufactured titanium implants-A review. *Materials (Basel).* **7,** 8168–8188 (2014).

55.   Park, J. Y. & Davies, J. E. Red blood cell and platelet interactions with titanium implant surfaces. *Clin. Oral Implants Res.* **11,** 530–9 (2000).

56.   Maitz, M. F., Pham, M., Wieser, E. & Tsyganov, I. Blood Compatibility of Titanium Oxides with Various Crystal. (2003). doi:10.1177/088532803033178

57.   Rosengren, A., Bjursten, L. M. & Danielsen, N. Analysis of the inflammatory response to titanium and PTFE implants in soft tissue by macrophage phenotype quantification. *Journal of Materials Science: Materials in Medicine* **9,** 415–420 (1998).

58.   Rosengren, A., Johansson, B. R., Danielsen, N., Thomsen, P. & Ericson, L. E. Immunohistochemical studies on the distribution of albumin, fibrinogen, fibronectin, IgG and collagen around PTFE and titanium implants. *Biomaterials* **17,** 1779–1786 (1996).

59.   Absolom, D. R., Zingg, W. & Neumann, A. W. Protein adsorption to polymer particles: Role of surface properties. *J. Biomed. Mater. Res.* **21,** 161–171 (1987).

60.   Hughes, A. D., Marsh, G., Waugh, R. E., Foster, D. G. & King, M. R. Halloysite Nanotube Coatings Suppress Leukocyte Spreading. *Langmuir* **31,** 13553–13560 (2015).

61.   Chen, M., Zamora, P. O., Som, P., Peña, L. A. & Osaki, S. Cell attachment and biocompatibility of polytetrafluoroethylene (PTFE) treated with glow-discharge plasma of mixed ammonia and oxygen. *J. Biomater. Sci. Polym. Ed.* **14,** 917–935 (2003).

62.   Streller, U., Sperling, C., Hübner, J., Hanke, R. & Werner, C. Design and evaluation of

novel blood incubation systems for in vitro hemocompatibility assessment of planar solid surfaces. *J. Biomed. Mater. Res. B. Appl. Biomater.* **66,** 379–90 (2003).

63. Hirsh, J. *et al.* Heparin: Mechanism of action, pharmacokinetics, dosing considerations, monitoring, efficacy, and safety. *Chest* **108,** (1995).

64. Sobel, M. *et al.* Heparin modulates integrin function in human platelets. *J. Vasc. Surg.* **33,** 587–594 (2001).

65. Helms, C. C. *et al.* Mechanisms of hemolysis-associated platelet activation. *J. Thromb. Haemost.* **11,** 2148–2154 (2013).

66. Ding, F. *et al.* A biomimetic membrane device that modulates the excessive inflammatory response to sepsis. *PLoS One* **6,** (2011).

67. Hagberg, I. a & Lyberg, T. Blood platelet activation evaluated by flow cytometry: optimised methods for clinical studies. *Platelets* **11,** 137–50 (2000).

Ultrathin Polybetaine Methacrylate Surface Modifications on Silicon: Study *In Vivo*

6.1 Introduction

In the United States, majority of the ~600,000 patients suffering from end-stage renal disease are dependent on hemodialysis.[1] While daily-extended hemodialysis has demonstrated better patient outcomes than in-center thrice weekly hemodialysis,[2] the current healthcare infrastructure cannot support daily-extended hemodialysis as a viable option. Although relatively inexpensive, current hollow-fiber dialyzers used for dialysis have limitations such as wide pore size distribution reducing their selectivity to permeability ratio and high resistance to flow requiring external pump for operation. These constraints hinder technological advancements that can lead to an implantable kidney. To address this issue, our lab has developed highly uniform, low resistance silicon nanopore membranes (SNMs) for hemofiltration and immunoisolation in implantable renal replacement therapy.[3] SNMs offer controllable pore size on the order of ~10 nm and variation of <1% across the wafer.[4] Additionally, SNMs' slit pore design and tight pore size distribution allows for strict molecular cut-offs and increased hydraulic permeability, making them ideal for biological filtration and immunoisolation.

Because such applications bring SNMs in direct contact with blood, hemocompatibility of the devices must be assessed. Although silicon is non-cytotoxic, non-leaching and non-irritant,[5–7] it must also be non-activating and non-fouling for implant applications. In this chapter, we have

modified silicon with zwitterionic polybetaines—poly(sulfobetaine methacrylate) (pSBMA) and poly(carboxybetaine methacrylate) (pCBMA)—in order to improve its hemocompatibility. To apply coatings on SNMs, in addition to being non-fouling the polymers must also be hydrophilic and sub-5 nm for pore patency. Both pSBMA and pCBMA allows us to have these properties: using a methacrylate backbone polymer brushes and hydrogels can be grown to a desired thickness with atom-transfer radical polymerization (ATRP).[8–10] Biomimetic zwitterions, such as sulfobetaine, carboxybetaine and phosphorylcholine are extremely hydrophilic and coordinate water molecules through hydrogen bonding and electrostatic interactions.[9,11] This hydration layer resists protein fouling[12–16] and thrombus formation.[8,11,17]

Before clinical testing, ultrathin pSBMA and pCBMA needs to be assessed in animal model. In this chapter, we present a summary of extracorporeal study using pSBMA and pCBMA over 6 hours, as well as implant studies using pSBMA for up to 26 days. We have chosen to use a porcine model, which has demonstrated very similar platelet behavior compared to human platelets *in vitro*.[18] The study shows that pSBMA had low levels of platelet adhesion and activation, and over 26 days with optimized flow path, implant channels remained patent, which would enable the device to be functional for bioartificial organs.

6.2 Materials and Methods

6.2.1 Surface Modification

All chemicals were purchased from Sigma-Aldrich (St. Louis, MO, USA), unless stated otherwise.

6.2.1.1 Synthesis of ATRP Initiator (BrTMOS)

ATRP initiator, 2-bromo-2-methyl-N-3[(trimethoxysilyl)propyl]-propanamide (BrTMOS) was synthesized as previously reported,[14,19] and described in Chapter 2. Briefly, a 1.2:1 ratio of σ-bromoisobutyryl bromide (98%) to (3-aminopropyl)trimethoxysilane (97%) was reacted in the presence of trimethylamine in anhydrous tetrahydrofuran (THF) under nitrogen (N_2) protection. The exothermic reaction was allowed to complete overnight, and the precipitate was removed. THF was evaporated and the oil was dissolved in 20 mL of dichloromethane. The solution was washed with 10% potassium bisulfate (2 x 20 mL), cold deionized (DI) water (1 x 20 mL), and saturated sodium chloride solution (2 x 20 mL), respectively. The organic phase was collected and dried using anhydrous magnesium sulfate ($MgSO_4$). $MgSO_4$ was removed and dichloromethane was evaporated off, yielding the final product, BrTMOS. ^{1}H NMR (400MHz, $CHCl_3$) was conducted on the colorless oil to verify BrTMOS formation: δ 6.90 (s, 1H, NH), 3.49 (s, 9H, $SiOCH_3$), 3.26 (t, 2H, CH_2N), 1.95 (s, 6H, CH_3), 1.66 (m, 2H, CH_2), 0.66 (t, 2H, $SiCH_2$). NMR spectrum is included in Appendix A. The chemical structure of BrTMOS is shown below:
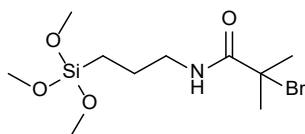
6.2.1.2 Synthesis of Carboxybetaine Methacrylate Monomer (CBMA)

Carboxybetaine methacrylate (CBMA) was synthesized as previously reported.[14] Briefly, 10 mmol (1.685 mL) of 2-(N,N'-dimethylamino)ethyl methacrylate (DMAEM) was dissolved in a flask containing 50 mL of dried acetone under nitrogen protection. Then, 12 mmol (758.5 µl) of β-propiolactone was added dropwise over 20 min. The reaction was allowed to run for ~5 hours

at 10 °C. CBMA formed as a white precipitate, which was collected onto a filter paper and washed with anhydrous acetone and anhydrous ether. As an additional drying step, CBMA was dried under reduced pressure overnight. ^{1}H NMR (400MHz, D_2O) was conducted to verify CBMA formation: δ 6.13 (s, 1H, =CH), 5.75 (s, 1H, =CH), 4.62 (t, 2H, OCH_2), 3.77 (t, 2H, CH_2N), 3.65 (t, 2H, NCH_2), 3.16 (s, 6H, NCH_3), 2.71 (t, 2H, $CH2COO$), 1.91 (s, 3H, $=CCH_3$). NMR spectrum is included in Appendix A. The chemical structure of CBMA is shown below:
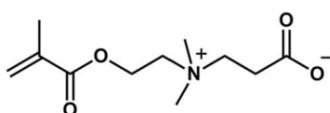
6.2.1.3 Sample Preparation

Double side polished, 400 μm thick, p-type silicon wafers were obtained from Ultrasil Corporation (Hayward, CA, USA) and diced into 1 cm^2 chips, 1 x 6.5 cm2 long chips and 3 by 6.5 cm^2 plates. The chips were cleaned by "piranha," a solution of 3:1 ratio of sulfuric acid (96%) to hydrogen peroxide (30%) for 20 min. Afterwards they were exposed to hydrofluoric acid for 5 min to remove the silicon dioxide that spontaneously forms on silicon surfaces exposed to atmospheric oxygen, followed by activation of the surface and another piranha clean. The silicon chips were then dried off with nitrogen gas and used immediately for surface modification.

6.2.1.4 PEG Surface Modification

Silicon surfaces were modified with PEG as previously described.[3,20] Briefly, substrates were dried on a hotplate at 110 °C for 1 hour. PEG-silane, 2-[methoxy(polyethyleneoxy)propyl]trimethoxysilane, was purchased from Gelest (Morrisville, PA, USA) and covalently bonded to silicon by immersing the substrates in a solution of 285 μl

PEG-silane in 25 mL of toluene for 2 hours at 70 °C. The substrates were then rinsed three times

at 10 min intervals with toluene, ethanol, and water respectively, to remove excess PEG. The

structure of PEG-silane is shown below:
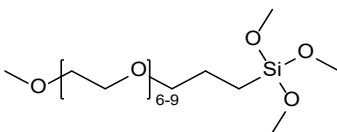
6.2.1.5 Zwitterionic Surface Modification

Zwitterionic surface modifications were conducted as previously published.[21] Briefly, the

substrates were placed in a 1% (v/v) BrTMOS solution in bicyclohexyl for 2 hours. The surfaces

were then rinsed with chloroform, ethanol, and water respectively, to remove excess BrTMOS.

The structure of 2-(methacryloyloxy)ethyl]dimethyl-(3-sulfopropyl)ammonium hydroxide

(SBMA) monomer is shown below:
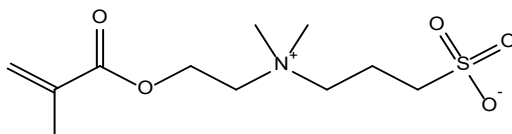
A degassed solution of 468 mg (3 mmol) of 2,2'-bipyridyl (≥98%) and individual monomers—

SBMA: 1.06g (3.8 mmol), and CBMA: 333 mg (1.5 mmol)—and 22.3 mg (0.1 mmol) of copper

(II) bromide (99%) was prepared in 5:5 mL of methanol:water. This mixture was added to a

reaction chamber housing four substrates and 143 mg (1 mmol) of copper (I) bromide (99.999%)

under nitrogen protection, and polymerization ran for 15 min for pSBMA and 25 min for

pCBMA. The substrates were then rinsed with chloroform, ethanol, Dulbecco's phosphate

buffered saline (D-PBS, UCSF Cell Culture Facility, San Francisco, CA, USA), and water

respectively, and dried using a stream of nitrogen gas.

6.2.2 Extracorporeal Experiment in Titanium Implant

a)   b)
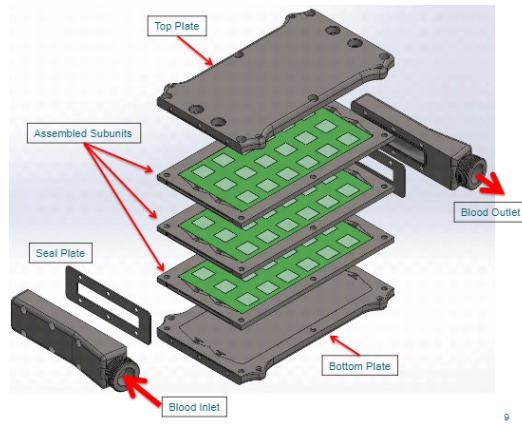
Figure 6.1: *Titanium housing (a) fully assembled, and (b) exploded view, showing three separate blood flow channels of 1 mm height.*

The titanium implant device is shown in Figure 6.1, where (a) shows a fully assembled device and (b) shows the exploded view. This custom designed implant, based on a design that has been previously published,[1] has curved flow paths at the headers that divide into three 1 mm high channels. The channels are capable of holding 18 1x1cm^2 chips on each side. Each of the three channels of the titanium implant held 18 single solid PEG-silicon, pSBMA-silicon and pCBMA-silicon chips, respectively.

The methods used were approved by University of California, San Francisco Institutional Animal Care and Use Committee, and conducted at the UCSF Laboratory Animal Resource Center. Tunneled catheters were placed in the carotid artery and jugular vein of a 55 kg Yorkshire female pig, and a closed external circuitry was set up as shown in Figure 6.2. Blood flowed from the carotid artery through Masterflex, Tygon E-LFL Tubing (L/S 25, 4.8 mm inner diameter from Cole-Parmer) to the extracorporeal device, then back through Tygon tubing to the catheter connected to the jugular vein. The pig was given 200 U/kg heparin, and a bolus of

heparin was given throughout the experiment in order to maintain a targeted activated clotting time (ACT) of ~300. The pig was also given aspirin and clopidogrel prior to the experiment. Before connecting the device to the pig, the whole system was sterilized with chlorohexadine. The system was then flushed and primed with heparinized saline. The flow experiment was run for 6 hours, at flow rate generated by the heart, which was measured to be ~60 ml/min. After 6 hours, saline was flown through the device to remove the blood. The device was taken apart and analyzed for gross blood clots. Single chips were removed and prepared for imaging for platelet adhesion and activation analysis as described below.

a)
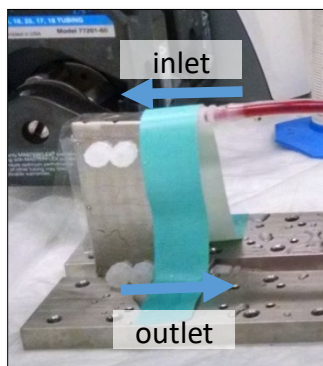
b)
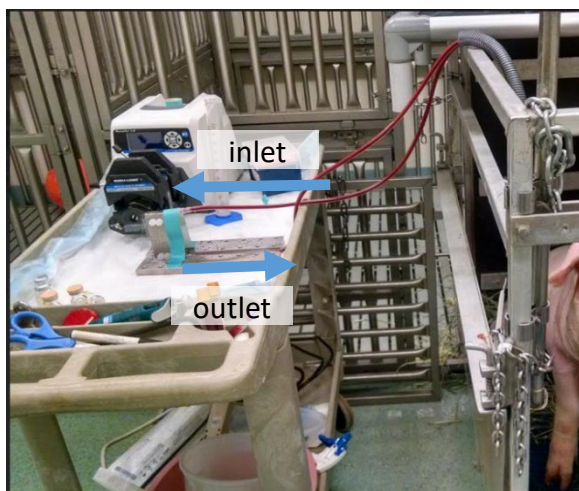
Figure 6.2: *Images from extracorporeal experimental setup: a) close up of titanium housing, indicating flow direction, and b) blood flows from the carotid artery through the titanium implant and returns to the animal via jugular vein.*

6.2.3 In Vivo *Experiments in Polycarbonate Implant Device*

Two implant studies were conducted in porcine model. The implant (Figure 6.3) holds four pSBMA-coated 6.5 cm by 1 cm solid silicon chips. The device was implanted intravascularly in two juvenile Yucatan minipigs for durations of 7-, and 26-days, respectively, in order to allow continuous exposure to flowing blood. Specifically, the device was implanted subcutaneously in

a dorsal-lateral cervical position. Six-mm expanded polytetrafluoroethylene (ePTFE) vascular grafts were anastomosed to the external jugular vein and common carotid artery, then tunneled and attached to the device, establishing an arteriovenous shunt across the device.

After surgical implantation and acute recovery, swine were monitored for behavior, appetite, activity and responsiveness twice daily. Daily hematologic assessment included complete blood count, serum C-reactive protein (CRP), serum lactate dehydrogenase (LDH) and plasma free hemoglobin. Blood flow patency was assessed daily through evaluation for a thrill and/or bruit. Additionally, Doppler ultrasonography was performed once weekly, and fluoroscopic angiography performed at 7-days and prior to device removal. The device was recovered after 7- and 26-days via a terminal re-look procedure. After device removal, animals were euthanized. All animal procedures were performed at a contract research organization (PMI, San Carlos, CA), and underwent IACUC review and approval.
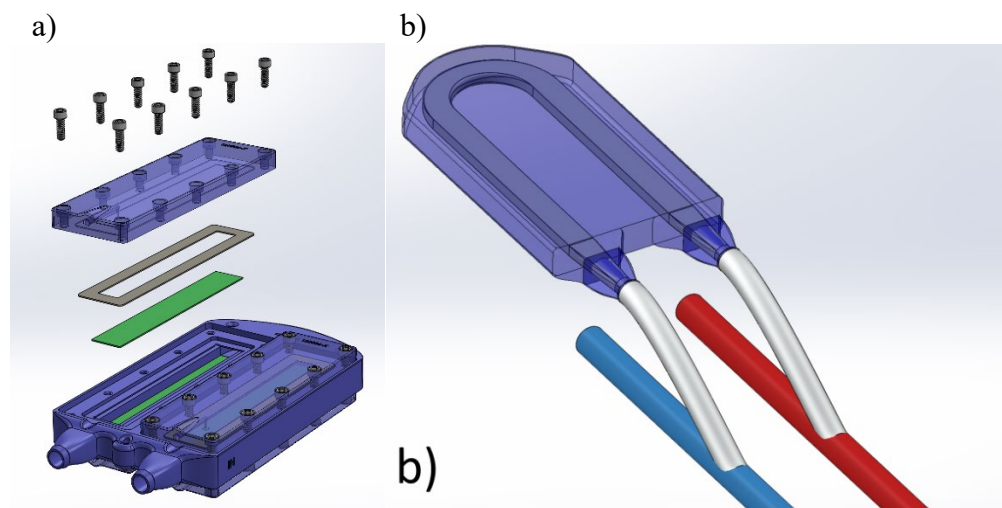
Figure 6.3: *a) exploded view and b) polycarbonate housing diagram of implant used for 7- and 26-day flow experiment in porcine model. Grafts are connected to carotid artery and external jugular vein.*

6.2.4 Post Experiment Surface Analysis

Following blood experiments, the setup was flushed with D-PBS until no trace of blood was detected in the tubing. The *in vivo* platforms were then taken apart, and the blood channels were analyzed for gross clots. For extracorporeal study, the 1x1 cm² substrates were removed and rinsed 3 times with D-PBS before preparation for analysis. The 1 x 6.5 cm² substrates in the implant study were rinsed 3 times with D-PBS and broken into ~1 cm pieces for surface analysis for cellular adhesion using scanning electron microscopy (SEM) and platelet adhesion and activation using immunohistochemistry (IHC).

6.2.4.1 Scanning Electron Microscopy (SEM)

Cellular adhesion was visualized using SEM. Samples were fixed by being placed in 3% glutaraldehyde (Sigma-Aldrich), 0.1 M sodium cacodylate (VWR) and 0.1 M sucrose solution (Sigma-Aldrich) for 48 hours. Afterwards, the substrates were removed and washed two times with deionized water and dehydrated by incubating in ethanol/water (v/v) solution for 10 min in each: 35%, 50%, 70%, 95% and two times in 100%. Samples were allowed dry overnight and mounted on aluminum stubs for imaging using a Carl Zeiss Ultra 55 Field Emission Scanning Electron Microscope (Zeiss, Dublin, CA, USA). Prior to imaging, samples were sputter coated with gold-palladium.

6.2.4.2 Immunohistochemistry (IHC)

IHC samples were fixed with 4% paraformaldehyde (Thermo Fisher Scientific) at room temperature for 30 minutes and allowed to remain in 1% paraformaldehyde at 4 °C until they were to be imaged (~1 week). Before imaging, the samples were marked for porcine platelets and platelet activation using FITC-labeled anti-CD41 (Biorbyt, Berkeley, CA, USA)) and Cy3-

labeled anti-CD62p (Bioss Inc.) markers, respectively. Samples were rinsed 3 times in PBS, and imaging was conducted using a Nikon TI-E Microscope (Nikon Instruments, Melville, NY, USA). Images were quantified for platelet adhesion and activation and averaged over 20 randomized locations using methods described in Chapter 5. Statistical significance was determined by two-way analysis of variance (ANOVA) using Sidak's multiple comparison test, and significance was defined at $p < 0.05$. Analysis was conducted using Graphpad Prism software (San Diego, CA, USA).

6.3 Results

6.3.1 6-Hour Porcine Extracorporeal Study

Initially, a 6-hour extracorporeal study was conducted, where three coatings were compared side-by-side: PEG, pSBMA, and pCBMA. Surface analysis using SEM and IHC for platelet adhesion and activation are presented in Figure 6.4 and 6.5, respectively.

There were no gross clots visible in the flow path. However, surface analysis shows a significant amount of platelet aggregates attached to the pCBMA-silicon surface, compared to PEG and pSBMA surfaces. Under visual analysis, PEG and pSBMA-modified silicon had similar levels of cellular adhesion.
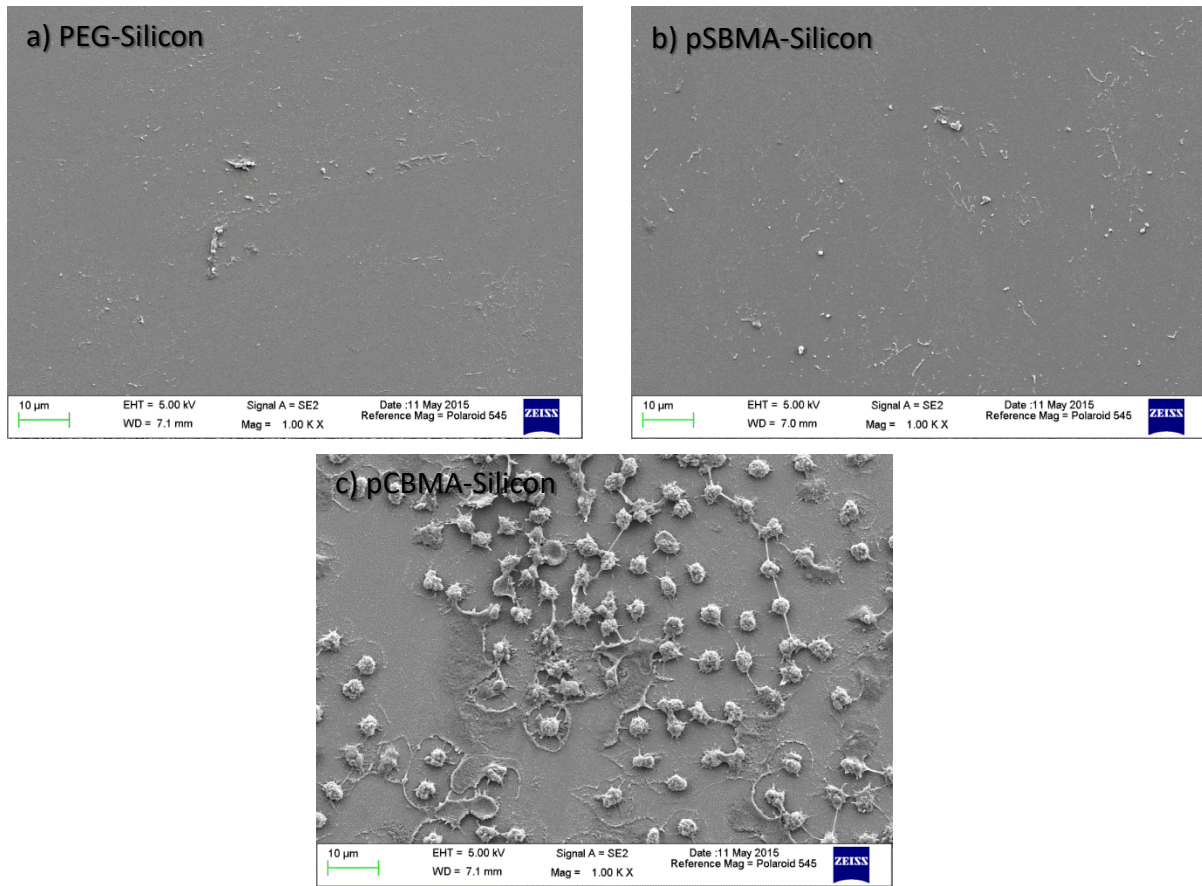
Figure 6.4: *Representative SEM images of surfaces following blood flow for 6 hours in extracorporeal porcine model for (a) PEG-silicon, (b) pSBMA-silicon and (c) pCBMA-silicon.*
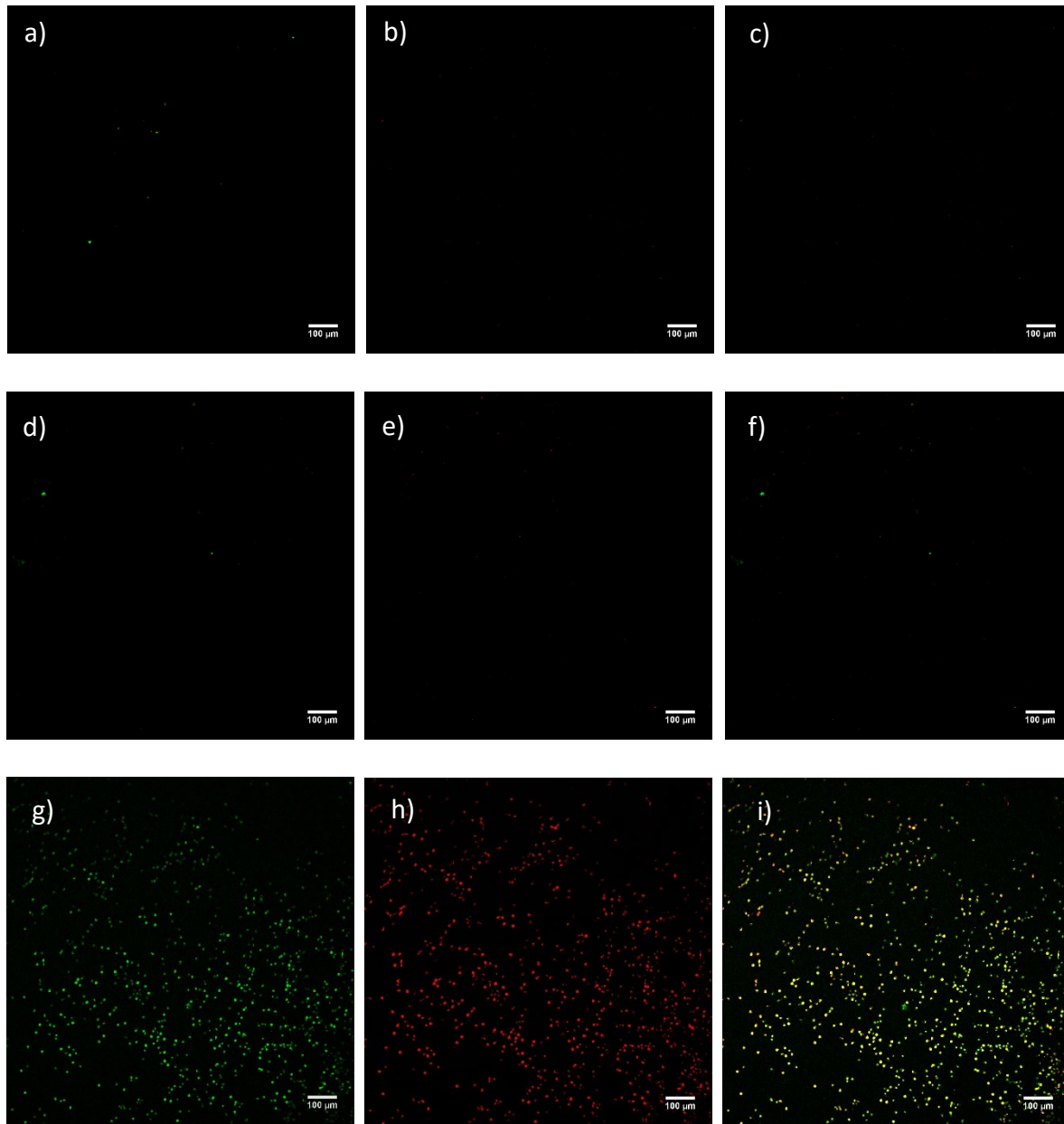
Figure 6.5: *Representative IHC images after 6-hour blood flow in extracorporeal porcine model. Top row (a-c) represents PEG-silicon, for platelet adhesion (CD41+), platelet activation (CD62+) and overlap of (a) and (b), respectively. Middle row (d-f) represents pSBMA-silicon, for platelet adhesion, activation and overlap of (d) and (e), respectively. Bottom row (g-i) represents pCBMA-silicon for platelet adhesion, activation and overall of (g) and (h), respectively.*

6.3.2 In Vivo *7- and 26-Day Porcine Implant Study*

For the two implant studies, both animals underwent successful device implantation and acute

recovery without incident. Throughout the post-implantation period, behavior, appetite, activity

202

and responsiveness remained appropriate. Serum and hematologic parameters demonstrated an

initial acute inflammatory response to surgery, characterized by elevated white blood cell count

and CRP, which resolved within seven to ten days. Following acute surgical blood loss, red

blood cell counts and hemoglobin levels improved to pre-surgical levels five days after surgery.

Serum plasma free hemoglobin remained at pre-surgical baseline, indicating negligible if any,

hemolysis. Throughout the implantation period, both devices remained patent based on physical

exam, Doppler ultrasonography, fluoroscopic angiography (Figure 6.6) and visual examination

upon device retrieval. Devices were removed intact and disassembled for analysis. As shown in

Figure 6.7, there was no gross clots evident in the flow path.
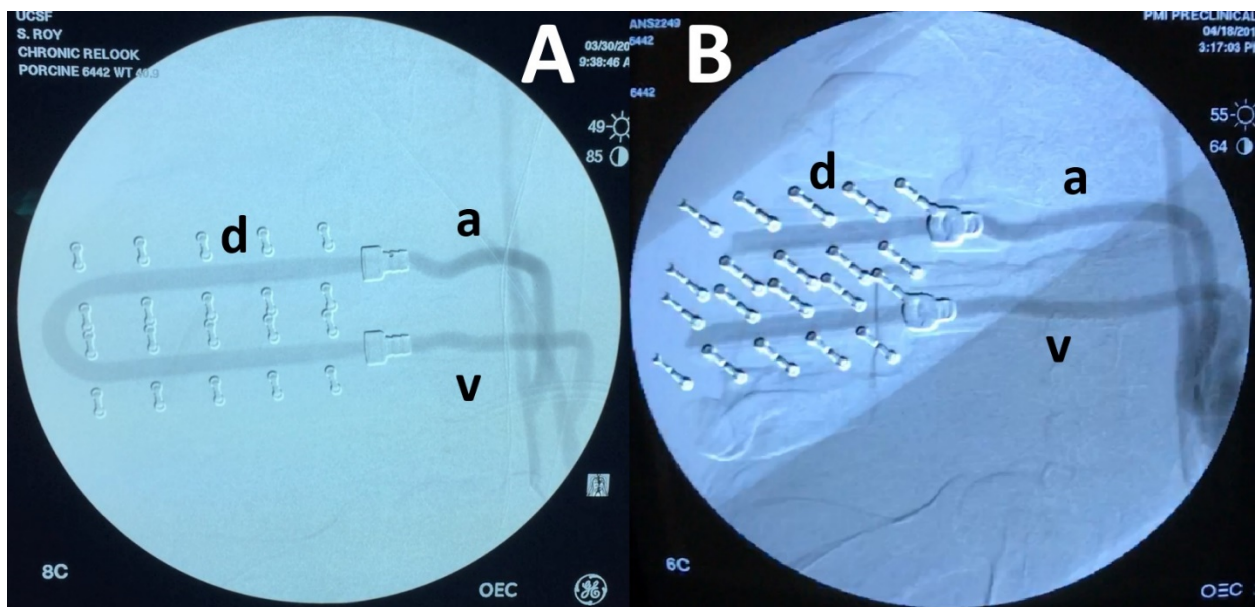
Figure 6.6: *Fluoroscopic angiography of the implanted device at (A) 7-day and (B) 26-days. The U-shaped blood flow path of the device (d), and arterial inflow (a) and venous outflow (b) grafts are widely patent at both time points.*
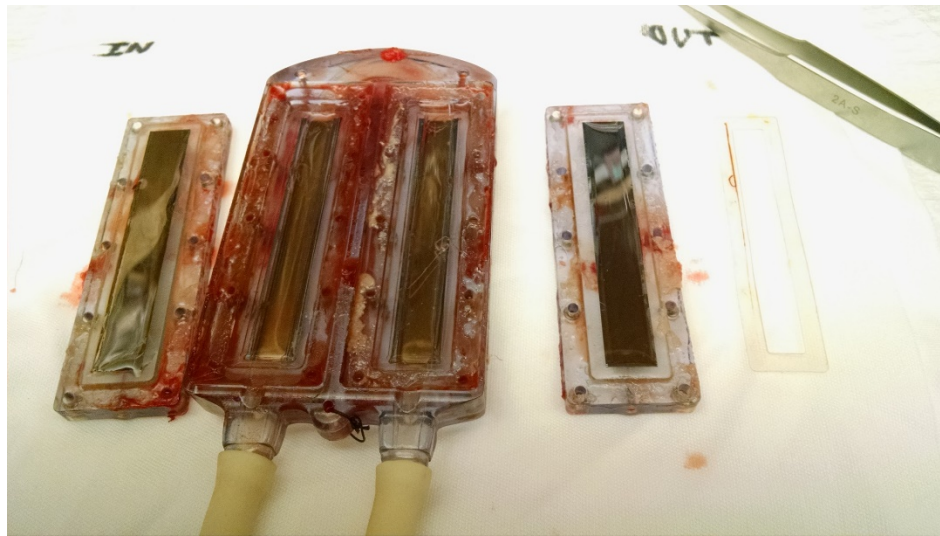
Figure 6.7: Explant after 7 days shows clot-free flow path.

Representative images of SEM and IHC surface analysis post-7-day and 26-day implant study

are shown in Figure 6.8 and Figure 6.9, respectively. These images show no presence of large

clots. However, there are platelets and platelet aggregates attached to the surface as evident in

IHC. Additionally, SEM shows a slight granularity at the surfaces, which may be due to protein

adhesion.

Figure 6.8: Representative SEM images of the pSBMA-silicon surfaces following (a) 7-day and (b) 26-day implant.
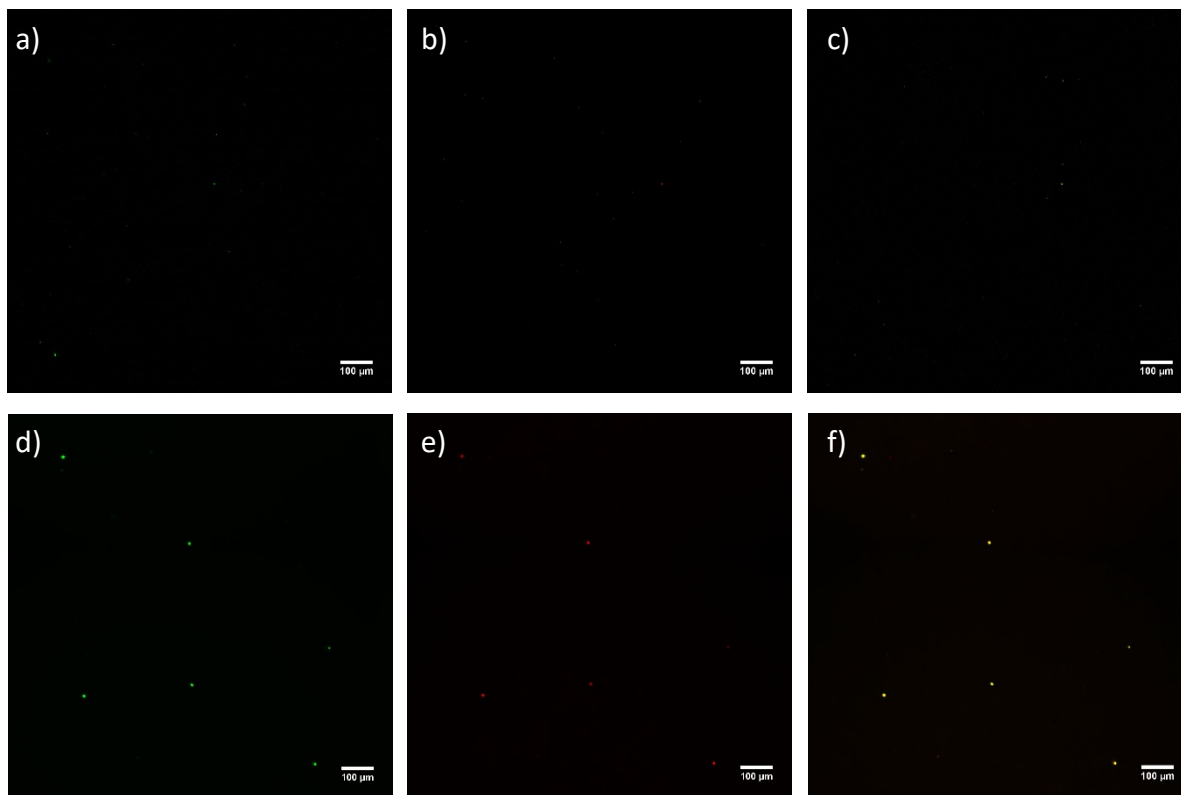
Figure 6.9: *IHC images of pSBMA-silicon surfaces after exposure to blood flow in vivo for (a-c) 7-days and (d-f) 26 days. First column (a and d) represents platelet adhesion (CD41+), second column (b and e) represents platelet activation (CD62+) and last column (c and f) represents the overlap of the first two columns.*

The IHC images were quantified and presented in Figure 6.10. After two-hour flow under *in vitro* conditions (as was presented in Chapter 5), pSBMA-modified silicon had adhered ~19 platelets/mm^2, of which ~9 platelets/mm^2 were activated. With implants, there was a positive trend in platelet adhesion. Following 7-day implant, the adhesion increased to ~74 platelets/mm^2. However, only ~14% of the platelets were activated. After 26 days under blood flow, the number of adhered platelets increased to ~159/mm^2, and ~36% of them were activated.
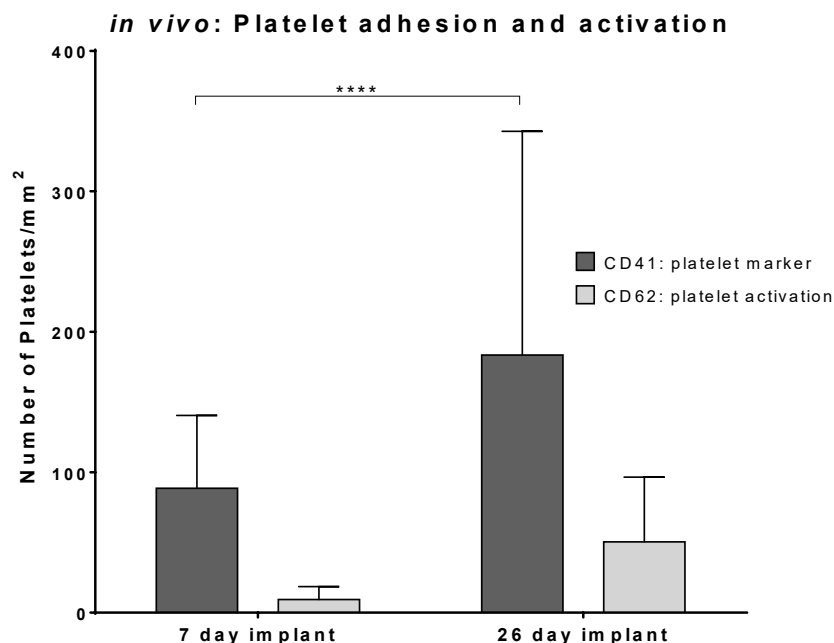
Figure 6.10: *Quantification of platelet adhesion and activation on implanted pSBMA-silicon substrates for 7 and 26 days in porcine model. **** represents p ≤ 0.0001.*

6.4 Discussion

Microelectro-mechanical systems (MEMS) technology has led to great advances in silicon-based biomedical implant applications, from diagnostic devices to artificial organs.[22–25] Although these devices meet the physical and mechanical criteria for implantation, thrombus formation on the silicon surface could lead to complications such as embolism, as well as retard the performance of the implant. Therefore, there is a need for stealth-mode, non-thrombogenic coatings to improve the hemocompatibility for long-term functionality. In this chapter, we demonstrate that ultrathin polymeric surface modifications with pSBMA has minimal activation and thrombus formation under blood flow for up to 26 days *in vivo* in porcine model. Even at sub-5 nm coating thickness, pSBMA on silicon has the potential to survive in long-term implants, clearing the way for devices such as the bioartificial kidney and pancreas.

A 6-hour study comparing coatings of PEG, pSBMA and pCBMA on silicon was initially conducted. Previous research have shown excellent non-fouling properties for all three coatings.[17,26,27] However, such a low coating thickness has not been previously studied for zwitterionic coatings. pSBMA was measured at ~3.5 nm, and pCBMA was measured at 1.7 nm. These measurements include an initiator layer, which is ~0.5 nm in thickness. This experiment showed that PEG and pSBMA had similar performance, with limited platelet adhesion and activation. Although, from previous literature, pCBMA should have been as non-fouling as pSBMA,[17] IHC and SEM imaging shows a large increase in platelet and cellular aggregates on pCBMA-silicon surface. This is most likely due to the low degree of polymerization of pCBMA on silicon surface compared to pSBMA, since coating thickness and grafting density play a critical role in their non-fouling performance.[28]

Results from the 6-hour extracorporeal study, as well as the *in vitro* data presented in Chapter 5, indicate that pSBMA is comparable to or outperforms PEG in its non-fouling and non-activating properties. Since PEG is known to degrade over a month,[21,29,30] pSBMA was chosen for further *in vivo* studies.

In vivo experimental results demonstrated that with ultrathin pSBMA on silicon, the implant remained patent over 26 days. There was no visible clot formation in the flow path, or on the pSBMA-silicon surfaces. These findings are comparable to our previous research, where uncoated and PEG-coated silicon shard and was implanted in rat femoral artery over 28 days.[31] In that experiment, PEG-coated silicon showed no thrombus formation where silicon had significant amount of clots on the surface. The porcine experiments conducted in this study demonstrated that pSBMA-silicon can also withstand clot formation on a similar time scale as PEG-silicon. Using IHC, platelet adhesion and activation was also studied, since attached

platelets can initiate coagulation cascade. While there were no presence of clots, individual platelet and platelet aggregates were found attached to the pSBMA-coated surfaces. After 7 days under blood flow, there were ~74 platelets/mm^2, with 14% activation. With 26-day blood flow, >4 times the 7-day time point, there was ~159/mm^2 adhered platelets, which is only about two-fold increase, of which 36% was activated. However, even with this positive trend, activated platelets on the surface did not lead to thrombus formation on the surface. If activated platelets initiated the coagulation pathway downstream, it was not evident in the grafts or in the animal.

6.5 Conclusions

Silicon coated with ultrathin pSBMA was tested *in vivo* in porcine model and was found to have very promising non-fouling properties. The implant remained patent over 26 days and there was minimal platelet adhesion and activation, with no thrombus formation on the surface. Although both *in vitro* fresh human blood experiments as well as *in vivo* porcine experiments indicated that pSBMA-modified silicon is a viable option for implants, clinical testing has not been done. Therefore, we have yet to determine what the human response will be. Additionally, for this study, the membrane features were not analyzed in order to isolate the effects of the surface coating. However, the added surface roughness and additional removal of filtrate from the fluid near the surface could lead to higher platelet adhesion and activation and needs to be the subject of future studies.

6.6 References

1.   Kim, S. *et al.* Preliminary diffusive clearance of silicon nanopore membranes in a parallel plate configuration for renal replacement therapy. *ASAIO J.* **62,** 169–175 (2016).

2.   Fissell, W. H., Fleischman, A. J., Humes, H. D. & Roy, S. Development of continuous implantable renal replacement: past and future. *Transl. Res.* **150,** 327–336 (2007).

3.   Kim, S. *et al.* Diffusive silicon nanopore membranes for hemodialysis applications. *PLoS One* **11,** 1–20 (2016).

4.   Fissell, W. H. *et al.* High-performance silicon nanopore hemofiltration membranes. *J. Memb. Sci.* **326,** 58–63 (2009).

5.   Fernández-Rosas, E. *et al.* Internalization and cytotoxicity analysis of silicon-based microparticles in macrophages and embryos. *Biomed. Microdevices* **12,** 371–379 (2010).

6.   Agrawal, a. a. *et al.* Porous nanocrystalline silicon membranes as highly permeable and molecularly thin substrates for cell culture. *Biomaterials* **31,** 5408–5417 (2010).

7.   Kotzar, G. *et al.* Evaluation of MEMS materials of construction for implantable medical devices. *Biomaterials* **23,** 2737–50 (2002).

8.   Nakabayashi, N. & Williams, D. F. Preparation of non-thrombogenic materials using 2-methacryloyloxyethyl phosphorylcholine. *Biomaterials* **24,** 2431–2435 (2003).

9.   Ladd, J., Zhang, Z., Chen, S., Hower, J. C. & Jiang, S. Zwitterionic polymers exhibiting high resistance to nonspecific protein adsorption from human serum and plasma. *Biomacromolecules* **9,** 1357–1361 (2008).

10.   Zhang, L. *et al.* Zwitterionic hydrogels implanted in mice resist the foreign-body reaction.

Nat. Biotechnol. **31,** 553–6 (2013).

11.   Smith, R. S. *et al.* Vascular Catheters with a Nonleaching Poly-Sulfobetaine Surface

       Modification Reduce Thrombus Formation and Microbial Attachment. *Sci. Transl. Med.*

       4, 153ra132-153ra132 (2012).

12.   Chen, S., Liu, L. & Jiang, S. Strong resistance of oligo(phosphorylcholine) self-assembled

       monolayers to protein adsorption. *Langmuir* **22,** 2418–21 (2006).

13.   Jiang, S. & Cao, Z. Ultralow-fouling, functionalizable, and hydrolyzable zwitterionic

       materials and their derivatives for biological applications. *Adv. Mater.* **22,** 920–932

       (2010).

14.   Zhang, Z., Chao, T., Chen, S. & Jiang, S. Superlow fouling sulfobetaine and

       carboxybetaine polymers on glass slides. *Langmuir* **22,** 10072–10077 (2006).

15.   Muthusubramaniam, L. *et al.* Hemocompatibility of silicon-based substrates for

       biomedical implant applications. *Ann. Biomed. Eng.* **39,** 1296–305 (2011).

16.   Carr, L. R., Zhou, Y., Krause, J. E., Xue, H. & Jiang, S. Uniform zwitterionic polymer

       hydrogels with a nonfouling and functionalizable crosslinker using photopolymerization.

       Biomaterials **32,** 6893–6899 (2011).

17.   Zhang, Z. *et al.* Blood compatibility of surfaces with superlow protein adsorption.

       Biomaterials **29,** 4285–4291 (2008).

18.   Goodman, S. L. Sheep , pig , and human platelet – material interactions with model

       cardiovascular biomaterials. (1998).

19.   Li, L., Marchant, R. E., Dubnisheva, A., Roy, S. & Fissell, W. H. Anti-biofouling

Sulfobetaine Polymer Thin Films on Silicon and Silicon Nanopore Membranes. *J. Biomater. Sci. Polym. Ed.* **22,** 91–106 (2011).

20.   Song, S. *et al.* Silicon nanopore membrane (SNM) for islet encapsulation and immunoisolation under convective transport. *Sci. Rep.* **6,** 23679 (2016).

21.   Li, L., Marchant, R. E., Dubnisheva, A., Roy, S. & Fissell, W. H. Anti-biofouling Sulfobetaine Polymer Thin Films on Silicon and Silicon Nanopore Membranes. *J. Biomater. Sci. Polym. Ed.* **22,** 91–106 (2011).

22.   Lueke, J. & Moussa, W. A. MEMS-based power generation techniques for implantable biosensing applications. *Sensors* **11,** 1433–1460 (2011).

23.   Cheung, K. C. & Renaud, P. BioMEMS for medicine: On-chip cell characterization and implantable microelectrodes. *Solid. State. Electron.* **50,** 551–557 (2006).

24.   Song, S. *et al.* An intravascular bioartificial pancreas device (iBAP) with silicon nanopore membranes (SNM) for islet encapsulation under convective mass transport. *Lab Chip* (2017). doi:10.1039/C7LC00096K

25.   Conlisk, a T., Datta, S., Fissell, W. H. & Roy, S. Biomolecular transport through hemofiltration membranes. *Ann. Biomed. Eng.* **37,** 722–36 (2009).

26.   Zhang, M., Desai, T. & Ferrari, M. Proteins and cells on PEG immobilized silicon surfaces. *Biomaterials* **19,** 953–960 (1998).

27.   Zhang, Z. *et al.* Zwitterionic hydrogels: an in vivo implantation study. *J. Biomater. Sci. Polym. Ed.* **20,** 1845–1859 (2009).

28.   Yang, W. *et al.* Film thickness dependence of protein adsorption from blood serum and

plasma onto poly(sulfobetaine)-grafted surfaces. *Langmuir* **24,** 9211–9214 (2008).

29. Han, S., Kim, C. & Kwon, D. Thermal/oxidative degradation and stabilization of polyethylene glycol. *Polymer (Guildf).* **38,** 317–323 (1997).

30. Sharma, S., Johnson, R. W. & Desai, T. a. Evaluation of the Stability of Nonfouling Ultrathin Poly (ethylene glycol) Films for Silicon-Based Microdevices. *Langmuir* 348–356 (2004). doi:10.1021/la034753l

31. Melvin, M. E., Fissell, W. H., Roy, S. & Brown, D. L. Silicon induces minimal thromboinflammatory response during 28-day intravascular implant testing. *ASAIO J.* **56,** 344–8 (2010).

CONCLUSIONS

The research work presented in this dissertation addresses the issues of hemocompatibility associated with silicon-based implants. Two ultrathin zwitterionic coatings of poly(sulfobetaine methacrylate) (pSBMA) and poly(2-methacryloyloxyethyl phosphorylcholine) (pMPC), were developed, characterized, and evaluated for hemocompatibility *in vitro* and *in vivo*. pSBMA and pMPC coatings were optimized to be at the highest functionality under sub-5 nm thickness. Their surface characterization using x-ray photoelectron spectroscopy, contact angle, atomic force microscopy and ellipsometry is presented in Chapter 2. The robustness of the coatings under biological shear (Chapter 3) and sterilization conditions (Chapter 4) were also evaluated. Data suggests the coatings are functional following shear up to 2000/s over 24 hours. Additionally, they are able withstand sterilization procedures, with best performance of pSBMA and pMPC after electron-beam sterilization and ethylene oxide gas treatment, respectively. Novel *in vitro* testing platform was designed, and modified silicon surfaces were tested against fresh human blood flow for 2 hours. Scanning electron microscopy and immunohistochemistry presented in chapter 5 demonstrated that pSBMA-silicon reduced platelet adhesion and activation by >97%. Finally, 6-hour, 7-day, and 26-day *in vivo* testing of pSBMA-silicon in porcine model in chapter 6 demonstrate that implants are patent with minimal platelet adhesion and activation.

Although these *in vitro* and *in vivo* results are promising, before application in bioartificial organs, such as on silicon nanopore membranes (SNMs) in the artificial kidney and pancreas, further studies need to be conducted. SNMs in the artificial kidney will be used for blood filtration. With the removal of fluids, blood components will become more concentrated at the surface of the membrane, which could raise additional challenge on hemocompatibility for the polymer coatings. Therefore, experiments coupling SNM filtration rates and surface coatings are critical.

In addition to coatings, there are other factors of an implant that play a critical role in blood activation. For example, non-ideal blood flow path and the shear rate can trigger coagulation or hemolysis and inflammation. Thus, experiments must be conducted to optimize the flow path and shear rate coupled with surface modifications to establish the best setup for the given application.

As presented in Chapter 6, preliminary *in vivo* experiments in porcine model demonstrated that with pSBMA coatings on silicon, the implant was able to remain patent up to 26 days. However, prior to application in long term implants, animal experiments need to be conducted for longer length of time as well, coupled with filtration to demonstrate functionality.

Finally, while platelet activation on pSBMA-silicon surfaces was low in porcine model and in *in vitro* experiments with fresh human blood, the same material could still elicit a response when implanted in humans. Therefore, carefully planned *ex vivo* clinical testing should be conducted in humans to test material hemocompatibility before its use in artificial organs.

NMR was conducted using Varian-400. BrTMOS H-NMR spectrum shown below. Based on the hydrogen atoms located on the BrTMOS molecule, each peak on the spectrum has been assigned by number. Additionally, the expected chemical shift is reported on the top left of the chart, and the measured chemical shift is reported in red.

BrTMOS (ATRP initiator) NMR:
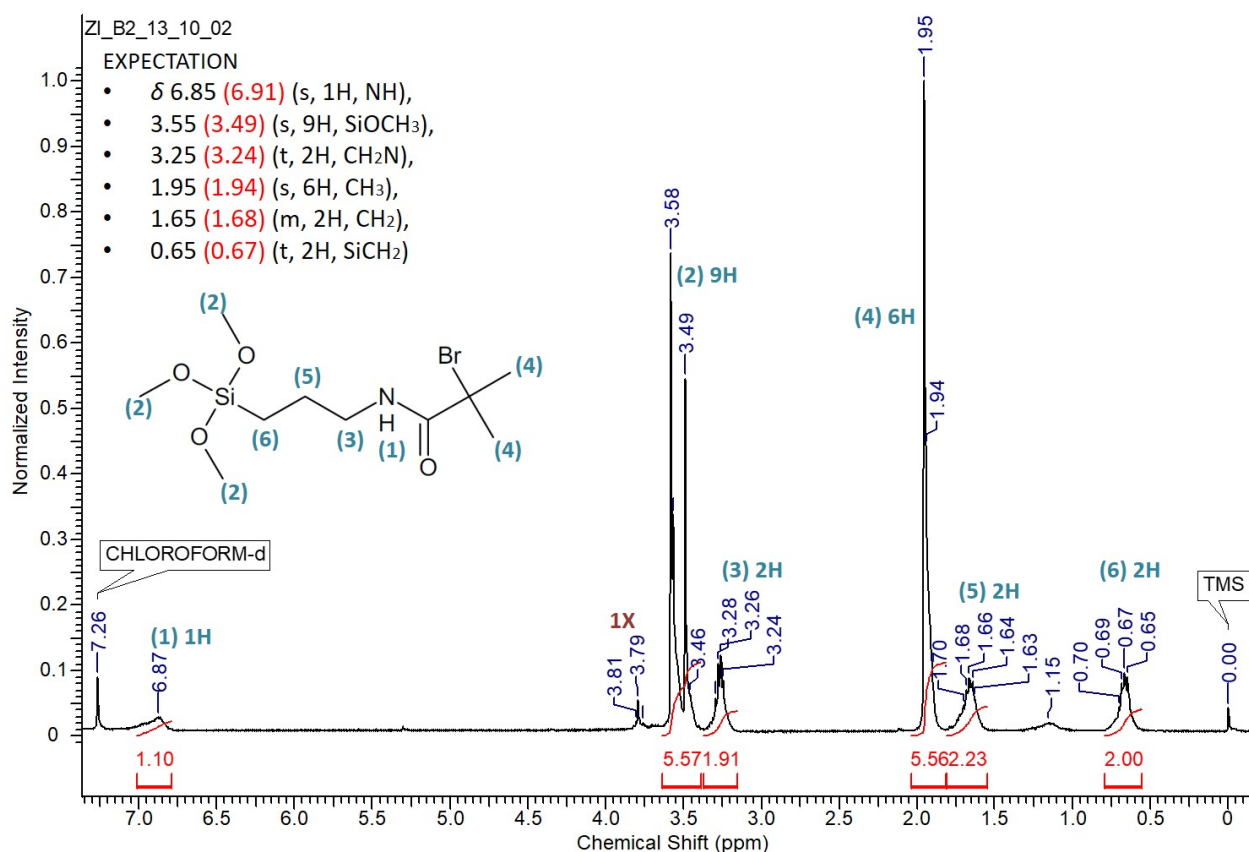
NMR was conducted using Varian-400. CBMA H-NMR spectrum shown below. Based on the hydrogen atoms located on the CBMA molecule, each peak on the spectrum has been assigned by letter. Additionally, the area under the curve, which indicates the number of hydrogen atoms is listed in red under the designated peaks.
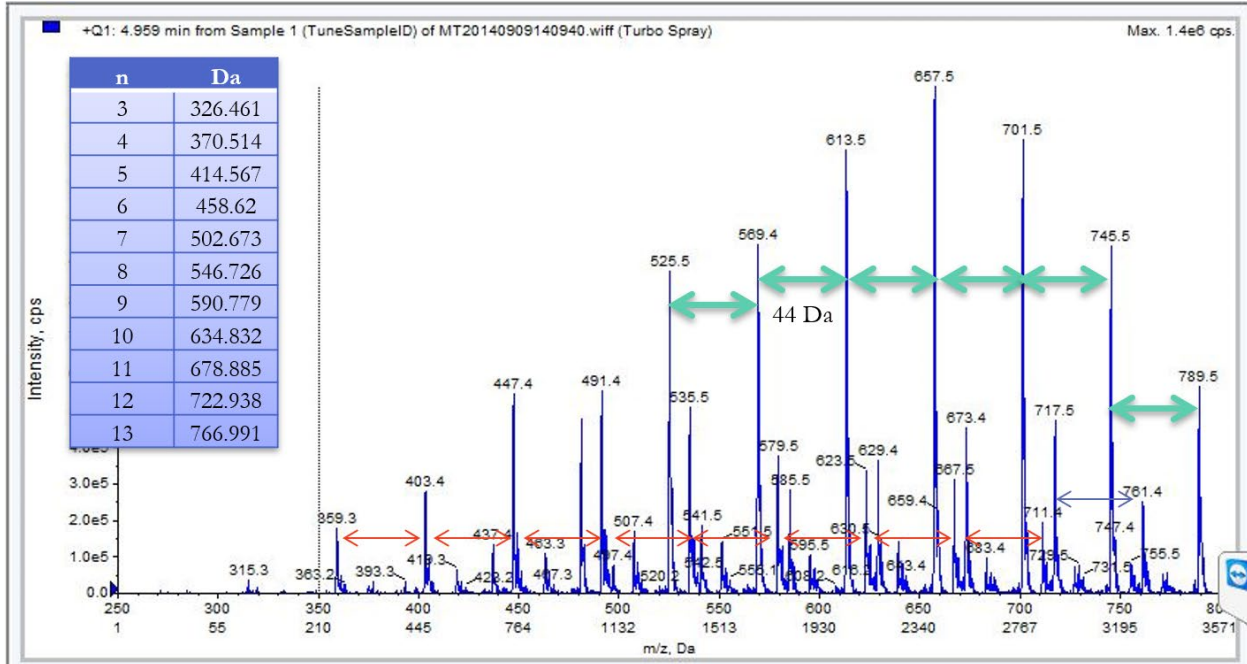
CBMA (Carboxybetaine methacrylate) NMR:
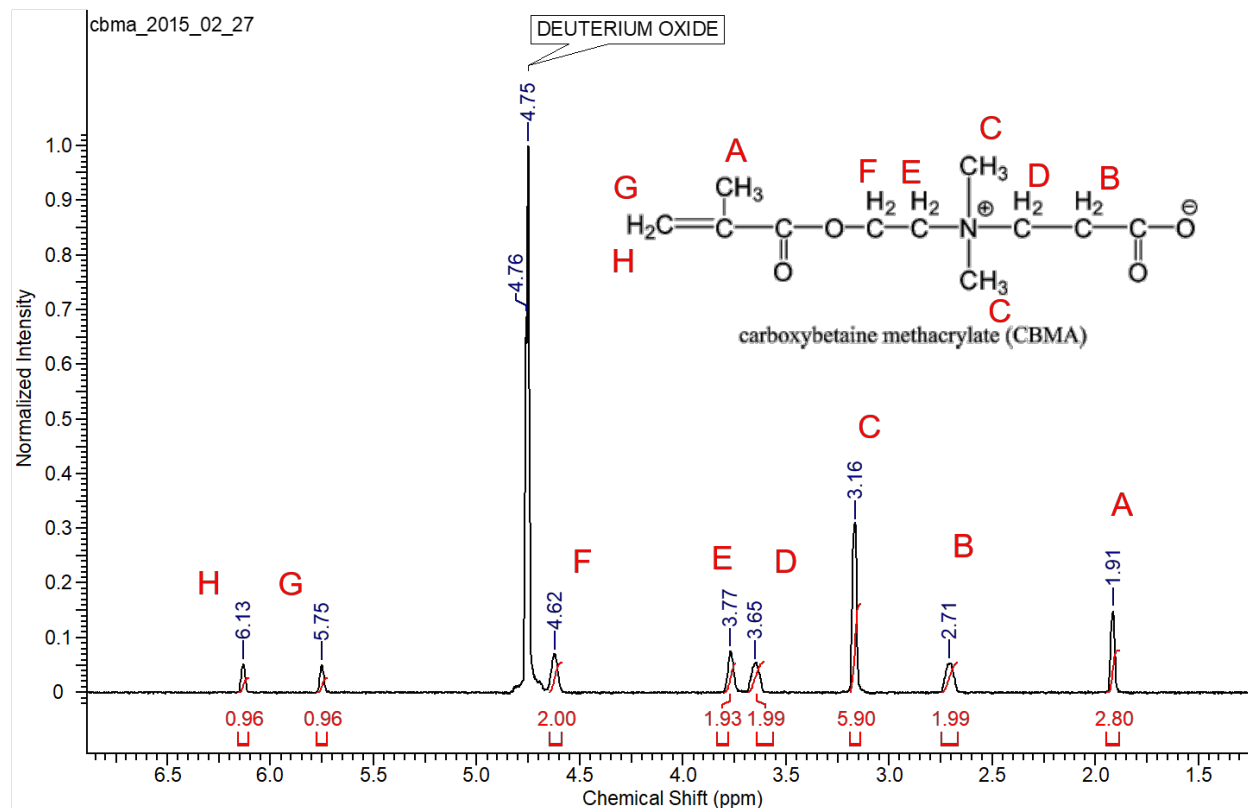
Appendix B:

Mass spectroscopy was run on polyethylene glycol (PEG) silane solution as was received by Gelest, Inc. Although expecting PEG chain on the order of 6-9 monomers in length, data shows a wide range of PEG chain distribution. Each monomer is 44 Da in size.

PEG (Gelest) Mass spectroscopy:

**Appendix C:**

Porcine Implant Experiment in Titanium Housing

Porcine model was used because of their similarity in immune response as well as comparable anatomy and physiology to humans.

| Date	09/03/15	09/03/15	11/20/15	12/14/15	01/15/16	02/08/16	02/29/16
	Animal 1 (5823)	Animal 2 (5824)		"Device 2"			
Coatings	PEG, SBMA, MPC	PEG, SBMA, MPC	PEG, SBMA, MPC	PEG, SBMA, MPC	PEG	SBMA	SBMA
Implant duration	3 days	3 days	4 days	~2 hours	4 days	8 day	3 days
Notes	thrombosed	thrombosed	Good Doppler signal x3 days, Gone on 4th day	Immediate cardiac arrest post-op	Flowed on POD3, day 4 catastrophic hemorrhage	Thrombosed	Thrombosed

The device was connected at the aortic artery and iliac vein. However, all the devices had thrombosed by the explant date. Several changes were made throughout the experiments to improve the outcome

- Changes the connectors (from just Dacron to Dacron and PTFE, to Dacron bonded to PTFE with the addition of silicone sleeve), as shown in left image below.
- Lowering the weight of the device by switching over the exterior from titanium to PEEK (40% decrease in weight)
- Anchoring (mesh jacket to anchoring points on PEEK housing)
- Anticoagulation regimen
- Surface coatings (PEG, pSBMA, pMPC)
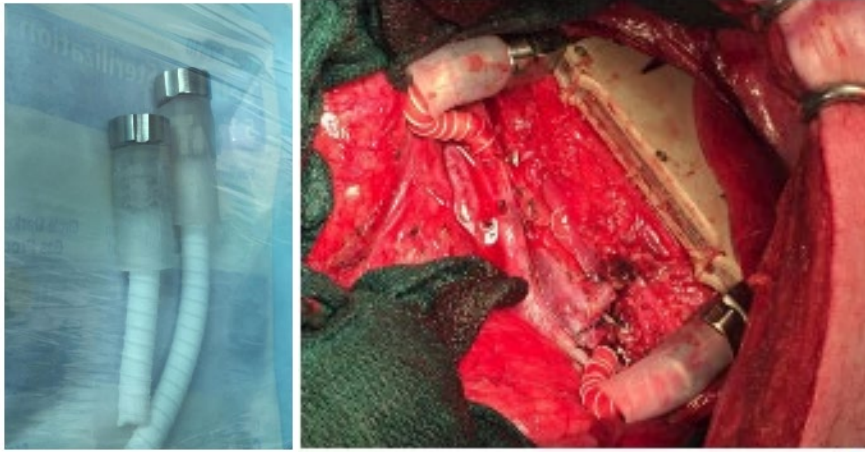
Below are some images taken of the device after explant, and device disassembly:
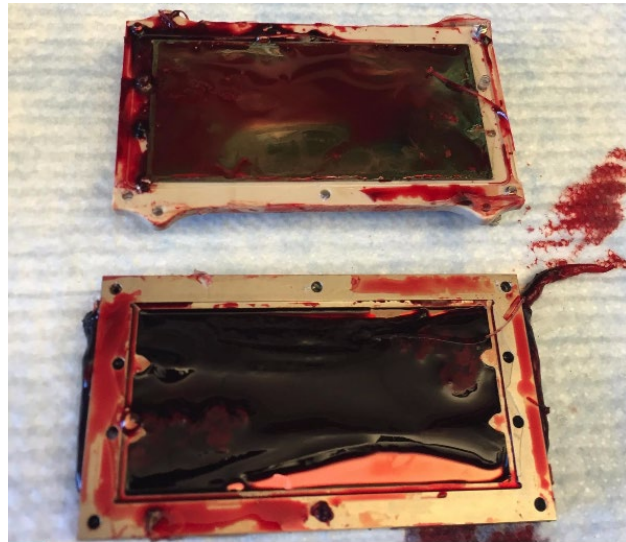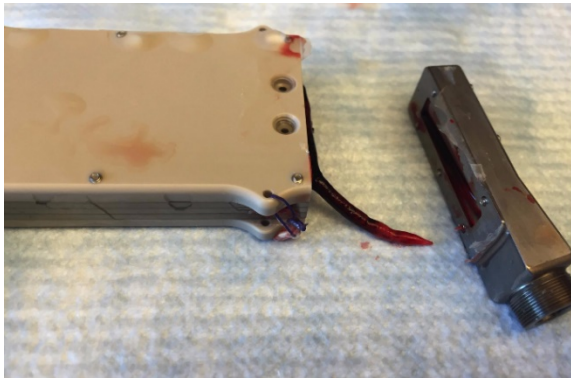
(02/08/16 Implant) Images above shows that older clot (lighter in color) is present at the inlet and outlet rather than the channel itself.
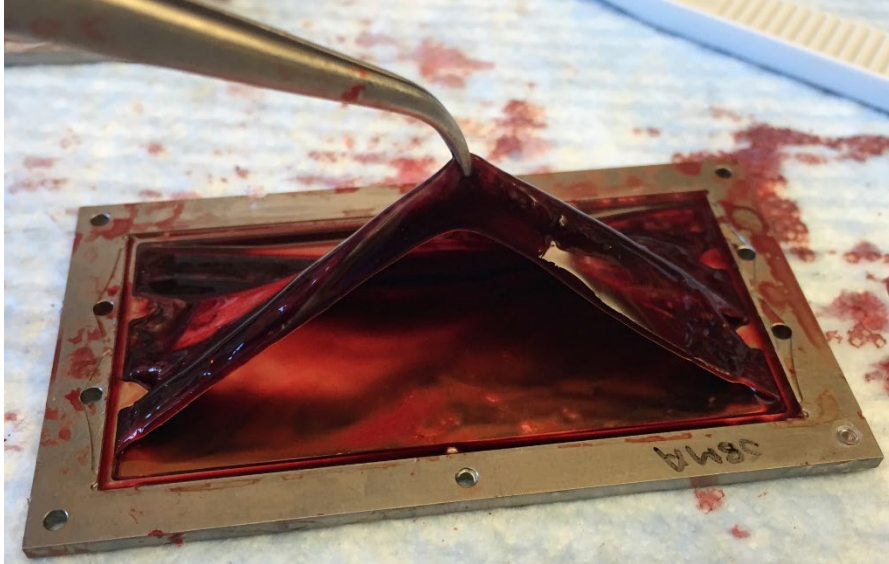
As shown in the image above, the clots do not attach strongly to the surface. Rather, they are anchored in the inlets and outlets of the channels. Nonetheless, the surfaces show presence of activated platelets using scanning electron microscopy and immunohistochemistry (as shown below).

From 8 day implant (02/08/16)
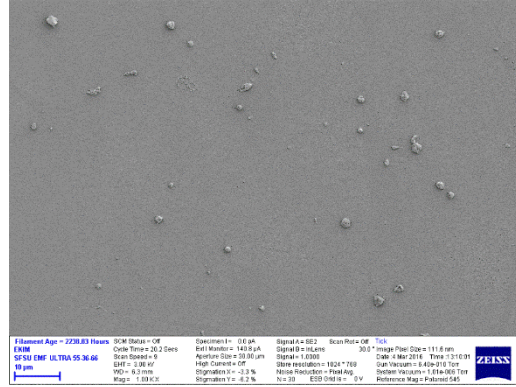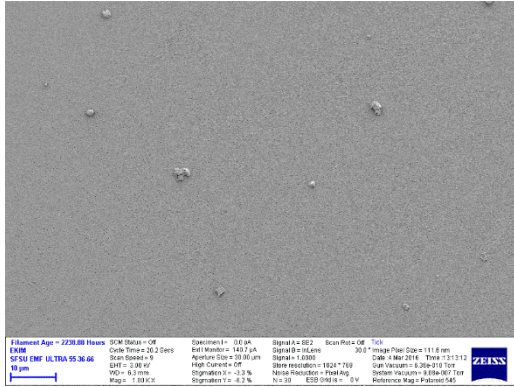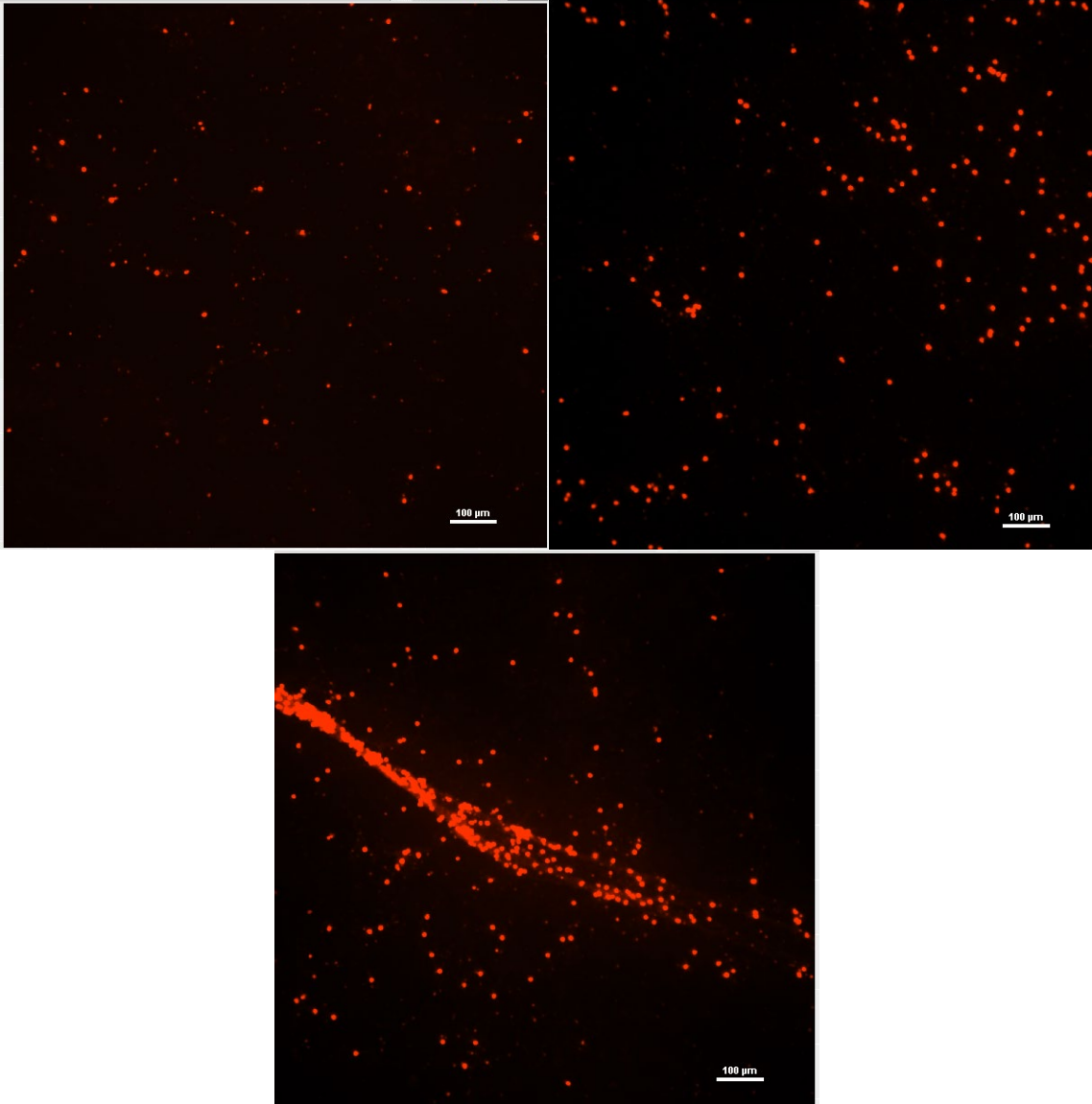
Appendix D:

Detailed protocols of polysulfobetaine methacrylate surface modification:

PolySBMA Coating on Silicon (10x10mm chips)

Time required: ~5 days   [Adapted from Li, et al. *J of Biomat Sci 22(2011)* and Zhang et al. *Lang 22 (2006)*]

DAY 1: Formation of Initiator (BrTMOS) Part I

Materials:

Chemicals

- Tetrahydrofuran (THF, HPLC grade)
- 3-aminopropyltrimethoxysilane (MW = 179.29g/mol; density = 1.027g/mL)
- Triethylamine (MW = 101.19g/mol; density = 0.7255g/mL)
- Alpha-bromoisobutyryl bromide (BIBB, 98%) (MW = 229.9g/mol; density = 1.86g/mL)
- Mineral Oil (Sigma: M5904-5x5mL)

Equipment

- N_2 supply (tank)
- 1x hot plate/stir plate
- Cork round-bottomed flask holder
- 2x Metal stand
- 3 clamps
- 3-neck flask
- 1x stir bar (medium size)
- 3 rubber septa
- 3 5ml syringes
- 1 20mL syringe
- long needles (for transferring)
- Gas bubbler
- Connector Pipe from setup output 1 to gas bubbler (short, flexible)
- Timer

Method

In organics fume hood

Note: if glassware not dried immediately before these next step, vacuum dry (12 hours) at 110° C

1. Setup system according to ***image 1***
   a. Place in the magnetic stir bar
   b. Run N_2 for 5 min to fill the chamber
2. Place **50 mL of dried THF** in 3-neck flask

3. Add **1.75mL (10 mmol) of 3-aminopropyltrimethoxysilane** to 3-neck flask
4. Add **1.39 mL (10 mmol) of triethylamine** to 3-neck flask.
5. Place in **1.35 mL (11 mmol) of BIBB** in the addition syringe
6. Slowly drip BIBB over 30 min: rate less than or equal to 1 drop/6 sec
7. Keep setup overnight (12 hours) under nitrogen protection.
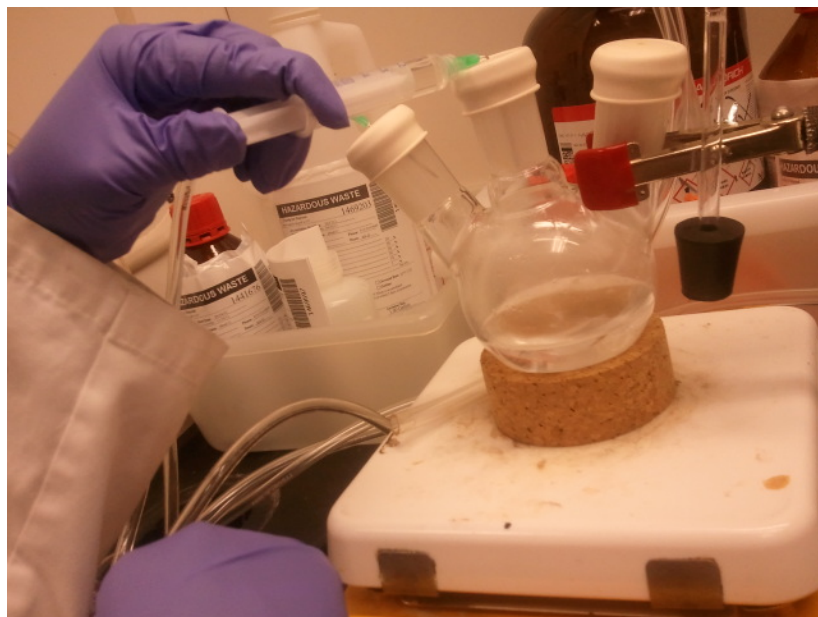
DAY 2: Extracting Initiator

Materials

Chemicals

- Tetrahydrofuran (THF, HPLC grade) dried by sodium before use.
- Dichloromethane
- 10% KHSO$_4$ solution
- Brine solution
- RO water
- Mg$_2$SO$_4$

Equipment

- Glass funnel
- Clamp
- Metal stand
- Pressure filtration system from sigma
- N$_2$ supply (tank)
- Connector Pipe from N2 tank to input 1 of filtration setup (long, flexible)
- Connector Pipe from input 2 of filtration setup to vacuum (medium flexible)

- 2x Frit funnel syringes
- Recovery Flask
- 1x Polyethylene stopper
- 1x rubber stopper (size 4)
- Rotary Evaporator

Method

1. Filter out precipitate using frit funnel under N_2 pressure
2. Evaporate off THF using Rotavap.
3. Redissolve oil in **20 ml of dichloromethane** (or ether).
4. Transfer solution to separation funnel
5. Wash solution 2x with **10% KHSO$_4$ solution (20mL)**.
6. Wash **with cold water 20mL**.
7. Wash with 2x **brine water 20mL** (until solution is clear)
8. Dry organic phase with **anhydrous Mg$_2$SO$_4$**.
9. Separate out Mg$_2$SO$_4$ using frit funnel.
10. Evaporate off dichloromethane using Rotavap.

NMR sample preparation

Materials

Chemicals

- Chloroform-D
- 3-aminopropyltrimethoxysilane
- SYNTHESIZED FROM ABOVE: BrTMOS: 2-bromo-2-methyl-N-3-[(trimethoxysilyl)propyl]-propanamide

Equipment

- 2x NMR tubes
- 1x glass pipette
- 2x 50mL falcon tube to hold NMR tubes and falcon tube holder
- 1000μl Pipette and tips

Method

1. Label NMR tubes (C = control, S = sample)
2. Using glass pipette, pick up some BrTMOS solution (approx. 3-5mm)
3. Place glass pipette on top of NMR tube S.
4. Add in 600-800 μl of Chloroform-D on top.
5. For Control, place in 1ul of amino-silane in NMR tube labeled S
6. Add in 600-800 μl of Chloroform-D on top.
7. Do NMR.
8. Clean out NMR tubes with chloroform.

DAY 3: Silicon Chip coating

Materials

Chemicals

- DI Water
- Ethanol
- Sulfuric Acid (H_2SO_4)
- Hydrogen Peroxide (H_2O_2)
- BrTMOS (made as described above)
- Bicyclohexyl
- Copper (I) bromide (CuBr, 99.999%)
- Copper (II) bromide (CuBr2, 99.999%)
- 2,2'-bipyridyl (BPY, 99%)
- [2-(methacryloyloxy)ethyl]dimethyl-(3-sulfopropyl)ammonium hydroxide (SBMA, 97%)
- Hexane
- Ethanol
- Methanol
- PBS
- Water

Equipment (sufficient for coating 8x [10x10 mm] chips)

- 1x hot plate/stir plate
- 1x stir bar (smallest available)
- Size 4 rubber stopper with 1 hole (5mm)
- 5mm thick glass tubing
- 2x Glass jar (1 closed; 1 with N2 opening)
- 50mL falcon tube
- 2 petri dishes
- Nitrogen Source

Method

1. Piranha
2. HF
3. Piranha
4. transfer chips from water to ethanol
5. rinse in ethanol 3 times (5 min each)
6. Make a solution of BrTMOS and anhydrous bicyclohexyl (1% ,v/v)
   a. In a petri dish, add 25 mL of bicyclohexyl
   b. Add 250 μL of BrTMOS
7. Cleaned Silicon chips were directly placed into solution made in step 3; leave for 2 hours
8. Substrates were removed from solution and rinsed with chloroform and DI water (3x each)
9. substrates remained in water.
10. Place substrates (2-4), 214.5 mg of CuBr, and stir bar in plate inside jar.
11. Place jar under nitrogen protection.

225

12. In a 50 mL falcon tube, add 7.5 ml of methanol, and 7.5 ml of water
    a. degas solution for 10 min
13. To the degassed methanol/water mix:
    a. Add 1.59g of SBMA
    b. Add 702 mg of BPY
    c. Mix until SBMA and BPY is well dissolved
14. Add 33.5 mg $CuBr_2$ to mixture and degas for 10 min
15. Transfer solution to jar containing substrates under nitrogen protection
16. Allow reaction to occur for 10 min, and 20 min
17. Remove substrates and rinse with ethanol and water, PBS
18. Substrates stored dry. (or in water in case of membrane)

BEFORE

19. In a 50ml falcon tube, add 5 ml of methanol and 5 ml of water
    a. Attach to vacuum to it
    b. Degas solution for 10 min
20. To the degassed methanol/water mix:
    a. Add 1.06 g (3.8 mmol) of SBMA
    b. Add 312 mg (2mmol) of BPY
    c. Mix until SBMA and BPY is well dissolved
21. Add 67 mg $CuBr_2$ (0.3 mmol) to mixture and degas for 20 min protection
22. Add 143 mg of CuBr (1mmol), and mix well
23. Transfer solution to jar containing substrates under nitrogen protection
24. Allow reaction to occur for 15 min
25. Remove substrates and rinse with ethanol and water
26. Samples stored in water overnight
27. Substrates dried in air before use.
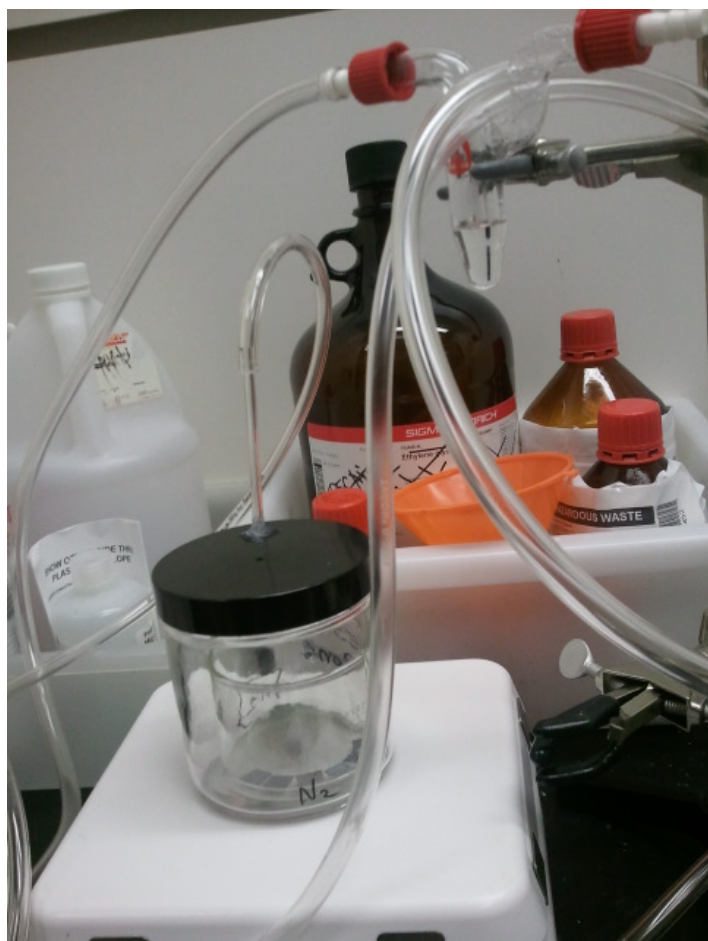
Appendix E:

Detailed protocols of polyethylene glycol (PEG) surface modification:

Liquid PEG Deposition on Silicon (10x10mm chips) [Adapted from Lingyan Li, Cleveland Clinic]

Time required: Day 1: 2 hr; Day 2: 5 hr

Materials

Chemicals

- Acetone (JT Baker)
- Methanol [MeOH] (JT Baker)
- Isopropyl Alcohol [IPA, 2-Propanol] (JT Baker)
- Ethanol anhydrous [EtOH] (Sigma Aldrich)
- Toluene (JT Baker)
- Sulphuric Acid [H_2SO_4] (JT Baker)
- Hydrogen Peroxide [H_2O_2] (JT Baker)
- PEG-silane (Gelest SIM6492.7 25g)

Equipment (sufficient for coating 8x [10x10 mm] chips)

- 1x hot plate
- 1x stir bar (5/16 x 1/2 in)
- 3x 100x20mm glass Petri dishes with covers
- 1x 50 mL, 1x 25 mL glass graduated cylinders
- 2x glass or plastic funnels

Method

In organics fume hood:

Step 1. Clean all glassware (see Glassware General Cleaning Protocol)

Step 2. Immerse SNM chips in 30 mL acetone ....[10 min]

Step 3. Drain acetone in solvent waste; immerse SNM chips in 30 mL MeOH...[5 min]

Step 4. Drain MeOH in solvent waste; immerse SNM chips in 30 mL IPA..[5 min]

Step 5. Drain IPA in solvent waste; rinse SNM chips in 30 mL DI H_2O ....[3x 5 min]

In acids fume hood:

Step 6. Place a sign reading "DANGER: Piranha" with your name/number; place on ledge of acids fume hood

Step 7. Use 1st funnel to pour 30 mL H_2SO_4 in 50 mL graduated cylinder

Step 8. Use 2nd funnel to pour 10 mL H_2O_2 in 25 mL graduated cylinder

Step 9. Combine H_2O_2 and H_2SO_4 in Petri dish (add H_2O_2 first, then H_2SO_4!)

Step 9. Immerse SNM chips in freshly prepared Piranha 3:1 (30 mL: 10 mL) H_2SO_4: H_2O_2 ....[20 min]

Step 8. Remove SNM chips and rinse in 30 mL DI H_2O ....[3x 5 min]

At lab bench:

Step 9. Place SNM chips on clean Alpha wipe in plastic Petri dish and dry in air................................[overnight]

In organics fume hood:

Step 10. Rinse SNM chips; use 2 clean dishes for rinsing each group of chips so that one dish can be cleaned with acetone and DI H_2O while the other is in use

- 30 mL EtOH...[3x 10 min]
- 30 mL toluene ....[2x 10 min]

Step 10. Completely dry SNM chips in glass Petri dishes on hotplate at 110 °C..[90 min]

Step 11. Remove SNM chips from Petri dish, set hotplate to 70 °C .... [wait for temperature to stabilize]

Step 12. Add 25 mL toluene to dish

Step 13. Immerse SNM chips and magnetic stir bar in toluene dish

Step 14. Add 285 μL PEG-silane; stir at speed 7 with cover on dish...[2 hr]

Step 15. Rinse SNM chips; use 2 clean dishes for rinsing each group of chips so that one dish can be cleaned with acetone and DI H_2O while the other is in use

- 30 mL toluene ....[2x 10 min]
- 30 mL EtOH...[3x 10 min]
- 30 mL DI H_2O..[3x 10 min]

At lab bench:

Step 16. Place SNM chips on clean Alpha wipe in plastic Petri dish and dry in air................................[overnight]

CBMA Synthesis

Adapted from Zhang et al, Langmuir 2006

Supplies:

- 250 ml Round bottom flasks
- ice and ice holder

Chemicals:

- Acetone
- MgSO4 (drying agent)
- DMAEM
- beta-propiolactone

1. Dry 75 mL of acetone with MgSO4
2. Place in 50 mL of dried acetone in flask: flask with ice and stir bar
3. Place in 1.685 mL (10 mmol = 1.5721g) of DMAEM
    a. keep DMAEM stored in 2-8C
4. Keep nitrogen protected

5. Add in 758.5 ul (12mmol = .87g) of B-propiolactone to 10 mL dried acetone into a falcon
6. add dropwise into DMAEM/acetone
7. let reaction run for 5 hours under ice
8. collect white precipitate on filter paper
9. wash precipitate with 50 mL of anhydrous acetone
10. wash precipitate with 100 mL of anhydrous ether (or hexane)
11. dry under reduced pressure

CBMA synthesis (precipitate forming) done under nitrogen protection.

Publishing Agreement

It is the policy of the University to encourage the distribution of all theses, dissertations, and manuscripts. Copies of all UCSF theses, dissertations, and manuscripts will be routed to the library via the Graduate Division. The library will make all theses, dissertations, and manuscripts accessible to the public and will preserve these to the best of their abilities, in perpetuity.

Please sign the following statement:

I hereby grant permission to the Graduate Division of the University of California, San Francisco to release copies of my thesis, dissertation, or manuscript to the Campus Library to provide access and preservation, in whole or in part, in perpetuity.

_____   12/26/2018
Author Signature   Date